Planets in a different light: Imaging and spectroscopy in the infrared

Dominique Petit dit de la Roche

München 2021

Planets in a different light: Imaging and spectroscopy in the infrared

Dominique Petit dit de la Roche

Dissertation
an der Fakultät für Physik
der Ludwig–Maximilians–Universität
München

vorgelegt von
Dominique Petit dit de la Roche
aus Blaricum, Nederland

München, den 01-08-2021

Erstgutachter: Prof. Dr. Markus Kissler-Patig
Zweitgutachter: Prof. Dr. Barbara Ercolano
Tag der mündlichen Prüfung: 28-09-2021

Because it's there.
George Mallory

Contents

List of Figures

List of Tables

Zusammenfassung

Das Forschungsgebiet der Exoplaneten vergrößert sich rasch und heutzutage sind über 4000 Exoplaneten bekannt. Die große Anzahl an bekannten Exoplaneten erlaubt statistische Untersuchungen der Populationen. Insbesondere ist die Charakterisierung von Planeten in ihrer heutigen Form essenziell, um die Entstehung und Entwicklung von Exoplaneten zu verstehen.

Planeten mit kleiner sowie mit großer Entfernung ihres Heimatsterns kommen mit unterschiedlichen Häufigkeiten vor, was auf verschiedene Entstehungsmechanismen hindeutet. Die Untersuchung von Planeten in großen Abständen von ihrem Stern ist daher wichtig und für Untersuchung dieser Objekte ist die direkte Bildgebung besonders gut geeignet verglichen mit anderen Methoden. Direkte Bildgebung im mittleren Infrarot wird die Charakterisierung von kälteren und daher älteren und kleineren Planeten ermöglichen, doch dies wurde noch nicht erreicht. Bildgebung im mittleren Infrarot mit dem VISIR Instrument und dessen Upgrade NEAR wurde von drei Arten von Systemen aufgenommen: sechs sehr junge Systeme mit Planeten, die sich vermutlich noch in ihrer Entstehungsphase befinden, das junge, aber vollständig geformte HR 8799 System und schließlich vier reife Systeme in der näheren Umgebung der Sonne. Mit einer Ausnahme haben all diese Systeme bereits bekannte oder vermutete Begleiter mit planetentypischen Massen. Keine dieser Begleiter wurden detektiert, doch es wurden die bislang strengsten Flusslimits im mittleren Infrarot für alle Systeme sowie für mögliche noch unentdeckte Begleiter bestimmt. Umgerechnet in Beschränkungen für Begleitermassen bedeutet dies, dass akkretierende Planeten mit zirkumplanetaren Scheiben weiter als 1″ um die meisten der sehr jungen Sterne ausgeschlossen werden können, was darauf hindeutet, dass Planetenentstehung mit großen Abständen zum Stern selten ist. Das Massenlimit für Begleiter des sonnenähnlichen Sterns ε Indi A zeigt, dass ein Begleiter am älteren Ende der Alterspanne sein muss, da ein junger Planet entdeckt worden wäre. Die erreichte Sensitivität in den Beobachtungen zeigt auch, dass Begleiter mit planetentypischen Massen mit heutigen Instrumenten entdeckt werden können und dass in unter 10 Stunden mindestens vier Planeten mit VISIR und mindestens 16 mit NEAR entdeckbar sind.

Es gibt auch einen Mangel an Supererden mit sehr kurzen Umlaufbahnen. Viele von diesen Planeten erhalten hohe XUV Strahlung, die ihre Atmosphären vergrößern und erodieren. Dies ist eine wichtige Phase in der Planetenentwicklung. Die vergrößerte Atmosphäre erleichtert die Messung dieser Planeten mit der Transitmethode und macht sie daher zu guten Beobachtungszielen für Transmissionspektroskopie. Die Supererde GJ 1214 b und der heiße Jupiter WASP-15 b sind solche Planeten. Die verdampfende Heliumatmosphäre von GJ 1214 b kann durch Messungen der Transittiefe bei 10,830 Å mit Archivdaten des X-Shooter Instruments besser beschrieben

werden. Diese Studie zeigt auch, dass X-Shooter die benötigte Stabilität aufweist, um diese Art von Messungen bei passenderen Objekten anzuwenden. Für den heißen Jupiter WASP-15 b werden Gauß-Prozesse benutzt, um korreliertes Rauschen aus den Daten zu entfernen und um ein Transmissionsspektrum der Atmosphäre zu konstruieren. Allerdings sind weitere Messungen notwendig, um bestimmte Atmosphärenmodelle auszuschließen.

Abstract

With over 4000 discoveries to date, the field of exoplanets is rapidly expanding. The large numbers of detections allow for population level statistical analyses. As a part of that, the characterisation of planets in their current form is vital to understanding the formation and evolution of exoplanets.

Different occurrence rates for planets close to and far from their host stars indicate there may be different formation mechanisms at play. The study of planets at large separations from their host stars is therefore important. Direct imaging is particularly suited to study these planets when compared to other methods. Expanding it to the mid-infrared will allow for the characterisation of cooler and therefore older and smaller planets, but this has not yet been achieved. With the mid-infrared imaging and spectroscopy instrument VISIR and its upgrade NEAR data is obtained of three types of systems: six very young systems with planets that are still expected to be in their formation stage, the young, but fully formed HR 8799 system, and finally four mature systems in the solar neighbourhood. All but one are already known or expected to have planetary mass companions. None of these are detected, but the most stringent mid-infrared flux limits to date are obtained for all of them and for additional companions beyond 1″ in any of the systems. The conversion to mass limits rules out accreting planets with circumplanetary disks beyond 1″ around most of the very young stars, which indicates that planet formation at large radii is rare. The mass limits for companions around the sun-like ε Indi A show that it is at the older end of the age range, as a younger planet would have been detected. The achieved sensitivity in the observations also shows that detection of planetary mass companions is within the range of present day instrumentation and that at least four planets are detectable with VISIR and at least sixteen with NEAR in less than 10 hours.

There is also a lack of super Earths on very short orbits. Many of these planets undergo high XUV irradiation, causing their atmospheres to puff up and erode. This is an important stage in the planets evolution. The expanded atmosphere also makes them easier to measure in transit and good targets for transmission spectroscopy, as it increases the signal size. The super Earth GJ 1214 b and the hot Jupiter WASP-15 b are such planets. An improved constraint is set on the evaporating helium atmosphere of GJ 1214 b through measurement of the excess transit depth at 10,830 Å in archival X-SHOOTER data. This also shows that X-SHOOTER has the required stability for these kinds of measurements on more suitable targets. For the hot Jupiter WASP-15 b Gaussian Process modeling is employed to remove correlated noise from the data and construct a transmission spectrum of the atmosphere, although further observations are required to rule out atmospheric models.

Chapter 1

Introduction

Compared to other areas of astronomy, the field of exoplanets is a very young one. The positioning of ancient sites to align with astronomical events, such as Stonehenge's alignment with the setting sun on the winter solstice (Urban and Schortman, 2019), makes it clear that humans have been measuring the sky for probably as long as they have been around. However, planets are small and dim enough that even the planets in our own solar system were not all discovered until 1846 (Galle, 1846). Even today there remains speculation about a possible Planet Nine far beyond the orbit of Pluto (e.g. Batygin and Brown, 2016; Clement and Sheppard, 2021). It is no surprise then that, despite centuries of speculation (e.g. Bruno, 1585; Newton, 1687), the first definite detection of a planet outside the solar system was not made until 1992 (Wolszczan and Frail, 1992). These planets were found around the remnants of a massive star and immediately showed that exoplanet systems don't have to be anything like our own solar system. The discovery of the first planet around a sun-like star was not far behind with the discovery of 51 Peg b in 1995 (Mayor and Queloz, 1995).

The field has boomed since, with over 4000 exoplanets discovered at the time of writing of this thesis (Exoplanet Team, 2021), including many Earth-like planets on orbits that we expect would make them habitable (e.g. Borucki et al., 2012; Anglada-Escudé et al., 2012; Bonfils et al., 2013; Tuomi et al., 2013; Barclay et al., 2013). Many of these systems have turned out to be totally different form the solar system. Some have giant planets so close to their stars that it takes only hours or days for them to complete their orbits (Wang et al., 2015). Others have multiple similarly-sized Earth-like planets in the same system, with seemingly no giant planets at all (Millholland et al., 2017). Some planet hosting systems are much smaller than the solar system, like the Trappist planets, all seven which would fit inside the orbit of Mercury (Gillon et al., 2016). Other systems have two, three or even four stars (e.g. Welsh et al., 2012; Winters et al., 2019; Schwamb et al., 2013).

Understanding these new systems is critical in understanding the existence of our own planet, and the need to explain them has driven large advancements in planet formation theories and our understanding of how planetary systems evolve. The ability to perform demographic studies on large numbers of exoplanets has further helped advance these theories. Our increasing ability to measure the atmospheres of some exoplanets is further refining them. These processes and planet compositions are also important in finding out what makes a planet habitable and, eventually, for

the search for extraterrestrial life.

This introduction examines the exact definition of what is and is not an exoplanet in Section 1.1, as well as what the different types of planets are. The two main theories of planet formation are discussed in Section 1.2, along with different ways for planets to migrate through their systems, which is required to explain many of the observed system architectures. Section 1.3 describes the different methods employed to detect and characterise exoplanets, with a focus on the two methods which are used in this thesis. Section 1.4 summarises the contents of the different chapters of the thesis.

1.1 Definition

Over time and with the continuous increase of information about the solar system, the definition of a planet has changed considerably. Originally, a planet was simply a bright object in the sky that moved with respect to the fixed stars. These objects were called "$\pi\lambda\alpha\nu\eta\tau\eta\varsigma$" (planètès) by ancient Greek philosophers, which translates into "wanderers". This definition excluded the Earth from being a planet, as the Greeks considered it fixed in place at the center of the universe. They therefore counted only five planets: Mercury, Venus, Mars, Jupiter and Saturn. The Earth did not become a planet until the acceptance of the heliocentric solar system, which placed the sun in the center with the planets orbiting around it (e.g. Copernicus, 1543). With the invention of the telescope came not just the discoveries of Uranus (Herschel and Watson, 1781) and Neptune (Galle, 1846), but also of more and more tiny objects orbiting between Mars and Jupiter. These were all considered planets, until in 1851 more than 20 such objects had been discovered in the solar system. Astronomers realised that the potential number of planets under this definition could be huge and, to the gratitude of schoolchildren everywhere, all the "planets" that had been discovered between Mars and Jupiter were re-classified as asteroids, of which almost 600,000 have been discovered as of June 2021 (NASA Jet Propulsion Laboratory, 2021). The number of planets in the solar system was then temporarily increased from 8 to 9 with the discovery of Pluto in 1930 (Slipher, 1930), but eventually it became clear that Pluto was in fact far smaller than expected and there were many similar objects near it in the Kuiper belt. This led the International Astronomical Union (IAU) to reclassify it as a dwarf planet and a Trans Neptunian Object (TNO) and formulate the currently accepted definition of a planet in 2006[1], leaving us with the present eight planets:

> A "planet" is a celestial body that
> (a) is in orbit around the Sun,
> (b) has sufficient mass for its self-gravity to overcome rigid body forces so that it assumes a hydrostatic equilibrium (nearly round) shape, and
> (c) has cleared the neighbourhood around its orbit.

For exoplanets the words "the Sun" are easily replaced by "a star", or even "one or more stars" for exoplanets orbiting stellar multiples. However, the need to distinguish between a very

[1] https://www.iau.org/static/archives/releases/doc/iau0603.doc

big planet and a very small ”failed” star means there is an additional requirement that sets an upper limit to the size of an exoplanet (which was, strangely enough, defined three years *before* the above definition of a planet[2]). Only objects below the limiting mass for deuterium fusion in the core qualify as planets, objects with masses above this limit are referred to as brown dwarfs. The deuterium burning limit depends on the metallicity of the object, but since this is very hard to determine, solar metallicity is usually assumed and the threshold is generally held to be 13 Jupiter masses.

There have been calls to change the definitions so that it is the formation mechanism, not the size, that distinguishes between exoplanets and brown dwarfs, and although the deciding IAU working group considered their requirements the basis for a working definition that could be updated as more information becomes available, this has not happened yet.

Planet types

The category of planets can be further divided into different sub-groups, depending on size and composition.

The smallest planets are the rocky or terrestrial planets (e.g. Izidoro and Raymond, 2018). These consist of a rocky core of up to a few Earth-masses and tend to have relatively little to no atmosphere. Examples in our own solar system are the four inner planets, Mercury, Venus, Earth and Mars. While the Earth is the biggest rocky planet in the solar system, super-Earths, which have radii and masses a few times larger than the Earth, have turned out to be very common, with occurence rates of over 30% around sun-like stars (Zhu et al., 2018a).

The next group are the ice giants (e.g. Fletcher et al., 2020). These are composed mostly of metals, such as water, ammonia, and sulfur. They have a rocky core, ice-rich interiors, and thick atmospheres composed largely of hydrogen and helium. Ice giants range in size from a few to around 10 Earth-radii. There is some overlap in size between super-Earths and sub-Neptunes, but they have different core structures and compositions and can be distinguished by their different densities. There are two ice giants in the solar system, Uranus and Neptune.

The largest are the gas giants, like Saturn and Jupiter (e.g. D’Angelo and Lissauer, 2018). These are composed almost entirely of hydrogen and helium, although they can have rocky cores. At large depth the pressure turns the gas into metallic hydrogen, which forms the bulk of the mass. Despite their capability of having high masses, their radii don’t get much larger than that of Jupiter, even in the brown dwarf regime. Ice giants are also referred to as gas giants, since it is the older of the two terms and was used for both groups before there was sufficient knowledge of the likely internal structure of the solar system planets to make a distinction.

1.2 Planet formation

The process and environment of planet formation have a large impact in the types and quantities of planets produced and are thus important in the study of exoplanets. Conversely, studies of exoplanet demographics can help us constrain the relevant formation processes. The study

[2] https://w.astro.berkeley.edu/~basri/defineplanet/IAU-WGExSP.htm

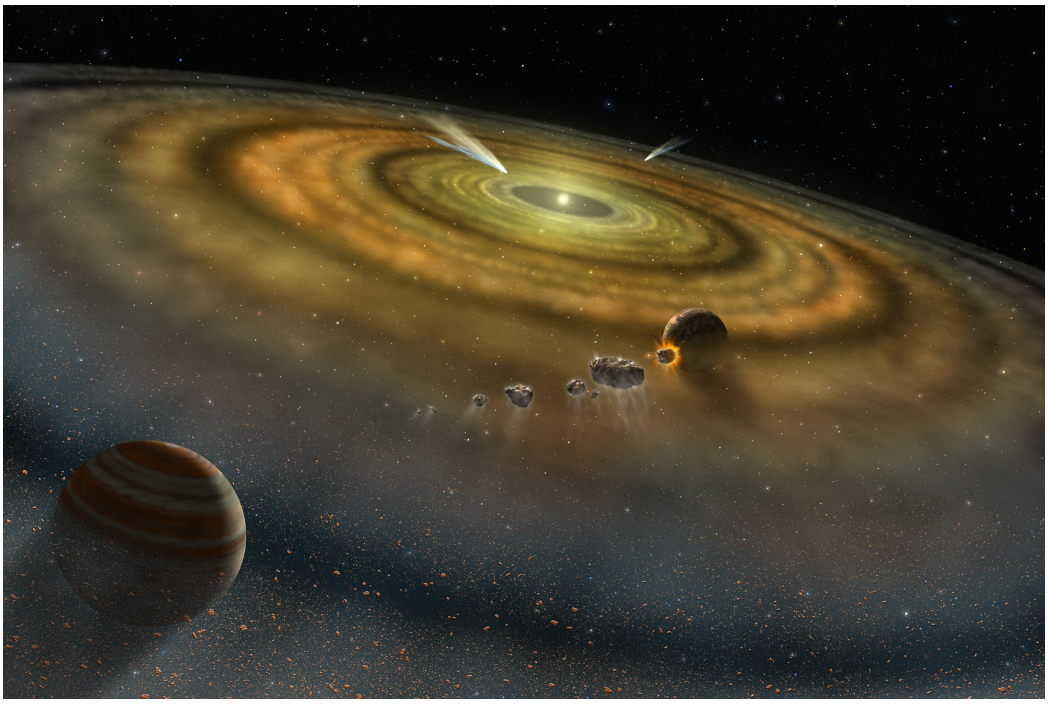

Figure 1.1: Artists impression of planets forming in the protoplanetary disk of a young star. *Image credits: NASA/FUSE/Lynette Cook.*

of circumstellar disks where planets are formed can also help us better understand their birth environment and evolution.

There are two main models for planet formation, both of which will be discussed in this section: the core accretion model and the gravitational instability model.

1.2.1 Disk formation

The formation of planets is, essentially, a by-product of star formation. Star formation happens when clouds of molecular gas in space form over-densities. When the gravitational force of one of these areas overcomes the internal gas pressure, it starts to collapse. Since the formation of these kinds of over-densities is not an isolated occurrence, and a collapsing cloud can fracture, stars tend to form in clusters.

As the molecular cloud collapses, the angular momentum of the gas is conserved, preventing it from falling directly onto the star. Instead, this results in the formation of an accretion disk perpendicular to the young protostar's rotational axis. This is called the circumstellar disk or the protoplanetary disk (PPD), since it is from the material and dynamics in this circumstellar disk that the planets are formed (see Sections 1.2.2 and 1.2.3). The growing planets exert gravitational torques on the surrounding gas, clearing their orbits and creating gaps and cavities in the disk in the disk. New gas continues to flow into the gaps and onto the planets, causing streams in the gaps and accretion disks around the planets, similar to the creation of a the circumstellar disk during star formation. This circumplanetary disk is likely the formation site of moons. As the

disk ages, material drifts inwards towards the star and gas is dissipated from irradiation by the host star. After around 10 Myr most of the gas is gone and solids remain behind in the form of a debris disk. At this point there is no longer sufficient gas for planet formation, meaning it must have occurred in the first 10 Myr.

1.2.2 Core accretion

The main theory for the formation of planets is the core accretion theory (e.g. Mizuno, 1980; Pollack et al., 1996), where a core is formed first. Depending on how much gas the core manages to accrete and attain, it then becomes a terrestrial planet, and ice giant or a gas giant.

The PPD contains micron sized dust particles. When these have the right masses and differential velocities, they stick together and coagulate to form larger aggregates. If the velocities are too small or to large, or the particles are too massive, the particles bounce or fragment instead. The maximum size that can be reached this way is of the order of mm to cm depending on the exact material and location in the disk. Icy particles beyond the snow line, where water freezes out of the gas phase and onto the dust, are ”stickier” and can therefore grow to larger sizes and don't fragment as easily compared to particles closer to the star. These mm-cm sized pebbles experience drag from the surrounding gas, which is only partially pressure supported and therefore orbits at sub-Keplerian speeds. This slows down the pebbles, causing radial drift inwards towards the star where the gas pressure is higher. Particles from beyond the snowline are particularly affected as the lower gas density at large radii increases the expected radial drift. Radial drift can also be slowed or stopped by local pressure maxima.

Since pebbles are too massive to keep coagulating into larger particles, a different mechanism is required to form planetessimals, which are gravitationally dominated and have km sizes. The streaming instability theory (Youdin and Goodman, 2005) predicts that the drift of solid particles through the gas of the disk causes local linear instabilities, which lead to small-scale clustering. The clusters grow faster than the radial drift and when the local density is high enough it triggers gravitational collapse of the clusters into planetessimals. This is followed by a period of rapid growth through pebble accretion, where the planetissimal accretes solids from the surrounding disk, as well as particles from further out in the disk that encounter the planetessimal on their radial drift inwards (Lambrechts and Johansen, 2012). This allows the planetessimals to grow into cores up to roughly $10\,M_\oplus$, depending on the amount of material available.

The cores then accrete gaseous envelopes. Gas from the surrounding disk that is traveling at a relative velocity to the core of less than the escape velocity becomes gravitationally bound to it. The pressure and temperature of the envelope increase and further accretion is limited until the existing envelope cools down. If the cooling time scale is too long, the planet does not accrete enough gas to form a proper gas giant, even if the core is large enough. Instead, super-Earths and ice giants are created. If the planet is able to capture an envelope of the same mass as the core, a short period of rapid gas accretion called run-away growth sets in and a gas giant is formed. Eventually the gas in the protoplanetary disk is dissipated and the planet can no longer accrete more material.

1.2.3 Gravitational instability

The alternative theory posits a top-down formation process, as opposed to the bottom-up core-accretion model. The gravitational instability model posits that a massive disk can fragment and the clumps can then condense into planets (e.g. Boss, 1997; Mayer et al., 2002). The required gravitational instabilities can happen when the Toomre Q parameter (Toomre, 1964), which describes the stability of a differentially rotating disk, exceeds a critical value. This value is generally 1 for axisymmetric drivers of instability such as rings, but can be larger for instabilities driven by local phenomena such as spirals and vortices. The Toomre Q parameter is dependant on the disk properties and given by equation 1.1.

$$Q = \frac{c_s \Omega}{\pi G \Sigma} \tag{1.1}$$

Here c_s is the sound speed in the gas, which depends on the temperature and the pressure of the local gas, Ω is the Keplerian angular velocity and Σ is the surface density of the disk. Because of the dependence of the Toomre Q parameter on the temperature, the density and the mass of the disk, fragmentation is most likely to occur in cold and therefore distant regions of very massive disks.

The fragmentation of a disk typically results in a large number of clumps. For any clumps to survive and form planets, they need to cool sufficiently quickly to avoid being torn apart by gravitational interaction with other clumps or tidal forces from the star if they drift too far inwards too quickly. The clumps that survive can form planets, brown dwarfs and even stellar companions, depending on their mass (Kratter and Lodato, 2016). Since massive disks are required for this mechanism to operate, the clumps tend to be too massive to form Earth-like planets, although if the clump moves inwards at just the right time, it is possible for the star to strip the planets envelope after a core has already formed, leaving behind a terrestrial planet (Nayakshin, 2010).

Gravitational instability is complementary to core accretion as a formation mechanism, as it results mostly in massive objects at large separations, where core accretion is least efficient, while core accretion operates mostly at shorter separations, where the disk is too hot to fragment. Both types of objects are supported through observations, although close-in and smaller objects tend to be far more common than gas giants at large radii, indicating planet formation through core accretion is more frequent (e.g. Forgan and Rice, 2013; Reggiani et al., 2016).

1.2.4 Planet migration

According to both the gravitational instability and core accretion models, planets should form on almost circular orbits. However, observations show that this is not always the case, with many eccentric planets having been observed. Additionally, it is difficult to form hot Jupiters in situ, as neither mechanism really allows for such close-in giant planets. Both these aspects point towards migration of planets either during or after their formation. This is possible in early formation phases through interactions between the (proto-)planet and the disk and in later phases through interaction with other objects in the system (D'Angelo and Lissauer, 2018).

For small planets, early migration happens in the type I regime, where the dominant forces are those exerted by the surroundings on the planet. The planet can excite spiral density waves in the disk, which then exert torques on the planet. The spiral outside the planet's orbit usually contributes the strongest force, causing the planet to move inwards. Another, lesser torque is exerted by co-rotating gas on horseshoe orbits, which causes a dense region in front of the planet, where the cold gas from outside its orbit gathers, and a less dense area behind it, where the warm gas from inside the orbit gathers. This process transfers angular momentum into the planet, causing it to move outwards.

For larger planets, the torque exerted by the planet on its surroundings becomes dominant instead and migration happens in the type II regime. The tidal torque from the planet on the surrounding gas causes the clearing of a gap. The angular momentum of the gas inside its orbit is decreased, causing it to move inwards, and the angular momentum of the gas outside its orbit is increased, moving it outwards. In the type II regime these torques are large enough to overcome the viscous torques of the gas disk and prevent replenishing of the gap. The planet migrates along with the direction of the viscous motion of the gas. In the inner disk this is inwards, but viscous spreading in the outer disk can cause outward migration.

In later phases when the planets have formed and the disk has dissipated, planets can still migrate through gravitational interactions with other objects in the system. Debris belts like the Kuiper belt can absorb angular momentum from the planet through scattering events, causing it to move inwards. Finally, if any of the above migration methods or some other perturber such as a secondary star causes planets to get too close, they can become excited, increasing their eccentricity, which in turn changes their semi-major axis, and potentially getting ejected from the system altogether. This is more common after dissipation of the disk, as the gas has a dampening effect. Both planetessimal scattering migration and planet-planet scattering migration are employed in the Grand Tack model that describes a possible history of our own solar system (Walsh et al., 2011).

1.3 Detection methods

Since it is clearly impossible to create an exoplanet system in the lab, all our information about the various different kinds of planets and their formations must necessarily come only from observing systems that already exist. Finding these planets is often difficult, as they are small and dim objects, especially compared to their host stars, and distances in space are large. Their proximity to their host stars is an additional complicating factor.

However, through various techniques it is possible to detect exoplanets and characterise their atmospheres. All the techniques tend to result in limited information, depending on the systems architecture, orientation, distance and relative brightness. As a result, different methods are sensitive to different types of planets, as is shown in Figure 1.2. The combination of multiple techniques is usually required to obtain a complete picture of an exoplanet system. The advent of more sensitive instrumentation from space missions and large surveys, such as the James Webb Space Telescope (JWST) and the Transiting Exoplanet Survey Satellite (TESS), is increasing the overlap in parameter space between the techniques, making full characterisation more accessible.

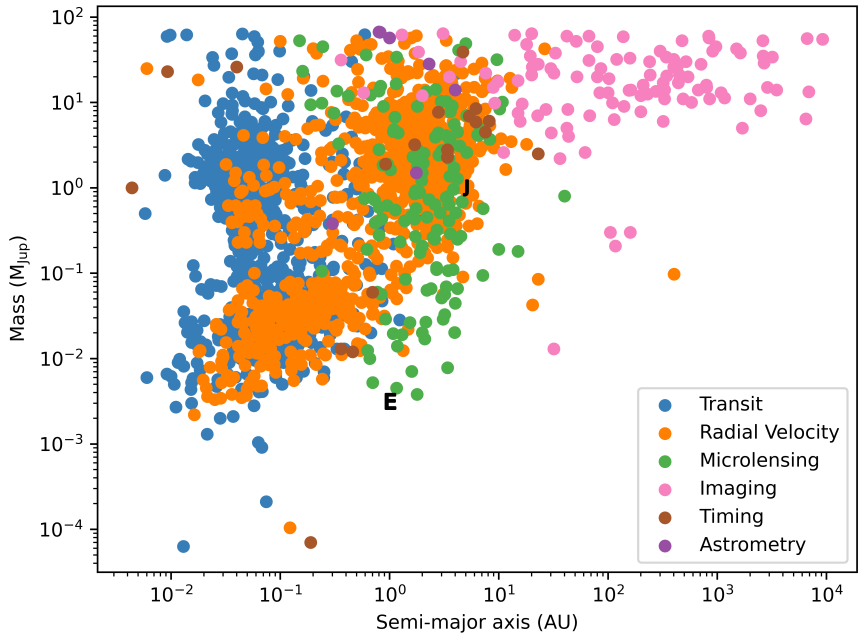

Figure 1.2: Mass and semi-major axis of planets discovered with the various different methods, plotted in order of the number of planets detected. The Earth (E) and Jupiter (J) are included for context. This plot shows that different methods favour different areas of parameter space. In particular, planets detected with direct imaging (pink) are massive and distant from their stars with semi-major axes of a few to a ten thousand AU, while planets detected with the transit method (blue) almost all orbit at less than 0.3 AU from their host stars. For the radial velocity planets, $M \cdot sin(i)$ is plotted instead, as explained in Section 1.3.3. Data is from the `exoplanet.eu` database (Exoplanet Team, 2021).

1.3.1 Transit method

The transit method detects the changing brightness of the system as the planet passes in front of and behind the star (e.g. Deeg and Alonso, 2018). Although the first transit detection didn't come until 8 years after the discovery of the first exoplanet (HD 209458 b; Henry et al., 1999; Charbonneau et al., 2000) and initial expectations of the method were low, the transit method is responsible for the discovery of over 70% of the currently known exoplanets (Exoplanet Team, 2021).

Figure 1.3 shows how the measured brightness changes over time with the orbit of the planet. When the planet passes between the star and the observer, the light coming from the star is partially blocked by the planet and the amount of flux is reduced. When the planet leaves the stellar disk the system returns to its previous magnitude. This dip is the primary transit (or simply the transit), as it is the biggest change in the magnitude of the flux during the planets orbit. At this point only the dark side of the planet, the night side, is visible. As the planet continues on its orbit, more and more of the brighter day side becomes visible to the observer and the flux from the system increases slightly. When the planet passes behind the star, the light from the

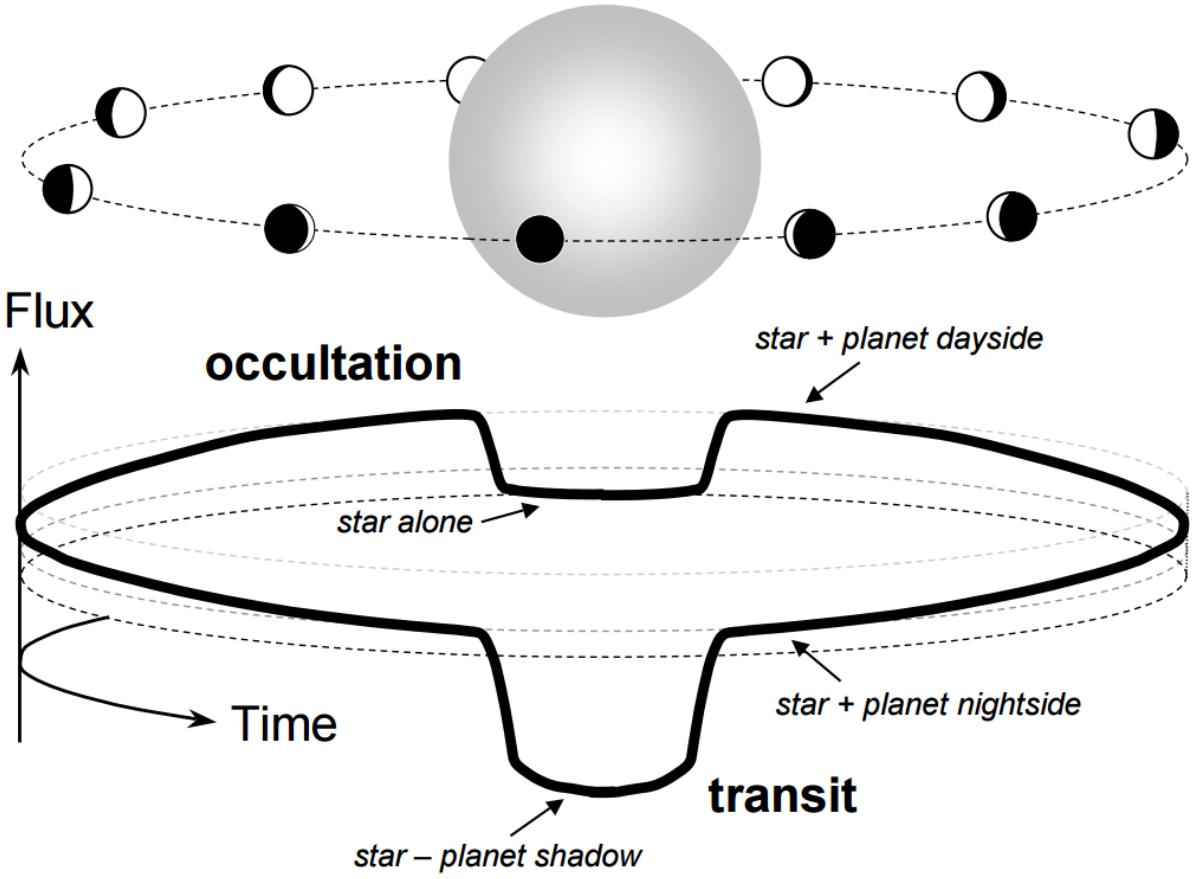

Figure 1.3: Illustration of the changing brightness of a transiting exoplanet system. The system periodically brightens and dims as the planet passes in front of the star (transit) and behind it (eclipse). *Image credit: Joshua Winn.*

planet is now blocked and brightness is again temporarily reduced. This is known variously as the secondary transit, the occultation, the secondary eclipse, or just the eclipse of the planet. Because the planet is much fainter than the star, this dip is significantly smaller than the primary transit. After the eclipse, the planets day side begins to disappear from view again and the flux reduces back to what it was at the beginning of the cycle.

The advantage of the transit method is that it can be done on bright stars, which make follow-up observations easy and possible to do from the ground. In its basic form it also only requires luminosity observations, which makes it possible to do large surveys relatively easily. The disadvantage is that the nature of the method means that it only works for systems that have orientations very close to edge-on. The further away the planet is from the star, the smaller the range of inclinations that will allow us to see the transit. Combined with the dependence of the transit depth on the relative size of the planet and the star, this means that the transit method is most sensitive to large, close-in planets and most of the first detections were hot Jupiters. In Figure 1.2, most of the planets detected through the transit method are within 1 AU of their host stars, and have masses of the order of a Jupiter mass, although there is a secondary group of lower mass planets that are likely detected around smaller stars. Additionally, there are many things that can cause light curves that look like transits and result in false positives, such as starspots and blended background binaries (e.g. Almenara et al., 2009). This means transit detections require careful analysis and follow-up observations. The initial discovery of new planets also requires long base-line monitoring of many stars, although dedicated large scale surveys both on the ground and in space alleviate this problem. Finally, flux changes from stellar variability can hide transit signals, making them more difficult to detect.

Primary transit

The amount of light that is blocked during transit is determined directly by the fraction of the stellar surface that is covered by the planet and therefore by the ratio of the planet radius (R_p) and the stellar radius (R_s), as shown in equation 1.2.

$$f = \frac{\pi R_p^2}{\pi R_s^2} = \left(\frac{R_p}{R_s}\right)^2 \tag{1.2}$$

Here f is the fractional dimming of the star. The equation ignores the luminosity from the planet night side, since this is negligibly small in most cases.

This relationship means that it is possible to determine the radius of the planet from the measured transit depth. A Jupiter-sized planet around a sun-like star has a transit depth of around 1%, which is quite easy to measure. But an Earth-sized planet around the same star has a transit depth of less than 0.01%. Fortunately, M dwarf stars are small enough that even Super-Earths can cause transit depth of almost a percent, and many habitability studies therefore focus on these systems (e.g. MEarth and CARMENES; Nutzman and Charbonneau, 2008; Quirrenbach et al., 2014). The period of the planet is measured by the spacing of the transits over time and the transit duration can put some constraints on the orbital parameters. These determine, for example, how fast the planet is going at the time of the transit, or, in the case of the inclination, whether the planet takes the longest path across the center of the star or some shorter path above or below

it. The shape of the transit can even indicate a grazing transit, where the planet only partially covers the edge of the star. Unfortunately, many of these parameters are degenerate and transit measurements alone are not sufficient to determine their individual values. Finally, dynamical interactions in multi-planet systems cause variations in the timing and duration of transits, with the largest changes coming from planets in resonance. This can be used to constrain the orbits in systems where multiple planets transit, or to detect additional non-transiting planets if there is only one known companion.

Transmission spectroscopy

During the transit a fraction of the light filters through the atmosphere of the planet. Depending on the chemical composition of the atmosphere, it will be opaque at some wavelengths and transparent at others. The result is that the planet radius and therefore the transit depth will vary with wavelength, creating a transmission spectrum. The visibility of the features in this spectrum depend on the size of the atmosphere relative to the planet. The size of the atmosphere is qualified with the scale height H which is defined as the distance over which the pressure decreases by a factor of e and is given by equation 1.3,

$$H = \frac{k_B T_{eq}}{\mu g} \tag{1.3}$$

where k_B is the Boltzmann constant, T_{eq} is the planet equilibrium temperature, g is the surface gravity and μ is the mean molecular weight of the atmosphere, typically assumed to be about 2.3 for hydrogen/helium dominated atmospheres (Kreidberg and Oklopčić, 2018). The size of the features compared to the continuum transit depth is roughly the total depth of the planet with its atmosphere minus the contribution from just the planet:

$$\delta_\lambda = \frac{(R_p + 2H)^2}{R_s^2} - \frac{R_p^2}{R_s^2} \approx 4\frac{H}{R_p} f \tag{1.4}$$

where δ_λ is the expected feature size relative to the continuum transit depth f as defined in equation 1.2. Even for ideal cases of hot Jupiters with extended, hydrogen dominated atmospheres, δ_λ is not expected to exceed $\sim 0.1\%$. As a result, most planets that have been characterised in this way are Hot Jupiters, although there are a few lower-temperature sub-Neptunes (e.g. GJ 1214 b; Bean et al., 2010).

The first atmospheric feature to have been detected this way was the 589 nm sodium doublet in the hot Jupiter HD 209458 b (Charbonneau et al., 2002). While sodium is not expected to be very abundant, it has a large absorption cross-section, making it relatively easy to observe. Sodium and potassium have both been found in a number of other planets since (e.g. Nikolov et al., 2018; Keles et al., 2019). Other metals have been found as well, as have atomic hydrogen and helium (e.g. Hoeijmakers et al., 2020; Spake et al., 2018). Ions of species like carbon and oxygen have been found in the inflated and ionised upper atmospheres of close-in exoplanets (e.g. Vidal-Madjar et al., 2003, 2004).

Molecular species have also been found. For example, water has been detected in many planets, thanks to its strong absorption in the near-infrared. Molecular hydrogen is expected to

be extremely common in exoplanet atmospheres and its presence has been inferred from Rayleigh scattering (e.g. Lecavelier des Etangs et al., 2008), although it is difficult to rule out other sources. Other expected molecules, such as CO, NH_3 and CH_4, have not yet been confirmed. This is at least partially due to the lack of high resolution instruments available at wavelengths where they have strong features (Kreidberg, 2018).

Spectra with no features at all are indicative of condensates high in the atmosphere, which scatter the incoming starlight and therefore prevent absorption lower in the atmosphere, truncating absorption features. Scattering from small particles can also introduce a steep slope in the optical and a more moderate one in the infrared. These slopes are typically from hazes, while clouds cause a more flat transmission spectrum due to their diffuse scattering.

Eclipse

At optical and near-infrared wavelengths the eclipse dimming is mostly reflected starlight and eclipse depths are very small. Observations of eclipses are rare at these wavelengths and the few available detections show flux differences from around 100 parts per million (ppm) down to (upper limits of) a few ppm in the optical and of the order of a few 100 ppm in the near-infrared (e.g. Rowe et al., 2008; Lendl et al., 2013). At longer wavelengths the planets thermal emission dominates and the eclipse depth is no longer just determined by the relative size of the planet, but also by it's blackbody emission, which in turn depends on the equilibrium temperature of the planet. Equation 1.2 instead becomes equation 1.5.

$$f_e = \frac{B(\lambda, T_{eq})}{B(\lambda, T_s)} \left(\frac{R_p}{R_s}\right)^2 \tag{1.5}$$

Here $B(\lambda, T_{eq})$ is the blackbody emission spectrum of the planet at equilibrium temperature and $B(\lambda, T_s)$ is the blackbody emission of the star which has temperature T_s. Because of this, the eclipse depth of Hot Jupiters increases to a fraction of a percent beyond a few micron (e.g. Swain et al., 2008; Kilpatrick et al., 2017; Garhart et al., 2018). Due to the required precision and the telluric absorption at many infrared wavelengths, measurements of eclipses often need to be done from space and ground-based detections require the observation of many eclipses of the same target.

Since the planet radius is known from the primary transit measurement, the eclipse can be used to constrain the temperature of the day side of the planet, which is important in determining atmospheric structure and chemistry. Additionally, the thermal emission by definition comes from a height in the atmosphere where the optical depth is unity. If the atmosphere is more opaque at certain wavelengths, the emission will come from higher in the atmosphere where the gas has a slightly different temperatures compared to lower in the atmosphere. This results in a change in the measured temperature and therefore eclipse depth with wavelength, making it possible to construct an emission spectrum of the planet, the spectral features of which depend on the temperature-pressure profile of the atmosphere.

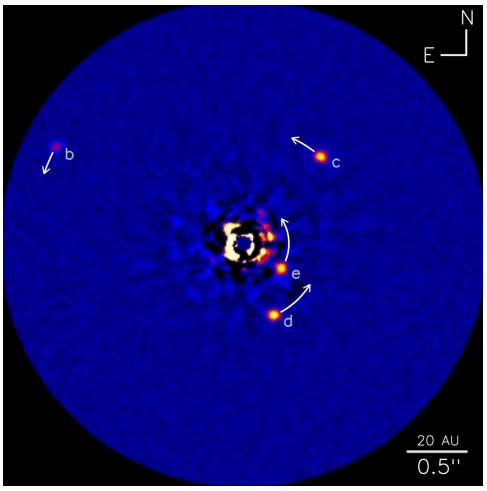

Figure 1.4: Direct image of the multi-planet system HR 8799. Four planets are observed at various separations from the host star and indicated in the image as b, c, d and e. *Image Credit: NRC-HIA, C. Marois, and Keck Observatory.*

1.3.2 Direct imaging

In direct imaging the planet is far enough from the star to be resolved and bright enough to appear as a separate source in the observations. Figure 1.4 shows the multi-planet system HR 8799 as an example (Marois et al., 2008, 2010). Even for wide separation planets, the brightness of the planet is a significant limiting factor in this method, as it emits far less flux than the star. The best targets are therefore large planets that still have some of their formation heat, as these can exist at large separations and emit the most flux, especially in the infrared where the peak of their blackbody flux is located. However, even for these observations the contrast between the planet and the star is expected to be $\sim 10^{-4} - 10^{-7}$ (Biller and Bonnefoy, 2018). For an Earth-like planet around a sun-like star this quickly becomes $\sim 10^{-10}$, even at 10 µm where the contrast is the best. Because of this, the method is also known as High Contrast Imaging (HCI). This difficulty also means that the number of planetary mass objects discovered with direct imaging is currently 77 (Exoplanet Team, 2021) and the discovery rate has been fairly stable since 2008. Figure 1.2 shows that the planets that have been detected tend be around $10\,M_{Jup}$ and almost all are located beyond 10 AU. The other reason for the lack of detections is that surveys have shown that giant planets at large radii are relatively scarce compared to the close-in planets that are preferentially detected by other methods like the transit method (Reggiani et al., 2016). However, direct imaging can offer valuable insights into planet parameters and atmospheric structures.

Additionally, imaging of systems with protoplanetary disks can show asymmetries, rings or spirals which can indicate the presence of a (proto)planet, although these features can also be caused by processes in the disk itself. If the disk is observed in narrowband spectral lines, deviations from Keplerian motion can be detected which also indicate the presence of a perturber.

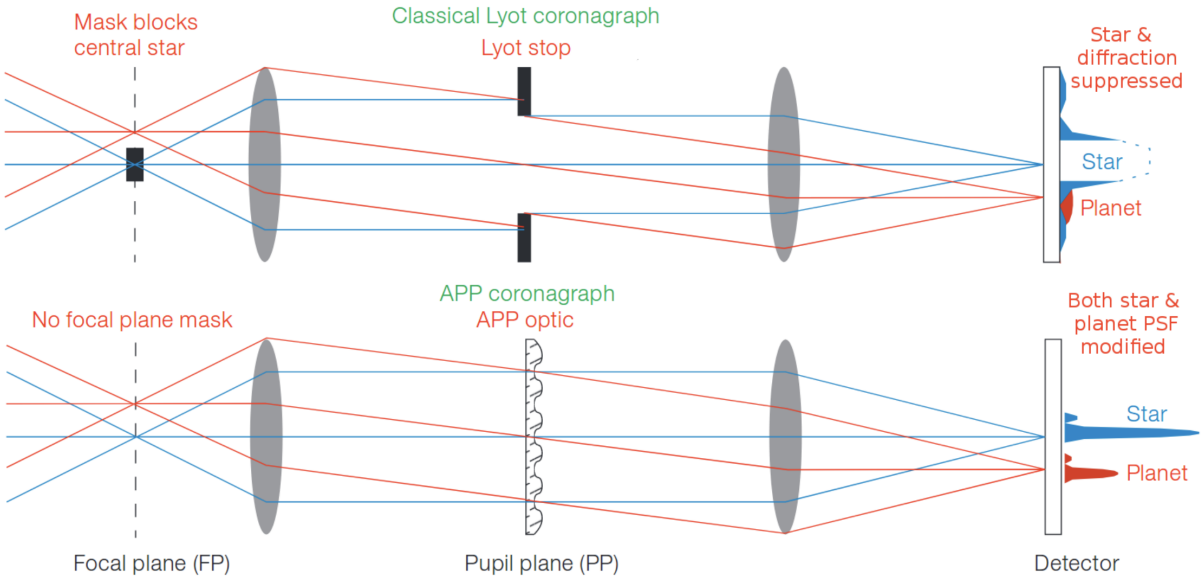

Figure 1.5: Illustration of the workings of the two types of coronagraphs. The top is the classical coronagraph which physically blocks the starlight, the bottom modifies the telescope PSF to create dark areas in the image. *Image credit:Kenworthy et al. (2010a)/Mike Wilby.*

Improving contrast

To make observations at these high contrast levels possible, a number of techniques are employed both during the observations and in the post-processing.

The easiest way to increase the contrast in the images is to reduce the amount of starlight at the planet location. This can be done with a coronagraph, so named because it was first used to look at the solar corona by blocking the emission from the disk (Lyot, 1939). There are two types. The classical type blocks the central region of the field of view. When the star is located behind the coronagraph the amount of starlight in the image is drastically reduced. Figure 1.4 shows the characteristic dark spot caused by the coronagraph in the center of the image where the starlight is blocked. This is effective, but movement of the star during the observations can cause light to leak past it and reduce the contrast at the planet location. The other type of coronagraph works by modifying the Point Spread Function (PSF) of the telescope to create destructive interference and therefore increase the contrast in certain areas of the image. Figure 1.5 shows an illustration of both kinds of coronagraph. Different coronagraphs are optimised for various functionalities, such as throughput, contrast, band width and inner working angle (e.g. Guyon, 2003; Mawet et al., 2010; Kenworthy et al., 2010b; Snik et al., 2012).

For large ground-based telescopes the use of adaptive optics (AO) is required to counter image degradation by the Earths atmosphere. Turbulence distorts the wavefront and causes the image to smear and move around on the detector as the light waves pass through various bubbles of air with different refractive properties. This reduces the resolution of the image to the characteristic scale of the turbulence (r_0) rather than the diffraction limit of the telescope. The movement of the image caused by the atmosphere can also result in decreased efficiency of the

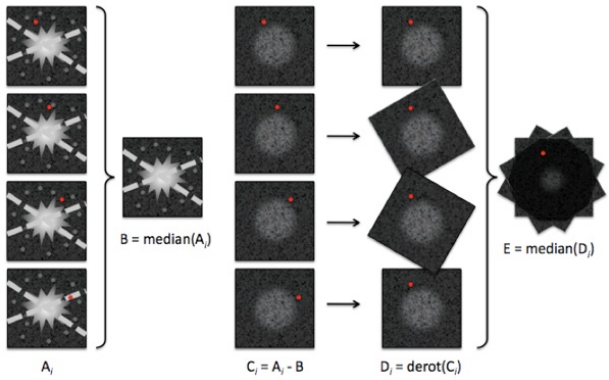

Figure 1.6: Diagram explanation of ADI. The first column shows the images taken during the night without the derotator. The stellar PSF shows smearing and speckles from seeing, as well as contributions from the spiders that support the secondary mirror. The red dot represents the planet, which moves across the CCD while the diffraction pattern stays stable. An average diffraction pattern is then subtracted from the data and the images are realigned with each other and combined. *Image credit: Christian Thalmann*

coronagraph if one is present, as the centering is not consistent. To correct for these effects, adaptive mirrors in the telescope are used to reconstruct the wavefront, increasing the Strehl ratio and therefore the resolution and contrast. The mid-infrared New Earths in the Alpha Cen Region (NEAR; Kasper et al., 2017a) instrument, for example, has a coronagraph and AO and was able to reach contrasts around alpha Cen A and B sensitive enough that it would have detected any present Neptune-sized planets.

Even after AO correction, the atmospheric residuals cause a quasi-static noise pattern called speckles. These look like points near the star and are therefore very similar to images of planets. They are visible around the center of Figure 1.4. One way to reduce speckles and increase contrast is through a technique called Angular Differential Imaging (ADI; Mawet et al., 2005). During normal observations, the image is rotated during the night to match the sky orientation. In ADI, the derotator is turned off and instead the image is allowed to rotate over the CCD. This causes the speckles to remain stable on the same location of the chip, while the planet moves. A map of the stellar PSF can then be created and subtracted, after which the images are realigned, as shown in Figure 1.6. Another option is the reference differential imaging technique, where a reference star is used to map the speckles instead of the target star, although simultaneous imaging of a nearby, sufficiently bright star can be difficult. Finally, statistical techniques can be used in post-processing to distinguish between remaining speckles and real planet signals. Since seeing is wavelength dependant, speckles are mainly a problem in the optical and near-infrared regimes, with the mid-infrared being mostly unaffected.

Photometry

Photometric measurements of planets allow not only for the determination of the location of the planet, but if the age of the system is known, it is possible to constrain the temperature, the radius and the mass of the planet based on evolutionary models. This makes direct imaging the only method that offers a direct constraint on the planetary mass. Additionally, imaging at

different wavelengths can constrain the temperature, cloudiness and spectral type of the planet by comparing the data points to spectral models and narrow band imaging can be used to detect some molecules with strong absorption/emission bands, such as water and methane.

Directly imaged planets are often observed at different times to create a photometric time series. The observation of a planet at different phases of its orbit makes it possible to use astrometry to determine the planets orbital parameters. In the case of multi-planet systems this can be combined with n-body simulations that constrain stable configurations (e.g. HR 8799; Wertz et al., 2017), allowing for the determination of the period, semimajor axis, eccentricity, inclination, longitude of the ascending node, time of periastron passage, and longitude of periastron passage. Gas giants at large separations are also expected to show the same kind of brightness variations that are present in brown dwarfs and operate on the timescales of their rotation periods (3-20h; Zapatero Osorio et al., 2006) due to surface inhomogeneities that can be caused by clouds or thermochemical instabilities (Tremblin et al., 2016a). Gas giants are expected to have similar features and are also fast rotators. Unfortunately, not many planets are currently bright enough to be able to detect these kinds of variations, but JWST will be able to find flux variations in a much larger sample of planets.

Spectroscopy

The advantages of spectra obtained from direct imaging are similar to those obtained from secondary eclipse spectra. However, directly detected spectra are easier to obtain and tend to be from a class of planets complementary to those observed in eclipse. Due to the need for an edge-on orientation to observe transits, only a fraction of planets can be measured this way and the odds of a planet having the right inclination decrease as it gets further from its host star, causing most transiting planets to be very close-in and hot. Direct imaging requires sufficient separation to resolve the planet from the star and are therefore further separated. For example, most habitable zone planets are too far from their star for many of them to transit and even then their long periods will be a hindrance. Direct imaging and spectroscopy will make it possible to determine whether a planet in the habitable zone is really habitable.

Because the planet is resolved from the star, observing techniques are different from secondary eclipse spectroscopy. The planet can be observed with an integral field unit (IFU) which combines images taken at many different wavelengths to make a low-to-mid resolution spectrum for each pixel in the field of view. These spectra can be cross-correlated with model spectra to create a map of where various molecules are present, allowing for the identification of species in the planet atmosphere and fitting of the planet spectrum. This way of identifying different molecules in the planet atmosphere is called molecule mapping (Hoeijmakers et al., 2018; Petit dit de la Roche et al., 2018). By fitting the planet spectrum it is also possible to obtain abundances and abundance ratios, such as the C/O ratio. These ratios give important insight into the formation and possible migration history of the planet. Further information on the formation of the planet can be obtained by, for example, detecting excess Hα emission from very young planets that are still accreting the material in the disk around them, such as PDS 70b (Haffert et al., 2019).

Since atmospheric turbulence, and therefore the size of the speckles in an image, varies with

wavelength, IFU data can also facilitate distinguishing between speckles and real planet signals. There are currently no instruments that allow the combination of high contrast imaging techniques with high resolution spectra in the way IFUs do with low and medium resolution, but this is planned for the ELT as it could increase the attainable star-planet contrast from 10^{-5} to 10^{-10}, which would allow the observation of fainter and therefore colder, older and smaller planets (Snellen et al., 2015).

Current high resolution spectra of resolved planets need to be obtained with long-slit spectrographs. These don't have as much spatial information, but the high resolution gives additional information on atmospheric processes. It means rotational broadening of lines from the planet and offsets of planet lines from stellar lines are visible. Line broadening has been used to determine a rotational velocity of 25 km/s in β Pic b, far faster than any solar system planets (Snellen et al., 2010), and offsets observed in CO lines of the HD 209458 b atmosphere have been used to prove the existence of night-side winds on the planet (Snellen et al., 2014).

1.3.3 Radial Velocity

Because the star and the planet in a planetary system orbit a common center of mass, the presence of a planet induces movement in the star. The amplitude of the velocity is determined by the masses of the planet and the star and the period and eccentricity of their orbits. While it is not possible to measure the velocity directly, it is possible to measure the radial velocity along the line of sight through a Doppler shift in the spectrum of the star. During its orbit the light of the star periodically shifts towards the red and blue, as the star is moving away from and towards the observer in its orbit. This is illustrated in Figure 1.7. Due to the inclination of the system

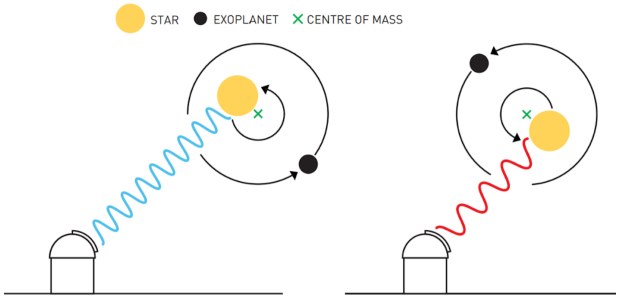

Figure 1.7: The stars motion around the common center of mass of the star-planet system induces a measurable wavelength shift in the observed light. *Image credit:Johan Jarnestad/The Royal Swedish Academy of Sciences.*

(i), the measured radial velocity amplitude K is a factor of $sin(i)$ different from the true velocity. Overall, the dependence of the measured velocity amplitude induced by the planet on the stellar and planetary parameters is given by equation 1.6 (Wright, 2018).

$$K \approx \left(\frac{2\pi G}{P M_*^2}\right)^{\frac{1}{3}} \frac{M_p \sin(i)}{\sqrt{1-e^2}} \tag{1.6}$$

Here G is the gravitational constant, M_* and M_p are the stellar and planetary masses respectively, and e is the eccentricity of the planets orbit.

This method has been highly successful and has resulted in the discovery of over 900 planets. Most of these are hot Jupiters on high inclinations, as their short orbits and high masses induce a relatively large velocity in their host star. This is similar to the transit method, and the two can be combined to great effect. Detecting smaller and more distant planets remains difficult, however. The velocity induced by a hot Jupiter in a sunlike star is of the order of 10s of m/s. Earth-like planets at habitable zone distances produce far lower velocities, with the Earth itself causing a velocity of only 9 cm/s in the Sun. Extremely stable spectrographs like ESPRESSO (Pepe et al., 2010) are currently capable of achieving a precision of the order of 25 cm/s with the goal of obtaining 10 cm/s, but at this point stellar effects often become the limiting factor. Factors such as stellar magnetic fields and photospheric activity can induce "jitter" in the radial velocity signal of the star. These effects can be somewhat avoided by observing older and colder stars that are not as active. The jitter can also be reduced by accurately identifying the stellar contributions through the use of magnetic activity indicators, line-shape analysis and wave-length dependence of the line shifts.

1.3.4 Astrometry

Like the radial velocity method, astrometry makes use of the fact that the presence of a planet induces motion in the host star. However, it is not the radial velocity that is measured, but the reflex motion in the plane of the sky. This means that it is once again easiest to detect giant planets that are close-in to nearby host-stars, although thanks to the effects of stellar activity being far smaller in astrometry than in the radial velocity method, it is possible to detect Earth-mass planets. This still requires sub-milliarcsecond (mas) precision measurements and as a result only four new planets have been discovered this way (Exoplanet Team, 2021).

The advantage of this method comes mostly from the combination with radial velocity measurements. With both the radial velocity and the reflex motion it becomes possible to constrain the inclination and therefore the absolute mass of the planet. Space-based missions have the potential to achieve the required precision to detect, confirm and characterise the orbits of more planets using astrometry. In fact, with Gaia's estimated precision of 59 mas for bright stars, it has already been used to confirm the planetary nature of many companion candidates and is expected to find the masses and orbital parameters of thousands of planets in the near future (e.g. Perryman et al., 2014; Kiefer et al., 2021).

1.3.5 Microlensing

Another indirect method of detecting planets is through microlensing. When light from a background source passes by a more foreground object in the plane of the sky, the foreground objects gravity works as a lens and bends the light. This is called gravitational lensing and increases the observed brightness of the source while it is close-to and behind the lens. In our own galaxy we can use this effect to detect exoplanets. If the source is a star and the lens is a star with a companion, then the gravity of the companion also works as a lens and a secondary, smaller increase in brightness happens when the source gets near the planet. Due to the small amplitude of the effect it is referred to as microlensing. Figure 1.8 shows a schematic of what such a light curve

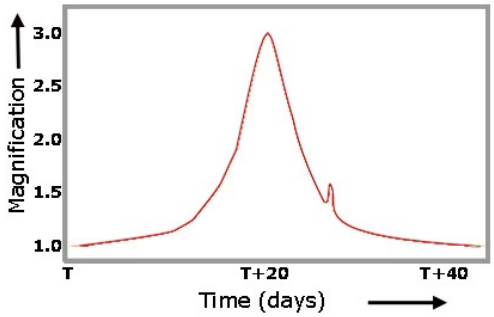

Figure 1.8: Schematic illustration of a light curve of a microlensing event. The main increase in brightness is caused by the lensing star, with the smaller peak on the right side of it being caused by the planet. *Image credit: ESA.*

looks like, with the main peak caused by the lensing around the foreground star and a very small second peak further to the right caused by lensing around the much lower mass planet.

The advantage of this method is that it is sensitive to small planets beyond the ice line, which are not observable with any other method (Batista, 2018). The distribution of planets beyond the ice line is important in constraining planet formation. However, because of the nature of the lens having to cross another object in the sky, these events are rare and don't repeat, meaning follow-up is essentially impossible. Surveys of large and densely populated areas have so far resulted in 154 detections of mostly sub-Jupiter mass planets (Exoplanet Team, 2021).

1.3.6 Pulsar timing

The first confirmed exoplanets have been detected through variations in the timing of radio pulses from a pulsar, a rapidly rotating neutron star (Wolszczan and Frail, 1992). These were caused by gravitational interactions between the planets and the host. Pulsar timings are usually extremely precise, so regular timing changes indicate the presence of a perturber, for which observations are sensitive down to asteroid sizes (Kramer, 2018). However, this method has not been very successful, as beyond the original system, only two others have been detected. This is probably because these types of planets are expected to be extremely rare due to the violence of the supernova process that is required to form a pulsar. Any planets the original host had would have been destroyed or ejected, so the current planets must be the result of a secondary planet formation process with new material from the supernova, a destroyed companion or a merging and subsequently destroyed white dwarf.

1.4 This thesis

The thesis is divided into two parts. The first part examines the possibilities of directly imaging exoplanets in the mid-infrared (mid-IR) and focuses on gas giant planets at large separations. There are far fewer of these planets than would be expected from extrapolation of populations found by other methods which favor close-in planets. One possibility is that the formation mechanism is different, with close-in planets being formed through core accretion (Section 1.2.2) and

further out planets being formed by gravitational instability (Section 1.2.3).

Solving this problem requires detecting and characterising planets at large separations, but so far this has only been done for a very small number of such planets and drawing a significant conclusion requires a larger sample size. Direct imaging is uniquely capable of observing these planets, as discussed in Section 1.3.2. The benefit of doing direct imaging in the mid-IR, as opposed to the usual near-IR, is that it is where most planets with known temperatures emit most of their flux. In particular, very young systems that are still accreting material onto their circumplanetary disk are expected to be very bright at these wavelengths. The mid-IR is also sensitive to cooler and therefore older and less massive planets, covering a part of parameter space ($R_P >$ a few R_{Jup}, $500 < T_P < 1000$K) to which the near-IR has been blind. Since stellar flux decreases with wavelength, the planet-star contrast is also naturally better. Further, the mid-IR contains many spectral features (e.g. CH_4, H_2O, and NH_3) which provide information on a planet's chemical composition, which in turn has the potential to provide a wide range of constraints on numerous atmospheric processes and planetary formation mechanisms (Madhusudhan, 2019).

In Chapter 2 I introduce a novel reduction method for mid-IR direct imaging data taken with VISIR of the young multi-planet system HR 8799. In Chapter 3 I analyse contrast limits produced by Prashant Pathak from data of four mature systems in the solar neighbourhood taken with the upgraded NEAR instrument, which allows for an increase in sensitivity and resolution compared to the former version, VISIR. Two of the systems are known to host at least one giant planet and three have hosts that are sun-like stars. In Chapter 4 I look at VISIR and NEAR data of six young systems that are expected to have planets that are still forming in the circumstellar disk and compare them to models run by Nick Oberg.

The second part of the thesis focuses on atmospheric characterisation results of two close-in exoplanets obtained with transmission spectroscopy. Close-in planets undergo large amounts of stellar irradiation, causing their atmospheres to puff up and potentially erode. This process can completely disperse the atmosphere and is consequently an important factor in planetary evolution and demographics, as evidenced by the lack of highly irradiated super-Earths.

In Chapter 5 I reduce archival data of the close-in super-Earth GJ1214 b, which is expected to be undergoing significant atmospheric mass loss. I look for evidence of an extended envelope of evaporating material by examining the He I 10,833 Å line, an absorption line of metastable helium that gets excited from X-ray and extreme ultraviolet radiation by the star. In Chapter 6 I identify and reduce archival spectroscopic data of a transit of the hot Jupiter WASP-15 b. This data is taken with the FORS2 spectrograph during a time when instrumental effects caused correlated noise in the data, which is of the order of the transit depth and needs to be removed with Gaussian Process modelling.

Finally, in Chapter 7 I present the conclusions of the thesis. I summarise the findings of the previous chapters and provide an outlook to future research in the field.

Chapter 2

New constraints on the HR 8799 planetary system from mid-infrared direct imaging

D. J. M. Petit dit de la Roche, M. E. van den Ancker, M. Kissler-Patig, V. D. Ivanov, D. Fedele
Monthly Notices of the Royal Astronomical Society, Volume 491, Issue 2, January 2020, Pages 1795–2799

Abstract: Direct imaging is a tried and tested method of detecting exoplanets in the near infrared, but has so far not been extended to longer wavelengths. New data at mid-IR wavelengths (8-20 μm) can provide additional constraints on planetary atmospheric models. We use the VISIR instrument on the VLT to set stringent limits on the 8.7 μm flux of the four planets surrounding HR 8799, and to search for additional companions. We use a novel circularised PSF subtraction technique to reduce the stellar signal and obtain instrument limited background levels and obtain optimal flux limits. The BT SETTL isochrones are then used to determine the resulting mass limits. We find flux limits between 0.7 and 3.3 mJy for the J8.9 flux of the different planets at better than 5σ level and derive a new mass limit of 30 M_{Jup} for any objects beyond 40 AU. While this work has not detected planets in the HR 8799 system at 8.7 μm, it has found that an instrument with the sensitivity of VISIR is sufficient to detect at least 4 known hot planets around close stars, including β Pictoris b (1700 K, 19 pc), with more than 5σ certainty in 10 hours of observing time in the mid-IR.

2.1 Introduction

HR 8799 is a young A star located at 41.3 ± 0.2 pc (Marois et al., 2008; Gaia Collaboration et al., 2018) that is unique in that it has four directly imaged exoplanets surrounding it. The planets orbit between 17 and 68 AU and have masses between 7 and 10 M_{Jup} (Marois et al., 2008; Marois et al., 2010). The system also contains a warm dust belt within the innermost planet e and a Kuiper belt-like debris disk outside the planets orbits from 145 AU to 450 AU (Su et al., 2009; Booth et al., 2016). Booth et al. (2016) suggested a possible fifth planet of 1.25 M_{Jup} at 110 AU that could be responsible for the gap between the outer planet b and the debris disk, although

the mass could be lower if the planet is further out or on an eccentric orbit. Due to this unique position the planets have been studied extensively in imaging and spectroscopy across the near infrared (IR) from the J to the M band since their discovery (e.g. Barman et al., 2011; Galicher et al., 2011; Zurlo et al., 2016; Petit dit de la Roche et al., 2018).

So far no direct imaging of planets has been done beyond 4.8 μm. Longer wavelength searches with *Spitzer* and *WISE* have revealed a number of brown dwarf companions at large separations and Geißler et al. (2008) have done ground based mid-infrared imaging of brown dwarfs in binary systems with VISIR, but no planets have been imaged (Luhman et al., 2007, 2012). Mid-IR observations can provide further constraints of planetary atmospheric models and the mid-IR wavelength range also contains biosignatures, which could indicate the presence of biological processes (Meadows and Seager, 2010; Rauer et al., 2011). *Spitzer* has made observations of secondary transits, occultations of exoplanets by their host stars, at longer wavelengths (e.g. Deming et al., 2005; Charbonneau et al., 2005; Deming et al., 2007), resulting in light curves and broad band emission spectra of some transiting exoplanets. These are useful for comparison to imaging data, but the planets observed with *Spitzer* cover a different area of parameter space than directly imaged planets due to the limitations of both methods. Finally, ground-based detection of exoplanets in the mid-IR will help the analysis and interpretation of future JWST exoplanet observations.

We aim to expand current observations to cover the mid-IR wavelength regime by imaging the HR 8799 system with the VLT Imager and Spectrometer for the mid-IR (VISIR, Lagage et al. 2004) at 8.7 μm. Additionally, we set constraints on potentially undiscovered companions further out from the star. While both flux limits and mass limits for additional companions have been calculated before in near IR bands (Metchev et al., 2009; Serabyn et al., 2010; Currie et al., 2011; Galicher et al., 2011; Esposito et al., 2013; Zurlo et al., 2016), only Metchev et al. (2009) and Serabyn et al. (2010) have searched for companions beyond 2″ and then only up to 3.5″ and 4″ respectively. VISIR will allow us to expand the search to a factor two larger separations, covering new sky areas.

The data and analysis are described in Section 2.2. The final images and derived limits are presented in Section 2.3 and we present our conclusions in Section 2.4.

2.2 Observations and data analysis

The observations of HR 8799 were taken with VISIR on the VLT UT3 telescope in the small-field imaging mode with a plate scale of 45 mas px^{-1}. They were taken in the J8.9 filter ($\lambda_0 = 8.72$ μm, $\Delta\lambda = 0.73$ μm) using the pupil tracking mode, in which field rotation is enabled to achieve a more stable image. The chopping and nodding sequence were enabled to subtract sky background with a chop throw of 8″ and a chopping frequency of 4 Hz. The nodding direction was perpendicular to the chop direction. Due to the chop throw, the total usable field of view was slightly smaller than 16″x16″. The observations were carried out between August and October of 2018, with a total on-target integration time of 8.7 h as shown in Table 2.1.

Data are provided in the form of time averaged chop difference frames with integration times of 50 s and units of counts per detector integration time (DIT, 0.0114 s). Since the automated

Date	Integration time	Airmass	Image quality FWHM
23-08-2018	1h	1.5	0.26″
09-09-2018	1h	1.5	0.24″
14-09-2018	1h	1.6	0.26″
16-09-2018	0.4h	1.4	0.29″
03-10-2018	1h	1.5	0.24″
11-10-2018	1.3h	1.6	0.31″
12-10-2018	1h	1.5	0.27″
16-10-2018	1h	1.5	0.32″
17-10-2018	1h	1.5	0.29″
Total	8.7h		

Table 2.1: A summary of the VISIR observations of HR 8799 taken between August and October of 2018. The integration time refers to the total on-source integration time of all the data taken on each night. The total on-target time over all nights is provided in the bottom line. The image quality is determined by the full width half maximum (FWHM) of the PSF during the night.

VISIR data reduction[1] is not equipped to reduce pupil stabilised data, the reduction was performed with special-purpose Python scripts. Images were pairwise subtracted between different nod positions to reduce non-common path errors. Beam combination and centering was achieved through fitting Gaussian functions to each of the sources in the nod difference images. The resulting images were stacked into cubes for each night.

Traditional angular differential imaging (ADI, Marois et al. 2006), requires enough time to have passed between the science and reference images for the planet to have moved by at least $1.2\lambda/D$ to avoid self-subtraction of the planetary point spread function (PSF). However, due to the small angular separations of the inner planets d and e this time is sufficiently large that there are (almost) no reference images available for most of the data. Instead, we apply a novel circularised PSF subtraction technique. A circularised PSF of the science data was created by rotating it 1 to 360 degrees in 1 degree steps and averaging over all rotated images. The resulting PSF is a circularly symmetric version of the science data that can then be subtracted from the original to reduce stellar contributions. Any visible secondary source will show up in this circularised PSF as a ring around the central star. The selfsubtraction caused by this ring is expected to be minimal (at most 5% for the innermost planet and less for the planets further out) due to averaging of the source brightness over the full 360 degrees of rotation. An example of the method for the α Cen system is shown in Fig. 2.1. Circularised PSF subtraction has the advantage that, unlike traditional ADI, it is not limited to sources with sufficient field rotation and can therefore be used more widely and on shorter observations. For instruments such as VISIR it is also less sensitive to variations in atmospheric conditions than traditional PSF subtraction, since in this case simultaneous observation of the PSF is not possible.

Once the stellar component has been reduced the images are derotated such that north is up

[1] `https://www.eso.org/sci/software/pipelines/visir/visir-pipe-recipes.html`

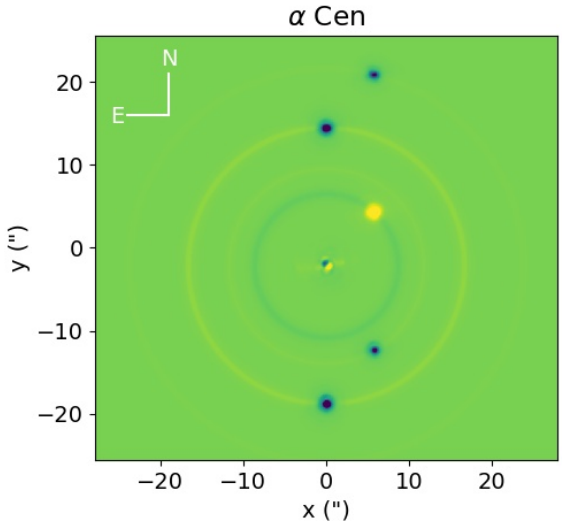

Figure 2.1: Example of circularised PSF subtraction for the binary stars of α Cen. α Cen A is the central source and α Cen B the companion. The central source is subtracted, while the subtraction of the circularised PSF results in a dark ring at the separation of the second source. The second source is still clearly visible, as are in this case the chop/nod shadows of both sources and their corresponding bright rings.

and then the derotated images are combined into a single master image using a weighted sigma-clipped median function with a threshold of 3σ. The weights were determined by the standard deviation and thus the quality of each image. The master image has a total integration time of 8.7 hours and therefore an expected 5σ background sensitivity of 0.7 mJy. The master image was calibrated by comparing it to an image of the stacked and derotated data where no PSF had been subtracted. HR 8799 is expected to have a flux density of 430 mJy in the J8.9 filterband. The conversion factor of the data in ADU / Jy was calculated following the procedures for reference stars in the VISIR pipeline manual and applied to the reduced master image.

2.3 Results and Discussion

Fig. 2.2 shows the reduced master image and the map of the 5σ flux limits derived from the master image. While none of the planets are detected, upper limits can be placed on their emission, as shown in Table 2.2. The upper limit of the flux was determined by calculating the expected flux in a Gaussian function with a full-width-half-maximum of one resolution element of the telescope and a peak flux of 5σ of the background in the surrounding area. The limits found for HR 8799 b and c correspond to the expected background sensitivity of the instrument over the observed time. The higher limits on HR 8799 d and e are the result of imperfectly subtracted stellar residuals, as due to seeing the stellar PSFs in the science data were no longer entirely circularly symmetrical.

The right panel in Fig. 2.2 shows that the 5σ flux limits decrease with distance from the star in all directions, further supporting that the increased limits are due to stellar residuals. No other

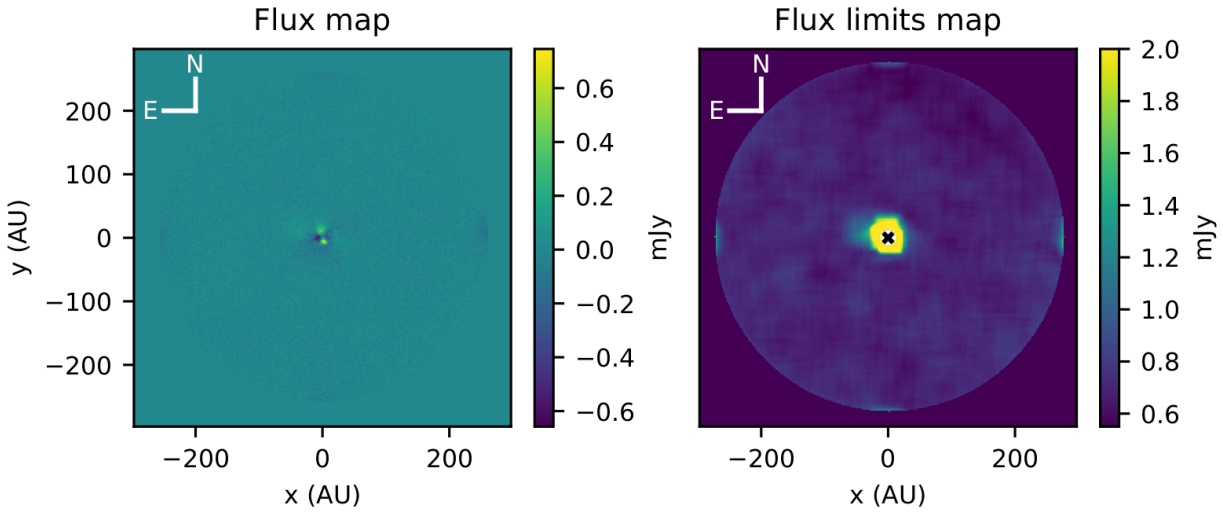

Figure 2.2: Left: Reduced master image of HR 8799, centered on the star. The planets are not visible in the reduced data. Positive and negative structures are visible in the center from imperfect subtraction of the stellar PSF. Right: 5σ flux limit map. The center of the image around the star where the limits are highest has been occulted for clarity. The decrease of the limits with radius shows that stellar features dominate the inner 40 AU, and further out a background sensitivity is achieved.

Planet	Separation	Position angle	5σ limits (mJy)
HR 8799 b	1.7″	71°	<0.7
HR 8799 c	1.0″	332°	<0.8
HR 8799 d	0.6″	230°	<2.9
HR 8799 e	0.4″	292°	<3.3

Table 2.2: Detection limits for the four planets in the HR 8799 system. Separations and position angles are taken from Marois et al. (2008; 2010) with position angles corrected for orbital motion based on the planets periods.

structures are visible and the background sensitivity is achieved beyond ~ 40 AU.

To verify these limits we injected 24 fake sources into the data before the psf subtraction. Figure 2.3 shows the reduced data with the injected sources. 12 sources are injected at increasing radii and 12 are injected at the same radius of 200 AU. Each source has a flux equal to the 5σ flux limit at that radius. The sources in the spiral are retrieved at 4.5σ confidence, but the sources on the ring at only 3.5σ. In both cases the difference with the injected magnitude is due to the contribution of the injected sources to the circularised PSF. For the spiral there is only one source at each radius and the effect is small, but for the ring there are 12 sources contributing to the PSF at 200 AU, resulting in a brighter ring being subtracted. This results in a dark ring at that radius and a reduced magnitude of the retrieved sources. Despite this effect all injected sources are retrieved and since planets are not expected to have identical orbital separations within one system, we conclude that our limits are valid.

Fig. 2.4 shows the model fits to the near infrared spectral energy distributions of the four planets (Marois et al., 2008; Marois et al., 2010). Our flux limits and the expected model pre-

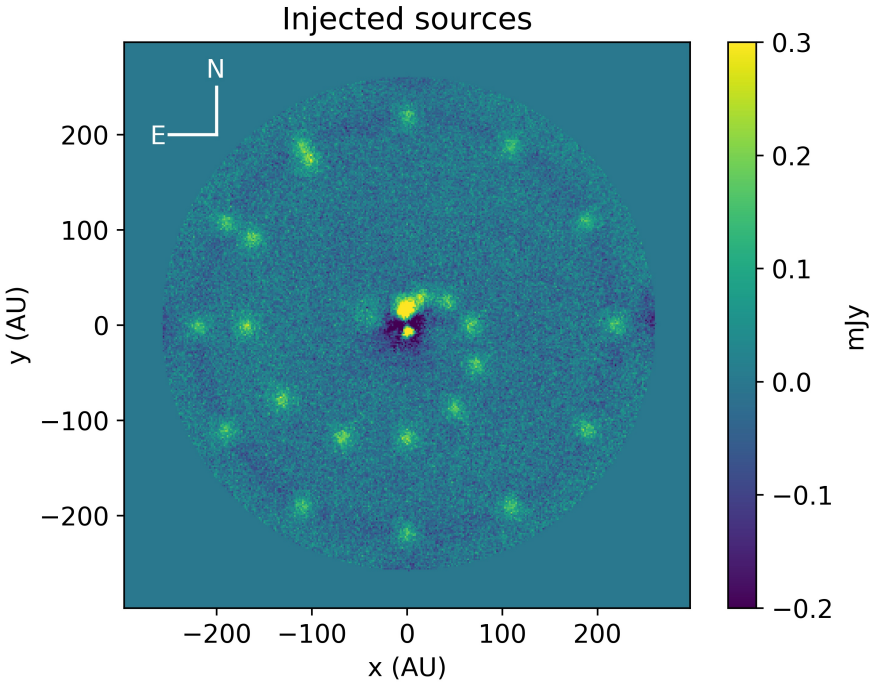

Figure 2.3: Reduced master image of HR 8799 with injected sources at the 5σ limit. 12 sources are injected at increasing radius and 12 at an outer radius of 200 AU. The sources in the spiral are retrieved at 4.5σ and sources in the ring at 3.5σ. The lower certainty retrievals are due to the sources contributing to the PSF that is subtracted from the background.

dicted flux densities of each planet in the J8.9 band are marked as well. This shows that the expected flux density lies below the derived limits in all cases.

To convert the obtained flux limits into mass limits, we condensed the flux limit map from Fig. 2.2 into a contrast curve, which is then converted into mass limits for any objects in the system. This is done using the BT SETTL evolutionary models of stars, brown dwarfs and exoplanets (Allard et al., 2012) and assuming an age for the system. Two ages have been considered in previous works: 30 Myr and 60 Myr, depending on whether the authors believe HR 8799 to be part of the Columba local association (eg. Galicher et al. 2011; Zurlo et al. 2016) or not (Metchev et al., 2009; Hinz et al., 2010). Doyon et al. (2010) and Zuckerman et al. (2011) have determined that HR 8799 is likely to belong to the Columba association and as such has an age of 30 Myr, while Hinz et al. (2010) have not found this to be the case and used an age of 60 Myr based on the original considerations regarding the disk mass, stellar class, HR diagram location and galactic motion by Marois et al. (2008). For this work we have examined the mass limits at both ages and found them to be nearly identical. The difference in the ages means a difference in available cooling time, resulting in ~150 K difference between the two models at ~30 M_{Jup}. The resulting difference in 8.7 μm flux is less than 0.1 mJy with the result that the returned mass limits are very similar. Our results are shown in Fig. 2.5 and show a sharp increase in mass inward of 40 AU, where stellar wings dominate the background. Outside of this distance the line levels out at

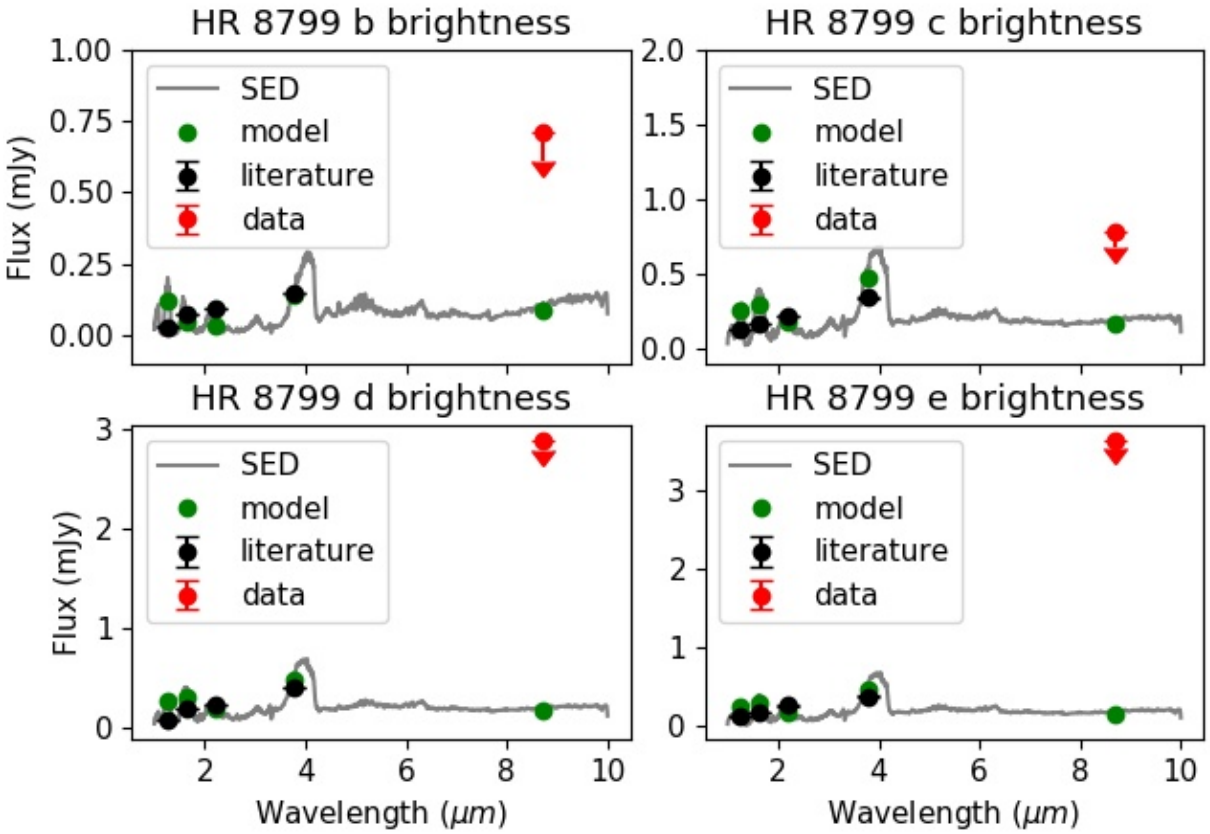

Figure 2.4: Theoretical spectral energy distributions (SED, grey) for HR 8799 bcde from top left to bottom right using the BT SETTL model with temperatures and surface gravities from Marois et al. (2008, 2010). The flux density values of the earlier measurements are marked in black and the values derived from the model are marked in green. The 5σ upper limits calculated in this work are marked in red. All four planets have expected J8.9 flux densities below the derived limits, resulting in a nondetection of the planets in the data.

30 M_{Jup}, which corresponds to the sensitivity limits of the instrument. Our result is in agreement with earlier work by Marios et al. (2008, 2010) and Wang et al. (2018) which places the masses of the four planets between 7 and 10 M_{Jup}. The calculated limits are further in agreement with limits set in the near infrared within 2″ by Zurlo et al. (2016). The sharp increase at around 8″ is due to the chop/nod shadows of the source in the data. The steps in the mass limits are caused by the stepsize in mass in the isochrone models, which is 10 M_{Jup} between planet masses of 20 and 100 M_{Jup}.

Mass limits for the same data reduced with ADI are also shown in Fig. 2.5 in green. Here an age of 30 Myr is assumed. The mass limits retrieved with this technique are around 100 M_{Jup}, three times higher than for the circularised PSF subtraction. This difference in mass limits represents a difference in flux limits of 0.26 mJy. Limits inside 1.5″ are not shown due to insufficient field rotation closer to the star.

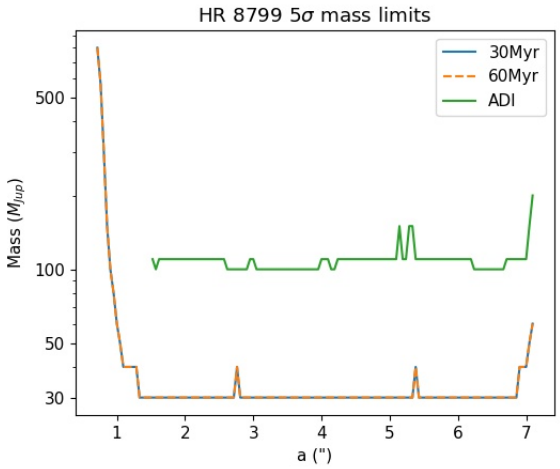

Figure 2.5: Upper mass limits (5σ) for the mass of any objects in the HR 8799 system as a function of separation from the star. At small separations the flux from stellar residuals causes high mass limits, but at 1″ (40 AU) these become negligible and the background dominates for the circularised PSF subtracted data. The mass limit levels out to 30 M_{Jup}, as indicated by the black dotted line. The increase furthest out is due to the chop/nod shadows located at 8″. The mass limits resulting from data reduced with traditional ADI beyond 1.5″ are shown in green and are around 100 M_{Jup}.

2.4 Conclusions

This work presents the first mid-infrared direct imaging observations of the HR 8799 planetary system and places constraints on the fluxes and masses of objects between 40 and 330 AU. It thus provides the most stringent limits obtained to date at the furthest separations so far. The results exclude further companions with fluxes of more than 0.7 mJy or masses exceding 30 M_{Jup} with a 5σ certainty, given an age of 60 Myr.

The achieved flux limits were insufficient to detect the HR 8799 planets, but we demonstrated that VISIR can reach sufficient sensitivity to detect planets in other systems which are hotter and/or closer to Earth. Excluding the HR 8799 system, the `exoplanet.eu` database (Exoplanet Team, 2021; Schneider et al., 2011) contains 22 directly imaged planets with a listed temperature and a known surface gravity within 50 pc. Of these, 4 planets are sufficiently bright to be imaged by instruments with similar sensitivities to VISIR at a 5σ detection level in less than 10 hours: these planets are β Pic b, CD-35 2722 b, HD 116434 b and G196-3 b. β Pic b has a temperature of 1800 K and is located at a distance of 19.8 pc. (Chilcote et al., 2017; Gaia Collaboration et al., 2018) It is expected to have an 8.7 µm flux density of 3.0 mJy. While β Pic b is currently very close to its star, Dupuy et al. (2019) have calculated that by 2028 the angular separation should be around 0.68-0.75″ for a predicted eccentricity of 0.24. The flux limit is then 2.4 mJy for 10 hours of observation and the planet becomes detectable. CD-35 2722 b and G196-3 b have similar temperatures and distances (Wahhaj et al., 2011; Rebolo et al., 1998), while HD 116434 b is a cooler, closer in planet with a temperature of 1300 K at 11 pc. (Chauvin et al., 2017)

Additionally, VISIR is being upgraded into the NEAR (New Earths in the Alpha Cen Region)

instrument, which, thanks to the addition of adaptive optics, is reported to have a 10σ sensitivity of 0.9 mJy in 1 hour, an improvement of approximately a factor of four. For the foreseeable future NEAR will only be observing the α Cen system, but this kind of advancement in technology will allow the previously mentioned planets, as well as four additional planets, to be imaged in under an hour. Eleven more planets, including HR 8799 c and d, become accessible with up to 10 hours of observation time, demonstrating the potential of directly imaging exoplanets at mid-IR wavelengths with present-day facilities.

Chapter 3

High contrast imaging at 10 micron, a search for exoplanets around: ε Indi A, ε Eri, τ Ceti, Sirius A and Sirius B

P. Pathak, D. J. M. Petit dit de la Roche, M. Kasper, M. Sterzik, O. Absil, A. Boehle, F. Feng, V. D. Ivanov, M. Janson, H.R.A. Jones, A. Kaufer, H.-U. Käufl, A.-L. Maire, M. Meyer, E. Pantin, R. Siebenmorgen, M. E. van den Ancker, G. Viswanath

Accepted for publication in Astronomy & Astrophysics

Abstract: The direct imaging of rocky exoplanets is one of the major science goals for upcoming large telescopes. The contrast requirement for imaging such planets is challenging. However, the mid-IR (InfraRed) regime provides the optimum contrast to directly detect the thermal signatures of exoplanets in our solar neighbourhood. We aim to exploit novel fast chopping techniques newly developed for astronomy with the aid of adaptive optics to look for thermal signatures of exoplanets around bright stars in the solar neighbourhood. We use the upgraded VISIR (Very Large Telescope Imager and Spectrometer for the mid-InfraRed) instrument with high contrast imaging (HCI) capability optimized for observations at 10 μm to look for exoplanets around five nearby ($d < 4$ pc) stars. The instrument provides an improved signal-to-noise (S/N) by a factor of ~4 in the N-band compared to standard VISIR for a given S/N and time. In this work we achieve a detection sensitivity of sub-mJy, which is sufficient to detect few Jupiter mass planets in nearby systems. Although no detections are made we achieve most sensitive limits within $< 2''$ for all the observed targets compared to previous campaigns. For ε Indi A and ε Eri we achieve detection limits very close to the giant planets discovered by radial velocity, with the limits on ε Indi A being the most sensitive to date. Our non-detection therefore supports an older age for ε Indi A. The results presented here show the promise for high contrast imaging and exoplanet detections in the mid-IR regime.

3.1 Introduction

The direct imaging of habitable exoplanets is one of the key science goals of current and upcoming large telescopes (Meyer et al., 2018). The field of high-contrast imaging (HCI), employing extreme adaptive optics (ExAO), coronagraphy and state-of the art post-processing techniques, has enabled direct imaging of young (up to about 30 Myr), several Jupiter-mass exoplanets with current 8-10 m class telescopes (Marois et al., 2008; Macintosh et al., 2015; Keppler et al., 2018; Chauvin et al., 2017; Nowak et al., 2020). Examples of current HCI instruments include the Spectro-Polarimetric High-contrast Exoplanet REsearch instrument (SPHERE), the Gemini Planet Imager (GPI) and Subaru Coronagraphic Extreme Adaptive Optics (SCExAO), all of which operate in the near-IR (1-2.5 μm) regime (Beuzit et al., 2019; Macintosh et al., 2014; Jovanovic et al., 2015). Compared to the near-IR, the mid-IR (8-13 μm) is more sensitive to colder planets and allows to probe less massive planets or, for a given mass, one is able to search around older stars (Quanz et al., 2015). This is because the planet to star flux contrast is more favourable in the mid-IR, where the thermal emission of the planet peaks in the Rayleigh-Jeans tail of target stars (Baraffe et al., 2003; Sudarsky et al., 2003; Marley et al., 2007; Fortney et al., 2008; Spiegel and Burrows, 2012). The key downsides of mid-IR HCI are reduced spatial resolution due to the larger diffraction limit and large sky-background for ground-based observations. Therefore, the mid-IR is best suited to look for exoplanets around nearby stars.

New Earths in the α Cen Region (NEAR) experiment was a collaboration between the Breakthrough Foundation and the European Southern Observatory (ESO). The project involved upgrading the existing VISIR (Very Large Telescope Imager and Spectrometer for the mid-InfraRed) instrument (Lagage et al., 2004) at the VLT with adaptive optics (AO) using the deformable secondary mirror (DSM) installed at UT4 (Arsenault et al., 2017), and a high-performance annular groove phase mask (AGPM) coronagraph (Mawet et al., 2005). The aim of the NEAR experiment was to enable HCI capability in the astronomical N-band and to look for low mass exoplanets in the α Centauri binary system in a 100 hr campaign (for details see Kasper et al., 2017b, 2019). The NEAR was able to reach sensitivity and contrast sufficient for detection of Neptune mass planets in the habitable zone of α Cen A, and a weak signal was found whose nature (e.g., planet, part of a zodiacal disk, image artefact) remains to be confirmed by follow-up observations (for details see Wagner et al., 2021).

In this work, we report the results of observations with NEAR to look for Jupiter size exoplanets around the nearest stars with spectral type earlier than M: ε Indi A, ε Eri, τ Ceti, Sirius A and Sirius B.

In Sect. 3.2 we briefly describe observed targets, in Sect. 3.3 and 3.4 we describe the data observation and reduction techniques. We discuss results in Sect. 3.5 and conclude with Sect. 3.6.

3.2 Target description

3.2.1 ε Indi A

ε Indi is a triple system at a distance of 3.6 pc (Gaia Collaboration et al., 2020a). It consists of

the primary K5V star ε Indi A and a brown dwarf binary (ε Indi Ba and Bb) on a wide orbit of 1459 AU (Scholz et al., 2003; McCaughrean et al., 2004). Age estimates of $1.4^{+1}_{-0.5}$ Gyr for ε Indi A were published based on chromospheric activity indicators such as the calcium R_{HK} as a proxy for rotation (Lachaume et al., 1999). Given the well-known relationships between rotation and age for FGK stars a similar value of 1.5 Gyr was suggested by Kasper et al. (2009). However, Dieterich et al. (2018) suggest an older age based on UVW kinematics and cooling curves for the brown dwarf companions. Recently Feng et al. (2019) use extensive time-resolved spectra to estimate a rotation period for the star of 36 days, suggesting an age of ∼4 Gyr based on the rotation-age calibration of Eker et al. (2015). This older age also agrees with the 3.7-4.3 Gyr estimated by King et al. (2010) for the brown dwarf binary from the dynamical system mass and the evolutionary models of Baraffe et al. (2003). The higher end of the age range is therefore more likely.

Endl et al. (2002) first identified a long-period, low-amplitude radial velocity signal in ε Indi A, which could be explained by a companion with P¿20 yr and a mass of at least 1.6 M_{Jup} . This signal has been confirmed by Janson et al. (2009) and Zechmeister et al. (2013), who also find that the binary brown dwarf companions ε Indi Ba and Bb are too far away to induce the measured trend. Feng et al. (2019) combine radial velocity data with astrometry to confirm the existence of a $3.25^{+0.39}_{-0.65}$,M_{Jup} planet on an eccentric orbit with a period of $45.2^{+5.74}_{-4.77}$ yr. In September 2019, at the time of our observations the separation of this planet from the host star is expected to be about 1.07″ (error bars are large due to the poorly constrained orbital solution).

3.2.2 ε Eri

ε Eri is an adolescent K2V type dwarf star at a distance of 3.2 pc (Gaia Collaboration et al., 2020a). The age of the star has been estimated through various means and is generally thought to be around 0.4-0.9 Gyr, with the higher end of the range being more likely (Henry et al., 1996; Song et al., 2000; Di Folco et al., 2004; Mamajek and Hillenbrand, 2008). ε Eri is surrounded by a narrow ring of debris located between 63 to 76 AU and a possible inner belt at 12 to 16 AU (see Mawet et al., 2019, for a full discussion of the disk structure).

A companion to ε Eri was first suggested by Walker et al. (1995) based on radial velocity data. Hatzes et al. (2000) argued that the most likely explanation for the observed decade-long radial velocity (RV) variations was the presence of a 1.5 M_{Jup} giant planet with a period P = 6.9 yr (3 AU orbit) and a high eccentricity (e=0.6). Very similar parameters for the planet ε Eri b were derived from a comprehensive set of RV as well HST astrometry data by Benedict et al. (2006). The most recent mass estimate to date was done by Mawet et al. (2019) and combined 30 years of radial velocity data with deep direct imaging data in a Bayesian analysis to constrain the properties of the companion. They found a mass of $0.78^{+0.38}_{-0.12}$ M_{Jup} at a separation of 3.48 ± 0.07 AU and an eccentricity of 0.007, which is lower than previous reported values. Direct imaging detections of ε Eri b in the L- and M-bands were attempted by Janson et al. (2008) and Mawet et al. (2019) and yielded an upper mass limits of around 4 M_{Jup} (for an age of 320 Myr) and 2 M_{Jup} (for 400 Myr), respectively. A second companion was first suggested by Benedict et al. (2006) at 12-20 AU based on radial velocity residuals, but this was not confirmed by Mawet et al. (2019). An alternative additional companion of 0.4-1.2 M_{Jup} has been suggested at 48 AU

by Booth et al. (2017) to explain the shape of the outer dust belt, and Mawet et al. (2019) also require an additional planet to stir this belt. Janson et al. (2015) are able to obtain sub-Jovian mass limits of 0.6-1 M_{Jup} at these larger separations, but this cannot rule out the lower end of the proposed mass range, so while the companion has not been confirmed, it can also not been ruled out.

3.2.3 τ Ceti

τ Ceti is a nearby (3.7 pc), sun-like G8.5V star with an extended debris disk (5-55 AU) that is more than 10 times as massive as the Kuiper belt (Gaia Collaboration et al., 2020a; Gray et al., 2006; Greaves et al., 2004; MacGregor et al., 2016). There is a large range in the literature for ages of τ Ceti: based on stellar activity the age is 5.8±2.9 Gyr (Mamajek and Hillenbrand, 2008), but astroseismological and interferometric measurements suggest an age closer to 8-10 Gyr (Di Folco et al., 2004; Tang and Gai, 2011) and chemical composition measurements point towards an age of $7.63^{+0.87}_{-1.5}$ Gyr (Pagano et al., 2015).

Tuomi et al. (2013) discovered 5 Earth-like planets in radial velocity data with periods from 14 to 642 days (0.1-1.35 AU). Two of these were confirmed by Feng et al. (2017), who discovered two further planets at periods of 20 and 49 days. They also suggest that the 14 day signal could be the result of stellar activity, rather than a planet and that candidates e, f and h might actually be too eccentric to be planets. Dietrich and Apai (2020) use dynamical arguments to provide statistical evidence for the existence of the remaining three planets suggested by Tuomi et al. (2013) and one additional candidate that could be located in the habitable zone. All the previously mentioned candidates are expected to be super-Earths ($M \cdot sin(i) \approx 1-4 M_{\oplus}$). However, Kervella et al. (2019) provided tentative evidence of a giant planet candidate (1-2 M_{Jup} , 3-20 AU) from Gaia data. Near infrared direct imaging has not been able to detect any of the planets, but has provided constraints of 10-20 M_{Jup} at separations larger than 2″ (7AU) and 30-50 M_{Jup} at 1″ (Boehle et al., 2019). The candidate detected by Kervella et al. (2019) is the only one that is not too small and close to be detected with present-day mid-IR facilities.

3.2.4 Sirius A

Sirius is a binary system at a distance of 2.7 pc, consisting of an A1Vm star and a WD with an age of 225-250 Myr (Gaia Collaboration et al., 2020a; Liebert et al., 2005; Bond et al., 2017). While there are no known planets around Sirius A or B, there are mass limits on possible companions from previous imaging campaigns, covering wavelengths of roughly 0.5-5 μm. The most sensitive limits on Sirius A exclude giant planets down to 11 M_{Jup} at 0.5 AU, 6-7 M_{Jup} in the 1-2 AU range and 4 M_{Jup} at 10 AU (Hunziker et al., 2020; Vigan et al., 2015; Thalmann et al., 2011; Bonnet-Bidaud and Pantin, 2008). In any case, the long-term orbital stability of planets around Sirius A or B would be impacted by the binarity of the system, which has a semi-major axis of about 20 AU and eccentricity 0.6. Bond et al. (2017) find that the longest periods for stable planetary orbits in the Sirius system are about 2.24 yr for a planet orbiting Sirius A, corresponding to a r = 2.2 AU circular orbit, and 1.79 yr for a planet orbiting Sirius B, corresponding to a r = 1.5 AU circular orbit. WDs are typically 10^3 to 10^4 times less

luminous than their progenitor stars. Thus, it would be much easier to achieve the contrast required to detect a planetary companion (Burleigh et al., 2002). This idea sparked direct imaging searches for planets around WDs (Gratton et al., 2020; Friedrich et al., 2007). While no planets have been found using direct imaging to date, a transiting planet was found around the white dwarf WD 1856+534 (Vanderburg et al., 2020), and an evaporating Neptune was proposed to explain the chemical fingerprints of hydrogen, oxygen and sulfur in the spectrum of WDJ0914+1914 (Gänsicke et al., 2019).

3.2.5 Sirius B

For Sirius B, as explained above a planet in a stable orbit would have a period of 1.79 yr for a r = 1.5 AU. No limits have been placed on companions within 3″, although near infrared imaging by Bonnet-Bidaud and Pantin (2008) did set limits of 10-30 M_{Jup} outside of that radius. Sirius B is the only target in the sample to have been previously imaged in the mid-IR at 8-10 μm between 2003 and 2006, but no limits on companions were determined from this dataset (Skemer and Close, 2011).

3.3 Observation and data reduction

All the observations employed a common observing strategy, including the use of AO, an AGPM coronagraph, chopping and nodding. The chopping was done with the DSM of the VLT. The chop throw of the DSM was ∼ 4.5″ and was performed at a speed of 8.33 Hz to reduce the excess low frequency noise common to the mid-IR arrays (Si:As array, Arrington et al., 1998). The chopping subtracts two images taken at different position on the sky thereby leaving a positive (coronagraphic, on-axis) and a negative (off-axis) image of the source separated by the chop throw and removing most of the sky and instrumental background flux bias. However, the optical path is slightly different for both chopping positions, which leaves some small residuals. In principle, these could be removed by nodding (for details see Lagage et al., 2004), but our data reduction is not affected by the small chopping residuals which are not point-like and do not degrade the point-source sensitivity. At 8.33 Hz chopping, each half-cycle is 60 ms consisting of 8 × 6 ms DITs (=48 ms) and 2 × 6 ms DITs (=12 ms) skipped during the chopping transition. The other half-cycle is taken with the star off the coronagraph. At each nodding position, 500 chopping frames half-cycles were recorded for a total observing time of 500 × 60 ms = 30 seconds out of which 250 × 48 ms = 12 were spent with the target on the coronagraph, that is, the observing efficiency was 40%. A summary of the observations and the atmospheric conditions affecting the sensitivity is outlined in the Table 3.1. The atmospheric data were taken from Paranal Astronomical Site Monitoring. To center the targets on the coronagraph and to minimize the leakage, a dedicated correction using the science images with the aid of the QACITS algorithm was used (for details see Maire et al., 2020). We derived a pixel scale of 45.25 mas/pixel using the α Cen campaign data, utilizing the well known orbit of the binary from Kervella et al. (2019). In the next section we discuss the steps employed for the data reduction.

Target	Parallax (mas)	N-band (Jy) brightness	Date observed	Observation time (hr)	On-coronagraph time (hr)	Seeing (arcsec)	Temp (°C)	PWV (mm)
ε Indi A	274.84	4.5	2019-09-14	2.35	0.81	0.8-2.0	10-11	0.8-2.2
			2019-09-15	4.23	1.47	0.5-1.0	12-13	0.4-0.9
			2019-09-17	3.31	1.33	0.5-0.9	9-12	0.9-3.0
ε Eri	310.58	7.6	2019-09-15	1.61	0.61	1.0-1.8	11-12	0.4-0.7
			2019-09-17	2.63	1.01	0.5-0.9	9-10	0.8-1.4
τ Ceti	273.81	7.5	2019-09-16	1.81	0.65	0.8-1.6	10-11	3.0-5.0
Sirius A	374.49	118.8	2019-12-15	2.38	0.74	0.4-0.7	13-14	3.8-5.2

Table 3.1: Observing parameters for all the targets under various conditions. All the observations were carried out using the NEAR N-band filter with a bandpass of 10-12.5 μm. The N-band brightness reported in the table assumes the central wavelength of the NEAR filter of 11.25 μm.
Note: The on-coronagraph time is 40% of the selected frames due to the observing strategy based on chopping and nodding, for details see Sec. 3.3.

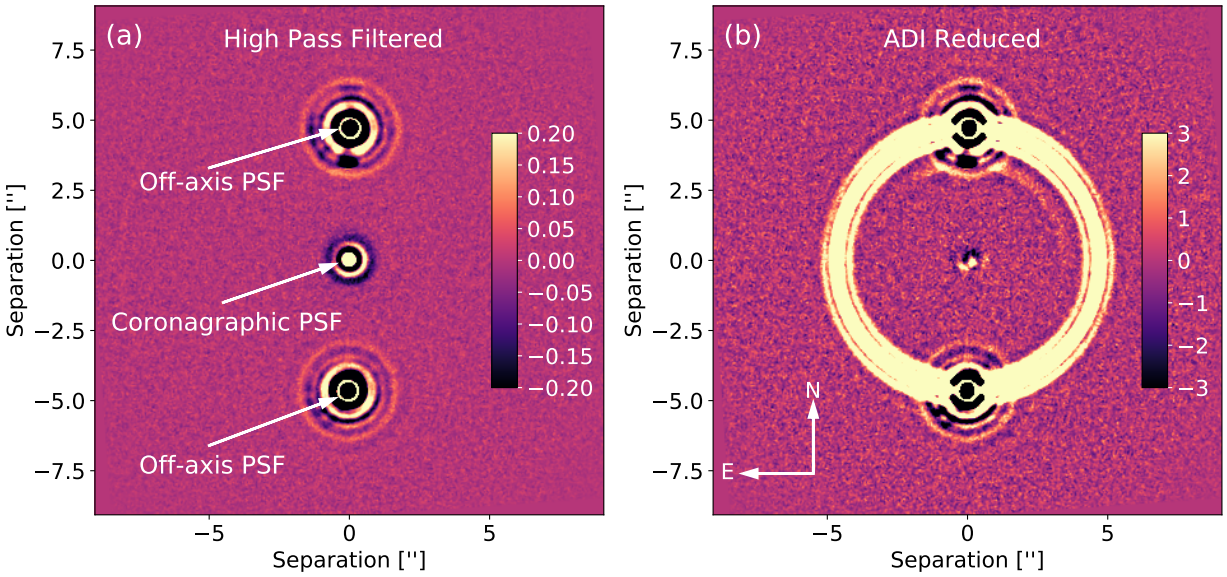

Figure 3.1: (a) Final derotated image of the ε Indi A target with high-pass filter applied. (b) ADI processed image.

3.3.1 Data Reduction

For all the targets a common data reduction strategy was followed, which included a chop subtraction of the off-axis from the on-axis source position frames adjacent in time. This provided images where the source was positive on the coronagraph and negative in the off-axis position.

Three selection criteria were employed to identify inferior frames and remove them from the data analysis: AO correction (ratio of flux in an annulus of radii 6-12 pix to flux in an aperture of r¡6 pix), coronagraphic leakage (flux in an aperture of 20 pix) and sky-background noise variance calculated using small regions of the non-chopped images. To further identify good, co-aligned frames, an additional parameter based on the positions of the off-axis PSFs was used. The employed selection criteria improved the overall sensitivity and contrast, and reduced false positives, especially at small projected separations. We lost about 14%, 5%, 10% and 22% of the observed frames for ε Indi A, ε Eri, τ Ceti and Sirius A respectively.

Once good chopped frames were identified, they were binned by averaging 250 frames. The binning of the frames to an exposure time of 30 seconds (250×0.12s) was chosen to be short enough to avoid smearing of potential companions by the field rotation, and long enough to provide a good sensitivity on binned frames and to reduce the data size for further post-processing. The averaged frames still show some smoothly varying structures (residual sky-background, left over after chopping), which was removed by applying a spatial high-pass filter. This filtering process creates a smoothed version of the image, by replacing each individual pixel by a median of 15×15 surrounding pixels, and then subtracts it from the image. The effect of such filtering on the point source signal was a flux reduction of less than 10% and had a negligible effect on the noise variance. Figure 3.1 (a) shows a final averaged and derotated image for the target ε Indi A, with the coronagraphic PSF at the center and the off-axis PSF's representing both the nod positions.

For the final Angular Differential Imaging (ADI) analysis (Marois et al., 2006), night by night data was processed using a global annular Principal component analysis (PCA) based algorithm. Specifically, for a given analysis frame, we identify all the frames obtained during that night which differ in field rotation angle by at least one PSF half width at half maximum (HWHM) at the smallest angular separation of interest. We set this separation to 8 pixels (or 360 mas) which corresponds to the 1st minimum of the VLT's N-band Airy pattern. For this set of calibration frames, first the mean of the set was subtracted from all individual frames. Then we select all pixels in an annular area with an inner radius of 8 pixels and an outer radius of 25 pix, corresponding to the 3rd minimum of the Airy pattern. As our images are usually very smooth and without residual speckle structure outside a radius of 25 pix (see Figure 3.1 a), we do not benefit from a larger outer radius. We perform the PCA analysis on these data, i.e., on the pixels in the annular area for the set of calibration frames arranged in a matrix of size #pixels $\times$ #frames. This yields the linear combinations of calibration frames (the principle components) which best reproduces the analysis frame. The optimization of the PCA parameters, such as inner and outer radius of the annulus and number of principal components, was done with artificial planet injection and recovery tests, to maximize the contrast sensitivity. We observed that 15 principal components yielded the best compromise between the reduction of PSF residuals and self-subtraction of artificial planets inserted into the data. A further analysis was performed by splitting the data into odd-even frames and dividing into different chunks, to see if any strong speckles remain for different analysis. This helped to identify suspected false positive detections such as a faint speckle visible just right of the coronagraph center in the Figure 3.1 (b).

In the case of targets observed for more than one night, the final processed image was produced by weighting each night's combined image by the inverse of the background noise as measured in the combined frame of the night, i.e., by applying a noise weighted mean. This step was used to compensate for variable atmospheric conditions (ambient temperature, humidity and precipitable water vapor in the atmosphere), this helped to improve the final noise variance in the image (Turchi et al., 2020).

3.4 Analysis

To quantify the results further, we calculate a background noise limited sensitivity and contrast curve using artificial planet injections and recovery tests for each target, which is discussed in the following sections.

3.4.1 Background noise limited imaging performance (BLIP)

We obtain a 5σ background noise limited imaging performance (BLIP) by calculating the standard deviation in 4-pix radius (=1.25 λ/D) apertures at various locations of the PCA reduced images. This value was then multiplied by 5 times the square root of the number of pixels in the aperture ($5 \times \sqrt{16\pi}$). To get the sensitivity with respect to the target, we used the off-axis stellar PSF for relative flux-calibration. This process was repeated for 20 angular and 17 radial

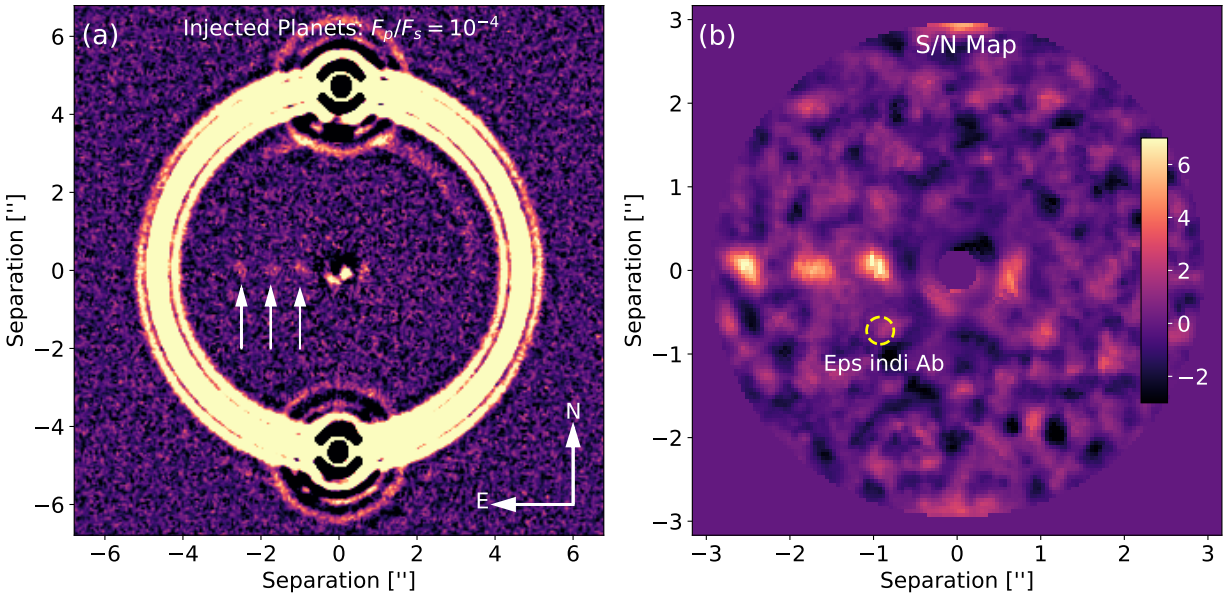

Figure 3.2: (a) ε Indi A image with injected planets at contrast of 10^{-4} with a separation from 1″ to 2.5″ marked with white arrows to left. On the right-hand side is a likely false positive identified from examination of the odd-even frames. (b) S/N map showing injected planets appearing with S/N in the range of 5 − 7. The approximate position of ε Indi Ab is shown by a circle, but the uncertainties are large (for details see Feng et al., 2019)

.

distances separated by 7 pix. A mean of angular values was then calculated to get a background noise limited sensitivity curve as shown by the dashed line in the Figure 3.3 panel (a)-(d).

The background noise limited sensitivity steeply increases at small separations ($\lesssim 1''$) for ε Indi A, ε Eri and τ Ceti, which is due to the coronagraphic glow. Because the AGPM is not located downstream of a cold stop in VISIR, a part of the thermal emission originating from outside the telescope pupil (incl. the central obscuration) is diffracted back inside the pupil by the vortex effect (see Absil et al. (2016) for details). This creates a significant additional amount of thermal background close to the center of the AGPM on the detector. Which could be mitigated by introducing a cold stop upstream of the AGPM.

The BLIP sensitivity would only be reached in the absence of coronagraphic PSF residuals (quasi-static speckles, QSS) from the central star. It can be compared to the point source sensitivity contrast introduced above to evaluate the angular separation beyond which BLIP sensitivity is reached. At such angular separations, the sensitivity improves with the square-root of integration time while sensitivity improvements in the inner regions dominated by QSS are much harder to achieve.

Figures 3.3 and 3.4 show that the gap between BLIP sensitivity and point source sensitivity contrast levels out at angular separations of around 1” or 3.5λ/D for the fainter stars of our sample (ε Indi A, ε Eri, τ Ceti and Sirius B). At such separations, QSS are no longer seen (cf. Figure 3.1) and pixel-pixel noise dominates the sensitivity. The shallow improvement of the point source sensitivity towards even larger angular separations can be attributed to the PCA algorithm which does not conserve flux and self-subtracts a diminishing fraction of the injected fake planets signal.

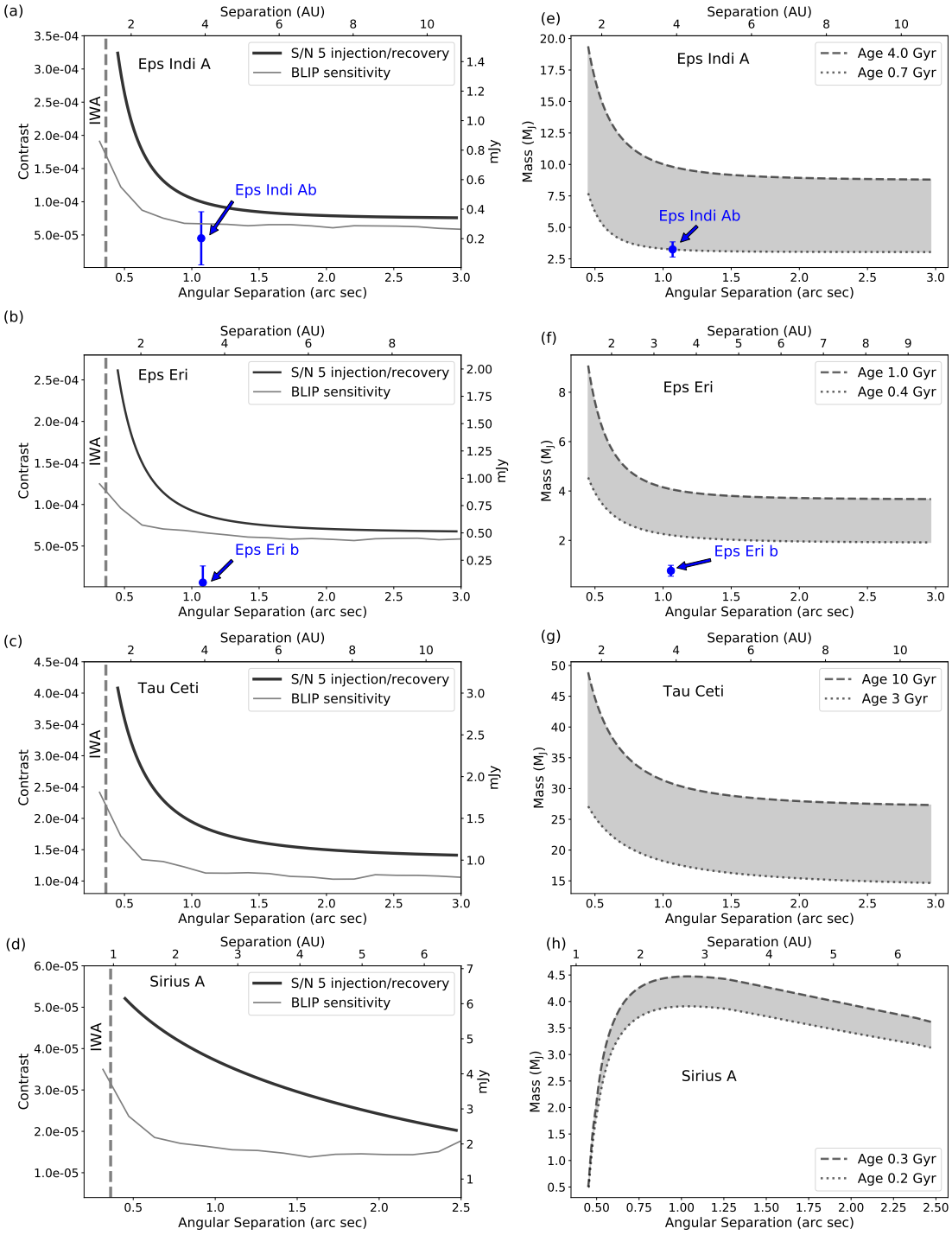

Figure 3.3: Panel (a), (b), (c), and (d) shows 5σ contrast curves and background noise limited imaging performance. Panel (e), (f), (g) and (h) shows the mass limits derived using contrast curves. The solid line is derived using artificial injection and recovery tests, the thin line represents the 5σ BLIP sensitivity. The detection limits would improve with $\sqrt{t_{obs}}$ and observing conditions. The different shape of the curves in (h) is due to the strong irradiation of the planet by the star, as discussed in Section 3.5.4.

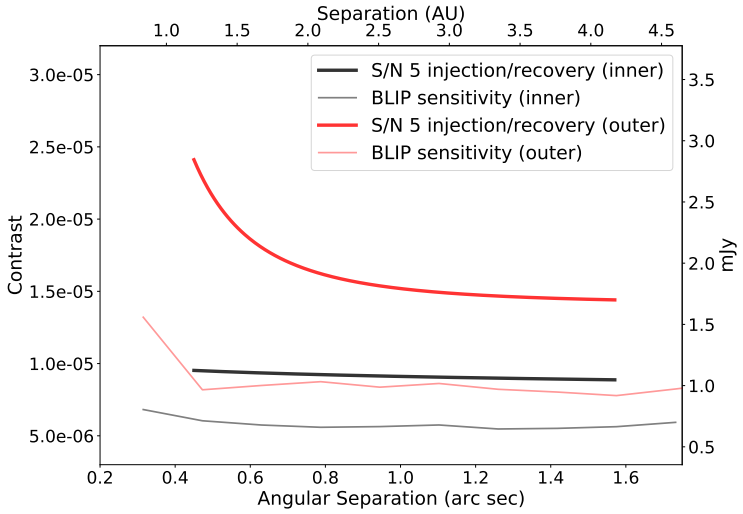

Figure 3.4: Sirius B 5σ contrast curves, same as in Figure 3.3. The outer and inner regions are represented by red and black lines respectively. The contrast curve for outer region increases at small separation due to edge of the inner frames.

The contrast around the very bright Sirius A instead is limited by QSS and PSF residuals out to an angular separation of several arcseconds. This is due to a slight misalignment between the star and the coronagraph during the observation, and to the use of a conventional Lyot-stop (LS). While the apodized LS used during the Alpha Cen observing campaign (Wagner et al., 2021) suppresses the off-axis Airy pattern at angular separations similar to the chopping throw of 4.5", this conventional LS does not reduce the Airy pattern of the off-axis chopping position and leaves residuals near the coronagraphic center which reduce sensitivity.

3.4.2 Point Source Contrast Sensitivity

To compute the planet detection sensitivity, we injected artificial planets at various angular and radial (0.7″, 0.85″, 1″, 1.5″, 2″, 2.5″) separations. To estimate signal-to-noise (S/N), we used the approach of Mawet et al. (2014), as implemented in the open source Vortex Image Processing library (Gomez Gonzalez et al., 2017). We found that a S/N of 5 using the above criteria was sufficient to visually identify inserted artificial planets, as can be seen from Figure 3.2. The Figure shows injected planets at a contrast of 10^{-4} with respect to ε Indi A, with separations of 1″, 1.7″, 2.5″. Panel (b) shows their S/N estimates, which varies from $5-7$ from the inner to the outer planets.

The overall contrast curve sensitivity was calculated by azimuthally averaging the contrast required to achieve 5σ S/N. We used a power law function to fit the radial points to obtain final contrast curves. The contrast curves of all our targets are shown in the Figures 3.3 panel (a)-(d). The contrast at small separation is affected by the coronagraphic glow similar to background noise limited sensitivity, except for the target of Sirius A, for the reason mentioned in the previous section.

Estimated contrasts of the known RV companions of ε Indi A and ε Eri are included in the

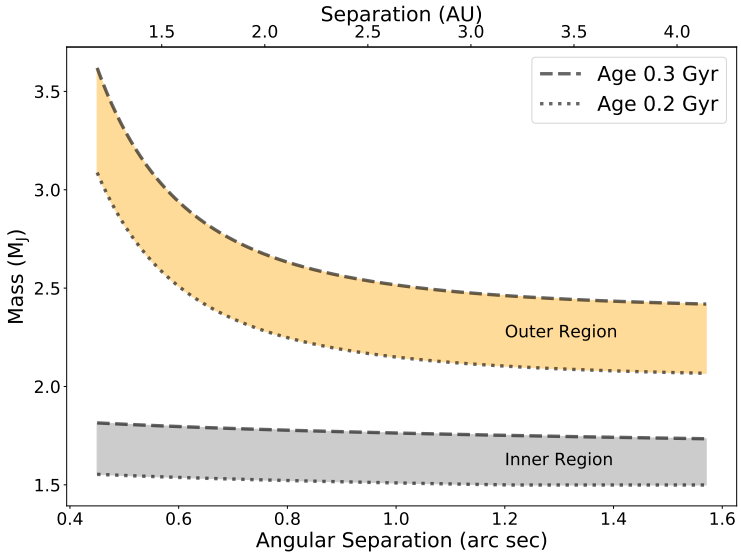

Figure 3.5: Planet mass upper limits derived for Sirus B. The two mass limits are based on the outer and inner region, see Figure 3.4.

Figure 3.3 for comparison. Planet fluxes in the NEAR filter are calculated from the ATMO 2020 spectral models (Phillips et al., 2020, see section 3.4.3) assuming literature values for the planet mass ($3.25^{+0.39}_{-0.65}$ M_{Jup} and 0.77 ± 0.2 M_{Jup}) and the system age ($2^{+2}_{-1.3}$ Gyr and 0.7 ± 0.3 Gyr). These values are plotted by blue points in the Figure 3.3. Since the masses are determined by radial velocity, radius measurements are not available. Both the planet radii and temperatures are taken from the ATMO evolutionary models.

3.4.3 Mass limits

The contrast curves were converted into mass limits using the ATMO 2020 exoplanet atmosphere models (Phillips et al., 2020). The models are computed using a state-of-the-art one-dimensional radiative-convective equilibrium code along a grid of self-consistent pressure–temperature profiles and chemical equilibrium abundances for a range of effective temperatures (200 to 3000 K) and gravities (2.5-5.5 dex). ATMO 2020 has key improvements over previous model families, including the use of updated molecular line opacities which results in warmer atmospheric temperature structures and improved emission spectra. We use the non-equilibrium models with weak vertical mixing and the isochrones of age-ranges obtained from literature to determine the masses corresponding to the contrast curves.

For absolute flux value of Sirius A, we use reported value from ESO's list of mid-IR standard stars[1]. It provides a flux of 118.8 Jy in the PAH2 filter, which has the same central wavelength (11.25 μm) as the broad NEAR filter with a bandpass of 10-12.5 μm. For the other stars, we estimated the absolute flux from the tabulated K-band magnitude and applying the K-M correction from Allen's astrophysical quantities (Cox, 2000). The M-N color of main sequence stars with

[1] https://www.eso.org/sci/facilities/paranal/instruments/visir/tools/

spectral type earlier than K5 is vanishingly small as this wavelength regime is well within the Rayleigh-Jeans part of the stellar spectrum. This procedure yields the 11.25 μm fluxes of ∼4.5 Jy for ε Indi A, ∼7.6 Jy for ε Eri and ∼7.5 Jy for τ Ceti. We also applied the procedure to some standard stars with tabulated K-band magnitude and PAH2 fluxes and found the values to agree within a few percent. For Sirius A, the estimate is 117 Jy in a very good agreement with the tabulated 118.8 Jy. We used Sirius A as a reference to calculate differential flux for other targets and find values agree with the calculation. We find no evidence of mid-IR excess in our targets consistent with previous work, Sirius A (White et al., 2019), Sirius B (Skemer and Close, 2011), ε Indi A (Trilling et al., 2008). ε Eri (Backman et al., 2009) and τ Ceti (Lawler et al., 2014) are known to have some IR excess from their extended debris disks, but this emission is mostly from cold dust and therefore at longer wavelengths. Also, our high-spatial resolution imagery would resolve the debris disk from the central star, such that no IR excess is measured on the central PSF.

3.5 Discussion

3.5.1 ε Indi A

To constrain the mass limits of companions to ε Indi A, we adopt an age range of 0.7-4 Gyr for our models and find limits of 3.3-10 M_{Jup} beyond 1″. Since the mass of the known planet is $3.25^{+0.39}_{-0.65}$, M_{Jup} , we would have likely detected it if the age of the system was 0.7 Gyr as shown in the Figure 3.3 (e). Our non-detection therefore supports an older age for ε Indi A. This is consistent with the majority of the age determinations as discussed in the introduction above. We can calculate the required observation time to detect the known giant planet by assuming a likely age of 3.8 Gyr, in a background limited regime and improved sensitivity at small separations (without coronographic glow). It will require 50 hrs of observing time to detect the planet associated with the RV signal.

The limits we obtain are more sensitive than any previous near IR imaging campaigns, which have constrained the masses of possible companions to 20 M_{Jup} in the inner regions of the system (Geißler et al., 2007) and 5-20 M_J at separations larger than 2″ (Janson et al., 2009). Another independent reduction of ε Indi A combining the NEAR and NaCO L′ data reaches similar mass limits as ours (Viswanath, 2021).

ε Indi Ba and Bb are not discussed in this paper, as their wide orbit (1459 AU, Scholz et al., 2003; McCaughrean et al., 2004) corresponds to approximately 6.7 arc minute separation, which is far outside the field of view of the NEAR instrument.

3.5.2 ε Eri

We adopt an age range of 0.4-1 Gyr for our models. We obtained a mass limits of 2-4 M_{Jup} , as shown in the Figure 3.3 (f). The obtained limits are more sensitive than most previous imaging data (Macintosh et al., 2003; Janson et al., 2008; Mizuki et al., 2016; Hunziker et al., 2020), with the exception of Mawet et al. (2019), who derive an upper mass limit of about 2 M_{Jup} for

an assumed system age of 400 Myr. Reaching similar mass limits at different wavelengths does, however, reduce the dependency on the planet atmosphere models. Our result therefore increases the confidence that there is indeed no planet more massive than 2 M_{Jup} around ε Eri, for an age of 400 Myr old. The debris disk around ε Eri (Backman et al., 2009) is too large for our field of view and too cold and faint at 11.25 μm to be detected in our observations. To estimate the required observing time for detecting ε Eri b for a likely age of 0.7 Gyr, we find that 1 M_{Jup} planet can be detected in less than 70 hrs with the current setup and sensitivity will improve at small separations, if the coronographic glow is eliminated (by introducing a cold pupil stop in front of the AGPM coronagraph mask).

3.5.3 τ Ceti

Because of the large range of age suggested in the literature, we adopt a wide range of 3-10 Gyr. The obtained mass limits of 15-30 M_{Jup} shown in the Figure 3.3 (g) are comparable to those of Boehle et al. (2019), who use a combination of radial velocity and 3.8 μm imaging data to find limits of 10-20 M_{Jup} beyond 2″ for a slightly younger age range (2.9-8.7 Gyr). Within 2″ we are more sensitive, and the non-detection of any of the known planets is consistent with the expectation, as the various Earth-mass planets of the system are far too low mass and are located within the inner working angle of our data and even the proposed giant planet candidate is well below our detection threshold (1-2 M_{Jup} at 3-20 AU).

3.5.4 Sirius A

For our models we assumed an age range of 0.2-0.3 Gyr for Sirius. For Sirius A we have also included the irradiation from the star when determining the expected magnitude of the planet, due to the brightness of the host star. We accounted for the irradiation by counting both the flux arriving at the planet surface and the intrinsic formation heat of the planet from the model as incoming energy when calculating the equilibrium temperature, which in turn determines the outgoing flux. Sirius A is 25 times more luminous than the Sun, and a potential planet on a 2 AU orbit would be heated to more than 400 K independent of the planet's age or mass. This leads to the peculiar shape of the mass contrast curve with better mass sensitivities at small separation from Sirius A shown in the Figure 3.3 panel h. As a result, the curve of the mass limit falls of sharply within ∼ 1″ or 2.6 AU, where the stellar radiation dominates. Beyond this the irradiation quickly becomes negligible due to falling off with the square of the distance and the curve looks more similar to those of the other systems. The other systems have smaller, fainter stars and therefore the amount of heating by the stellar flux is negligible at the separations resolved by our imagery. While we do not detect any planets, we do obtain the most sensitive mass limits to date within 1.5″ and comparable limits to the most sensitive limits of previous imaging campaigns outside that radius (Bonnet-Bidaud and Pantin, 2008; Thalmann et al., 2011; Vigan et al., 2015; Hunziker et al., 2020). We cannot rule out the possibility of planets that could be hidden behind or too close to the star.

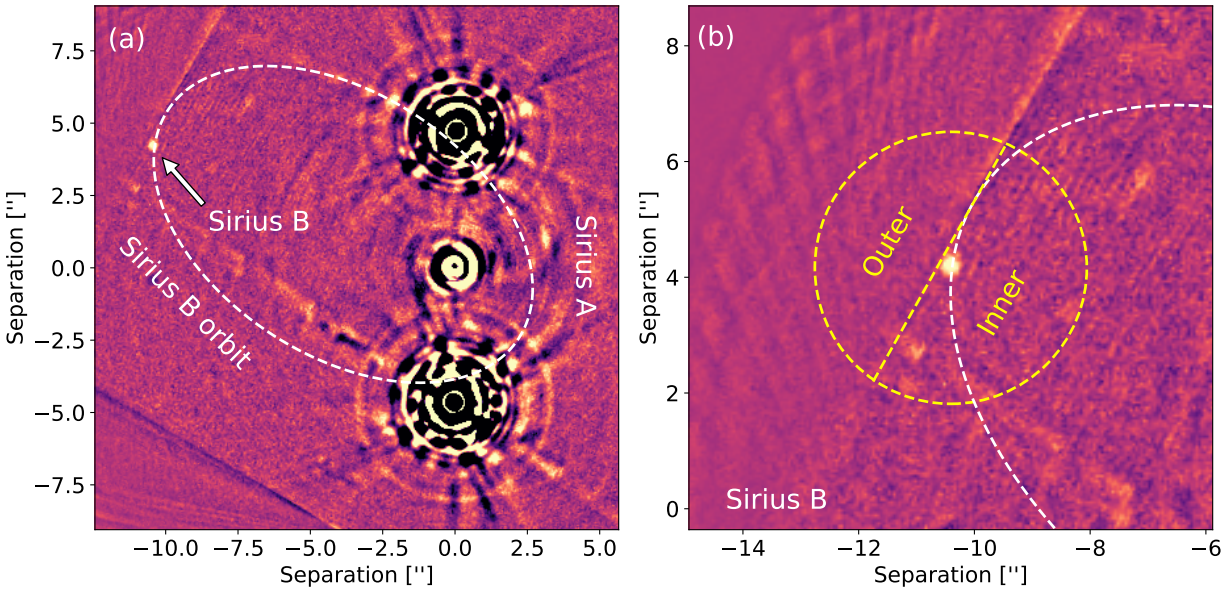

Figure 3.6: (a) Final derotated image showing Sirius A and Sirius B. (b) Zoomed in on Sirius B, divided into two regions (inner and outer) based on the number of frames in the outlined area.

3.5.5 Sirius B

No ADI reduction had to be applied to the Sirius B data, because the star is 4×10^{-5} times fainter than Sirius A and no PSF residuals are seen besides the PSF core. Also the target was far from Sirius A and the noise of its coronagraphic PSF, so no further processing was necessary. The final image of Sirius A and B is shown in the Figure 3.6. Sirius B was very close to edge of the NEAR's field of view, and even outside of it for some individual frames, which were then excluded before derotation and averaging. To calculate the sensitivity around Sirius B, we divided that area of the image into two regions, an inner and an outer region, as shown in the Figure 3.6 (b). The inner region provides a better sensitivity for both the background noise limited and injected planet, as it includes more frames.

The astrometry measurements for Sirius B, put it at a separation of 11.18″ from Sirius A. Relative photometry with respect to Sirius A has been performed using an optimum $r = 4$ pix photometric aperture. The 11.25 µm contrast ratio between the two stars is 4×10^{-5} corresponding to a Sirius B flux of 4.7 mJy at an S/N of about 40. This value is consistent with the low S/N measurement of 4.9 mJy reported for a similar observing band by Skemer and Close (2011).

For our models we have assumed the same age range as we did for Sirius A, giving us limits of $1.5 - 1.8\,M_{Jup}$ for the "inner" region and $3.1 - 3.6\,M_{Jup}$ for the "outer" region. The mass limits in the inner region are comparable to previous near IR limits of $1.6\,M_{Jup}$ from Thalmann et al. (2011). According to the models and assuming the sensitivity improving with $\sqrt{t_{obs}}$, a 4× more observation time would be enough to reach $0.5\,M_{Jup}$.

3.6 Summary and Conclusions

In this work we demonstrate high-contrast imaging of a small sample of very nearby (<4 pc) stars with spectral type earlier than M at 11.25 μm with NEAR. While we do not detect any known or new planets, we are able to set upper mass limits of the order of a few Jupiter masses for most of the targets and of $15 - 30\,M_{Jup}$ for the older τ Ceti. For ε Indi A and ε Eri we achieve detection limits very close to the giant planets discovered by RV, with the limits on ε Indi A being the most sensitive to date. Also for τ Ceti and Sirius A we obtain the most sensitive limits to date at small separations (<1.5″ and <2″ respectively). Our mass limit for Sirius B is similar to the one achieved previously at a shorter wavelength.

The ADI analysis was performed using a PCA based algorithm with artificial planet injections and recovery tests yielding some of the most stringent upper mass limits to date. For ε Indi A and ε Eri, we almost reach the detection limit for the known planets if they were at the young end of the possible age estimates but fail to detect any signal. We achieve an unprecedented sub-mJy detection sensitivity.

We demonstrate close to background noise limited imaging for most of our target stars apart from the glaring Sirius A, for which the data is contrast limited. Assuming likely ages and background noise limited imaging, the giant planets orbiting ε Eri and ε Indi A can be imaged in 70 and 50 hrs respectively. Finally, for our closest and youngest (together with Sirius A) target Sirius B, the sub-Jupiter mass regime could be reached by merely doubling the observation time.

This work shows the potential of direct imaging in the mid-IR regime and prospects for upcoming mid-IR HCI instruments. Upcoming mid-IR HCI instrument such as METIS at the ELT would be able to detect known planets around ε Indi A and ε Eri in a few minutes of observation time and reach sensitivities to detect Earth size exoplanets in a few hours (Brandl et al., 2018).

Acknowledgements

The authors would like to thank the ESO and the Breakthrough Foundation and all the people involved for making the NEAR project possible. The observations were carried out under the ESO program id: 60.A-9107(D) and 60.A-9107(F). MRM acknowledges the support of a grant from the Templeton World Charity Foundation, Inc. The opinions expressed in this publication are those of the authors and do not necessarily reflect the views of the Templeton World Charity Foundation, Inc. Part of this work has received funding from the European Research Council (ERC) under the European Union's Horizon 2020 research and innovation programme (grant agreement No. 819155), and by the Wallonia-Brussels Federation (grant for Concerted Research Actions).

Chapter 4

New mid-infrared imaging constraints on companions and protoplanetary disks around six young stars

D. J. M. Petit dit de la Roche, M. E. van den Ancker, I. Kamp, R. van Boekel, D. Fedele, V. D. Ivanov, M. Kasper, H. U. Käufl, M. Kissler-Patig, P. A. Miles-Páez, E. Pantin, S. P. Quanz, Ch. Rab, R. Siebenmorgen, L. B. F. M. Waters

Astronomy & Astrophysics, Volume 648, Id A92, April 2021

Abstract:

Context: Mid-infrared (mid-IR) imaging traces the sub-micron and micron-sized dust grains in protoplanetary disks and it offers constraints on the geometrical properties of the disks and potential companions, particularly if those companions have circumplanetary disks.

Aims: We use the VISIR instrument and its upgrade NEAR on the VLT to take new mid-IR images of five (pre-)transition disks and one circumstellar disk with proposed planets and obtain the deepest resolved mid-IR observations to date in order to put new constraints on the sizes of the emitting regions of the disks and the presence of possible companions.

Methods: We derotated and stacked the data to find the disk properties. Where available, we compare the data to ProDiMo (**Pro**toplanetary **Di**sk **Mo**del) radiation thermo-chemical models to achieve a deeper understanding of the underlying physical processes within the disks. We applied the circularised point spread function subtraction method to find upper limits on the fluxes of possible companions and model companions with circumplanetary disks.

Results: We resolved three of the six disks and calculated position angles, inclinations, and (upper limits to) sizes of emission regions in the disks, improving upper limits on two of the unresolved disks. In all cases the majority of the mid-IR emission comes from small inner disks or the hot inner rims of outer disks. We refined the existing ProDiMo HD 100546 model spectral energy distribution (SED) fit in the mid-IR by increasing the PAH abundance relative to the ISM, adopting coronene as the representative PAH, and increasing the outer cavity radius to 22.3 AU. We produced flux estimates for putative planetary-mass companions and circumplanetary disks, ruling out the presence of planetary-mass companions with $L > 0.0028\,L_{\odot}$ for $a > 180$ AU in

the HD 100546 system. Upper limits of 0.5 mJy-30 mJy are obtained at 8 μm-12 μm for potential companions in the different disks. We rule out companions with $L > 10^{-2}\,L_{\odot}$ for $a > 60$ AU in TW Hydra, $a > 110$ AU in HD 169142, $a > 150$ AU in HD 163296, and $a > 160$ AU in HD 36112.

Conclusions: The mid-IR emission comes from the central regions and traces the inner areas of the disks, including inner disks and inner rims of outer disks. Planets with mid-IR luminosities corresponding to a runaway accretion phase can be excluded from the HD 100546, HD 163296, HD 169142, TW Hydra, and HD 36112 systems at separations $> 1''$. We calculated an upper limit to the occurrence rate of wide-orbit massive planets with circumplanetary disks of 6.2% (68% confidence). Future observations with METIS on the ELT will be able to achieve a factor of 10 better sensitivity with a factor of 5 better spatial resolution. MIRI on *JWST* will be able to achieve 250 times better sensitivity. Both will possibly detect the known companions to all six targets.

4.1 Introduction

Transition disks are believed to represent an intermediate stage of planet formation between the protoplanetary disk and a gasless, fully formed planetary system. Scattered light imaging in the near-infrared (near-IR) and thermal sub-millimetre observations with ALMA have revealed detailed structures in many transition disks, including rings, spirals, and warps (e.g. Francis and van der Marel, 2020). These features can be a result of the accretion of gas and dust onto a planet, although they can also be explained by other processes in the disk such as shadowing from the inner rim, snowlines, or hydrodynamic effects (e.g. Siebenmorgen and Heymann, 2012; van der Marel et al., 2018). Studying transition disks is an important step in understanding planet formation. Mid-infrared (mid-IR) direct imaging traces dust of ∼150 K in the disk. Additionally, the disk is expected to re-emit a large fraction of the stellar flux in the infrared (e.g. Dullemond and Monnier, 2010). Mid-IR imaging can thus further constrain disk properties, especially when combined with observations at other wavelengths. It also allows us to search for thermal emission from (planetary) companions, especially if these companions still have circumplanetary disks (CPDs), which are expected to be bright in the mid-IR.

We used the VLT Imager and Spectrograph for the mid-InfraRed (VISIR; Lagage et al., 2004) and its upgraded version Near Earths in the AlphaCen Region (NEAR; Kasper et al., 2017a) to obtain the deepest resolved mid-IR images of five Herbig Ae/Be (pre-)transition disks and one other circumstellar disk to date. The instruments that we used are more sensitive and the observation time is longer than in any previous studies (Liu et al., 2003; van Boekel et al., 2004; Leinert et al., 2004; Verhoeff, 2009; Panić et al., 2014; Mariñas et al., 2011; Doucet et al., 2006; Honda et al., 2012; Okamoto et al., 2017; Maaskant et al., 2013; Ratzka et al., 2007; Arnold et al., 2012; Khalafinejad et al., 2016). Additionally, the use of adaptive optics (AO) on NEAR provides us with better angular resolution and PSF stability. These new data allowed us to put new constraints on the disk and the presence of possible companions of each of the six targets.

To contextualise the observations of our primary target HD 100546 and secondary targets, we used the radiation thermo-chemical disk modelling code ProDiMo (**Pro**toplanetary **Di**sk **Mo**del;

see Sect. 4.4). Our HD 100546 disk model is the result of a multi-wavelength spectral energy distribution (SED) fit, which will allow us to compare the predicted and observed total flux within the observed bands (Woitke et al., 2019). Our synthetic images of the HD 100546 circumstellar disk enabled us to search for a non-axisymmetric disk structure. The radiative transfer results allowed us to determine the mid-IR extinction along line-of-sights to the midplane and the resulting obscuration of putative embedded companions. The disk modelling code can be applied further to produce SEDs for planetary companions and circumplanetary disks to compare theoretical fluxes with detection limits (Rab et al., 2019).

Section 4.2 describes the targets and in Sect. 4.3 we show the observations and the data analysis. The ProDiMo model is discussed in Sect. 4.4 and compared to the data in Sect. 4.5. Limits on possible companions are discussed in Sect. 4.6 and for three of the targets planetary models with circumplanetary disks are analysed. Finally, our discussion and conclusions are presented in Sect. 4.7.

4.2 Targets

The following targets were observed: HD 100546, HD 163296, HD 169142, TW Hydra, HD 100453, and HD 36112/MWC 758 (see Table 4.1). These stars were selected to study the influence of features such as spiral arms, circular gaps, and inner cavities, seen in near-IR scattered light images on the mid-IR morphology of the disk which is dominated by thermal emission.

All six targets are young disks with ages of 3-16 Myr and, with the exception of HD 163296, are classified as (pre-)transition disks with a central cavity (or large inner gap). While HD 163296 does not have the traditional (pre-)transition disk SED and only some evidence of possible inner clearing, it nonetheless has other structures in the disk and proposed companions, similar to the remaining targets in the sample and was therefore included here (Espaillat et al., 2014; Isella et al., 2016). In addition to central cavities, sub-millimetre dust emission and near-IR scattered light imaging have revealed features such as rings, clumps, and spirals in all the disks. At distances of 60-160 pc, the extended disks of the targets are expected to be large enough to be resolved with the Very Large Telescope (VLT) at Paranal in the 8-12 μm wavelength range.

Below, we provide an overview of the structure and possible companions of the targets, specifically those inferred through direct imaging.

4.2.1 HD 100546

This disk is divided into an inner disk and an outer disk, separated by a single gap from ~1-21 AU (e.g. Bouwman et al., 2003; Grady et al., 2005; Menu et al., 2015; Jamialahmadi et al., 2018; Pineda et al., 2019). It is possible that the inner and outer disks are misaligned (Pineda et al., 2019; Kluska et al., 2020). The outer disk has spiral structures that have so far only been detected in the near-IR (Follette et al., 2017; Quillen, 2006) and there is a tentative detection of a bar-like structure across the gap which could indicate small-scale inflow or be the base of a jet (Mendigutía et al., 2017; Schneider et al., 2020). There have been some suggestions of warping

Target	Age (Myr)	M_* ($M_\odot$)	T (K)	L_* ($L_\odot$)	d (pc)[a]	PA (°)	i (°)	Structures	Companions detected
HD 100546[b]	5	2.5	10600	30	108.1	140	46	gap, spiral arms	3
HD 163296[c]	6	2.5	9000	34.7	101.0	137	43	rings	3
HD 169142[d]	4-16	1.8	7800	9.8	114.9	5	13	rings	3
TW Hydra[e]	3-15	0.8	4000	0.2	60.1	150	7	rings	1
HD 100453[f]	11	1.5	-	6	103.8	145	35	gap, spiral arms	M dwarf
HD 36112[g]	4	2.0	8200	22	155.9	62	21	cavity, rings, clumps, spirals	2

Table 4.1: Stellar and disk properties of the target stars. Stellar masses, luminosities, and temperatures, where possible, have been taken from the DIANA models of the targets, which are fit to multiple data sets. *(a)* Gaia Collaboration et al. (2020b). *(b)* Wichittanakom et al. (2020); Miley et al. (2019); Casassus and Pérez (2019); Jamialahmadi et al. (2018); Mendigutía et al. (2017); Pineda et al. (2014); Avenhaus et al. (2014); Walsh et al. (2014); Leinert et al. (2004). *(c)* Garufi et al. (2014); Wichittanakom et al. (2020). *(d)* Pérez et al. (2019); Panić et al. (2008); Raman et al. (2006); van Boekel et al. (2005). *(e)* Nayakshin et al. (2020); Sokal et al. (2018). *(f)* Wichittanakom et al. (2020); Rosotti et al. (2020); Yu et al. (2019); Long et al. (2017); Benisty et al. (2017); Wagner et al. (2015). *(g)* Isella et al. (2010); Meeus et al. (2012).

in the inner and outer disk, but this has so far remained inconclusive (e.g. Quillen, 2006; Panić et al., 2014; Pineda et al., 2014; Walsh et al., 2017; Sissa et al., 2018; Kluska et al., 2020).

There has been much discussion about possible companions. One companion, HD 100546 b, was identified at a separation of 55 AU at a position angle of 9° (Quanz et al., 2013; Currie et al., 2014; Quanz et al., 2015). However, this has been called into question by Rameau et al. (2017), who failed to detect any accretion at the planet location in Hα and posit the L′ band (3.8 µm) detection might be related to the chosen method of data reduction. The lack of detection in Hα is supported by Cugno et al. (2019). A different companion, HD 100546 c, may have been detected just inside the central cavity at ˜13 AU (Brittain et al., 2014; Currie et al., 2015), although this too has been contested (Fedele et al., 2015; Follette et al., 2017; Sissa et al., 2018). ALMA observations at 1.3 mm have revealed a 6σ point source of 92 ± 9 µJy at a position angle of 37° and a projected separation of 7.8 AU, which could represent an additional planetary candidate (herafter HD 100546 d; Pérez et al., 2020). A final planet candidate has also been suggested by the presence of a Doppler flip observed in the disk ^{12}CO kinematics. Such a planet would be embedded within the disk continuum emission region exterior to the gap, corresponding to a projected radial distance of 20.5 ± 5 AU (Casassus and Pérez, 2019).

4.2.2 HD 163296

Near-IR and sub-millimeter wavelength observations show that HD 163296 has four gaps. They are centred on 10 AU, 50 AU, 81 AU, and 142 AU with bright rings in between (e.g. Garufi et al., 2014; Isella et al., 2016; Isella et al., 2018).

Companions have been suggested based on their possible role in forming the ring structures in the disk. For example, Liu et al. (2018) fitted three half-Jovian-mass planets and Teague et al. (2018) found the radial pressure gradients can be explained by two Jupiter-mass planet at 83 and 137 AU (see also Teague et al. 2019). Additionally, Pinte et al. (2018) found a Jupiter-mass companion at 223 AU based on deviations from Keplerian velocity in the gas of the disk. So far, observations have not been able to confirm or rule out such companions due to a lack of sensitivity. Guidi et al. (2018) claim to have found a 5-6 M_{Jup} companion at a separation of 50 AU from the star in the L′ band with Keck/NIRC2, but neither this object nor the one proposed by Pinte et al. (2018) was found by Mesa et al. (2019), who set upper limits of 3-5 M_{Jup} on possible companions in the gaps of the disk with SPHERE H band (1.6 µm) and K band (2.2 µm) data. Due to extinction from the disk setting, these kinds of mass limits remain challenging, especially outside the gaps, as only a fraction of the intrinsic, modelled flux of the companion may be observable.

4.2.3 HD 169142

The disk around HD 169142 has been imaged at near-IR and at sub-millimetre wavelengths. Various teams have imaged two (Fedele et al., 2017; Quanz et al., 2013; Momose et al., 2015; Pohl et al., 2017), three (Macías et al., 2017; Osorio et al., 2014), or four (Macías et al., 2017; Pérez et al., 2019) rings around the star. The inner ring is located at 20 AU and is more than twice as bright as the outer rings. As a result, it was found in all the previously mentioned works.

The three outer rings (located between 45 AU and 80 AU) are faint and close together, leading to blending in some observations and resulting in the different numbers of rings found in different studies.

Four disk features that could be associated with forming planets have been found. The first was found between the 20 AU and 50 AU dust rings by Osorio et al. (2014) at 7 mm, the second was found in the L′ band just within the edge of the inner gap by Reggiani et al. (2014) and Biller et al. (2014). However, the L′ band source was not recovered by either team in the J (1.3 μm), H, or K bands and it is concluded by Biller et al. (2014) that the feature cannot be due to planet photospheric emission and must be a disk feature heated by an unknown source, although Reggiani et al. (2014) argue that the accretion of material in the gap enhances the L′ band flux, resulting in a lower mass planet, which is not as easily observed in other bands. The presence of circumstellar material with entrained dust grains spreading across the gap or being accreted onto a planet could also subject the planet to further extinction in the J band. Biller et al. (2014) detected the third source in the H band, with no L′ band counterpart, but Ligi et al. (2018) show that this is actually part of the inner ring. They did find another H band structure close to the star that is consistent with the detections by Biller et al. (2014) and Reggiani et al. (2014), but it appears to be extended and they cannot rule out that it is not part of a marginally detected ring at the same separation. Finally, Gratton et al. (2019) combined different SPHERE datasets and suggest that this source could actually be a combination of two extended blobs observed in the disk. They find a different, fourth, feature located between the inner and outer rings that does not correspond to any of the previous detections and could indicate the presence of a $2.2 \pm 1.4\,M_{Jup}$ planet.

4.2.4 TW Hydra

TW Hydra is a 3-15 Myr old T Tauri star (Vacca and Sandell, 2011; Weinberger et al., 2013; Herczeg and Hillenbrand, 2014). At a distance of 60.14 ± 0.06 pc (Gaia Collaboration et al., 2020b), it is one of the nearest known hosts of a protoplanetary disk. Studies in the near-IR and sub-millimetre wavelength regimes have found between three and six different gaps in eight different locations between 0.6 AU and 90 AU (Nomura et al., 2016; Tsukagoshi et al., 2016; Andrews et al., 2016; van Boekel et al., 2017; Huang et al., 2018).

Tsukagoshi et al. (2016) suggest the presence of a $\lesssim 26\,M_{\oplus}$ planet interacting gravitationally with the gap at 22 AU. Tsukagoshi et al. (2019) found an azimuthally elongated 1.3 mm continuum source in the south-west of the disk at a radial separation of 54 AU that could be either dust that has accumulated into a clump in a vortex or a circumplanetary disk associated with an accreting Neptune mass planet. Nayakshin et al. (2020) argue the feature can be explained by a Neptune-mass planet disrupted in the process of accretion and expelling dust into the circumstellar disk. Observations with SPHERE suggest from the gap profiles that if planets are responsible for forming the gaps in the circumstellar disk, they are at most several $10\,M_{\oplus}$ (van Boekel et al., 2017).

4.2.5 HD 100453

HD 100453 has been found to possess a misaligned inner disk, a gap between 1 AU and 21 AU, and an outer disk with two shadows, two spiral arms around 30 AU, and a faint feature in the south-west of the disk (Benisty et al., 2017; Kluska et al., 2020). It also has an M dwarf companion at a separation of 125 AU whose orbit is not aligned with the disk plane (van der Plas et al., 2019).

Dynamical modelling has shown that tidal interactions with the M dwarf companion are responsible for at least some of the disk features, such as the spirals and the truncation of the outer disk (Wagner et al., 2018; van der Plas et al., 2019; Gonzalez et al., 2020). However, they have also suggested that the presence of a planet is required to fully explain the origin of the features in the disk, particularly the misalignment between the inner and the outer disks (e.g. Nealon et al., 2020). There have been no direct detections of planet candidates to date.

4.2.6 HD 36112

HD 36112 (MWC 758) has a large cavity with a radius of 32 AU. Its broad outer disk has rings, clumps, and spiral arms (e.g. Dong et al., 2018; Wagner et al., 2019).

For the spiral structures in the disk of HD 36112 to be caused by a perturber, it is estimated that it must have a mass of ~5-10 M_{Jup} (Grady et al., 2013; Dong et al., 2015). However, upper limits on companion fluxes obtained in the same works and by Reggiani et al. (2018) rule out the presence of > 5 M_{Jup} planets beyond 0.6″, or 94 AU. Reggiani et al. (2018) found an L band (3.5 μm) point source at 18 AU that they interpret as a planet with a circumplanetary disk that is embedded in the disk. Wagner et al. (2019) did not find this object in the L′ and M′ bands, even though they achieved better sensitivities. Instead, they found a point source at the outer end of one of the spiral arms that could be a planet with a CPD and could be responsible for driving the spirals.

4.3 Observations and data analysis

Observations of HD 100546 were obtained during April 2018, with the VLT Imager and Spectrometer for the mid-IR (VISIR, Lagage et al. 2004), and of all six disks during the science verification of its upgrade, with NEAR (Kasper et al. 2017a) in September and December of 2019. The benefit of NEAR is its use of AO, which results in improved angular resolution, PSF stability, and sensitivities (a factor of ~4) across the N-band. An overview of the observations used in this paper is presented in Table 4.2.

For all targets, all observations were taken in the pupil tracking mode, where the derotator is turned off to allow for field rotation during the observation sequence. For the NEAR observations, AO was enabled and the targets themselves were used as the reference star for wavefront sensing. The chopping and nodding sequence was enabled to subtract the sky background. In the VISIR data, the chop throw is 8″ in the direction perpendicular to the nodding direction; whereas, in the NEAR data, the chop throw is 4.5″ in the parallel direction. Since the throw

Target	Instrument	Date	Filter	λ_0 (µm)	$\Delta\lambda$ (µm)	Integration time (s)
HD 100546	VISIR	28-04-2018	J8.9	8.70	0.74	3600
	NEAR	11-12-2019	PAH1	8.58	0.41	540
			ARIII	8.98	0.14	540
			PAH2	11.24	0.54	540
		12-12 2019	PAH2_2	11.68	0.37	540
HD 163296	NEAR	14-09-2019	PAH1	8.58	0.41	600
		13-09-2019	NEAR	11.25	2.5	600
HD 169142	NEAR	13-09-2019	PAH1	8.58	0.41	600
			NEAR	11.25	2.5	600
TW Hya	NEAR	13-12-2019	PAH1	8.58	0.41	600
		16-12-2019	NEAR	11.25	2.5	600
HD 100453	NEAR	12-12-2019	PAH1	8.58	0.41	600
			NEAR	11.25	2.5	600
HD 36112/MWC 758	NEAR	18-12-2019	NEAR	11.25	2.5	600

Table 4.2: Overview of the observations used in this paper. HD 100546 was observed as part of different programmes than the other observations, leading to the difference in filters and observation times.

determines the useful field of view, the VISIR and NEAR data have an effective field of view of 16″x16″ and 9″x9″, respectively. The VISIR data have a chopping frequency of 4 Hz and a detector integration time (DIT) of 0.012 s. The NEAR data have a chopping frequency of 8 Hz and a DIT of 0.006 s. Both NEAR and VISIR have platescales of 0.0453″.

The standard VISIR data reduction pipeline[1] is not suited to reduce data taken in the pupil tracking mode, so special purpose python scripts were employed to reduce and analyse the data. VISIR and NEAR data are delivered in chop difference images with integration times of 20-50 s each. Data from the different nod positions are subtracted from each other and the resulting images are derotated. The beams from the chopping and nodding from all images are then median combined with 3σ sigma clipping into a single master image. Only the VISIR observations of HD 100546 have a reliable reference star (HD 93813) with which to calibrate the result, leading to an observed flux of 27 ± 3 Jy. For HD 100546 observations in other bands and in the cases of HD 163296, HD 169142, and TW Hya, we used the flux predicted by the ProDiMo models (described in Section 4.4) to calibrate the data. Since the model is fitted to SED data from a collection of previous observations of the targets taken with other instruments, including data around 8-12 μm, it is the most accurate way available to determine the brightness in the images and this allowed us to calculate the flux in the specific wavelength ranges of the different filters (Dionatos et al., 2019; Woitke et al., 2019). The calibration is done by multiplying the model fluxes with the filter and sky transmissions and averaging the total flux over the required wavelength range. This is then set as the total flux of the data. As there are no models available for HD 100453 and HD 36112, the averages of previous flux measurements in similar filters had to be used (van Boekel et al., 2005; Carmona et al., 2008; Verhoeff, 2009; Mariñas et al., 2011; Khalafinejad et al., 2016; Li et al., 2018).

The final master images of the disks are shown in Figures 4.1 and 4.2. The star is not visible in any of the images as it does not contribute significantly to the flux in the mid-IR (<10% of the total flux in the ProDiMo models). Most of the central emission at these wavelengths is from unresolved inner disks or inner rims of outer disks.

4.3.1 HD 100546

The master images of HD 100546 in the different filters are shown in Figure 4.1, along with the corresponding model images after convolution with an appropriate PSF. For the J8.9 filter, this is the PSF of reference star HD 93813. While there were no appropriate flux calibration observations for the other filters, point sources were observed in the PAH1 and ARIII filters, which were used as PSF references. For the PAH1 filter and the ARIII filter, we used our own observations of HD 163296 and HD 27639, respectively. As there were no reference PSFs available in either the PAH2 or PAH2_2 filters, we used scaled versions of the ARIII reference instead. Since the different filters on the NEAR instrument result in similar sensitivities over time, and the observations in the different filters have similar exposure times, all master images are expected to have similar sensitivities. The exception are the observations with the J8.9 filter which were taken with VISIR and where the increased observation time compensates for the lack of AO, meaning

[1] https://www.eso.org/sci/software/pipelines/visir/visir-pipe-recipes.html

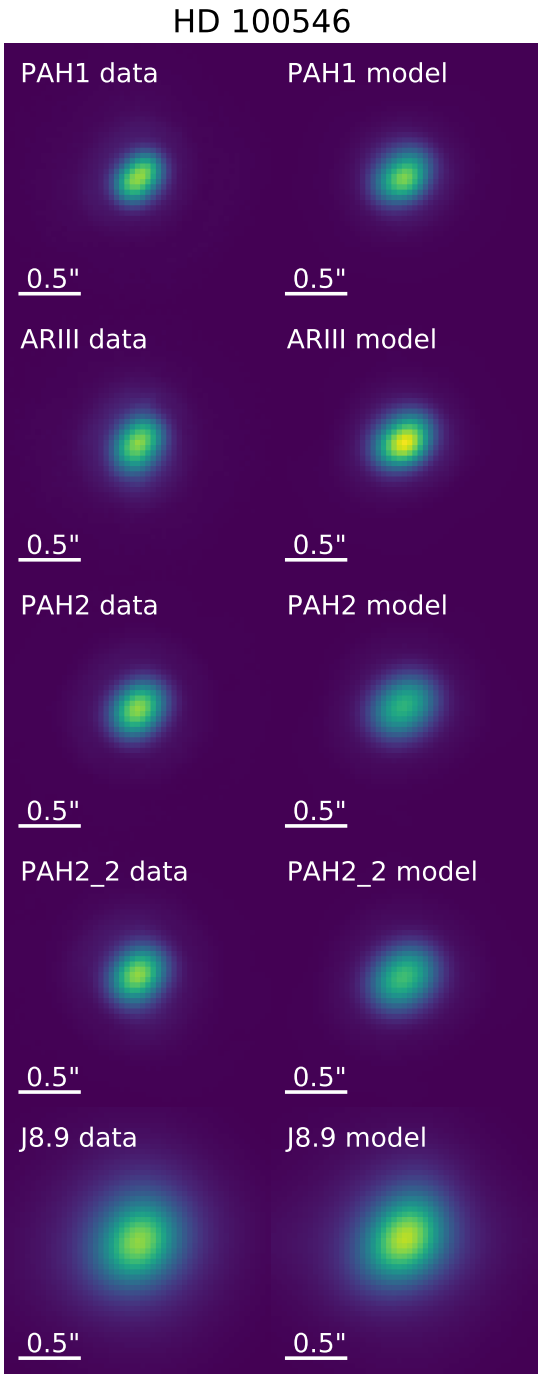

Figure 4.1: Master images (left) and model images (right) of HD 100546 in various filters. North is up and east is left in all images. The observations were scaled to have the same flux as the model images. The PAH1, ARIII, PAH2, and PAH2_2 filter master images were taken with NEAR and show a resolved, inclined disk. The J8.9 data were taken with VISIR and are more extended compared to the NEAR data due to image elongation from the telescope resulting in a distorted and enlarged PSF. The model images provide a good match for the master images in each filter.

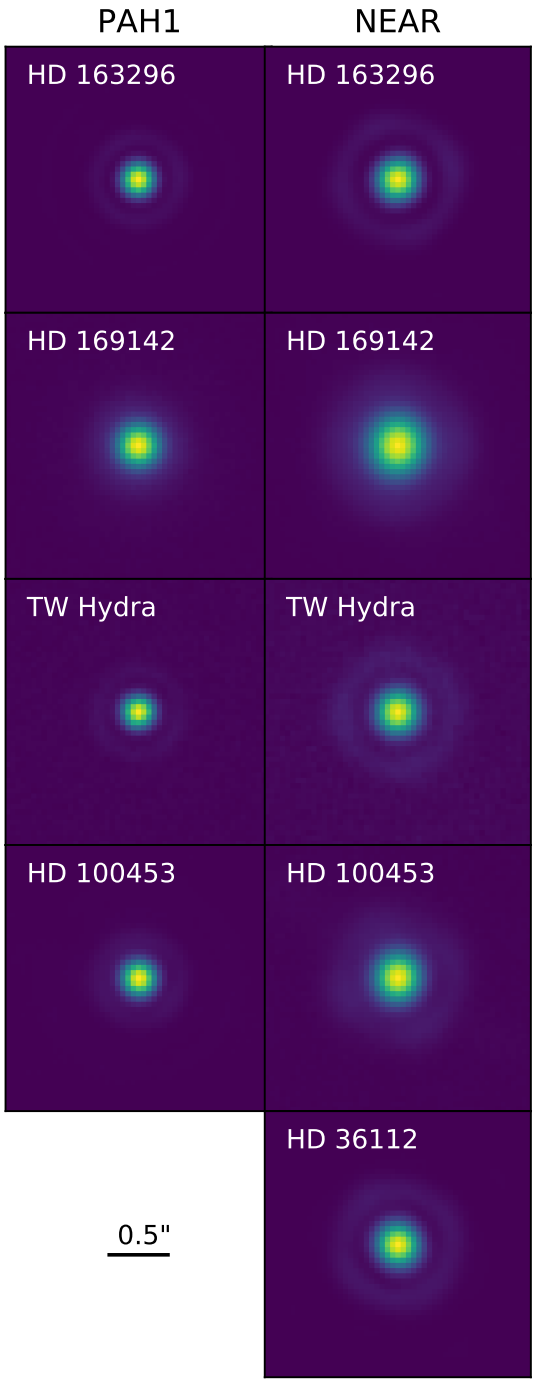

Figure 4.2: Normalised master images of the disks observed with NEAR. North is up and east is left in all images and the scale bar in the bottom left indicates 0.5″. The left column shows the disks in the PAH1 filter and the right column in the NEAR filter. HD 163296 and TW Hydra are unresolved in both filters. HD 36112 was not imaged in the PAH1 filter, but it is unresolved in the NEAR filter. Compared to these images, it can be seen that HD 169142 and HD 100453 are more extended in both filters.

the final sensitivity of the master image is still expected to be similar to those in the other filters. While the disk is resolved in all filters, the VISIR data are clearly more extended than the NEAR data. The J8.9 band contains both the PAH1 and ARIII bands and so the VISIR image would be expected to have a similar extent as the NEAR images in these bands. Some of the difference is because the AO on NEAR means the images are more compact, but mostly due to the telescope operations during the VISIR observations. During this night, there was a decrease in the precision of the altitude axis of the telescope, resulting in elongation of the image along the paralactic angle (de Wit, 2020). As this was at an angle of 40 degrees with the semi-major axis of the disk, the image is smeared along both axes and the smearing is not immediately obvious without a comparison. This is accounted for by using a reference PSF of the standard star HD 93813. Since this data set was taken immediately preceding the science observations in the same filter, it has a similar smearing effect.

The central bright emission in each image is from the unresolved inner disk, as the star is expected to be an order of magnitude fainter than the disk at mid-IR wavelengths based on the model data. Beyond that, emission is expected to be dominated by the inner rim of the outer disk, which is irradiated by the star and puffed up as a result. The rest of the outer disk is not warm enough to be detected in the image.

Using a Levenberg-Marquardt algorithm and least squares statistic to fit a simple two dimensional Gaussian to the surface brightness of the disk in each filter results in an average position angle of 141 ± 2°. Since we are fitting a two-dimensional function to a three-dimensional disk, we are sensitive to projection effects. This is especially the case because the inner wall of the outer disk is only visible on the far side of the disk and not on the close side. This means what we are calculating is actually the position angle of the two-dimensional projection of the disk, which we call the projected position angle. We also applied this method to model images of HD 100546 at the same wavelengths and found that the projected position angle is ∼ 130°, compared to the input of 140°, so we expect a difference between the projected position angle and the real position angle of roughly 10 degrees. This would still be in agreement with previous position angle values of 135-150° (Miley et al., 2019; Casassus and Pérez, 2019; Jamialahmadi et al., 2018; Mendigutía et al., 2017; Pineda et al., 2014; Avenhaus et al., 2014; Walsh et al., 2014; Leinert et al., 2004). A more precise determination of the disk orientation requires extensive modelling and is outside the scope of this paper.

The deprojected disk has a full-width-half-maximum (FWHM) of 0.82″ in the J8.9 filter and 0.35″-0.41″ in the other filters. The larger size of the J8.9 image is due to the above-mentioned PSF smearing from uncertainty in the altitude axis of the telescope. The FWHM values for all the disks and filters are listed in Table 4.3. From the disk FWHM and the PSF FWHM (the diffraction limit is 0.22″ – 0.30″ depending on the filter), we can calculate the true size of the emitting region, assuming that both the data and the PSF are well described by Gaussian functions (e.g. Mariñas et al., 2011; van Boekel et al., 2004), as follows:

$$\mathrm{FWHM_{disk}} = \sqrt{\mathrm{FWHM_{data}}^2 - \mathrm{FWHM_{PSF}}^2}. \tag{4.1}$$

Due to the PSF smearing in the J8.9 image, we used the reference PSF FWHM rather than the theoretical diffraction limit for this filter. Since the other data were observed with the NEAR

instrument, which thanks to its adaptive optics is expected to have a Strehl ratio of close to one (Kasper et al., 2017a), the FWHM of a point source PSF corresponds to the diffraction limit. This can be seen in the data of HD 163296, TW Hydra, and HD 36112, as is discussed in Sect. 4.3.2. The deconvolved FWHM of all resolved sources and the corresponding 5σ upper limits for unresolved sources are also listed in Table 4.3. While spectroscopic data show that the disk is more extended in PAH emission bands (van Boekel et al., 2004; Verhoeff, 2009), the PAH1 and PAH2 filter images are no more extended than their continuum counterparts. This is because the extent of the emission is averaged over the filter wavelength range and the PAH emission is estimated to be around 22% of the total flux in the PAH1 filter and 13% in the PAH2 filter (van Boekel et al., 2004). As a result, both PAH filter images are dominated by the continuum emission and have similarly sized emission regions as the images in the continuum filters. The 2σ discrepancy between the J8.9 and the PAH1 and ARIII deconvolved FWHM means the errorbars on the J8.9 image are probably underestimated, possibly due to a worsening of the smearing effect as the night went on.

Removing the PSF component along both axes also gives a more accurate inclination, since the semi minor axis of the disk is relatively more extended by the PSF than the semi-major axis. The calculated inclination is 47 ± 3°. The projection effect is not expected to be as strong here, since even on the model data the resulting inclination was well within 1σ of the input value. The projected inclination is in agreement with literature inclination values of 42-50°. (Miley et al., 2019; Casassus and Pérez, 2019; Jamialahmadi et al., 2018; Mendigutía et al., 2017; Pineda et al., 2014; Avenhaus et al., 2014; Walsh et al., 2014). This value is the combined inclination across all the available filters, except for J8.9 due to the deformed PSF in this image.

4.3.2 Other sources

HD 163296 is unresolved in both filters and has FWHMs around the diffraction limit of the telescope which is 0.22″ in the PAH1 filter and 0.30″ in the NEAR filter. This results in 5σ upper limits of 7 AU and 6 AU, respectively. Previous mid-IR observations between 8 μm and 13 μm have not resolved the disk, but set an upper limit on the FWHM of the emission region of 21 AU at 11.7 μm (Jayawardhana et al., 2001; van Boekel et al., 2005; Mariñas et al., 2011; Li et al., 2018). Our images of HD 163296 improve on the emission size upper limits by a factor of three.

HD 169142 is the most resolved disk in the sample after HD 100546. The measured and deconvolved FWHM are listed in Table 4.3. Additionally, the measured projected inclination of the deconvolved disk is 13 ± 2°, which is in agreement with previously measured inclinations of 13 ± 1° (Pérez et al., 2019; Panić et al., 2008; Raman et al., 2006).

TW Hydra is unresolved in our observations with upper limits of 3 AU in the PAH1 band and 49 AU in the NEAR band. The high limit in the NEAR band is due to the data being taken with the coronograph. While this allows for increased sensitivity for finding planets, it also means that the extent has to be calculated with the off-axis chop and nod beams. Based on the PAH1 data taken the same night, the beams are expected to be smeared by ∼10%. These limits are consistent with previous interferometry measurements which found the size of the emitting region of the disk to be 1-2 AU around 8-12 μm (Ratzka et al., 2007; Arnold et al., 2012).

Object	Filter	$FWHM_{data}$ ($''$)	$FWHM_{disk}$ (AU)
HD 100546	J8.9	0.82 ± 0.10	61 ± 11
	PAH1	0.349 ± 0.003	28.9 ± 0.5
	ARIII	0.356 ± 0.002	29.0 ± 0.3
	PAH2	0.392 ± 0.002	28.2 ± 0.4
	PAH2_2	0.414 ± 0.002	30.5 ± 0.3
HD 163296	PAH1	0.216 ± 0.002	<7
	NEAR	0.282 ± 0.001	<6
HD 169142	PAH1	0.336 ± 0.003	28.6 ± 0.5
	NEAR	0.465 ± 0.003	41.1 ± 0.5
TW Hydra	PAH1	0.219 ± 0.001	<3
.	NEAR	0.297 ± 0.029	<49
HD 100453	PAH1	0.234 ± 0.002	9.3 ± 0.6
	NEAR	0.352 ± 0.035	20.7 ± 6.6
HD 36112	NEAR	0.315 ± 0.002	<13

Table 4.3: FWHM of the disks in each filter is given in arcseconds. HD 100546 is clearly resolved in all bands. HD 169142 and HD 100453 are resolved in both the PAH and NEAR bands, while HD 163296, TW Hydra, and HD 36112 are unresolved point sources. For resolved images, the FWHM after deconvolution is listed in AU. For unresolved images, the 5σ upper limits are listed instead.

HD 100453 is resolved in both bands. Similar to TW Hydra, the NEAR band images of HD 100453 were taken with the coronograph, resulting in a 10% error in the extent of the emission region. The difference between the deconvolved PAH1 and NEAR band sizes suggests this might still be an underestimate. The disk has a calculated projected inclination of 35 ± 5°, which is in agreement with literature values of the inclination of 30-38° (Rosotti et al., 2020; Long et al., 2017; Benisty et al., 2017; Wagner et al., 2015).

Finally, HD 36112 is unresolved, with a NEAR band upper limit of the size of the emission region of 13 AU. This is an improvement by almost a factor of 10 over previous observations which set an upper limit of 120 AU on the 11.7 μm emission size (Mariñas et al., 2011).

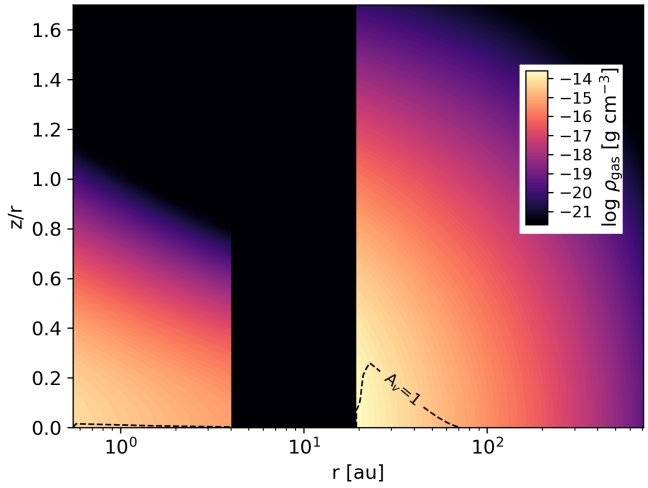

Figure 4.3: Gas density profile of the ProDiMo HD 10056 disk model. The dashed contour line traces the surface where the minimum optical extinction A_V in the combination of the vertical or radial direction is 1.

4.4 Protoplanetary disk modelling with ProDiMo

We used the radiation thermo-chemical disk model ProDiMo[2] (Woitke et al., 2009; Kamp et al., 2010; Thi et al., 2011) to simulate observations of the HD100546 system. ProDiMo self-consistently and iteratively determines the physical and chemical state anywhere within the disk with a frequency dependent 2D dust continuum radiative transfer, including gas-phase and photo-chemistry, ice formation, and non-LTE heating and cooling mechanisms. ProDiMo performs a 2D continuum radiative transfer with a ray-based, long-characteristic, accelerated Λ-iteration method at every disk grid point to calculate the local radiation field $J_\nu(r,z)$ (Woitke et al., 2009). The full radiative transfer methodology is described in Woitke et al. (2009). We adopt the standard DIANA[3] dust opacities as described in Woitke et al. (2016) and Min et al. (2016).

The parameters for the HD 100546 disk model were derived from the SED fitting work done as part of the European FP7 project DIANA[4] (Woitke et al., 2019). Parameters of the HD 100546 disk and stellar model can be found in Table 4.4 and the 2D gas density profile can be found in Fig. 4.3. The fitting was performed for a pre-Gaia distance of 103 pc (van den Ancker et al., 1997). Further details regarding the disk modelling and SED fitting process can be found in Appendix 4.A.1.

As ProDiMo finds formal solutions to the continuum radiative transfer during the calculation of the SED, the resulting modelled intensity can be visualised as an image. ProDiMo includes only the effect of isotropic scattering, and hence the preferential forward-scattering of light by larger dust grains is not represented realistically. As a result, the ProDiMo model appears

[2] `https://www.astro.rug.nl/~prodimo/`

[3] `https://dianaproject.wp.st-andrews.ac.uk/data-results-downloads/fortran-package/`

[4] More information about the fitted stellar and disk parameters, the 2D modelling results, and the predicted observables can be found at `http://www-star.st-and.ac.uk/~pw31/DIANA/DIANAstandard`

Parameter	Symbol	Value
Stellar Mass	M_*	2.5 $M_\odot$
Stellar Luminosity	L_*	30.46 $L_\odot$
Effective Temperature	$T_{\rm eff}$	10470 K
Interstellar Extinction	A_V	0.22 mag
Dust composition:		
$Mg_{0.7}Fe_{0.3}SiO_3$		58.17 %
Amorphous carbon		16.83%
Vacuum		25%
Dust size power law	p	3.34
Disk Inner Zone		
Mass	$M_{\rm d}$	8.81×10^{-8} $M_\odot$
Inner Radius	$R_{\rm in}$	0.55 AU
Outer Radius	$R_{\rm out}$	4.00 AU
Col. Density Power Index	ϵ	0.35
Minimum dust size	$a_{\rm min}$	0.042 μm
Maximum dust size	$a_{\rm max}$	2.9 μm
PAH abundance	$f_{\rm PAH}$	0.0028
Disk Outer Zone		
Mass	$M_{\rm d}$	7.15×10^{-3} $M_\odot$
Inner Radius	$R_{\rm in}$	19.34 (22.3) AU
Outer Radius	$R_{\rm out}$	600 AU
Tapering Radius	$R_{\rm tap}$	100 AU
Col. Density Power Index	ϵ	1.12
Minimum dust size	$a_{\rm min}$	0.042 μm
Maximum dust size	$a_{\rm max}$	2983 μm
PAH abundance	$f_{\rm PAH}$	0.0028 (0.0034)
Inclination	i	42°
Dust to Gas Ratio	d/g	0.01

Table 4.4: DIANA SED-fit parameters for the HD 100546 system used in the ProDiMo disk model. Parameters that were modified to improve the mid-IR fit are included in parenthesis.

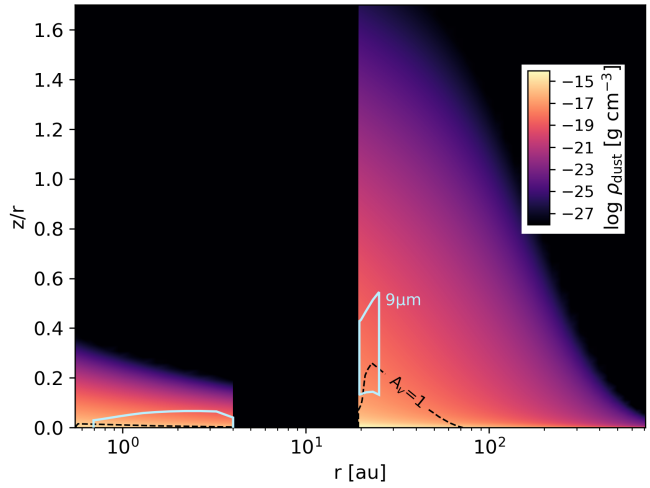

Figure 4.4: Dust density profile of the ProDiMo HD 100546 disk model. The light blue contour outlines the region where half of the total 9 μm emission originates. The dashed contour line traces the surface where the minimum optical extinction A_V in the combination of the vertical or radial direction is 1.

brighter on the far side than on the near side and it cannot reproduce the observed asymmetry in brightness of actual disks. While this effect is cancelled out in the disk SED model and radial intensity profile, it must be taken into consideration when comparing the model image to data on a per-pixel basis. The resulting ProDiMo data cube was attenuated by multiplying each synthetic disk image with the VISIR and NEAR relative filter transmission curves created with the VISIR imaging detector and VISIR calibration unit, and then by the sky transmission[5] at each wavelength. Subsequently the data cube was flattened into a single image for each filter. The images were then convolved with a reference PSF to simulate our observations. This was HD 93813 for the J8.9 filter, HD 27639 for the ARIII filter, and the HD 163296 data for the PAH1 and NEAR filters. For the PAH2 and PAH2_2 filters, reference PSFs were not available and the PSF from the ARIII filter was scaled to the new central wavelength and used instead.

4.5 Comparison to ProDiMo disk models

4.5.1 Spectral energy distribution HD 100546

Figure 4.5 illustrates the resulting SED for variants of the fiducial ProDiMo HD 100546 model between 7.5 and 10 μm, along with the averaged flux of the J8.9 band observation. The VISIR observations are included in black, as are the flux measured by *AKARI* and the spectrum from *ISO* (Malfait et al., 1998; Ishihara et al., 2010). Near 8.7 μm, the observational data to which the SED was fit includes the *ISO-SWS* spectrum and a photometric data point from *AKARI* with the S9W filter (Malfait et al., 1998; Ishihara et al., 2010). While our data are in agreement

[5] `https://www.eso.org/observing/etc/bin/gen/form?INS.MODE=swspectr+INS.NAME=SKYCALC`

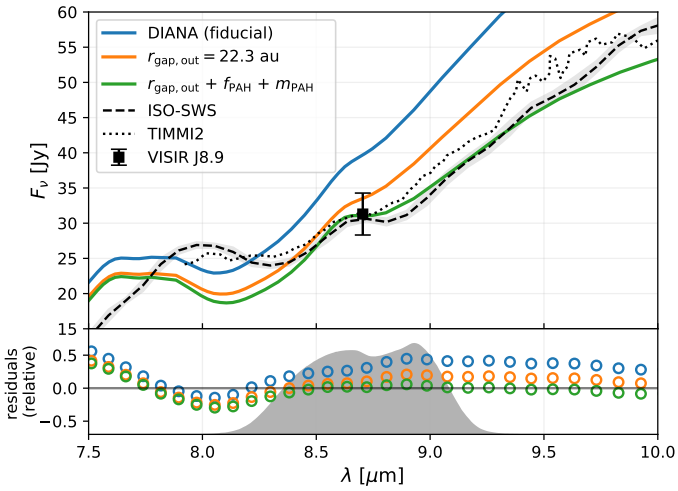

Figure 4.5: Comparison between the fiducial ProDiMo HD 100546 disk model (Woitke et al., 2019) and multi-parameter variants of the model. We include the observational VISIR data corrected for sky transmission and additional observational data (Malfait et al., 1998; van Boekel et al., 2004; Ishihara et al., 2010). The grey filled area illustrates the J8.9 filter response curve (arbitrary vertical scaling). Residuals between the various disk models and the *ISO-SWS* spectrum are shown in the lower panel as the ratio between the model SED and the observed spectrum.

with previous observational data, the expected flux of the basic ProDiMo model falls outside the uncertainty interval. We consider both disk parameter modifications included and not included in the previously performed SED fitting process that may improve upon the local fit in the mid-IR without reducing the quality of the global fit.

In our disk model, the continuum flux at 8.7 µm is emitted largely from the surface of the inner disk between 1-4 AU, while in the outer disk the 8.7 µm flux originates largely from the gap wall which is directly illuminated by the star and heated to ~300 K (see Fig. 4.4). Modifying the location of the cavity's outer rim (r_ϵ of the disk outer zone) allowed us to reduce the temperature of the gap wall and reduce the continuum emission in the mid-IR. We find the optimal balance between moving the gap outer wall further outwards and maintaining the quality of the global fit occurs where the gap wall is moved outwards from 19 to 22.3 AU. As demonstrated in Fig. 4.5 by the line $r_{in} = 22.3$ AU, this brings the SED within formal agreement to our observed mid-IR flux. Of the observed excess flux over the continuum around 10 µm, ~60% has been explained by the presence of amorphous olivine and crystalline forsterite emission features with the remainder explained by PAHs (Malfait et al., 1998). We thus also consider further refinements to the mid-IR fit by exploring the properties of the disk PAH population. These considerations can be found in Appendix 4.A.2.

Across the wavelength coverage of the *ISO-SWS* spectrum, we reduced the sum of the squares of the ratio between the old fit $F_\nu^{\rm old}$ and the new fit $F_\nu^{\rm new}$, that is $\Sigma(F_\nu^{\rm new}/F_\nu^{\rm old})^2$, from 12.6 to 4.2. It should be noted that while dust settling allows for a variety of average grain sizes across the vertical extent of the disk model, dust grains are not radially segregated by size in ProDiMo, such that within our model's disk zones, every grid column contains the same underlying dust

grain size distribution. Hence we can solve for only one gap outer radius, rather than a radius for each corresponding grain size.

4.5.2 Radial intensity profile

Radial intensity profiles of all the disks in the sample in the different filters were constructed by azimuthally averaging over the deprojected disks for both the observations and the convolved models and this is shown in Figs. 4.6 and 4.7. In all cases the radial profile is dominated by the telescope PSF. The unresolved sources show clear Airy rings in the images (see Fig. 4.2). The Airy rings are less obvious in the resolved sources and the central disk of the Airy pattern is larger, but they are still visible in the radial profiles. None of the profiles show signs of spirals, rings, or other features in the extended disk. Although the models do not include these previously observed features, this result is still consistent with the models, which show that the mid-IR emission is dominated by the central regions and the outer regions where features have been detected at other wavelengths contribute less than 5% of the flux at 8.7 μm.

For most models used in this comparison, the distance was measured before the Gaia data release. With the release of the Gaia data, it appears that these distances were off by around 10% in most cases (HD 100546, HD 163296, TW Hydra). For these disks, it was not necessary to rerun the model, as the differences between the old and new distances are small. Simply rescaling the model to the new distance is sufficient to compare the extent of the disks. However, for HD 169142, the difference between the distance assumed in the model and the distance measured by Gaia is more significant: The assumed distance is almost 30% too large. Because of this, the model was rerun with an adapted luminosity for the new distance.

HD 100546

The normalised radial flux distribution of both the real, deprojected data in each filter and the corresponding simulated data are shown in Fig. 4.6. The model and the data are in good agreement out to ~160 AU, where the noise starts to dominate the signal. The peak in the noise in the data is caused by the source subtraction in the chopping and nodding. The subtraction shadows are located at ~500 AU (4.5″) in the four NEAR filters and at ~900 AU (8″) in the J8.9 filter. In Fig. 4.7 we can compare the different filters to each other for the observed and synthetic data. In both cases the shorter wavelength filters PAH1 and ARIII result in narrower profiles with a smaller FWHM than the longer wavelength filters PAH2 and PAH2_2. Due to the smearing of the PSF, the J8.9 filter profile is much wider in both cases. The residuals from subtracting the model curves from the data are shown in Fig. 4.8. The errorbars in the image represent the 1σ error. The residuals show that the synthetic data is a good representation of the real data. The residuals at larger separations are 0 because the chopping and nodding process removes the background emission from the data and the model does not include sky or instrument background emission.

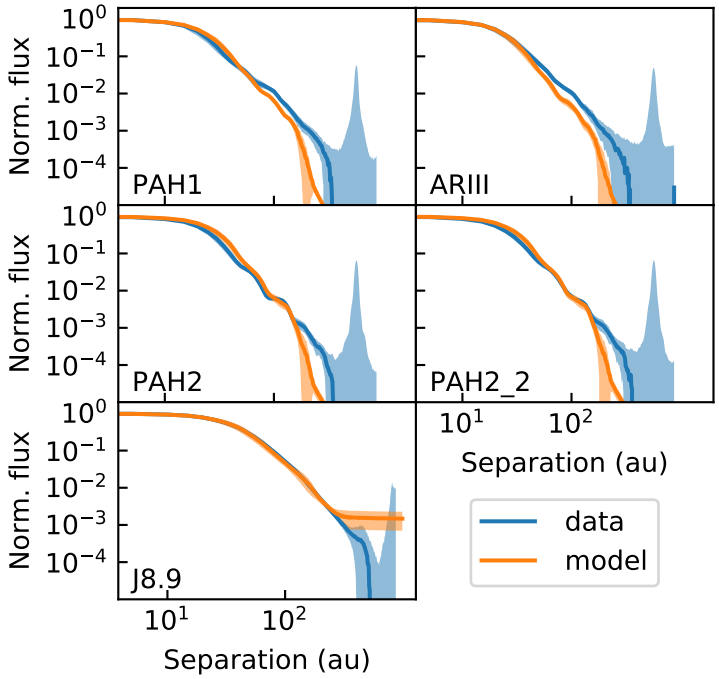

Figure 4.6: Radial profile of the HD 100546 protoplanetary disk in the PAH1, ARIII, PAH2, PAH2_2, and J8.9 filters. The profile from the data is shown in blue with the 1σ range in light blue. The profile from synthetic observations based on the ProDiMo model is shown in orange with the 1σ range indicated in lighter orange.

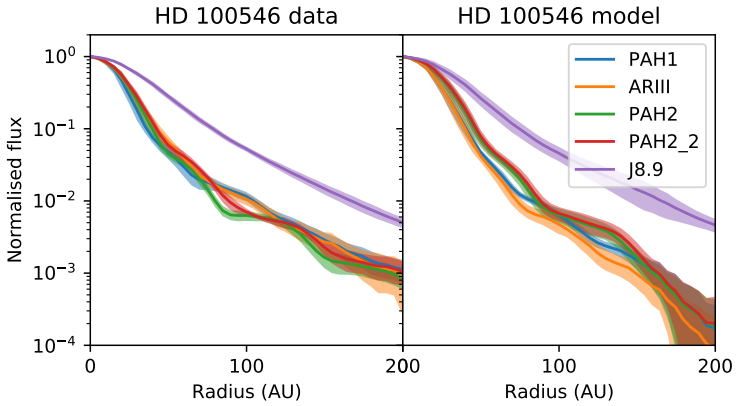

Figure 4.7: Radial flux profile of the HD 100546 protoplanetary disk in the PAH1, ARIII, PAH2, PAH2_2, and J8.9 filters, with the real data profiles on the left and the synthetic data profiles on the right. The shaded areas indicate 1σ errors for the data and confidence intervals for the models. For the model profiles, these intervals come from the PSF convolution and the azimuthal averaging and deprojection. In both the data and the model, it can be seen that the radial extent at $1/10^{th}$ the maximum flux is smaller for the shorter wavelength filters (PAH1, ARIII) than for the larger wavelength filters (PAH2, PAH2_2). This is expected as the PSF is larger for larger wavelengths. The J8.9 data, both real and synthetic, remain far more extended due to the smeared PSF.

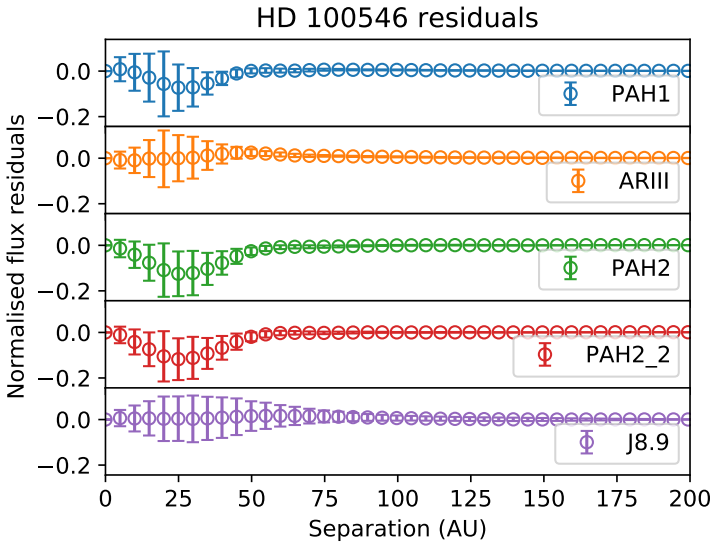

Figure 4.8: Residuals from subtracting the radial profile of the synthetic data from that of the observed data in each of the observed filters. The errorbars indicate 1σ uncertainties. The residuals all being within 1σ of 0 show that the model represents the data well.

HD 163296

Previous observations in near-IR and sub-millimetre wavelengths show that HD 163296 has multiple bright rings (e.g. Garufi et al., 2014; Isella et al., 2016; Isella et al., 2018). The ProDiMo model does not include rings, but instead assumes a flared, optically thick inner region up to 0.02″ and a shadowed outer region beyond that. As a result, it predicts that 95% of the flux is contained within a radius of 0.01″ in the PAH1 band and within 0.04″ in the NEAR band. This makes the emitting region much smaller than in the case of HD 100546, where there is a cavity and the inner rim of the outer disk also contributes to the flux. It is also entirely consistent with an unresolved image.

HD 169142

ALMA observations have detected three bright rings between 0.2″ and 0.6″ (45 – 80 AU) in the disk around HD 169142 (Pérez et al., 2019). Again, the model does not include the rings, but instead divides the disk into an inner and an outer zone with a gap at 0.1″ (22 AU), which is consistent with the inner gap seen at other wavelengths. Assuming the observed disk is described by a Gaussian function, the apparent size as defined by ProDiMo (the radius containing 95% of the flux) corresponds to the 2σ radius of the Gaussian, which is larger than the FWHM, which only contains half the flux. After deconvolution, the apparent size of HD 169142 is 24 ± 1 AU in the PAH1 band and 35 ± 1 AU in the NEAR band. This means that the inner gap is unresolved and part of the flux in both bands is from the inside of the inner ring, but the outer two rings are too faint to be observed.

The HD 169142 model has an apparent size of 43 and 45 AU in the PAH1 and NEAR bands.

While this is approximately consistent with the observed apparent size in the NEAR band, there is a discrepancy with the smaller PAH band observation. This is consistent with observations by Okamoto et al. (2017), who find that the size of the emitting region is much smaller at 8.6 and 8.8 μm than it is at 12.6 μm. They conclude that at wavelengths smaller than 9 μm, the inner disk and halo dominate; whereas, at wavelengths larger than 9 μm, the inner wall of the disk dominates which results in a larger observed size. Modelling performed by Maaskant et al. (2014) suggests that gas flowing through disk gaps can contribute significantly to the observed ionised PAH emission. This could manifest as an increase in emission at ∼8 μm relative to ∼12 μm, corresponding to the angular size of a gap. If the neutral PAH emission primarily originates from the gap wall, we would expect a correspondingly smaller emitting region for the predominantly ∼8 μm PAH flux. This difference is not reproduced by the model, leading to a mismatch with the data in the PAH band. This can be due to the complete lack of gas and dust in the model gap and hence lack of associated emission.

The previously derived inclination of 13 ± 2° is consistent with the model value of 13°. It is also consistent with previous literature (Pérez et al., 2019; Panić et al., 2008; Raman et al., 2006).

TW Hydra

Studies in near-IR and sub-millimetre have found six gaps located between 0.11″ and 0.84″ (6 – 44 AU Tsukagoshi et al., 2016; Andrews et al., 2016; van Boekel et al., 2017). The model assumes an optically thin inner region corresponding to the inner gap and a dense outer region for the rest of the disk. All the emission in both bands is predicted to be from this thin inner region and the inner wall of the outer disk. The other gaps are not expected to be visible as they are further out in the disk, where there is no more emission. This means that there is an apparent size of 3-4 AU in both filter bands and this is consistent with the observations being unresolved. More recent observations also suggest the central optically thin region may be much smaller than in the model, which would shrink the expected apparent size (e.g. van Boekel et al., 2017; Andrews et al., 2016).

HD 100453

Deconvolving the data results in apparent sizes of 7 ± 1 and 18 ± 1 AU in the PAH1 and NEAR filter bands, respectively. The contribution of PAHs to the flux in the PAH1 band is expected to be weak, as Meeus et al. (2001) did not detect any PAH features at 8.6 μm in *ISO* data. We therefore expect the flux in the PAH1 band to be dominated by the continuum emission. The emission in both bands is well inside the radius where spiral arms have been found and this suggests that HD 100453 follows the other targets in the sample in which the mid-IR emission is dominated by the central regions. Since the outer disk starts at 17 AU, the PAH emission seems to come from inside the gap and the NEAR band emission includes the inner wall of the disk which is heated by the star, similar to what is seen in HD 169142.

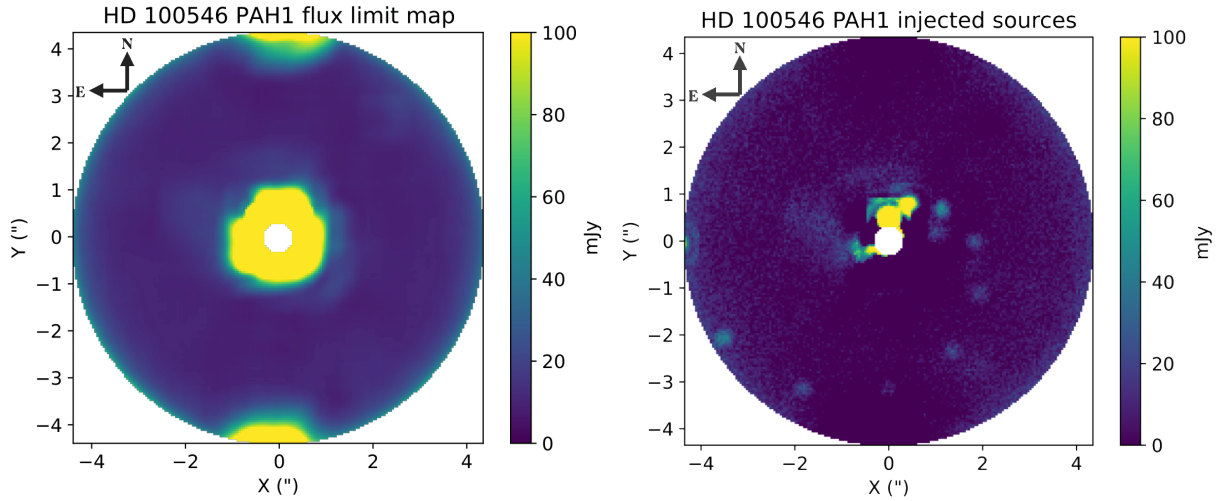

Figure 4.9: *Left:* Mapped 5σ flux limits of the HD 100546 PAH1 data, where the disk image is the most elliptical. The shape of the emitting region does not significantly influence the flux limits, especially beyond 1″ where the data are background limited. *Right:* HD 100546 PAH1 data with sources injected at different separations and position angles at 5 sigma. Most of the sources are clearly visible.

HD 36112

HD 36112 has a large cavity, with an outer disk that has rings, clumps, and spiral arms (e.g. Dong et al., 2018; Wagner et al., 2019). However, in our observations, the cavity is unresolved. Since the cavity has a radius of 0.2″ and the upper limit for the 95% flux radius is 0.07″, this means that most of the emission comes from inside the cavity and not from the inner rim of the outer disk, unlike the NEAR filter emission of the other sources.

4.6 Companions

The proposed companions of the disks in this sample are potential hosts to circumplanetary disks, which thus far have only been tentatively identified in the PDS 70 system (Keppler et al., 2019; Christiaens et al., 2019; Haffert et al., 2019; Isella et al., 2019). To search for planetary companions and associated dust concentrations in the disk, the circularised PSF subtraction described in Petit dit de la Roche et al. (2020) was applied to the data. This method creates an individual reference PSF from the data for every nod-subtracted image by azimuthally averaging it. The resulting rotationally symmetric PSF was then subtracted from the original data to remove the radially dependent stellar flux. This was decided upon because there is not sufficient rotation in the images to do angular differential imaging and most of the data do not have reference stars available for standard PSF subtraction. Standard PSF subtraction would also not subtract any spatially extended disk emission. Subtracting a circularly symmetric PSF from an elliptical disk image does leave residuals, but the bulk of the disk emission (>80%) is subtracted. Additionally, the sizes of the emitting regions in our data are small and the flux limits are not influenced by their shapes beyond the very inner pixels, where the disk is visible. This is the case even within

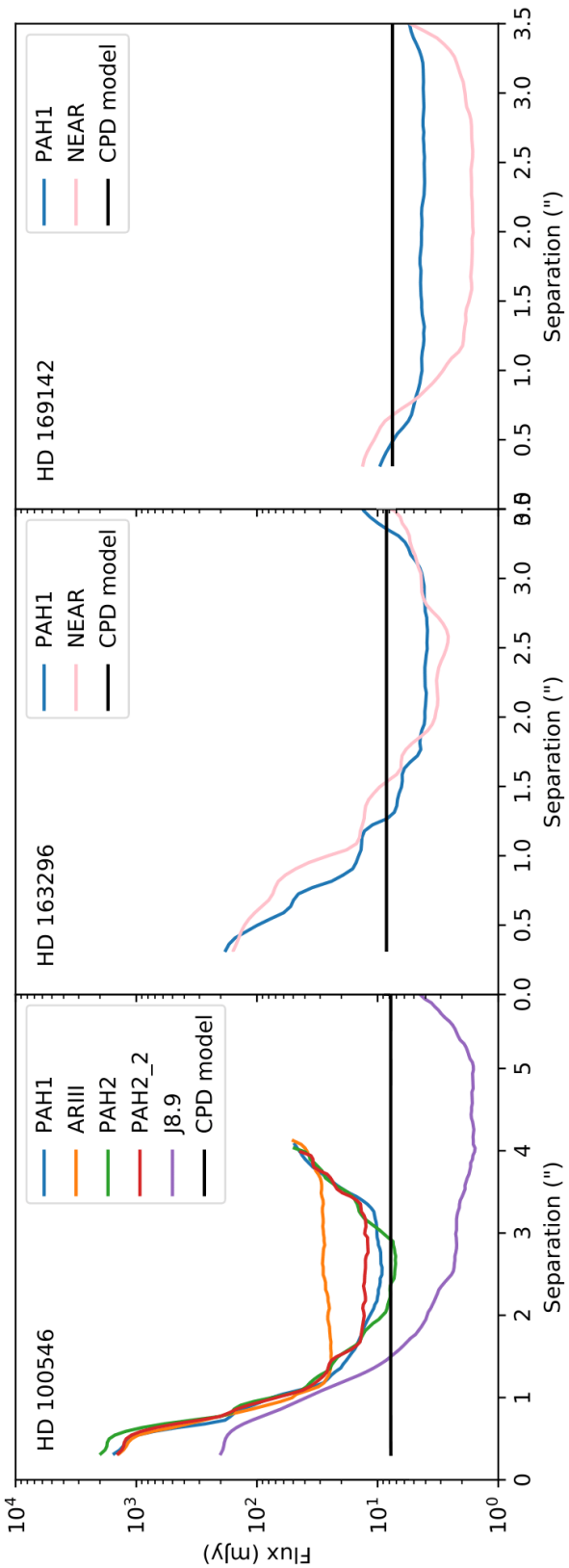

Figure 4.10: 5σ flux limits of potential companions to three targets compared to the CPD model described in Table 4.5 inserted in the circumstellar disk. *Left:* limits for the different observations of HD 100546 in PAH1 (blue), ARIII (orange), PAH2 (green), PAH2_2 (red), and J8.9 (purple) filters. The black line indicates the estimated flux as a function of radial separation for our fiducial CPD model as described in column 2 of Table 4.5. Only one line is included as the model values are similar across the different filters. The increase at 7″ in the J8.9 filter and at 4″ in the other filter are the results of chopping and nodding shadows. *Middle:* Limits for the observations of HD 163296 in the PAH1 (blue) and NEAR (pink) filters, along with the expected flux of the same CPD in the HD 163296 disk. *Right:* The same as the middle figure, but for HD 169142.

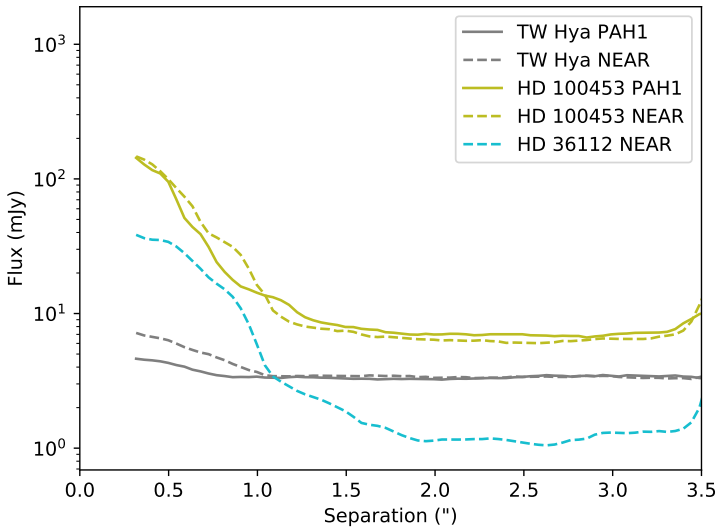

Figure 4.11: Observational limits on potential companions to TW Hya (grey), HD 100453 (yellow-green), and HD 36112 (turquoise) in the PAH1 (solid lines) and NEAR (dashed lines) filters. The increase at 4″ is the result of shadows from the chopping and nodding in the observations.

roughly 1″, beyond which the background dominates and the shape of the emitting region becomes irrelevant. An example of this can be seen in the left panel of Fig 4.9, where the limits are mapped for HD 100546 in the PAH1 filter, which has the most elliptical image of our entire dataset. While none of the proposed companions are detected in any of the disks, it is possible to set 5σ upper limits on the fluxes of any possible companions, based on the residual noise at each possible location. A limit of 5σ was chosen, since injected 5σ sources were clearly recovered in the reduced data, as can be seen in the right panel of Figure 4.9. The only exception is the source directly to the south of the star, which, although still present, is less clear due to its proximity to one of the shadows induced by the nodding. However, the affected areas around these shadows are small.

Fig. 4.10 and 4.11 show the resulting flux limits, with Fig. 4.10 including the flux of a model planet with a circumplanetary disk, which is discussed in the next section. The obtained limits are of the order of a few millijanskys between 1″ and 3.5″ separation up to a few tens of millijanskys at 0.5″. This is more sensitive than any previous mid-IR imaging observations by a factor of 10-100. Beyond 3.5″, the limits are dominated by the shadows induced by the chopping and nodding procedure in the observations. The differing sensitivities between objects with the same integration times are the result of different observing conditions influencing the data quality of the different targets.

4.6.1 Companion models

The presence of planetary accretion and a CPD or circumplanetary dust envelope can act to significantly increase the mid-IR luminosity of a putative companion (e.g. Zhu, 2015). To determine our own mid-IR observational limits for the planet candidates with accompanying CPDs, we ex-

plored a grid of CPD models using ProDiMo. Our model grid consists of a range of possible planet CPD masses, CPD dimensions, dust grain size distributions, and planet luminosities.

Properties of the planet and CPD models

We consider planetary masses of 1 to 10 M_{Jup}, with correspondingly sized CPDs defined by the planet's Hill radii. As CPDs could be tidally truncated to ~1/3 of this radius (Quillen and Trilling, 1998; Martin and Lubow, 2011), or even photoevaporatively truncated to 0.1-0.16 R_{Hill} (Mitchell and Stewart, 2011; Oberg et al., 2020), we set our CPD surface density tapering radius to the point at which the surface density begins to decline exponentially at $R_{Hill}/3$ and the outer radius at R_{Hill}.

We considered a range of CPD masses relative to the planet masses $M_{CPD} = 10^{-4} - 10^{-2} M_p$, and a range of planetary luminosities corresponding to various stages of accretion such that $L_p = 10^{-6} - 10^{-2}\,L_\odot$ (Mordasini et al., 2012). Marley et al. (2007) found that a 10 M_{Jup} planet in a 'hot start' evolution scenario can decline monotonically in luminosity from an initial $\sim 4 \times 10^{-3}\,L_\odot$ to $\sim 4 \times 10^{-4}\,L_\odot$ within 5 Myr. In the core accretion case, they found a peak luminosity during runaway accretion of $> 10^{-2}\,L_\odot$ which lasts $\sim 3 \times 10^5$ yr, rapidly declining to $\sim 2 \times 10^{-6}\,L_\odot$ by 3 Myr. Given that the planetary luminosity is expected to peak only briefly at or above $L_p \sim 10^{-2}\,L_\odot$, we consider the case of $L_p = 10^{-2}\,L_\odot$ to be the most optimistic detection scenario.

Pressure bumps at gap edges are suspected to act as filters for dust grain size, preventing the accretion of grains significantly larger than 10 μm onto planets within the gap (Rice et al., 2006). We thus also considered CPDs where the dust grain size population is limited to maximum sizes of 100 and 10 μm.

A companion orbiting within an optically thin region of the circumstellar disk can be exposed to significant UV radiation from its host star (Oberg et al., 2020). Photons of energy 6-13.6 eV are known as FUV and can efficiently heat disk surfaces. The significant FUV luminosity of the host star can act to heat the surface of the CPD and increase its IR luminosity. We parameterised the FUV flux with the Draine field $G_0 = 1.6 \times 10^{-3}$ erg cm^{-2} s^{-1}, which was integrated from 6-13.6 eV (Habing, 1968). We extracted the G_0 field intensity using ProDiMo from the results of the 2D radiative transfer within the DIANA circumstellar disk models and applied this as a UV background field to our own CPD models. Given that dust is the dominant source of opacity in the UV, it should be noted that the gaps in the DIANA disk models (see Fig.4.4 for the HD100546 dust structure) are free of dust and do not contribute to the UV opacity.

Companion flux estimates

We extracted the planet and CPD flux from the SEDs produced by the ProDiMo continuum radiative transfer and weighed it across the filter response curves. This flux represents the idealised total flux emitted by the unresolved companion, unconvolved with the observational PSF. We find that for high planetary luminosities ($> 10^{-4}\,L_\odot$), the mid-IR flux is dominated by the planet itself, whereas the CPD only contributes 3 – 6% of the combined emission largely independent of CPD properties.

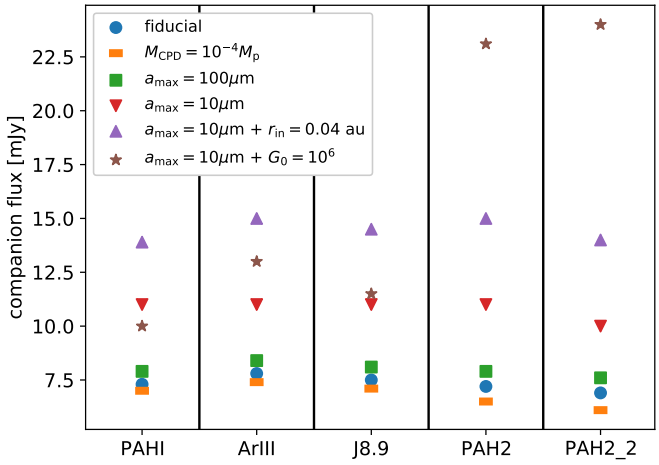

Figure 4.12: Model companion (planet and CPD) unextincted flux estimates. The 'fiducial' case is described by the planet and CPD parameters found in column 2 of Table 4.5 at 55 AU for the HD 100546 system. We also consider a variety of maximum dust grain sizes a_{max}, CPD mass M_{CPD}, CPD inner radius r_{in}, and background FUV radiation field strength G_0.

For our disk models, the size of the CPD as estimated by its Hill stability and the strength of the background FUV field both vary in predictable ways. For a given CPD model, our parameter grid exploration thus allowed us to fit for the resulting planet and CPD flux given an arbitrary radial separation from the star. As the vertical dust opacity at arbitrary wavelengths was also calculated as part of our model radiative transfer for various circumstellar disks, we were able to determine the radial dependence of the extinction to the midplane as well. We solved for the dust column density as a function of the viewing inclination for each radial position in the disks, and from this we derived the resulting 9 µm optical depth. The black line in Fig. 4.10 represents the resulting expected flux of the planet and CPD model in the J8.9 filter for a 10 M_{Jup} planet with a CPD of mass $10^{-2} M_p$ as described in Table 4.5. The line was derived from a fit performed to the J8.9 flux of our model grid of CPDs in which the background FUV radiation field, the disk size, and extinction to the midplane were simultaneously varied as a function of radial separation, although the predicted flux is relatively flat for planets found outside of the optically thick regions of the circumstellar disks. For low radial separations, the background FUV field heats the CPD surface and results in increased mid-IR emission. The CPD size grows with increasing distance from the star as the companion's Hill sphere increases correspondingly; however, as the majority of the CPD mid-IR emission originates from the innermost regions of the CPD, this contribution becomes negligible at large separation. The flux of our CPD models in the other filters is similar, varying for non-pathological model cases by at most ~10%, and they are thus roughly comparable, as illustrated in Fig. 4.12.

Parameter	Symbol	18 AU	55 AU	100 AU
Planet mass [$M_{\rm Jup}$]	$M_{\rm p}$	10	10	10
Planet luminosity [L_*]	$L_{\rm p}$	10^{-2}	10^{-2}	10^{-2}
CPD mass [$M_{\rm p}$]	$M_{\rm CPD}$	10^{-2}	10^{-2}	10^{-2}
CPD inner radius [AU]	$R_{\rm CPD,in}$	0.01	0.01	0.01
Minimum dust size [μm]	$a_{\rm min}$	0.05	0.05	0.05
Col. density power index	ϵ	1	1	1
Dust to gas ratio	d/g	0.01	0.01	0.01
Reference scale height	$H_{0.1\rm au}$	0.01	0.01	0.01
Planet semi-major axis [AU]	$a_{\rm p}$	18	55	100
CPD tapering radius [AU]	$R_{\rm tap,CPD}$	0.40	1.99	3.61
CPD outer radius [AU]	$R_{\rm out,CPD}$	1.19	5.96	10.84
Maximum dust size [μm]	$a_{\rm max}$	10	3000	3000
FUV background	G_0	$10^{6.7}$	$10^{4.1}$	3500
Optical depth at 8.7 μm	τ	~ 0	1.27	0.43
Predicted 8.7 μm flux (extincted) [mJy]	$F_{\rm P,1}$	11.5	2.1	4.88
Predicted 8.7 μm flux (unextincted) [mJy]	$F_{\rm P,0}$	11.5	7.6	7.5

Table 4.5: HD100546 candidate planets and CPD model parameters for our optimistic detection scenario (parameters listed above the first horizontal divider) for a variety of radial separations (parameters below the first horizontal divider) and associated J8.9 band predicted fluxes. Dust composition is identical to that listed in Table 4.4.

Results for HD 100546

While previous estimates of the age of HD 100546 indicate an older ($\sim$ 10 Myr) system (van den Ancker et al., 1997), Fairlamb et al. (2015) derived an age of 7.02 ± 1.49 Myr and an accretion rate of $\dot{M} \approx 10^{-7}\,M_\odot\,yr^{-1}$. The mass of the HD 100546 inner disk was fit to be $8.72 \times 10^{-8}\,M_\odot$ (Woitke et al., 2019), thus requiring continuous replenishment from the outer zone across the gap. The plausibility of an actively fed circumplanetary accretion disk is thus supported by the ongoing presence of radially evolving dust within the circumstellar disk (Marley et al., 2007; Mordasini et al., 2012).

We considered companions placed in the midplane at multiple radial separations from the star to study the influence of the background radiation field and circumstellar dust extinction on the predicted flux. We considered the properties of the planet candidate HD 100546b described by Quanz et al. (2015), which was found at a radial separation of 53±2 AU. When the planet was treated as a single-temperature blackbody, Quanz et al. (2015) found the best fit solution to be an emitting region of $R = 6.9^{+2.7}_{-2.9}\,R_{Jup}$ with $T = 932^{+193}_{-202}$ K for a luminosity $L = 2.3^{+0.6}_{-0.4} \times 10^{-4} L_\odot$. As the addition of a CPD may produce an emission signature diverging significantly from a single-temperature blackbody, we loosened the constraints on the temperature and emitting area. For a 2.5 $M_\odot$ star, a planet of 1, 5, or 10 M_{Jup} at 55 AU has a Hill radius of 2.77, 4.73, or 5.96 AU, respectively. We considered three cases in detail: a planet immediately interior to the outer gap wall at 18 AU, a planet embedded within the outer gas and dust disk at 55 AU, and a wide-separation planet in the optically thin region of the PPD at 100 AU, with correspondingly sized CPD outer radii, maximum dust grain sizes, FUV backgrounds, and optical depths to the midplane (see Table 4.5). While the CPD size, as set by the Hill radius, only varies by a factor of 100 across the disk surface from 5-500 AU, the background UV radiation field varies more dramatically by a factor $> 10^6$.

At the radial location of the 55 AU planet candidate, we extracted an FUV flux of $G_0 = 10^{3.65}$ in the midplane from the results of our circumstellar disk model radiative transfer. At 5 AU in the shadow of the inner disk, we find $G_0 = 10^{5.4}$ and at 18 AU $G_0 = 10^{6.5}$. The maximum G_0 within the gap is found to be 3×10^6. The gas component of a CPD experiencing such irradiation acquires an optically thin heated envelope with a temperature of around 5000 K at $z/r \sim 0.4$. The ~70 K optically thick surface below this envelope gives rise to significant re-radiated emission peaking at 30-50 μm. The short-wavelength tail of this component contributes non-negligibly to the J8.9 flux across the entire CPD surface for $G_0 > 10^5$.

From the HD 100546 disk model dust density distribution and dust opacities, we determined the optical depth to the midplane along the line-of-sight to the observer across the J8.9 band to determine extinction at arbitrary radii. While emission arising from planets inside the gap would be largely unextincted, immediately outside of the gap we find a maximum optical depth $\tau_{J8.9}$ of 5.6. The disk becomes optically thin at 8.7 μm only outside of 82 AU. We find that at the large separations where our sensitivity is maximal at $a > 160$ AU, $\tau_{9\mu m}$ is at most 0.18 and $\tau \propto a^{-2.4}$.

The model planet with a mass of 10 M_{Jup} and a luminosity of $10^{-2}\,L_\odot$ would have been detected in the J8.9 data beyond this radius and in PAH2 between 2″ and 3″. Hence, our new mid-IR imaging data prove that no such massive, luminous planets exist in the HD 100546 system at radii larger than 160 AU from the central star. A companion with a luminosity of $10^{-3}\,L_\odot$

would be marginally detectable at angular separations of 4-5″ only.

Results for other systems

We used a single best-case representative planet and CPD to derive detection limits for the other observed systems as a function of separation. The model CPD mid-IR flux levels are constant at large radii, because at large separations the UV radiation emitted by the star no longer significantly contributes to the heating and re-radiation of the CPD. The fact that the CPD is free to physically increase in size as the planet's Hill radius increases also no longer acts to increase the flux, as for the optically thick CPDs we consider, the planet acts only to heat the innermost regions of the CPD, from which the majority of the 9 μm emission originates.

For HD 163296, we excluded a $10\,M_{Jup}$, $10^{-2}\,L_{\odot}$ companion between 1.5″ and 3.5″, as it would have been observed in both filters. For HD 169142, TW Hydra, and HD 36112, we excluded it beyond 1″. HD 100453 is the only system in which it would remain undetected.

4.6.2 Reconciling prior observational constraints

In previous work, the planet candidate HD 100546 b at 55 AU separation is the only companion that has had its putative CPD constrained in mass to $1.44\,M_{\oplus}$ (or $2.7 \times 10^{-3}\,M_p$ for a planet mass $1.65\,M_{Jup}$) in the optically thin case, and a size of 0.44 AU in radius for the optically thick case, although this rests on assumptions regarding the grain size population of the CPD and the ratio between planetary and CPD mass (Pineda et al., 2019). ALMA observations of HD 100546 at 870 μm set a 3σ limit of 198 μJy for any planet candidate (Pineda et al., 2019) with which we can further constrain any CPD's longwave emission.

We find that for our fiducial CPD surrounding a $10\,M_{Jup}$ planet of $10^{-2}\,L_{\odot}$, we overpredicted the upper limit set by ALMA observations at 870 μm by a factor of 13. When the fiducial CPD is modified with a maximum grain size of 10 μm, this overprediction is reduced by a factor of ∼2. Our planet and CPD models can be brought into agreement with the ALMA flux limits by reducing the mass of the CPD relative to the planet or by reducing the dust-to-gas ratio. We find that while the 9 μm flux of the CPDs is largely insensitive to their mass, the continuum flux in ALMA band 10 is primarily dependent on our CPD mass, radius, and dust-to-gas ratio owing to the emission region corresponding to cooler dust at larger separation from the planet (Rab et al., 2019). For a fixed radius, dust-to-gas ratio, maximum and minimum dust grain size, and grain size power law, the 870 μm flux is proportional to the CPD mass as $F_{870\mu m} \propto M_{\rm CPD}^{0.81}$ for the range $M_{\rm CPD} = 10^{-6} - 10^{-2}\,M_p$. We find that the maximum CPD mass allowed by the constraint is $3.2 \times 10^{-7}\,M_{\odot}$. A smaller, optically thick CPD of a higher mass still satisfies the constraint. We find that a modification to our fiducial CPD of a mass $> 9.5 \times 10^{-6}\,M_{\odot}$ with a tapering radius of 0.2 AU and an outer radius of 0.6 AU has a 870 μm flux of 190 μJy and would thus satisfy the constraint set with ALMA. This places no additional constraints on our 9 μJy flux prediction, as the mid-IR flux is instead primarily dependant on the planet's luminosity and the CPD's inner radius.

4.7 Discussion and conclusions

We analysed images of HD 100546 in five different mid-IR filters and a further five young stellar objects in the PAH1 and NEAR infrared filters with the VISIR instrument and its upgrade NEAR. The resolved disks had their FWHMs and inclinations determined. HD 100546 has a FWHM of 28-61 AU across five different filters, a projected inclination of 44±4°, and a projected position angle of 130°. HD 169142 has FWHMs of 29 AU and 41 AU in the PAH1 and NEAR filter bands, respectively, and a projected inclination of 13±2°. HD 100453 has a FWHM of 9 AU in the PAH1 band and 21 AU in the NEAR band and an inclination of 35±2°. The observed values are consistent with the DIANA circumstellar disk models and previous observations of the sources. We set upper limits of 6 AU and 7 AU on the size of the emission region of HD 163296 in the PAH1 and NEAR filter bands, respectively, thus improving previous limits by a factor of three. We set upper limits of 3 AU and 7 AU on TW Hydra in the same filters, which is consistent with previous observations. Finally, we set an upper limit of 13 AU on the size of the NEAR filter emission of HD 36112, which is an improvement over previous values of a factor of 10. The fact that we did not resolve these targets is also consistent with the DIANA ProDiMo models (Woitke et al., 2019). Because of the method by which the variety of observational data were weighted during the original fitting procedure performed by Woitke et al. (2019), and because of the non-complete set of disk model parameters for which the fits were performed, localised improvements to the SED were still possible. After a minimal adjustment of the HD 100546 disk model gap geometry, an examination of the disk radial profile showed that our ProDiMo model was a good match for the data and that it reproduces the radial profile of the disk to within 1σ without the need to include a companion object. In all cases, the mid-IR emission originates from the central area of the disk from the most highly irradiated areas: unresolved inner disks and/or the inner rims of the outer disks.

Given our new flux estimate for the HD 100546 system, we have improved upon the global SED fit from 2-18 μm by simultaneously increasing the gap outer edge from 19.3 AU to 22.3 AU, increasing the abundance of PAHs in the outer disk relative to the ISM from 2.8×10^{-3} to 3.4×10^{-3}, and replacing the representative PAH circumcoronene with coronene. The details of the PAH properties fitting can be found in Appendix 4.A.2. Given that the spectral properties of alternative dust compositions have not been thoroughly explored nor the marginal improvement of the detailed PAH fit, we tend to favour the simple modification of only the disk gap geometry. The χ^2 statistic between the model SED and the *ISO-SWS* spectrum for 2-18 μm reduces from 588 to 278 when the inner radius is increased to 22.3 AU. It should be noted that increasing the model gap outer radius would act to increase the tension with the location of the dust continuum gap edge observed with ALMA at 16-21 AU (Pérez et al., 2020), although as ALMA traces millimetre-sized grains, this may not be inconsistent. Additionally, the model gap outer radius is the one parameter that we adjusted which was previously fit by means of a genetic algorithm (Woitke et al., 2016; Kamp et al., 2017; Woitke et al., 2019; Dionatos et al., 2019).

We produced planet and CPD flux estimates using the thermochemical disk modelling code ProDiMo for the VISIR filters with a variety of CPD parameters, finding that in the absence of extreme external FUV radiation fields, the maximum unextincted flux in the J8.9 band is expected to be ∼15 mJy for a CPD with an inner radius of 0.04 AU and a maximum dust grain

size of 10 μm. We find that this flux is largely dependent on the planet properties and not on those of the circumplanetary disk. The CPD is found to contribute $3-6\%$, at most, of the companion flux at 9 μm. The CPD contribution at 9 μm is greatest when the maximum grain size is reduced to 10 μm and the CPD is irradiated by a significant FUV field of $G_0 \geq 10^6$.

Such conditions are found within the gap of the HD 100546 disk, where we determined that the G_0 field strengths up to 3×10^6, despite the presence of the inner disk. A planet and CPD within the gap at 18 AU, while more gravitationally truncated than our test cases at 55 and 100 AU, is unobscured by dust and we expect $F_{\mathrm{J8.9}} = 11.5$ mJy. We note that while the 9 μm emission of the CPD is largely unaffected for $G_0 \leq 10^6$, it rises precipitously above this, and for a $G_0 = 10^7$ we find $F_{\mathrm{J8.9}} = 0.6$ Jy. While a CPD within the gap would be found at angular separations of less than $0.2''$ and thus be unresolved in our observation, the contribution to the flux of the star and circumstellar disk (31 ± 3 Jy) would thus be non-negligible. It should be noted however that a significantly FUV irradiated CPD can become photoeveporatively truncated such that the effective emission region is greatly reduced (Oberg et al., 2020).

For our $a = 55$ AU HD 100546 companion test case, we find $F_{\mathrm{J8.9}} = 2.1$ mJy owing to significant dust extinction. In the event that the planet is able to clear obscuring dust from its immediate neighbourhood in a localised cavity, the observed flux may increase to 7.5 mJy. Even in this 'best case' scenario of high planetary luminosity, it can be seen in Fig. 4.10 that the flux limiting sensitivity at 55 AU is 200 mJy. For our $a = 100$ AU companion case, we find $F_{\mathrm{J8.9}} = 4.9$ mJy, 7.9 mJy unobscured, and the accompanying limiting sensitivity is 30 mJy. Only outside of 180 AU would such a planet and CPD be detectable. Outside of 180 AU, we find a limit on planetary luminosity of $0.0028\,\mathrm{L}_\odot$, above which we would have detected any companion.

In the HD 100546 system, we rule out the presence of planetary mass companions with $L > 0.0028\mathrm{L}_\odot$ for $a > 180$ AU. We find that the contribution of a planet and CPD would still be of the order of the uncertainties inherent in the model, as relatively minor modifications to the HD 100546 gap dimensions (an increase of 2-3 AU in the outer radius) produce changes in expected continuum flux of 7-10 Jy at 9 μm. We place no stringent constraints on the planetary mass, CPD radius, or CPD grain size distribution. In the HD 169142, TW Hydra, and HD 100453 systems, we can exclude companions with $L > 10^{-2}\,\mathrm{L}_\odot$ beyond $1''$.

We consider whether the lack of detection of wide-separation ($a > 50$ AU) planetary mass companions (PMCs) of mass $< 20\,M_{\mathrm{Jup}}$ in the five studied systems is remarkable. While the presence of a dusty CPD may act to enhance the observability of a companion, it has been found that rapid dust evolution in CPDs of isolated wide-separation PMCs could act to suppress the dust-to-gas ratio of CPDs on short timescales ($d/g \leq 10^{-4}$ after 1 Myr), rendering a continuum detection more challenging (Pinilla et al., 2013; Zhu et al., 2018b; Rab et al., 2019). Sub-stellar companions have been detected in wide orbits around young stars (Neuhäuser et al., 2005; Ireland et al., 2011; Bryan et al., 2016; Naud et al., 2017; Bohn et al., 2019). It has been suggested that such objects may form in situ by the fragmentation of massive, self-gravitating disks (Boss, 1997, 2011; Vorobyov, 2013) by the direct collapse of molecular cloud material (Boss, 2001), or by core- or pebble accretion (Lambrechts and Johansen, 2014) and subsequent outwards scattering by an interaction with other massive planets (Pollack et al., 1996; Carrera et al., 2019). In the latter case, a detection of a wide-separation PMC may thus directly imply the presence of additional massive planets in the inner system.

Bowler (2016) suggests that around single, young (5-300 Myr) stars, 5–13 $M_{\rm Jup}$ companions at separations of 30-300 AU occur $0.6^{+0.7}_{-0.5}$% of the time. With VLT/NaCo, Vigan et al. (2017) found that 0.5-75 $M_{\rm Jup}$ companions at separations of 20-300 AU are found around $0.75 - 5.7$% of stars, and with the Gemini Planet Imager Exoplanet Survey, Nielsen et al. (2019) found that 5-13 $M_{\rm Jup}$ companions with separations of 10-100 AU occur around 9^{+5}_{-4}% of stars. Our sensitivity at the limiting angular resolution restricted our search to relatively wide separation companions ($a > 160$ AU). Given the PMC occurrence rate of Bowler (2016), we expect an absolute upper bound of $\sim 3.4^{+3.9}_{-3.3}$% probability of a single detection in our sample, assuming a perfect detection efficiency from 30-300 AU. In this context, it is difficult to make new conclusions regarding the prevalence of wide-separation PMCs in our observed systems given the relatively low a priori likelihood of detection and the relatively large companion luminosity ($10^{-3} - 10^{-2}\,L_{\odot}$) necessitated. We were able to set an upper limit to the occurrence rate for wide-separation PMCs with a luminosity $\geq 10^{-2}$ of ≤ 6.2% at 68% confidence.

Future observations with METIS (Brandl et al., 2018) on the ELT are expected to achieve ten times better sensitivities than NEAR and 40 times better sensitivities than VISIR at the same wavelengths, as well as improving the spatial resolution by a factor of 5, allowing for one to image more close in companions. MIRI[6] on *JWST* is expected to achieve 250 times better sensitivities than NEAR and 1000 times better sensitivities than VISIR. Both will be able detect the known companions to all six targets.

Acknowledgements

This project was made possible through contributions from the Breakthrough Foundation and Breakthrough Watch program, as well as through contributions from the European Southern Observatory.

4.A Modelling information

4.A.1 Standard disk models and SED fitting methodology

To perform the SED fits, a comprehensive set of publicly available observational data, consisting of photometric fluxes, interferometric data, low and high resolution spectra, emission line fluxes, line velocity profiles, and maps were used from which the physical and chemical parameters of the disk could be derived (references for which can be found in Dionatos et al. (2019)). The fits were performed by iteration of parameter sampling in MCFOST radiative transfer models by means of a genetic algorithm. HD 100546 was fit with 120 data points, two disk zones, PAHs, and 16 free parameters total after 632 generations and 7584 models. Further details of the standard disk models, SED fitting procedures, and the limitations of SED fitting can be found in Woitke et al. (2016), Kamp et al. (2017), Woitke et al. (2019), and Dionatos et al. (2019).

[6] https://www.stsci.edu/jwst/science-planning/proposal-planning-toolbox/sensitivity-and-saturation-limits

Limitations

The DIANA SED fitting procedure was performed with dust opacities corresponding to a mixture of amorphous pyroxene silicates and amorphous carbon (see Table 4.4; Dorschner et al., 1995; Zubko et al., 1996). Due to the use of standard dust opacities and a fixed PAH morphology, only the power-law of the dust size distribution and volume fraction of amorphous carbon was varied for the fit, so detailed matching of the spectral features is not expected. The 8.6 μm PAH complex feature, associated with in-plane C-H bending modes, is not fit in detail relative to the *ISO-SWS* spectrum. The presence of an unidentified broad feature at 7.9-8 μm is not explained by the model, but it has been suggested by Joblin et al. (2009) to originate from a PAH population known as PAH^x consisting of compact but large ionised PAHs with ∼100 or more carbon atoms not included in our radiative transfer modelling.

We opted not to explore the parameter space of possible dust compositions to perform a detailed opacity fitting across the mid-IR given that properties such as the amorphous carbon volume fraction can have a large impact on the SED at all wavelengths, such as by changing the millimetre and centimetre slopes (Woitke et al., 2016). While the mid-IR traces the disk surface, any features may not be indicative of the disk global dust properties and could represent surface effects, for example, PAHs confined to the surface which are generated locally. In this case, altering global dust properties may not be the correct approach.

We did not re-perform the global SED fitting procedure to account for the increased GAIA EDR3 distance for HD 100546, but we did consider the implications of an increased stellar luminosity to match the observed luminosity and new distance. To test the sensitivity of the SED to this adjustment, we considered a modest increase in our stellar effective luminosity to 34.74 $L_\odot$. If we were then to scale the physical dimensions of the disk and its gap accordingly, the resulting SED would exhibit a net decrease in mid-IR emission; across the J8.9 band, we find a deficit in emission over the fiducial model of 2.9%. As this falls within our own observational uncertainty, we do not consider the implications of the new distance estimate further.

4.A.2 HD 100546 disk model PAH properties exploration

Several PAH features contribute to the disk opacity near 9 μm. The broadband filter used in these observations covers an area around 8.6 μm where PAH C-H in-plane bending modes can contribute to the continuum emission. ProDiMo uses synthetic PAH opacities for neutral and charged PAHs as calculated according to Li and Draine (2001). Exploring the properties of PAHs in the model offers the possibility of modifying the disk flux across the J8.9 filter without globally modifying the disk dust properties and breaking the quality of the global SED fit.

The contribution of PAHs was estimated by van Boekel et al. (2004) to be around 22% of the total flux near 9 μm. They found the PAH emission to be more extended than the continuum along the spatial dimension of their longslit spectra, with a FWHM of ≈150 AU. Using the low resolution spectroscopic mode of VISIR, Verhoeff (2009) found a statistically significant increase in the spatial extent of the disk emission at 8.6 μm over the resolved continuum emission at a 27 σ level. While they found the ratio between the continuum subtracted peak flux at the 8.6 μm PAH feature over the peak flux was only 2.4%, the deconvolved FWHM size of the continuum

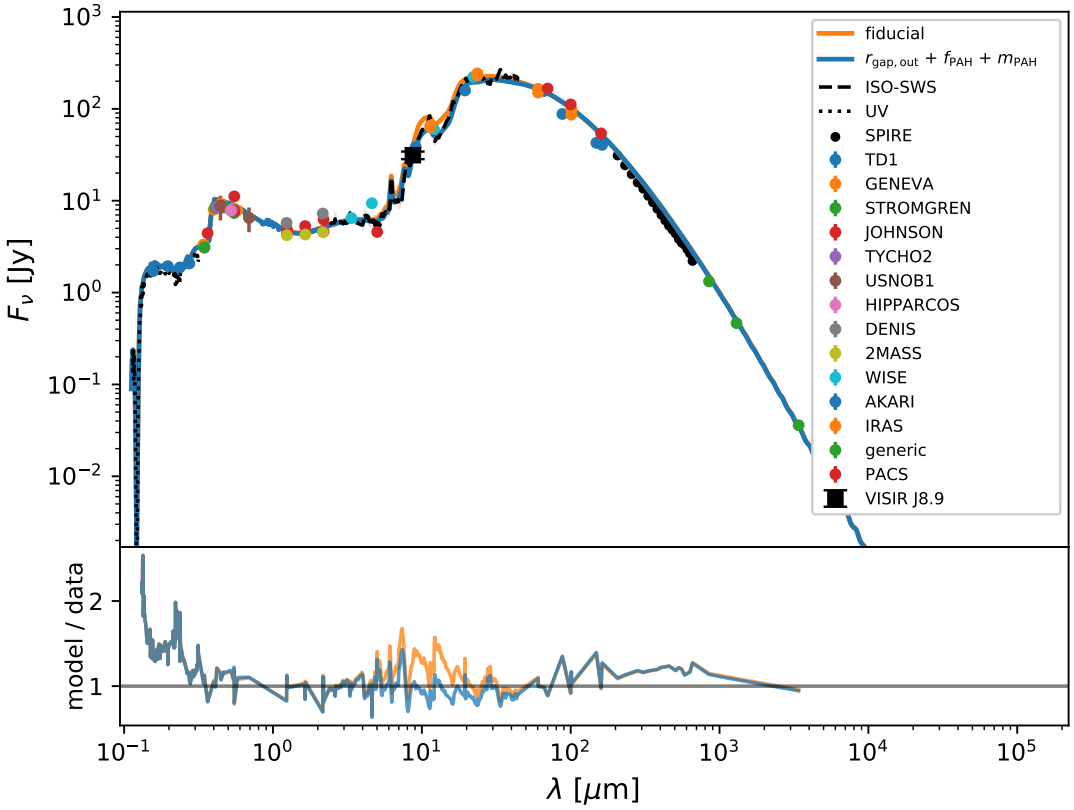

Figure 4.13: Global SED of the HD100546 disk models and comparison to the observational data folded into the fit. The fiducial model SED is the orange curve and our adjusted disk gap geometry model is the blue curve. The relative residual as defined by dividing the model by the data is shown at the bottom.

subtracted feature was $1.64^{+0.37}_{-0.38}$ ″. At a distance of 108 pc, this corresponds to a disk radius of 178^{+40}_{-41} AU. Furthermore, the variability of the 8.6 μm features between *ISO* and TIMMI2 spectra and their respective slit sizes implies that the PAH emitting region is at least 100 AU in size (Verhoeff, 2009). Additionally, Panić et al. (2014) found the 8.6 μm PAH emission to be emitted primarily from angular scales corresponding to ∼100 AU from the star.

While the HD 100546 disk model PAH abundance and charge fraction was fit for, these parameters were not varied between the inner and outer disk zones. We thus considered modifications to the PAH population in the outer disk, outside of $r = 22$ AU, specifically. The DIANA models use a single representative PAH, circumcoronene ($C_{54}H_{18}$), and a constant mixture of charged and neutral opacities throughout the disk (Woitke et al., 2016). For HD 100546, the abundance of PAH relative to the ISM $f_{\rm PAH}$ (defined such that in the ISM $f_{\rm PAH} = 1$) is 0.0028. The mean PAH charged fraction is 0.9. We considered both differing PAH types and abundances in the inner and outer disk zones to refine our fit.

We have explored a grid of a PAH abundance and morphologies in an attempt to minimise the residuals with our mid-IR observational data. Simultaneously allowing for the outer wall of the gap, the abundance of the PAHs, and the type of the PAHs to vary has allowed us to improve upon the standard SED fit without reducing the quality of the fit globally (see Fig.4.13). The result of this multi-parameter exploration can be seen in the green line in Fig. 4.5. We find that a smaller PAH, coronene ($C_{24}H_{12}$), and a 22% increase in $f_{\rm PAH}$ outside of the gap wall produce the best agreement with an observation across the J8.9 filter.

Chapter 5

An upper limit on the extended helium atmosphere of GJ 1214 b

Based on: D. J. M. Petit dit de la Roche, M. E. van den Ancker, P. A. Miles-Páez
Research Notes of the American Astronomical Society, Volume 4, Number 12, December 2020, Page 231

Abstract: The He I 10,830 Å absorption line in transit spectra traces the upper atmospheres of exoplanets and their mass loss, which in turn is important in determining their evolution and demographics. We use archival VLT/X-Shooter data to set new, more sensitive limits on the extended helium atmosphere of GJ 1214 b, a sub-Neptune orbiting an M-dwarf. We determine limits for the excess absorption at 10,830 Å of 0.38%±0.47%, which corresponds to an extended atmosphere scale height of $0.14\pm0.15\,R_p$ (95% confidence limit of $< 0.43\,R_p$). This is an improvement on previous upper limits set by Crossfield et al. (2019) and shows that X-shooter is a suitable instrument for these types of observations.

5.1 Introduction

Observations with the Kepler space telescope of close-in exoplanets have revealed a surprising gap in their occurrence rates around $1.8\,R_\oplus$ (e.g. Fulton et al., 2017; Owen and Wu, 2013). This can be seen in Figure 5.1. For small planets, the distribution of the number of observed planets by radius is bimodal, with peaks at 1.3 and $2.5\,R_\oplus$. The planets in the first peak are considered to be mostly rocky, with a small atmosphere and are called super-Earths. The larger planets likely still have a large hydrogen/helium (H/He) envelope and are considered mini-Neptunes.

It is theorised that post-formation mass-loss decreases the atmospheres and therefore the radius of planets that originally formed inside the gap. A number of processes can cause this, such as collisions and core-powered mass-loss where the formation heat of the planet causes the envelope to evaporate (e.g. Gupta and Schlichting, 2019; Ginzburg et al., 2018). However, the main driver for mass loss in close-in planets appears to be photo-evaporation due to their high incident stellar flux (e.g. Owen and Wu, 2017; Jin and Mordasini, 2018; Mordasini, 2020;

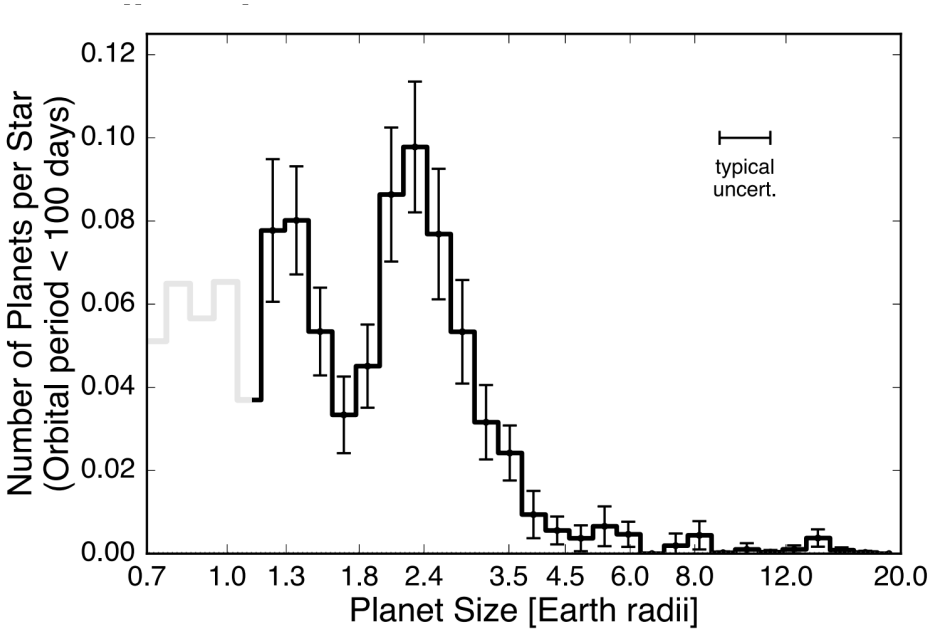

Figure 5.1: Figure 7a from Fulton et al. (2017) showing completeness-corrected histogram of planet radii for planets with orbital periods shorter than 100 days. The light gray region of the histogram for radii smaller than 1.14 $R_\oplus$ suffers from low completeness. The median radius uncertainty is plotted in the upper right portion of the plot.

Modirrousta-Galian et al., 2020), in particular in the X-ray and extreme ultraviolet (EUV) wavelength regimes. The evaporation time scales of planets in the radius gap is smaller than their cooling timescales, causing them to loose significant amounts of atmosphere, leaving only the rocky cores that make up the peak of the smaller planets in the radius distribution. Larger planets can hold onto their atmospheres better, causing the evaporation timescale to be longer than the cooling time scale and limiting the decrease in radius. Atmospheric evaporation is thus a major factor in exoplanet evolution and demographics. Transmission spectroscopy allows for the measurement of atmospheric evaporation. By comparing the spectrum of the star and planet in transit to that of the out-of-transit stellar spectrum the radius of the planet can be determined at different wavelengths, resulting in a transmission spectrum. As the atmospheres are expected to mostly consist of hydrogen and helium, looking for excess depth in these lines during transit can reveal an extended, evaporating atmosphere. An asymmetry in the transit at the wavelength of the line can also indicate a comet-like tail of evaporating gas. This has been done with both the Ly α hydrogen line (e.g. Lecavelier des Etangs et al., 2012) and, more recently, with the 10,830 Å helium line (e.g. Spake et al., 2018). Of the two, the helium line is the most advantageous, as it can also be measured by ground-based facilities and is more sensitive to low densities, making it less affected by the interstellar medium (Oklopčić, 2019; Fuhrmeister et al., 2020). It has been identified from early on as one of the most promising spectral signatures. While the first detection of this line in an exoplanet atmosphere by Spake et al. (2018) is still recent, it has since been detected with ground-based facilities in six other planets, and upper limits on the presence of

helium have been set on the atmospheres of a further eleven (e.g. Nortmann et al., 2018; Guilluy et al., 2020; Vissapragada et al., 2020; Paragas et al., 2021).

The 10,830 Å line is caused by resonance scattering, where the scattering of photons causes electrons to move from the first excited 2^3S state to the 2^3P state. The radiative transition between triplet and singlet states is strongly suppressed (Oklopčić and Hirata, 2018). The ground state (1^1S) is a singlet state, so the triplet 2^3S state is only populated by recombination or collisional excitation and the timescale for radiative decay is long, causing the state to be meta-stable. As a result excited helium in this form is expected to be particularly prevalent in planets that orbit close to active host stars due to the high incident X-ray and EUV flux. The 2^3P state is also a triplet state, so the transitions causing the 10,830 Å line are not forbidden and a large population of meta-stable helium results in deep absorption lines (Oklopčić, 2019) for such targets. These are also the planets where atmospheric evaporation is expected to be prevalent.

One such planet is GJ 1214 b (2.7 $R_\oplus$,6.5 $M_\oplus$; Charbonneau et al., 2009). It is on a close orbit (0.02 AU) around a nearby M4.5V star (Harpsøe et al., 2013) and has been extensively studied in optical and near infrared (NIR) wavelength ranges (e.g. Bean et al., 2010). Despite being commonly referred to as a super-Earth, its interior structure can be described as both a rocky planet and an ice-giant, depending on weather the atmosphere is H/He dominated or not and the amount of water present (e.g. Rogers and Seager, 2010; Nettelmann et al., 2011). Various transmission spectra lack strong molecular features, indicating either a H/He dominated atmosphere with clouds and hazes, or one dominated by water vapour. Both are supported by various measurements and neither can be completely ruled out (e.g. Bean et al., 2010; Berta et al., 2012; Angerhausen et al., 2017). The fact that such a fundamental property of one of the most well-studied planets of its kind remains uncertain, shows the importance of investigating planet evolution in the radius gap. GJ 1214 b is not just a close-in planet, observations of the host star have shown a high X-ray luminosity, which is expected to lead to significant atmospheric evaporation, with an estimated total mass loss of 2-5.6 $M_\oplus$ over its lifetime (Lalitha et al., 2014) and the hard spectral shape of M-dwarfs is likely to result in a large population of meta-stable helium, which should lead to a deep 10,830 Å absorption line.

Due to the lines location between the most common optical and NIR wavelength ranges, there is only one previous investigation into this particular line, which was done at low resolution (R≈500) and only found an upper limit to the helium absorption (Crossfield et al., 2019). In this work we use archival medium-resolution data from the X-Shooter instrument on the very large telescope (VLT) to measure the excess transit depth in the He I 10,830 Å line and set new, more constrained upper limits on the extended helium atmosphere of the exoplanet GJ 1214 b. We compare these limits to the $1.0\pm0.6 R_p$ ($< 2.1 R_p$) values previously calculated by Crossfield et al. (2019).

5.2 Observations and data reduction

Table 5.1 shows the obtained archival data and the corresponding atmospheric conditions of three transits of GJ 1214 b taken on 5-7-2011, 3-7-2011 and 22-7-2011 with VLT/X-Shooter (Vernet et al., 2011). X-Shooter provides mid to high resolution spectra in the ultraviolet-blue, visible

Date	Exposure time	Airmass	Seeing
07-05-2011	213x30s	1.2	$0.7'' \pm 0.2''$
03-07-2011	110x60s	1.3	$1.4'' \pm 0.4''$
22-07-2011	126x60s	1.4	$> 2''$

Table 5.1: Overview of the observations of GJ 1214 b.

and NIR wavelengths. We focus on the 10,830 Å He I line, so we only use the NIR data. The data were taken with a $5''$x$11''$ slit with a resolution of R∼2600. For each night there is a total of ∼1.4 hours of data available before and after the transit and half an hour in transit. The data of the last night was badly affected by seeing, so had to be discarded.

We reduced the data similarly to the Crossfield et al. (2019) analysis of IRTF/Spex data in order to best compare the results. The raw data was reduced with the X-Shooter Esorex pipeline[1] to create an in-transit spectrum and an out-of-transit spectrum for each night. The transit absorption fraction at each wavelength was calculated by dividing the in-transit spectrum by the out-of-transit spectrum. This was done separately for each night to account for factors like airmass and turbulence which cause the absolute brightness to vary between observations.

The area around the He I line (±200 Å) was then simultaneously fitted with a 4^{th} order polynomial to represent the continuum and a Gaussian to model the excess absorption depth at He I line (see Fig. 5.2). The 4^{th} order polynomial was chosen for the continuum as it was found to be the best fit among a series of polynomials with orders 0-20. This was based on the Akaike and Bayesian information criteria (AIC and BIC), which estimate the relative quality of different models compared to the data, as shown in Equation 5.1.

$$\begin{aligned} AIC &= 2k - 2ln(\hat{L}) \\ BIC &= kln(n) - 2ln(\hat{L}) \end{aligned} \tag{5.1}$$

Here $\hat{L}$ is the maximised likelihood value of the model given the data, k is the number of parameters, in our case the order of the polynomial, and n is the number of data points. The likelihood function is a function for the goodness of fit of a model to the data by calculating the probability that randomly drawing from the model results in the observed data points. The maximum likelihood represents the combination of parameters that result in the best fit for a certain model. Both the AIC and the BIC include a maximum likelihood term to evaluate the goodness of the best fit of each model ($2ln(\hat{L})$) and a penalty term that increases with the number of parameters in the model to prevent overfitting ($2k$ and $kln(n)$ respectively). Since the penalty for overfitting of the BIC includes the number of data points, it is stronger than that of the AIC. The result is a larger likelihood of underfitting when using the BIC and a larger likelihood of overfitting when using the AIC. The model that minimises both information criteria is therefore the most appropriate model for the dataset. The Gaussian representing the excess absorption in the line has a fixed full-width-half-maximium (FWHM) corresponding to the resolution of the spectrograph at the location of the helium line, which is 4.2 Å.

[1] `https://www.eso.org/sci/software/pipelines/xshooter/`

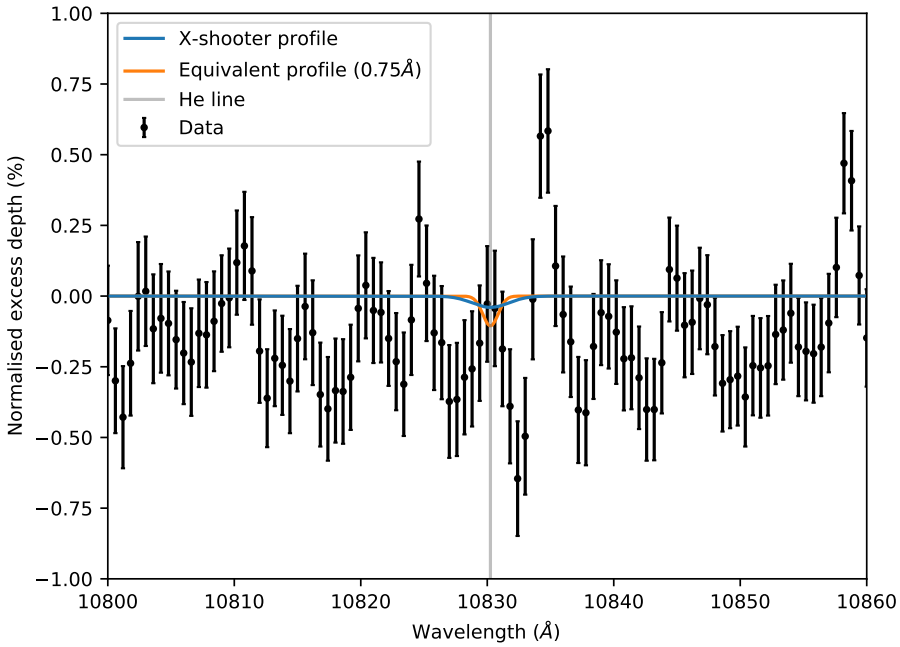

Figure 5.2: Second night transmission spectrum of GJ 1214 b after subtraction of the continuum, centered around the He I 10,830 Å line. The Gaussian profile fitted to the excess absorption is shown in blue and the equivalent profile with the intrinsic line width of 0.75 Å is shown in orange. It is clear that the scatter in the data dominates the photon noise in the individual data points.

5.3 Results and Discussion

The best fitting helium lines have equivalent widths of 29 ± 3 mÅ (statistical) ± 24 mÅ (systematic) and 4 ± 4 mÅ ±11 mÅ for the first and second nights respectively. The statistical error has been calculated according to equation 6' in Cayrel (1988):

$$< \delta W^2 >^{1/2} = 1.5 \cdot \sqrt{FWHM \cdot \delta\lambda} \cdot \epsilon \tag{5.2}$$

Here $< \delta W^2 >^{1/2}$ is the statistical error of the calculated equivalent width. $FWHM$ is the full-width-half-maximum of the line, which is determined by the instrument and for our set-up is equal to 4 Å at the wavelength of the He I line. $\delta\lambda$ is the wavelength resolution of the detector, 0.06 Å, and ϵ is the photometric accuracy of the reduced spectrum, which is determined by the photon noise. The systematic error is the standard deviation of the depth across 40 evenly-spaced locations in the analysed subsection of the spectrum and is the dominant noise source in our result.

We assume an intrinsic width of the He I line of 0.75 Å, following Crossfield et al. (2019). There is some uncertainty in this value, considering Spake et al. (2018) find that the line-width should not exceed 0.4 Å for K-dwarf stars, according to both theoretical and observational constraints. This is corroborated by later measurements of F-K stars, which find intrinsic line widths

of 0.3-0.4 Å (Nortmann et al., 2018; Alonso-Floriano et al., 2019; Guilluy et al., 2020; Gaidos et al., 2020). However, Allart et al. (2019) state that the typical width of the helium feature is about 1 Å and both Allart et al. (2019) and dos Santos et al. (2020) use a bandwidth of 0.75 Å to measure the helium absorption of planets transiting a K and a G star respectively. Additionally, Palle et al. (2020) find that thermal and turbulent line broadening alone would already cause a line width of roughly 0.6 Å in the M-dwarf GJ 436, with their actual measurement being 1 Å due to the presence of winds. GJ 1214 is also an M-dwarf and thus likely to have a broader intrinsic absorption line width. A value of 0.75 Å is a medium between the intrinsic widths from Spake et al. (2018) and Allart et al. (2019) and allows us to follow Crossfield et al. (2019) more closely. This then corresponds to an excess depth of 0.38%±0.44%.

The atmospheric scale height of helium is then given by:

$$H_{He} = \sqrt{\frac{D + E_{He}}{D}} \tag{5.3}$$

where H_{He} is the scale height of the helium atmosphere in units of planetary radii, D the average depth of the transit across the spectrum and E_{He} the excess depth in the He I line. Since this includes the planet, the subtraction of one planet radius needs to be applied to find the extent of the helium beyond the rest of the planets atmosphere. The resulting extended scale height after the data of the two nights is combined is $0.14\pm0.15\,R_p$ (68% confidence interval, or 1σ error). The upper limit of the 95% confidence interval (2σ error range) is then $< 0.43\,R_p$ equivalent absorbing atmosphere.

This non-detection is consistent with the Crossfield et al. (2019) result of $1.0\pm0.6 R_p$ and constrains the extended helium atmosphere better than their upper limit of $< 2.1 R_p$. The accuracy is improved by more than a factor of four, which is expected when taking into account the differences in the observing set-ups and integration times.

5.4 Conclusions

We have found and reduced archival X-Shooter data of three transits of the super-Earth GJ 1214 b. While one night had to be discarded due to weather conditions, the other two were suitable for transmission spectroscopy. We compared the in-transit and out-of-transit spectra of each night and fitted and removed large-scale continuum variations to find the excess depth in the 10,830 Å He I absorption line. We found an extended scale height for the helium atmosphere of $0.14\pm0.15\,R_p$, with an upper limit to the 95% confidence interval of $< 0.43\,R_p$ equivalent absorbing atmosphere. This is an improvement over previous limits by a factor of four, consistent with the differences in the observations.

Of the seven that have so far been discovered to have helium, three are gas giants and four are Earth to Neptune size range. These limits show that all three gas giants and one of the super Neptunes have signals that would be detectable with X-SHOOTER (WASP-69 b, HAT-P-11 b, HD 209458 b and HD 189733 b; Nortmann et al., 2018; Allart et al., 2018; Alonso-Floriano et al., 2019; Guilluy et al., 2020). The excess absorption ranges from more than 3% to slightly under 1%, but even the smallest signal of 0.91 % excess absorption in HD 209458 b would result

in a significant detection. X-SHOOTER is therefore a suitable instrument to detect extended helium atmospheres in close-in gas giants. Additionally, observations of GJ 1214 b and other similar sized planets could be obtained with instruments such as CRIRES+, FORS2 and KMOS, which also cover the He I wavelengths and have similar or better spectral resolving power.

Acknowledgements

We would like to thank Carlo Manara and Sabine Möhler for their help in reducing the X-Shooter data and Ian Crossfield for his help with the analysis.

Chapter 6

Atmospheric characterisation of the hot Jupiter WASP-15 b with Gaussian Processes

D. J. M. Petit dit de la Roche, M. E. van den Ancker, P. A. Miles-Páez, H. Boffin
To be submitted to A&A

Abstract: Transmission spectroscopy offers valuable insight into the composition of exoplanet atmospheres. The FORS2 instrument has been very successful at such observations, but between 2010 and 2014 instrumentally induced correlated noise in the data made analysis difficult. We use Gaussian Process modeling to remove the correlated noise from 2012 data of the transit of hot Jupiter WASP-15 b and obtain transit parameters and the first transmission spectrum of this planets atmosphere. We find a white light radius of $1.299 \pm 0.085\,R_{Jup}$ (8000-10400 Å), consistent with previous observations in this wavelength range. We also find a more accurate ephemeris for the planets orbit. We obtain a 100 Å resolution transmission spectrum, with errors within a factor of two of the photon noise, but the scatter around 9100 Å means the data are consistent with cloudy, hazy and clear atmospheres and further observations are required to distinguish between different atmospheric models.

6.1 Introduction

Transiting planets offer a unique opportunity to constrain the composition and structure of atmospheres of exoplanets through transmission spectroscopy. Depending on the atomic and molecular species present in an exoplanet atmosphere, the apparent radius of the planet changes with wavelength, as the gas is transparent in some wavelengths and opaque in others. This has lead to the first detection of an exoplanet atmosphere by Charbonneau et al. (2002) through an increase in transit depth in the sodium line and the detection of many atmospheres and species since (e.g. Vidal-Madjar et al., 2003; Lecavelier des Etangs et al., 2008; Spake et al., 2018; Nikolov et al., 2018; Keles et al., 2019; Hoeijmakers et al., 2020).

Chemical species from exoplanet atmospheres can give us many insights into the make-up and thermal structure of the planets, which in turn can tell us about their formation history and evolution. Determining the C/O ratio can show how and where in the disk the planet was formed and what its migration history is (Madhusudhan, 2019). The detection of large extended envelopes of hydrogen and helium gas indicates the evaporation of the atmosphere from stellar irradiation, an important phase in the evolution of small close-in planets (Owen, 2019). Other identifiable phenomena include the identification of winds through spectral line broadening and the presence or absence of clouds and hazes, which are important in determining the atmospheric chemistry (e.g. Brogi et al., 2016; Spake et al., 2018; Hoeijmakers et al., 2020).

Since the size of the absorption feature of a given atom or molecule in the transmission spectrum depends on the relative size of the planet compared to the star and the scale height of the atmosphere, low-mass, high-radius planets on close orbits, such as hot Jupiters, are particularly favorable targets for transmission spectroscopy. In such systems, the high stellar irradiation causes the atmosphere to expand, increasing the predicted feature size. Hot Jupiters are also highly unlikely to have formed in-situ, making identifying their formation locations and migration history import factors of their evolution (D'Angelo and Lissauer, 2018).

The FOcal Reducer and low dispersion Spectrograph 2 (FORS2; Appenzeller et al., 1998) has been shown to be an excellent instrument for such observations and can be used even for small exoplanets, such as Super-Earths and Sub-Neptunes as demonstrated by Bean et al. (2010) in their observations of the Super-Earth GJ 1214 b. However, due to degradation of the surface coating of the linear atmospheric dispersion corrector (LADC), unexpectedly high systematics are present in light curve data from about 2011 until November 2014, causing further attempts at transit studies in this period to fail (Boffin et al., 2015). The degradation caused surface features across the field of view that affected the throughput and sensitivity. The LADC rotates relative to the sky, causing stars to drift across the surface features during the night and introducing systematics that are unique to the different targets, depending on their location in the field of view and the corresponding path across the LADC surface (Moehler et al., 2010; Berta et al., 2011). The systematics could therefore not be removed by using comparison stars. The issue was solved in 2014 by replacing the LADC prisms with their counterparts from the decomissioned FORS1 instrument (Boffin et al., 2015). The coating had been removed from the FORS1 parts before their installation into FORS2, almost entirely eliminating the systematics. This was demonstrated by Sedaghati et al. (2015), who used FORS2 to create a transmission spectrum of the gas giant WASP-19 b. However, there are several data sets of exoplanet transits in the ESO Science Archive that were taken when the peeling LADC coating was still in place that have not yet been analysed in detail.

Gaussian Processes (GPs) are used commonly in machine learning applications for classification and regression (e.g. Kapoor et al., 2010; Kim and Lee, 2007). They have also been used in various areas of astronomy, including for tasks such as photometric redshift prediction (Way and Srivastava, 2006) and transient classification (Mahabal et al., 2008). In particular, Gaussian Process regression has been used to model correlated noise systematics in data, including in FORS2 transmission spectroscopy data taken after the replacement of the LADC prism (e.g. Gibson, 2014; Gibson et al., 2017). In this work we demonstrate the use of GP modelling to remove the systematics in an archival data set of WASP-15 b, taken in 2011. This planet is a hot

Parameter	Value	Reference
Spectral type	F7	West et al. (2009)
Mass [$M_\odot$]	1.305 ± 0.051	Southworth et al. (2013)
Radius [$R_\odot$]	1.522 ± 0.044	Southworth et al. (2013)
Luminosity [$L_\odot$]	3.09 ± 0.34	West et al. (2009)
Age [Gyr]	2.4 ± 0.6	Southworth et al. (2013)
Teff [K]	6300 ± 100	West et al. (2009)
Metallicity [Fe/H]	-0.17 ± 0.11	West et al. (2009)

Table 6.1: Stellar parameters of WASP-15.

Jupiter at a distance of 286.6±1.5 pc (West et al., 2009; Gaia Collaboration et al., 2020b) and its large radius (1.4 R_{Jup}) and low mass (0.5 M_{Jup}) make it an excellent candidate for atmospheric characterisation.

The data and the basic reduction are presented in section 6.2, as well as background on GPs. The the modelling and results of both the white light curve and the transmission spectrum are shown and discussed in section 6.3, along with possible transit timing variations. Section 6.4 contains the conclusions.

6.2 Observations and data analysis

Archival observations of the WASP-15 b system taken with the FOcal Reducer and low dispersion Spectrograph 2 (FORS2; Appenzeller et al., 1998) were retrieved from the ESO archive[1].

The data were taken in the spectroscopic mask (MXU) mode, in which a custom mask is inserted into focal plane of the instrument, allowing for the simultaneous observation of the science target WASP-15 and several reference stars, in this case six. The slit width was 12″, which minimises slit losses of flux, but results in a lower spectral resolution than the use of narrower slits. The grism 600z was used in combination with the order separation filter OG590. This setup has a maximum wavelength range of 737-1070 nm, but the positions of the stars on the detector can cause part of the spectrum to fall off the chip. Our effective wavelength range was therefore reduced to 796-1042 nm. The observations consist of a total of 428 spectra with integration times of 16 s each, taken between 23:00 and 6:00 on the night of 24 April 2011. 180 of the spectra are baseline out-of-transit observations. Further systematics were introduced into the data by increased airmass and bad seeing conditions at the beginning and end of the observing sequence.

The data are first reduced using the publicly available Esoreflex 2.11.0 pipeline for FORS[2], version 5.5.6 (Izzo et al., 2010). The pipeline applies bias subtraction, flat-fielding and wavelength calibration. A sky model is made local to each slit and subtracted. The flux can be calibrated using reference observations of a spectro-photometric standard star, but this option was

[1] `http://archive.eso.org`

[2] `https://www.eso.org/sci/software/pipelines/fors/fors-pipe-recipes.html`

Table 6.2: Overview of the observations of WASP-15

Observing conditions	
Right Ascension	13:55:42.71
Declination	-32:09:34.62
Observation start	22:58 24-05-2011
Observation end	05:48 25-05-2011
Airmass	1.01-1.45
Seeing	0.77″-3.05″
Number of exposures	428
Exposure time	16s

not applied, as it did not improve the light curve and reduced the available wavelength range. For the extraction of the spectrum a larger window with an extraction radius of 20 pixels (compared to the default 12) was selected due to the brightness of WASP-15. This value was obtained by varying the extraction radius in a range of 15 to 40 pixels, at 5 pixel intervals. A radius of 20 pixels resulted in the least noise in the white light curve and in the wavelength binned light curves.

After the pipeline reduction the most suitable reference stars were selected. The spectra of WASP-15 and the three best references are clipped to wavelengths for which data is available in all four stars and outliers due to missed cosmic rays or hot pixels are replaced by the median value of the star at that wavelength across the observation period, scaled to the rest of the spectrum. A reference telluric spectrum was created from the reference stars for each observation and divided out to remove the impact of absorption by the Earth's atmosphere. Light curves were created for each star by summing over the wavelength range and the curves of the reference stars are then combined to make a model of the seeing-induced variations in the light curve. Figure 6.1 shows the light curve after this noise has been removed and the flux has been normalised, along with a model transit based on the best-fit planet parameters from West et al. (2009). The shape of a transit is visible, particularly the egress at Julian Date (JD) 2455706.64, but there are clear systematics of nearly the same amplitude as the transit depth. Even after removing the seeing-induced variations obtained from the reference stars, there is still scatter in the data points at the beginning and end of the observation period. In the middle of the transit the seeing was good and as a result the scatter in the data is very small and we see instead the smooth correlated noise from the variable transmission caused by the non-homogeneous coating of the LADC.

In order to obtain the transit parameters and transmission spectrum, a model of the systematic noise is required. Gaussian process (GP) regression is used to obtain this model, as it is a non-parameteric way of modelling systematic, correlated noise (Gibson et al., 2012; Gibson, 2014). A Gaussian process is a collection of random variables, where any combination of those variables has a multivariate normal distribution, making it a distribution of possible functions containing those variables (Mackay, 2003). This means that rather than assuming a deterministic noise model based on instrument parameters, GPs allow us to marginalise over a distribution of possible noise models to find the most appropriate. The data can be seen as a realisation of

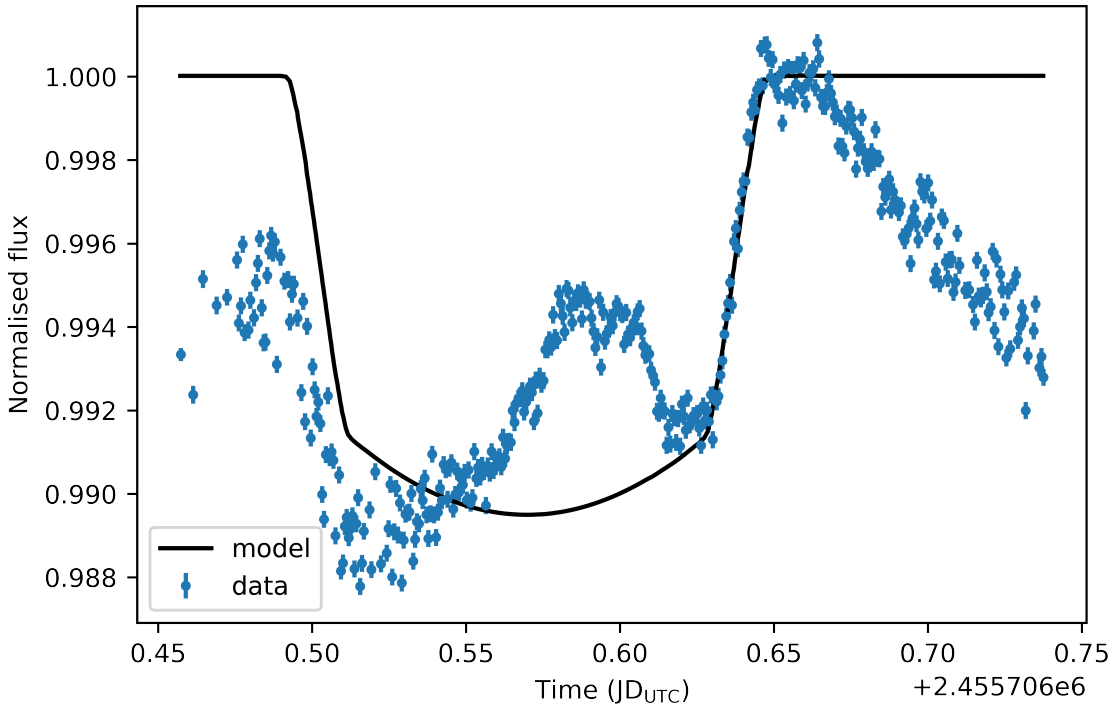

Figure 6.1: Light curve of WASP-15 after correction for seeing. A model of the transit based on parameters from West et al. (2009) is plotted in black over the data (blue). The general shape of the transit is visible in the data, but there are clearly very large systematics that make interpretation of the light curve in this form impossible. The large scatter in the data at the beginning and end of the observations are due to the poorer seeing at these times.

a distribution of possible models which has a mean function and a covariance function. In our case, the mean function is the expected planet transit and the covariance function is the correlated noise from the LADC. Marginalising over the systematics models then allows us to extract the underlying mean function in the data.

The model can be described as follows:

$$y(\vec{t}) \sim \mathcal{GP}\left(T(\vec{t},\vec{\phi}),\vec{\Sigma}(\vec{t},\vec{\theta})\right), \tag{6.1}$$

where $y(\vec{t})$ is the model of the observed light curve ($\vec{y}$) as a function of the time at which the observations are done, $\mathcal{GP}$ indicates the GP with a mean and a covariance function. The mean function, $T(\vec{t},\vec{\phi})$, is the transit model which has the time t as it's input and parameters ϕ, such as the transit depth and the period. $\vec{\Sigma}(\vec{t},\vec{\theta})$ is the covariance function with parameters θ. Both ϕ and θ are referred to as hyperparameters of the GP.

The covariance function is also called a kernel and expresses the correlation between different data points depending on their separations. The hyperparameters of the kernel are typically the maximum amplitude of the noise and the length scale of the correlation, which we write as σ and ρ respectively, so that $\vec{\theta} = \{\sigma,\rho\}$. We used an approximate Matérn-3/2 kernel (Rasmussen and

Williams, 2006; Stein, 1999), the elements of which we show in Equation 6.2. This kernel is less smooth than other, simpler kernles, making it a better representation of physical processes. The elements k_{mn} of the matrix Σ that describes the kernel are dependant on the distance between t_m and t_n.

$$k_{mn}(t_m, t_n) = \sigma^2 \left(1 + \frac{\sqrt{3}(t_m - t_n)}{\rho}\right) exp\left(-\frac{\sqrt{3}(t_m - t_n)}{\rho}\right) \tag{6.2}$$

Since we are using GPs, the joint probability of the observations is by definition a multivariate Gaussian distribution with the same mean and covariance functions as Equation 6.1. The log marginal likelihood is then expressed as a function of the residual vector and the kernel.

$$\ln p(y|\vec{t}, \vec{\theta}, \vec{\phi}) = -\frac{1}{2}\left(N\ln 2\pi + \ln|\vec{\Sigma}| + \vec{r}^T\vec{\Sigma}^{-1}\vec{r}\right) \tag{6.3}$$

Where the residual vector, $\vec{r}$, is the difference between the data, y, and the mean function, $T(\vec{t}, \vec{\phi})$. Posterior probabilities can be computed after the addition of prior distributions for the hyperparameters, from which posterior distributions for each hyperparameter can be found by marginalising over the other hyperparameters.

The Juliet python package (Espinoza et al., 2019) combines previously developed packages to do simultaneous transit and GP fitting (Foreman-Mackey et al., 2017; Kreidberg, 2015; Speagle, 2020). It adds a couple of terms to the basic GP described in the previous section. The mean function is not just a transit function, but includes a photometric dilution factor in case the light curve is diluted by flux from nearby stars and an offset for the out-of-transit flux, resulting in Equation 6.4.

$$\mathcal{M}(\vec{t}) = \frac{T(\vec{t}, \vec{\phi})D + 1 - D}{1 + DM} \tag{6.4}$$

Here $\mathcal{M}(\vec{t})$ is the mean function used in the GP, $T(\vec{t}, \vec{\phi})$ is still the transit model, D is the photometric dilution factor, and M is an offset in the out-of-transit light curve. Additionally, the white noise term in the kernel is actually split into two parts, one for the formal uncertainty in the data point, and one for jitter in the instrument, so that the covariance is given by Equation 6.5.

$$\vec{\Sigma}_{mn} = k(t_m, t_n) + \delta_{mn}(\sigma_{y_m}^2 + \sigma_w^2) \tag{6.5}$$

Here δ_{mn} is the Kronecker delta, σ_{y_m} is the uncertainty in data point y_m, and σ_w is jitter in the instrument. This means there is an additional hyperparameter in the noise model and we get $\vec{\theta} = \{\rho, \sigma, \sigma_w\}$.

Juliet allows the user to confine the fitting of the limb-darkening parameters to the physically plausible values (those resulting in only positive intensities and decreasing gradients towards the limb of the star) by using a parametrisation from Kipping (2013). Both parameters, referred to

as q_1 and q_2, are defined as being between 0 and 1 and for the quadratic law, which we use in this work, are given by Equation 6.6, where u_1 and u_2 are the limb darkening parameters.

$$\begin{aligned} q_1 &= (u_1 + u_2)^2 \\ q_2 &= \frac{u_1}{2(u_1 + u_2)} \end{aligned} \tag{6.6}$$

6.3 Results and discussion

6.3.1 White light curve

We simultaneously fit the transit model and the noise model to the white light curve. For the transit model, the free parameters are the transit midpoint, T_0, the size of the planet relative to the star as a measure of transit depth, $p = \frac{R_p}{R_*}$, and the semi-major axis, a. Since we only have one transit the orbital parameters (period, eccentricity and argument of periastron) are fixed to the literature values from West et al. (2009) and Southworth et al. (2013), which have the strongest constraints on the system architecture thanks to their inclusion of radial velocity data. The same is done for the impact factor b and inclination i, as they are degenerate with the GP noise and do not converge in the fit. We fix strict priors on the free parameters based on the same literature. Since the limb darkening parameters are also very degenerate with the GP noise and do not converge during the fit, they are fixed to theoretical values calculated with the Python Limb Darkening Toolkit (Parviainen and Aigrain, 2015) based on the PHOENIX stellar spectrum models (Husser et al., 2013). We fix the dilution parameter to 1 (no dilution), because we do not expect any other sources to be in the slit with WASP-15, but leave the out-of-transit offset free. the jitter and the GP hyperparameters are left free with wide priors.

We perform two short "burn-in" runs to narrow down the parameter space and improve the priors for the final fit. The resulting values for all the free parameters in the white light fit are presented the rightmost column of Table 6.3, with the final radius ratio corresponding to a planet radius of $1.299 \pm 0.085\, R_{Jup}$. The resulting transit midpoint and transit depth are consistent within 2σ with previous observations in the optical, the near infrared and the mid infrared.

6.3.2 Transit timing

We also combine our transit midpoint measurement from the white light curve with previous literature, and amateur observations to obtain a new, more precise linear ephemeris for the transit midpoint:

$$T_0(BJD_{TDB}) = 3.7520982(6) \cdot N + 2454584.6985(3). \tag{6.7}$$

Here T_0 is given as the Barycentric Julian Date (BJD) in the Barycentric Dynamical Time (TDB) standard. This is done for consistency with previous measurements and to correct for leap seconds, clock offsets and the influence of the motion of the Earth around the sun on the measured time (Eastman et al., 2010). N is the number of orbits since the reference epoch,

Parameter	Prior	Posterior value
Period (days)	3.752099	-
Transit midpoint (JD_{UTC})	$\mathcal{N}(2455706.5701, 0.008)$	2455706.5694±0.0004
Planet radius (R_p/R_*)	$\mathcal{N}(0.096, 0.078)$	0.0935±0.0039
Impact parameter	0.570	-
Semi-major axis (AU)	$\mathcal{N}(0.0499, 0.018)$	0.04902± 0.00027
Inclination (°)	85.5	-
Eccentricity	0	-
Argument of periastron (degrees)	90	-
q_1	0.218	-
q_2	0.360	-
Dilution	1	-
Flux offset	$\mathcal{N}(0, 0.1)$	-0.0019±0.0020
Instrument jitter	Lognormal(0.1,1000)	552±15
GP parameter σ	Lognormal(1e-6,1e6)	0.0053±0.0020
GP parameter ρ	Lognormal(1e-3,1e3)	0.074±0.022

Table 6.3: Priors for the different fit parameters used in the simultaneous transit and GP fitting. Orbital parameters are held fixed (Period, eccentricity, argument of periastron), while planet parameters are based on previous literature (transit midpoint, impact parameter, semi-major axis, inclination), with the exception of the radius. Noise and stellar parameters are left free, with only the dilution being fixed at 1, since we do not expect interference from other stars.

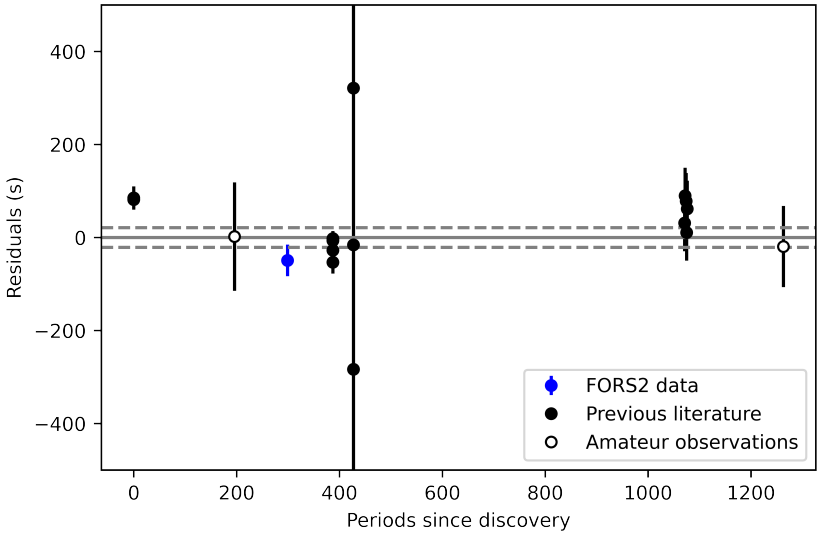

Figure 6.2: Residuals of observations compared to the ephemeris shown in Equation 6.7. The 1σ errorbars of the ephemeris are indicated by gray, dashed lines. Midpoint time values from previous literature are marked in filled circles, values from amateur observations from the ETD that included a full transit are marked in empty circles and the new value from the FORS2 observations is marked in blue.

which we have taken to be the midpoint of the original discovery transit by West et al. (2009). The numbers in brackets show the uncertainty in the preceding digits. For the amateur transit midpoints, the values were retrieved from the Exoplanet Transit Database (ETD; Poddaný et al., 2010) for observations that included a full transit. All transit midpoint values that were not already in the Barycentric Dynamical Time standard have been converted to it for consistency. The residuals of the observations from this ephemeris are shown in Figure 6.2.

The large uncertainties on the points in the points at 427 periods are because they are based on the timings of secondary transits in the mid-infrared by Kilpatrick et al. (2017). There is a significant tension between the original West et al. (2009) discovery data and the ephemeris and our data of 3.4σ. This increases to 4.5σ if the errorbars from the Triaud et al. (2010) analysis of the same data are used. Additionally, the points between 200 and 500 orbits are mostly below the line, while the points around 1000 orbits tend to be above it, which could be an indication of possible transit timing variations due to an unseen planet. The fit is marginally improved and the tension removed by adding a sinusoidal signal with an amplitude of 55 s and a period of 534 days, but due to the addition of extra parameters in the fit this difference is not significant and rather is overfitting the data. Further observations are required to determine whether such a variation is indeed present.

We use our new period for the rest of the analysis, although since we only have one transit the change in the assumed period is not expected to significantly affect the results.

6.3.3 Transmission spectrum

To construct a transmission spectrum, the data was divided into wavelength bins. The size of the bins was determined by analysing the noise at different wavelengths as a function of bin size. The smallest bin with the lowest noise depends on wavelength. At short wavelengths there is more flux, so smaller bin sizes of ∼50 Å are possible. However, at larger wavelengths where there is significantly less flux, the increase in noise means that the optimal bin size becomes 100 Å. For consistency we divide the data in equal sized bins of 100 Å.

A light curve is constructed for each bin and detrended with the white light noise model. Another fit of the transit model and GP is then applied, this time with the mid-transit time, impact parameter, semi-minor axis, and inclination values fixed to those of the white light curve, as these are not expected to change with wavelength. The limb-darkening parameters are wavelength dependant and recalculated for each bin. The only free transit parameter is the transit depth. The noise parameters now fit the wavelength dependent component of the noise. Due to the low signal at long wavelengths, the transmission spectrum is cut off at 10300 Å.

The corrected light curves are shown in Figure 6.3. The grey curve in the upper left is the white light curve. The light curves of the wavelength binned data are offset, but plotted at the same scale. Almost all of the correlated noise is removed from the light curves, although some residuals remain, especially in the redder curves. The varying gaps in the different curves are a result of the sigma clipping process to remove excess scatter from outliers.

The resulting spectrum is shown in Figure 6.4, with the radii from the binned data marked in blue and the radius based on the white light curve in cyan, offset to the side for clarity. The white light curve is 1σ separated from the Southworth et al. (2013) photometric value in a similar

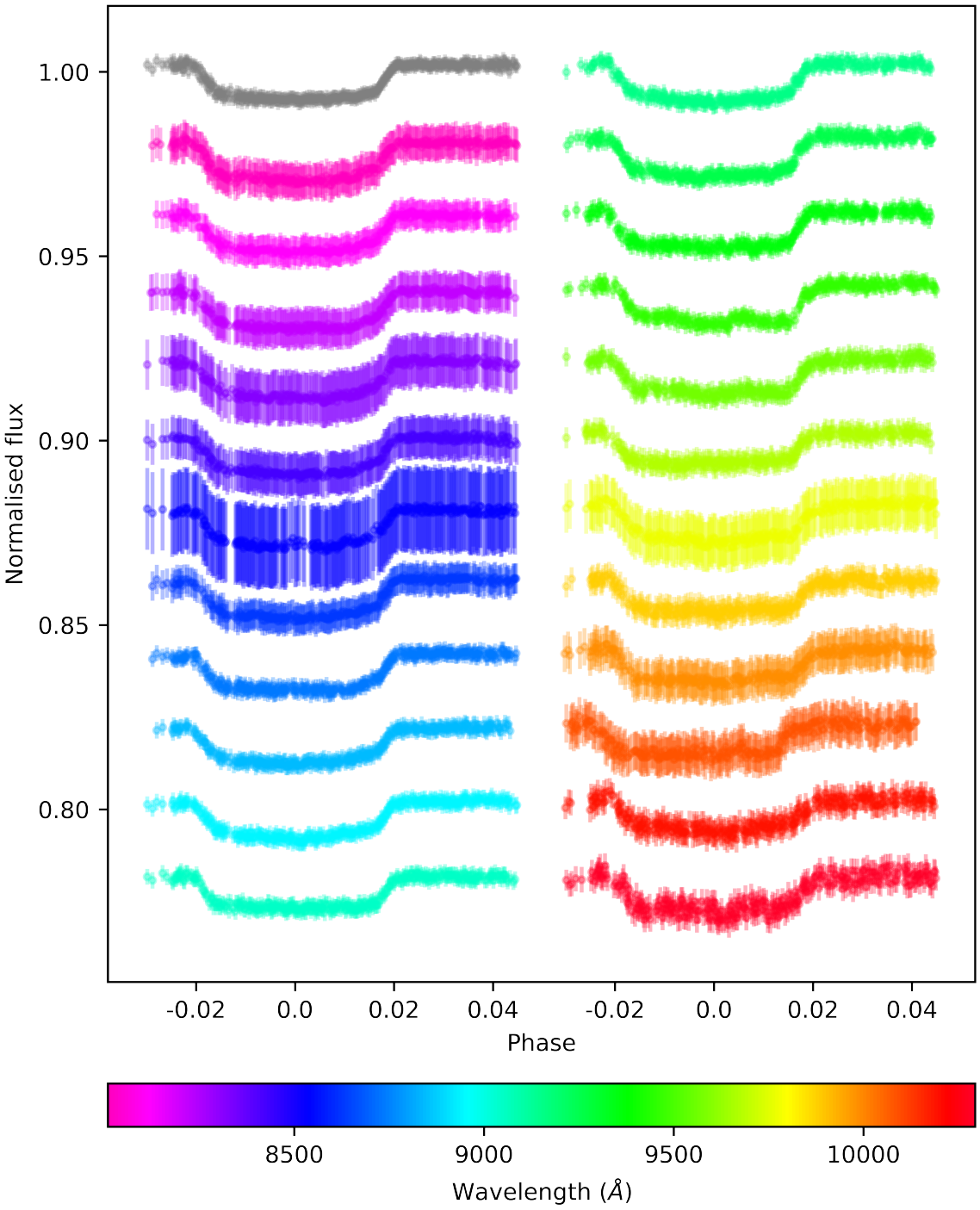

Figure 6.3: Light curves after removal of correlated noise. The white light curve is indicated in gray in the upper left of the figure. Curves for the different wavelength bins are offset by 0.02 from each other for clarity. The colour of the wavelength binned light curves indicates the central wavelength of the bin. Each bin has a width of 100 Å. Errors of varying degrees are introduced into the light curves by the subtraction of the GP models, depending on the goodness of the fit. Bins beyond 10300 Å are omitted due to lack of signal.

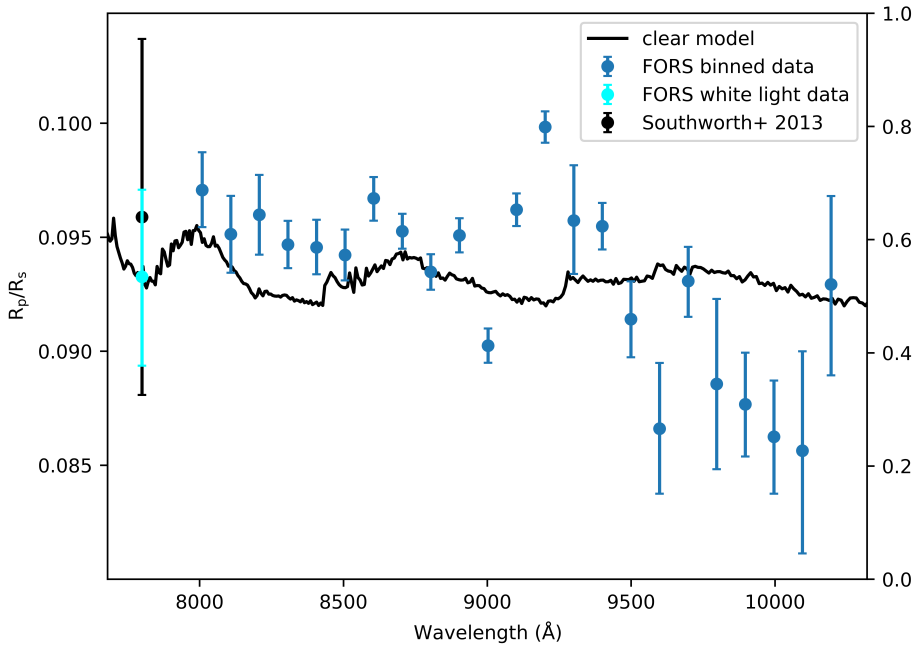

Figure 6.4: Transmission spectrum of WASP-15 b with a wavelength resolution of 100 Å. The planet radius measured in the white light curve is marked in cyan at 7400 Å to clearly separate it from the radii of the binned data, which are marked in blue. The black point is a photometric measurement by Southworth et al. (2013) that covers a similar wavelength range and is included for comparison at the same location as the white light radius. A clear, low-metallicity model at the expected temperature of WASP-15 b (black) is also included for comparison. With the exception of the points between 8900 Å and 9300 Å, most of the points are within 3σ of the model spectrum. Given that these points coincide with a major water absorption band, their errors may be underestimated.

wavelength range. The smaller errorbars around 9000 Å are caused by the noise at these wavelengths being closest to that of the white light curve due to their position in the middle of the spectrum. The larger errorbars in the reddest part of the spectrum are a consequence of the low signal and the corresponding increased noise at these wavelengths. The data are consistent with a featureless spectrum. Closer investigation of the areas around possible sodium (~ 8200 Å), potassium (~ 8250 Å) and calcium (~ 8500 Å) features in the blue part of the spectrum with smaller wavelength bins of 40 Å show no indications of increased absorption.

The errors on the transit depth are consistent with the residuals after fitting and with the photon noise of the light curves in the middle range of the spectrum (8200-9500 Å), with values of 600-1200 parts per million (ppm) depending on the wavelength. The photon noise of the light curves is itself determined by the reference stars, which are fainter than WASP-15. While the photon noise at long wavelength increases significantly, it does not entirely explain the larger errorbars beyond 9500 Å indicating that even after correction, residuals from the correlated noise are still a limiting factor at the extreme ends of the spectrum, although the effect is much more pronounced at long wavelengths. However, the scatter in the radii is larger than expected from the individual errorbars and occurs particularly between 8700 and 9700 Å. This coincides with

two major telluric water absorption bands, and is possibly a consequence of the bad seeing during the observations. However, a smaller absorption band at 8200 Å does not seem to have had such an effect. The points in this are are also sensitive to changes in the choice of continuum when removing the telluric contribution from the stellar spectra.

6.3.4 Atmospheric models

To interpret the spectrum we compare it to a generic grid of forward model transmission spectra computed by Goyal et al. (2019). This grid is based on the ATMO 1D-2D radiative-convective equilibrium model for planetary atmospheres (Amundsen et al., 2014; Tremblin et al., 2015, 2016b, 2017; Drummond et al., 2016; Goyal et al., 2018) and is computed for two treatments of condensation over a range of 22 planetary equilibrium temperatures (400K-2600K), four planetary surface gravities (5-50 m/s^2), five atmospheric metallicities (1-200x solar), four carbon-to-oxygen ratios (0.35-1), four scattering haze parameters (1-1100x Rayleigh scattering), and four uniform cloud parameters (0-1). Since we can calculate the surface gravity from the fit and the literature as 6.5 m/s^2, we take the grid with the smallest value and rescale it to the exact value using the relation given in Goyal et al. (2019). We then further scale the spectra to have the same mean amplitude as the data. Due to our use of GP noise models we can not rely on the absolute value of the model, but rather compare the relative size of the features.

In general, flat spectra are considered to indicate cloudy/hazy atmospheres, but the observed transmission spectrum has a standard deviation around the mean of 0.005, larger than any of the models (<0.002), so no such constraints can be determined. For comparison, a model spectrum of a planet with a temperature of 1500K, based on *Spitzer* measurements by Kilpatrick et al. (2017), low metallicity and a clear atmosphere, so with larger features, has been included in Figure 6.4. The variation in the data is clearly significantly larger than that in the model.

The scatter in the data, not the errorbars on the individual points are prohibiting the interpretation of the results, so observations that are more stable around 9000 Å are required in the future to constrain the atmosphere of WASP-15 b. Identifying the presence or absence of major features such as those of Na and K should be possible with the current FORS2 instrument in better seeing conditions. Lendl et al. (2016) for example use a similar precision of 600-800 ppm in the same wavelength range to determine the presence of a cloud deck on WASP-49 b, a hot Saturn with a similar transit depth and host star brightness as WASP-15 b. For targets with fainter host stars or available references or with smaller transit depths, the observation of additional transits will likely be required.

6.4 Conclusion

We have obtained archival data of the hot Jupiter WASP-15 b that was observed with the FORS2 instrument at 7400-11000 Å. We have reduced the data and have used GP modelling to remove wavelength dependant correlated noise from the peeling LADC coating. In the middle of the spectral range the noise was reduced to 600-1200 ppm, on the order of the photon noise, which is dominated by the faintness of the reference stars. Some residuals of correlated noise remained at

the extreme ends of the spectrum, particularly the red end. Since the reference stars are the limiting factor in our noise, any observations where the target and the references as bright or brighter than our faintest reference (1.4 magnitudes fainter than WASP-15 in the measured wavelength range) can be expected to result in similar precision in the middle range of the spectrum, although the fact that there are less residuals from the correlated noise at the blue end indicates that a better signal results in a better removal of correlated noise, favouring bright targets and short wavelength observations for GP modelling.

We were able to obtain a white light transit curve and model the noise and transit parameters. The midpoint and transit depth are consistent within 1σ with previous literature and we calculate a new, more precise ephemeris for the planets orbit. Tension between this ephemeris and the discovery data is significant, but could not be explained through the presence of possible other companions in the system. We further obtain the first transmission spectrum of WASP-15 b by dividing the data into wavelength bins, de-trending them with the white light noise and fitting transit and GP models. The resulting transmission spectrum has significant scatter around 8900-9300 Å, which is likely the result of underestimation of the errors due to telluric water absorption. It has no other significant features of more than 3σ and is consistent with hazy, cloudy and clear models, as the model variation is smaller than that in the data.

Future observations with better seeing are required to constrain the atmosphere of WASP-15 b and distinguish between hazy, cloudy and clear atmospheres, preferably at shorter wavelengths without major telluric absorption bands. The current analysis can also be extended to other unpublished archival data sets from this period, such as 2012 data of WASP-31, another bright star with a hot Jupiter around it. This data covers a larger wavelength range where telluric water absorption should be less of a problem and includes wavelengths where no other high resolution spectra are available.

Chapter 7

Conclusions

In the first part of this thesis we examined the potential of mid-infrared direct imaging of wide separation planets. These targets are important to understand planet formation mechanisms and the mid-infrared offers a number of advantages compared to the commonly used near infrared, but so far no planets have been detected at this wavelength.

In Chapter 2 we used the J8.9 filter in the imaging mode of VISIR to obtain the first mid-infrared direct imaging observations the HR 8799 planetary system at 8.9 μm. We achieved background limited 5σ upper flux limits of 0.7 mJy for any further companions between 40 and 330 AU, corresponding to a mass limit of 30 M_{Jup} for a given age of 60 Myr. These constitute the most stringent limits at the furthest distances so far for this system. While this was not sufficient to observe the known companions, these sensitivities showed that it would be possible to image at least four other planets within 50 pc in 10 hours or less with VISIR, and predicted that at least another eleven planets could be observed in the same time with the upgraded version of VISIR, NEAR.

In Chapter 3, we used data of four nearby systems taken at 11.25 μm with the upgraded NEAR instrument, which has the addition of a coronagraph and adaptive optics. Both the ε Indi A and ε Eri systems have a gas giant that was expected to be observable with NEAR. While detecting these planets was ultimately unsuccessful, 5σ upper limits very close to the planet masses were found for companions in both systems. The limit obtained for ε Eri was 2-4 M_{Jup} beyond 1″ for an age range of 0.4-1 Gyr, compared to a planet mass of around 0.8 M_{Jup}. For the somewhat older (0.7-4 Gyr) ε Indi we achieved the most sensitive mass limits to date at 3.3-10 M_{Jup} beyond 1″. Considering the fact that the mass of the known companion is 3.25 M_{Jup}, the non-detection confirmed an age at the older side of the range for this system, as a younger planet would have been observable. The τ Ceti system has a number of known Earth-sized planets, but no confirmed gas giants and the Sirius system has no known planets. In both cases the most sensitive mass limits to date were achieved at small separations, 15-30 M_{Jup} at $1 - 2''$ for an age of 3-10 Gyr for τ Ceti and 0.5-4.5 M_{Jup} at 0.5-1.5″ for an age range of 200-300 Myr for Sirius A. For companions to Sirius B we achieved limits of 1.5-3.6 M_{Jup} at the same age as Sirius A, depending on the amount of data available on different sides of the star and comparable to previous observations. Except for the extremely bright Sirius A, all observations were close to background limited.

In Chapter 4, we looked at six young stellar objects that still have circumstellar disks around them. We used a combination of VISIR J8.9 data and NEAR data in four other filters for HD 100546 and NEAR data taken in the PAH1 and NEAR filters for the other targets. We were able to resolve three of the disks and measure their projected position angle and inclination and their size. For the other three targets we calculated upper limits to their sizes, improving constraints on the mid-IR emitting regions of both HD 163296 and HD 36112 by a factor of 3 and 10 respectively. All measurements were consistent with the DIANA ProDiMo disk models, with the mid-IR emission originating from the central, highly irradiated unresolved inner disks and in some cases from the inner rims of the outer disks. We were able to improve the global SED fit of the DIANA ProDiMo model of HD 100546 by expanding the inner edge of the outer disk from 19.3 to 22.3 AU. Additionally, after modelling a planet with a circumplanetary disk, we obtained upper limits of 0.5-30 mJy for the 8-12 μm flux of possible companions beyond 1″ in the different disks, which allowed us to rule out planetary mass companions with luminosities of $> 0.0028\ L_{\odot}$ beyond 180 AU around HD 100546 and with luminosities of $10^{-2}\ L_{\odot}$ at large separations around HD 163296, HD 169142, TW Hydra and HD 36112. This meant we could exclude the presence of young planets in runaway accretion phases beyond 1″ in all but one of the systems, leading to an upper limit on the occurrence rate of wide orbit giant planets with CPDs of 6.2% with 68% confidence.

In all three chapters background limited imaging was achieved. Combined with mass limits of the order of a few Jupiter masses in the best cases, this shows the potential for direct imaging at mid-IR wavelengths. Even with the current version of NEAR, 11 planets that have been previously imaged in the near IR can be detected in less than 10 hours and the nearby giant planets around ε Indi A and ε Eri can be imaged in 50 and 70 hours respectively. Upcoming instruments with mid-IR imaging capabilities will be able to access far more planets. The ELT mid-infrared imager METIS will be more than ten times more sensitive than NEAR currently is (see Fig. 7.1; Brandl et al., 2018) and thanks to the ELTs 39 m diameter it will also have a five times better spatial resolution. This means that of the 102 planets detected through near IR direct imaging that have known temperatures, at least 80 will be detectable with METIS in less than two hours, including the HR 8799 planets. Both ε Indi A b and ε Eri b would be detectable in only a few minutes of observation time, which would allow for the direct measurement of both the masses and luminosities of these planets. The detection of Earth-like planets in the habitable zones of nearby stars, such as τ Ceti e and f, would be possible in only a few hours. MIRI on the JWST (Rieke et al., 2015; Glasse et al., 2015) is expected to be another 40 or so times more sensitive, further increasing the number of characterisable planets, although its smaller diameter means that the inner working angle will be larger and ground based instruments are likely to stay competitive in the inner few arcseconds.

In the second part we use transmission spectroscopy to examine the atmospheres of two close-in planets. Transmission spectroscopy has been used to identify the presence of various atoms and molecules in transiting planets and can be used to identify atmospheric processes like evaporation or the presence of winds.

In Chapter 5 we searched the ESO Archival Database for X-SHOOTER data of transiting planets and reduced two nights of observations of the super-Earth GJ 1214 b. We compared the in-transit and out-of-transit spectra of each night and measured the excess depth of the 10,830 Å

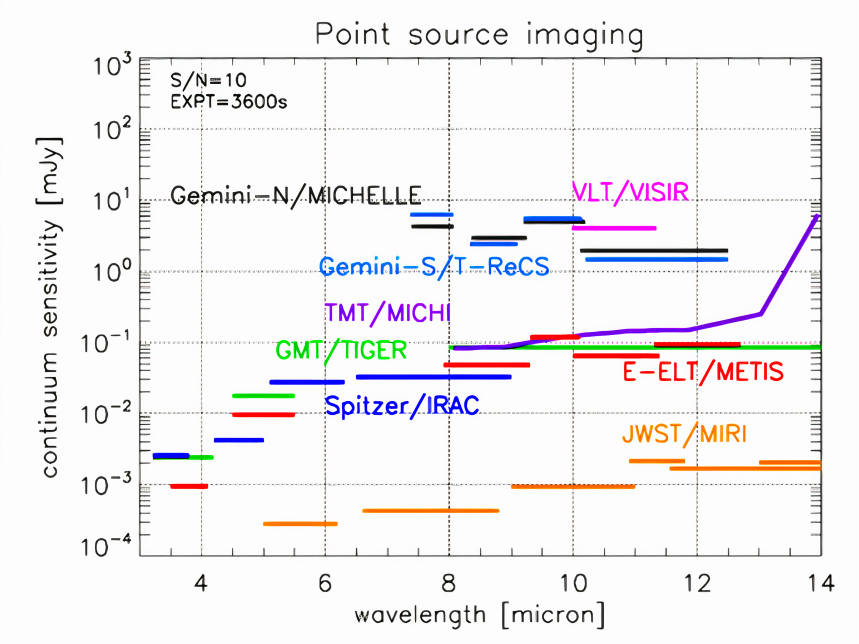

Figure 7.1: Point source sensitivities of for a 10σ detection in one hour (including overheads) for various mid-IR instruments. *Image credit: Brandl et al. (2014).*

absorption line of meta-stable helium. We were able to put an upper limit of $0.14 \pm 0.15\,R_p$ on the extended helium atmosphere. This was an improvement of a factor of four over the previous limit, which was expected given the instrumental and observational differences. These limits showed that of the seven planets where helium has so far been detected in the atmosphere, four have large enough signals to be detectable with X-SHOOTER in the same amount of integration time, making it a suitable instrument to detect helium in the atmospheres of large, close-in planets. To detect helium in GJ 1214 b other instruments that cover the He I line with similar or better resolving power are required, such as CRIRES+, FORS2 or KMOS (Dorn et al., 2014; Appenzeller et al., 1998; Sharples et al., 2013).

In Chapter 6 we reduced archival data of the hot Jupiter WASP-15 b taken with FORS2 in 2011. Due to the placement of the reference stars on the CCD the wavelength range was limited to 8000-10400 Å. Since the coating of the LADC was peeling at the time, data from between 2010 and 2014 have significant correlated noise in them, making this data difficult to work with. We used GP modelling to remove this correlated noise and measure the transit in the white light curve. The calculated midpoint and depth of the transit were consistent within 1σwith previous data taken around the same wavelength range. We used our measured midpoint and previous data to find a new, more precise ephemeris for the orbit of WASP-15 b. We also obtained the first transmission spectrum of the planet by dividing the data into 100 Å bins, from which the white light noise model was subtracted. GP modeling of the binned data removed the wavelength dependant part of the correlated noise entirely in the middle of the spectral range, reducing the noise to 600-1200 ppm, but residuals remained at the extremes of the spectrum, particularly the red side. We found that scatter in the center of the spectrum coincided with large telluric water

absorption bands and no features of 3σ or larger were visible in the rest of the spectrum. Comparison to model spectra revealed that the data are consistent with hazy, cloudy and clear models, as the variation in the data is larger than that in any of the models. Especially around 9100 Å it is likely that we are still dominated by residual noise that is larger than the expected atmospheric features. Future observations will have to have a lower photon noise to better constrain the planet radius, and should preferably be done in the visible wavelength range, where there is less telluric absorption. The current version of FORS2 that has no coating on the LADC should be capable of constraining the haziness or cloudiness of the atmosphere, particularly if more than one transit can be obtained. This would improve the signal to noise ratio and reduce the photon noise, as well as mitigate noise from atmospheric conditions.

With the many instruments available for transmission spectroscopy more and more planet atmospheres are being characterised. Ongoing surveys like CARMENES (Quirrenbach et al., 2014) are adding to the available data even further, allowing a more population based approach to characterising close-in planets and their evolution under heavy stellar irradiation. Future instruments on 40m class telescopes will also allow for the observation of biosignatures in Earth-like planets in the habitable zones of nearby stars (e.g. Serindag and Snellen, 2019). Combined with the prospects for direct imaging discussed in the first section of this chapter, we can expect full characterisation of these kinds of systems and their atmospheres in the near future.

Bibliography

Absil, O., Mawet, D., Karlsson, M., Carlomagno, B., Christiaens, V., Defrère, D., Delacroix, C., Femenía Castella, B., Forsberg, P., Girard, J., Gómez González, C. A., Habraken, S., Hinz, P. M., Huby, E., Jolivet, A., Matthews, K., Milli, J., Orban de Xivry, G., Pantin, E., Piron, P., Reggiani, M., Ruane, G. J., Serabyn, G., Surdej, J., Tristram, K. R. W., Vargas Catalán, E., Wertz, O., and Wizinowich, P. (2016). Three years of harvest with the vector vortex coronagraph in the thermal infrared. In Evans, C. J., Simard, L., and Takami, H., editors, Ground-based and Airborne Instrumentation for Astronomy VI, volume 9908 of Society of Photo-Optical Instrumentation Engineers (SPIE) Conference Series, page 99080Q.

Allard, F., Homeier, D., and Freytag, B. (2012). Models of very-low-mass stars, brown dwarfs and exoplanets. Philosophical Transactions of the Royal Society of London Series A, 370(1968):2765–2777.

Allart, R., Bourrier, V., Lovis, C., Ehrenreich, D., Aceituno, J., Guijarro, A., Pepe, F., Sing, D. K., Spake, J. J., and Wyttenbach, A. (2019). High-resolution confirmation of an extended helium atmosphere around WASP-107b. Astronomy & Astrophysics, 623:A58.

Allart, R., Bourrier, V., Lovis, C., Ehrenreich, D., Spake, J. J., Wyttenbach, A., Pino, L., Pepe, F., Sing, D. K., and Lecavelier des Etangs, A. (2018). Spectrally resolved helium absorption from the extended atmosphere of a warm Neptune-mass exoplanet. Science, 362(6421):1384–1387.

Almenara, J. M., Deeg, H. J., Aigrain, S., Alonso, R., Auvergne, M., Baglin, A., Barbieri, M., Barge, P., Bordé, P., Bouchy, F., Bruntt, H., Cabrera, J., Carone, L., Carpano, S., Catala, C., Csizmadia, S., de La Reza, R., Deleuil, M., Dvorak, R., Erikson, A., Fridlund, M., Gandolfi, D., Gillon, M., Gondoin, P., Guenther, E., Guillot, T., Hatzes, A., Hébrard, G., Jorda, L., Lammer, H., Léger, A., Llebaria, A., Loeillet, B., Magain, P., Mayor, M., Mazeh, T., Moutou, C., Ollivier, M., Pätzold, M., Pont, F., Queloz, D., Rauer, H., Régulo, C., Renner, S., Rouan, D., Samuel, B., Schneider, J., Shporer, A., Wuchterl, G., and Zucker, S. (2009). Rate and nature of false positives in the CoRoT exoplanet search. Astronomy & Astrophysics, 506(1):337–341.

Alonso-Floriano, F. J., Snellen, I. A. G., Czesla, S., Bauer, F. F., Salz, M., Lampón, M., Lara, L. M., Nagel, E., López-Puertas, M., Nortmann, L., Sánchez-López, A., Sanz-Forcada, J., Caballero, J. A., Reiners, A., Ribas, I., Quirrenbach, A., Amado, P. J., Aceituno, J., Anglada-Escudé, G., Béjar, V. J. S., Brinkmöller, M., Hatzes, A. P., Henning, T., Kaminski, A., Kürster, M., Labarga, F., Montes, D., Pallé, E., Schmitt, J. H. M. M., and Zapatero Osorio, M. R.

(2019). He I λ 10 830 Å in the transmission spectrum of HD209458 b. Astronomy & Astrophysics, 629:A110.

Amundsen, D. S., Baraffe, I., Tremblin, P., Manners, J., Hayek, W., Mayne, N. J., and Acreman, D. M. (2014). Accuracy tests of radiation schemes used in hot Jupiter global circulation models. Astronomy & Astrophysics, 564:A59.

Andrews, S. M., Wilner, D. J., Zhu, Z., Birnstiel, T., Carpenter, J. M., Pérez, L. M., Bai, X.-N., Öberg, K. I., Hughes, A. M., Isella, A., and Ricci, L. (2016). Ringed Substructure and a Gap at 1 au in the Nearest Protoplanetary Disk. The Astrophysical Journal Letters, 820(2):L40.

Angerhausen, D., Dreyer, C., Placek, B., Csizmadia, S., Eigmüller, P., Godolt, M., Kitzmann, D., Mallonn, M., Becklin, E. E., Collins, P., Dunham, E. W., Grenfell, J. L., Hamilton, R. T., Kabath, P., Logsdon, S. E., Mandell, A., Mandushev, G., McElwain, M., McLean, I. S., Pfueller, E., Rauer, H., Savage, M., Shenoy, S., Vacca, W. D., Van Cleve, J. E., Wiedemann, M., and Wolf, J. (2017). Simultaneous multicolour optical and near-IR transit photometry of GJ 1214b with SOFIA. Astronomy & Astrophysics, 608:A120.

Anglada-Escudé, G., Arriagada, P., Vogt, S. S., Rivera, E. J., Butler, R. P., Crane, J. D., Shectman, S. A., Thompson, I. B., Minniti, D., Haghighipour, N., Carter, B. D., Tinney, C. G., Wittenmyer, R. A., Bailey, J. A., O'Toole, S. J., Jones, H. R. A., and Jenkins, J. S. (2012). A Planetary System around the nearby M Dwarf GJ 667C with At Least One Super-Earth in Its Habitable Zone. The Astrophysical Journal Letters, 751(1):L16.

Appenzeller, I., Fricke, K., Fürtig, W., Gässler, W., Häfner, R., Harke, R., Hess, H. J., Hummel, W., Jürgens, P., Kudritzki, R. P., Mantel, K. H., Meisl, W., Muschielok, B., Nicklas, H., Rupprecht, G., Seifert, W., Stahl, O., Szeifert, T., and Tarantik, K. (1998). Successful commissioning of FORS1 - the first optical instrument on the VLT. The Messenger, 94:1–6.

Arnold, T. J., Eisner, J. A., Monnier, J. D., and Tuthill, P. (2012). New Spatially Resolved Mid-infrared Observations of the Transitional Disk TW Hya and Tentative Evidence for a Self-luminous Companion. The Astrophysical Journal, 750(2):119.

Arrington, D. C., Hubbs, J. E., Gramer, M. E., and Dole, G. A. (1998). Impact of excess low-frequency noise (ELFN) in Si:As impurity band conduction (IBC) focal plane arrays for astronomical applications. In Dereniak, E. L. and Sampson, R. E., editors, Infrared Detectors and Focal Plane Arrays V, volume 3379 of Society of Photo-Optical Instrumentation Engineers (SPIE) Conference Series, pages 361–370.

Arsenault, R., Madec, P. Y., Vernet, E., Hackenberg, W., La Penna, P., Paufique, J., Kuntschner, H., Pirard, J. F., Kolb, J., and Hubin, N. (2017). The Adaptive Optics Facility: Commissioning Progress and Results. The Messenger, 168:8–14.

Avenhaus, H., Quanz, S. P., Meyer, M. R., Brittain, S. D., Carr, J. S., and Najita, J. R. (2014). HD100546 Multi-epoch Scattered Light Observations. The Astrophysical Journal, 790(1):56.

Backman, D., Marengo, M., Stapelfeldt, K., Su, K., Wilner, D., Dowell, C. D., Watson, D., Stansberry, J., Rieke, G., Megeath, T., Fazio, G., and Werner, M. (2009). Epsilon Eridani's Planetary Debris Disk: Structure and Dynamics Based on Spitzer and Caltech Submillimeter Observatory Observations. The Astrophysical Journal, 690(2):1522–1538.

Baraffe, I., Chabrier, G., Barman, T. S., Allard, F., and Hauschildt, P. H. (2003). Evolutionary models for cool brown dwarfs and extrasolar giant planets. The case of HD 209458. Astronomy & Astrophysics, 402:701–712.

Barclay, T., Burke, C. J., Howell, S. B., Rowe, J. F., Huber, D., Isaacson, H., Jenkins, J. M., Kolbl, R., Marcy, G. W., Quintana, E. V., Still, M., Twicken, J. D., Bryson, S. T., Borucki, W. J., Caldwell, D. A., Ciardi, D., Clarke, B. D., Christiansen, J. L., Coughlin, J. L., Fischer, D. A., Li, J., Haas, M. R., Hunter, R., Lissauer, J. J., Mullally, F., Sabale, A., Seader, S. E., Smith, J. C., Tenenbaum, P., Kamal Uddin, A. K. M., and Thompson, S. E. (2013). A Super-Earth-sized Planet Orbiting in or Near the Habitable Zone around a Sun-like Star. The Astrophysical Journal, 768(2):101.

Barman, T. S., Macintosh, B., Konopacky, Q. M., and Marois, C. (2011). Clouds and Chemistry in the Atmosphere of Extrasolar Planet HR8799b. The Astrophysical Journal, 733(1):65.

Batista, V. (2018). Finding Planets via Gravitational Microlensing, page 120. Springer.

Batygin, K. and Brown, M. E. (2016). Evidence for a Distant Giant Planet in the Solar System. The Astronomical Journal, 151(2):22.

Bean, J. L., Miller-Ricci Kempton, E., and Homeier, D. (2010). A ground-based transmission spectrum of the super-Earth exoplanet GJ 1214b. Nature, 468(7324):669–672.

Benedict, G. F., McArthur, B. E., Gatewood, G., Nelan, E., Cochran, W. D., Hatzes, A., Endl, M., Wittenmyer, R., Baliunas, S. L., Walker, G. A. H., Yang, S., Kürster, M., Els, S., and Paulson, D. B. (2006). The Extrasolar Planet $\in$ Eridani b: Orbit and Mass. The Astronomical Journal, 132(5):2206–2218.

Benisty, M., Stolker, T., Pohl, A., de Boer, J., Lesur, G., Dominik, C., Dullemond, C. P., Langlois, M., Min, M., Wagner, K., Henning, T., Juhasz, A., Pinilla, P., Facchini, S., Apai, D., van Boekel, R., Garufi, A., Ginski, C., Ménard, F., Pinte, C., Quanz, S. P., Zurlo, A., Boccaletti, A., Bonnefoy, M., Beuzit, J. L., Chauvin, G., Cudel, M., Desidera, S., Feldt, M., Fontanive, C., Gratton, R., Kasper, M., Lagrange, A.-M., LeCoroller, H., Mouillet, D., Mesa, D., Sissa, E., Vigan, A., Antichi, J., Buey, T., Fusco, T., Gisler, D., Llored, M., Magnard, Y., Moeller-Nilsson, O., Pragt, J., Roelfsema, R., Sauvage, J.-F., and Wildi, F. (2017). Shadows and spirals in the protoplanetary disk hd453. Astronomy & Astrophysics, 597:A42.

Berta, Z. K., Charbonneau, D., Bean, J., Irwin, J., Burke, C. J., Désert, J.-M., Nutzman, P., and Falco, E. E. (2011). The GJ1214 Super-Earth System: Stellar Variability, New Transits, and a Search for Additional Planets. Astrophysical Journal, 736(1):12.

Berta, Z. K., Irwin, J., Charbonneau, D., Burke, C. J., and Falco, E. E. (2012). Transit Detection in the MEarth Survey of Nearby M Dwarfs: Bridging the Clean-first, Search-later Divide. The Astronomical Journal, 144(5):145.

Beuzit, J. L., Vigan, A., Mouillet, D., Dohlen, K., Gratton, R., Boccaletti, A., Sauvage, J. F., Schmid, H. M., Langlois, M., Petit, C., Baruffolo, A., Feldt, M., Milli, J., Wahhaj, Z., Abe, L., Anselmi, U., Antichi, J., Barette, R., Baudrand, J., Baudoz, P., Bazzon, A., Bernardi, P., Blanchard, P., Brast, R., Bruno, P., Buey, T., Carbillet, M., Carle, M., Cascone, E., Chapron, F., Charton, J., Chauvin, G., Claudi, R., Costille, A., De Caprio, V., de Boer, J., Delboulbé, A., Desidera, S., Dominik, C., Downing, M., Dupuis, O., Fabron, C., Fantinel, D., Farisato, G., Feautrier, P., Fedrigo, E., Fusco, T., Gigan, P., Ginski, C., Girard, J., Giro, E., Gisler, D., Gluck, L., Gry, C., Henning, T., Hubin, N., Hugot, E., Incorvaia, S., Jaquet, M., Kasper, M., Lagadec, E., Lagrange, A. M., Le Coroller, H., Le Mignant, D., Le Ruyet, B., Lessio, G., Lizon, J. L., Llored, M., Lundin, L., Madec, F., Magnard, Y., Marteaud, M., Martinez, P., Maurel, D., Ménard, F., Mesa, D., Möller-Nilsson, O., Moulin, T., Moutou, C., Origné, A., Parisot, J., Pavlov, A., Perret, D., Pragt, J., Puget, P., Rabou, P., Ramos, J., Reess, J. M., Rigal, F., Rochat, S., Roelfsema, R., Rousset, G., Roux, A., Saisse, M., Salasnich, B., Santambrogio, E., Scuderi, S., Segransan, D., Sevin, A., Siebenmorgen, R., Soenke, C., Stadler, E., Suarez, M., Tiphène, D., Turatto, M., Udry, S., Vakili, F., Waters, L. B. F. M., Weber, L., Wildi, F., Zins, G., and Zurlo, A. (2019). SPHERE: the exoplanet imager for the Very Large Telescope. Astronomy & Astrophysics, 631:A155.

Biller, B. A. and Bonnefoy, M. (2018). Exoplanet Atmosphere Measurements from Direct Imaging, page 101. Springer.

Biller, B. A., Males, J., Rodigas, T., Morzinski, K., Close, L. M., Juhász, A., Follette, K. B., Lacour, S., Benisty, M., Sicilia-Aguilar, A., Hinz, P. M., Weinberger, A., Henning, T., Pott, J.-U., Bonnefoy, M., and Köhler, R. (2014). AN ENIGMATIC POINT-LIKE FEATURE WITHIN THE HD 169142 TRANSITIONAL DISK,. The Astrophysical Journal, 792(1):L22.

Boehle, A., Quanz, S. P., Lovis, C., Ségransan, D., Udry, S., and Apai, D. (2019). Combining high-contrast imaging and radial velocities to constrain the planetary architectures of nearby stars. Astronomy & Astrophysics, 630:A50.

Boffin, H., Blanchard, G., Gonzalez, O., Moehler, S., Sedaghati, E., Gibson, N., van den Ancker, M., Smoker, J., Anderson, J., Hummel, C., Dobrzycka, D., Smette, A., and Rupprecht, G. (2015). Making FORS2 Fit for Exoplanet Observations (again). The Messenger, 159:6–9.

Bohn, A. J., Kenworthy, M. A., Ginski, C., Manara, C. F., Pecaut, M. J., de Boer, J., Keller, C. U., Mamajek, E. E., Meshkat, T., Reggiani, M., Todorov, K. O., and Snik, F. (2019). The Young Suns Exoplanet Survey: Detection of a wide-orbit planetary-mass companion to a solar-type Sco-Cen member. Monthly Notices of the Royal Astronomical Society, 492(1):431–443.

Bond, H. E., Schaefer, G. H., Gilliland, R. L., Holberg, J. B., Mason, B. D., Lindenblad, I. W., Seitz-McLeese, M., Arnett, W. D., Demarque, P., Spada, F., Young, P. A., Barstow, M. A.,

Burleigh, M. R., and Gudehus, D. (2017). The Sirius System and Its Astrophysical Puzzles: Hubble Space Telescope and Ground-based Astrometry. The Astrophysical Journal, 840(2):70.

Bonfils, X., Lo Curto, G., Correia, A. C. M., Laskar, J., Udry, S., Delfosse, X., Forveille, T., Astudillo-Defru, N., Benz, W., Bouchy, F., Gillon, M., Hébrard, G., Lovis, C., Mayor, M., Moutou, C., Naef, D., Neves, V., Pepe, F., Perrier, C., Queloz, D., Santos, N. C., and Ségransan, D. (2013). The HARPS search for southern extra-solar planets. XXXIV. A planetary system around the nearby M dwarf ¡ASTROBJ¿GJ 163¡/ASTROBJ¿, with a super-Earth possibly in the habitable zone. Astronomy & Astrophysics, 556:A110.

Bonnet-Bidaud, J. M. and Pantin, E. (2008). ADONIS high contrast infrared imaging of Sirius-B. Astronomy & Astrophysics, 489(2):651–655.

Booth, M., Dent, W. R. F., Jordán, A., Lestrade, J.-F., Hales, A. S., Wyatt, M. C., Casassus, S., Ertel, S., Greaves, J. S., Kennedy, G. M., Matrà, L., Augereau, J.-C., and Villard, E. (2017). The Northern arc of ∈ Eridani's Debris Ring as seen by ALMA. Monthly Notices of the Royal Astronomical Society, 469(3):3200–3212.

Booth, M., Jordán, A., Casassus, S., Hales, A. S., Dent, W. R. F., Faramaz, V., Matrà, L., Barkats, D., Brahm, R., and Cuadra, J. (2016). Resolving the planetesimal belt of hr 8799 with alma. Monthly Notices of the Royal Astronomical Society: Letters, 460(1):L10–L14.

Borucki, W. J., Koch, D. G., Batalha, N., Bryson, S. T., Rowe, J., Fressin, F., Torres, G., Caldwell, D. A., Christensen-Dalsgaard, J., Cochran, W. D., DeVore, E., Gautier, T. N., Geary, J. C., Gilliland, R., Gould, A., Howell, S. B., Jenkins, J. M., Latham, D. W., Lissauer, J. J., Marcy, G. W., Sasselov, D., Boss, A., Charbonneau, D., Ciardi, D., Kaltenegger, L., Doyle, L., Dupree, A. K., Ford, E. B., Fortney, J., Holman, M. J., Steffen, J. H., Mullally, F., Still, M., Tarter, J., Ballard, S., Buchhave, L. A., Carter, J., Christiansen, J. L., Demory, B.-O., Désert, J.-M., Dressing, C., Endl, M., Fabrycky, D., Fischer, D., Haas, M. R., Henze, C., Horch, E., Howard, A. W., Isaacson, H., Kjeldsen, H., Johnson, J. A., Klaus, T., Kolodziejczak, J., Barclay, T., Li, J., Meibom, S., Prsa, A., Quinn, S. N., Quintana, E. V., Robertson, P., Sherry, W., Shporer, A., Tenenbaum, P., Thompson, S. E., Twicken, J. D., Van Cleve, J., Welsh, W. F., Basu, S., Chaplin, W., Miglio, A., Kawaler, S. D., Arentoft, T., Stello, D., Metcalfe, T. S., Verner, G. A., Karoff, C., Lundkvist, M., Lund, M. N., Handberg, R., Elsworth, Y., Hekker, S., Huber, D., Bedding, T. R., and Rapin, W. (2012). Kepler-22b: A 2.4 Earth-radius Planet in the Habitable Zone of a Sun-like Star. The Astrophysical Journal, 745(2):120.

Boss, A. P. (1997). Giant planet formation by gravitational instability. Science, 276:1836–1839.

Boss, A. P. (2001). Formation of planetary-mass objects by protostellar collapse and fragmentation. The Astrophysical Journal, 551(2):L167–L170.

Boss, A. P. (2011). Formation of Giant Planets by Disk Instability on Wide Orbits Around Protostars with Varied Masses. The Astrophysical Journal, 731(1):74.

Bouwman, J., de Koter, A., Dominik, C., and Waters, L. B. F. M. (2003). The origin of crystalline silicates in the Herbig Be star HD 100546 and in comet Hale-Bopp. Astronomy & Astrophysics, 401:577–592.

Bowler, B. P. (2016). Imaging Extrasolar Giant Planets. Publications of the Astronomical Society of the Pacific, 128(968):102001.

Brandl, B. R., Absil, O., Agócs, T., Baccichet, N., Bertram, T., Bettonvil, F., van Boekel, R., Burtscher, L., van Dishoeck, E., Feldt, M., Garcia, P. J. V., Glasse, A., Glauser, A., Güdel, M., Haupt, C., Kenworthy, M. A., Labadie, L., Laun, W., Lesman, D., Pantin, E., Quanz, S. P., Snellen, I., Siebenmorgen, R., and van Winckel, H. (2018). Status of the mid-IR ELT imager and spectrograph (METIS). In Ground-based and Airborne Instrumentation for Astronomy VII, volume 10702 of Society of Photo-Optical Instrumentation Engineers (SPIE) Conference Series, page 107021U.

Brandl, B. R., Feldt, M., Glasse, A., Guedel, M., Heikamp, S., Kenworthy, M., Lenzen, R., Meyer, M. R., Molster, F., Paalvast, S., Pantin, E. J., Quanz, S. P., Schmalzl, E., Stuik, R., Venema, L., and Waelkens, C. (2014). METIS: the mid-infrared E-ELT imager and spectrograph. In Ramsay, S. K., McLean, I. S., and Takami, H., editors, Ground-based and Airborne Instrumentation for Astronomy V, volume 9147 of Society of Photo-Optical Instrumentation Engineers (SPIE) Conference Series, page 914721.

Brittain, S. D., Carr, J. S., Najita, J. R., Quanz, S. P., and Meyer, M. R. (2014). NIR Spectroscopy of the HAeBe Star HD 100546. III. Further Evidence of an Orbiting Companion? The Astrophysical Journal, 791(2):136.

Brogi, M., de Kok, R. J., Albrecht, S., Snellen, I. A. G., Birkby, J. L., and Schwarz, H. (2016). Rotation and winds of exoplanet hd 189733 b measured with high-dispersion transmission spectroscopy. The Astrophysical Journal, 817(2):106.

Bruno, G. (1585). Gli Heroici Furori.

Bryan, M. L., Bowler, B. P., Knutson, H. A., Kraus, A. L., Hinkley, S., Mawet, D., Nielsen, E. L., and Blunt, S. C. (2016). Searching for Scatterers: High-Contrast Imaging of Young Stars Hosting Wide-Separation Planetary-Mass Companions. The Astrophysical Journal, 827(2):100.

Burleigh, M. R., Clarke, F. J., and Hodgkin, S. T. (2002). Imaging planets around nearby white dwarfs. Monthly Notices of the Royal Astronomical Society, 331(4):L41–L45.

Carmona, A., van den Ancker, M. E., Henning, T., Pavlyuchenkov, Y., Dullemond, C. P., Goto, M., Thi, W. F., Bouwman, J., and Waters, L. B. F. M. (2008). A search for mid-infrared molecular hydrogen emission from protoplanetary disks. Astronomy & Astrophysics, 477(3):839–852.

Carrera, D., Raymond, S. N., and Davies, M. B. (2019). Planet-planet scattering as the source of the highest eccentricity exoplanets. Astronomy & Astrophysics, 629:L7.

Casassus, S. and Pérez, S. (2019). Kinematic Detections of Protoplanets: A Doppler Flip in the Disk of HD 100546. The Astrophysical Journal Letters, 883(2):L41.

Cayrel, R. (1988). Data Analysis. In Cayrel de Strobel, G. and Spite, M., editors, The Impact of Very High S/N Spectroscopy on Stellar Physics, volume 132 of IAU Symposium, page 345.

Charbonneau, D., Allen, L. E., Megeath, S. T., Torres, G., Alonso, R., Brown, T. M., Gilliland, R. L., Latham, D. W., Mandushev, G., O'Donovan, F. T., et al. (2005). Detection of thermal emission from an extrasolar planet. The Astrophysical Journal, 626(1):523.

Charbonneau, D., Berta, Z. K., Irwin, J., Burke, C. J., Nutzman, P., Buchhave, L. A., Lovis, C., Bonfils, X., Latham, D. W., Udry, S., Murray-Clay, R. A., Holman, M. J., Falco, E. E., Winn, J. N., Queloz, D., Pepe, F., Mayor, M., Delfosse, X., and Forveille, T. (2009). A super-Earth transiting a nearby low-mass star. Nature, 462(7275):891–894.

Charbonneau, D., Brown, T. M., Latham, D. W., and Mayor, M. (2000). Detection of Planetary Transits Across a Sun-like Star. The Astrophysical Journal Letters, 529(1):L45–L48.

Charbonneau, D., Brown, T. M., Noyes, R. W., and Gilliland, R. L. (2002). Detection of an extrasolar planet atmosphere. The Astrophysical Journal, 568(1):377.

Chauvin, G., Desidera, S., Lagrange, A. M., Vigan, A., Gratton, R., Langlois, M., Bonnefoy, M., Beuzit, J. L., Feldt, M., Mouillet, D., Meyer, M., Cheetham, A., Biller, B., Boccaletti, A., D'Orazi, V., Galicher, R., Hagelberg, J., Maire, A. L., Mesa, D., Olofsson, J., Samland, M., Schmidt, T. O. B., Sissa, E., Bonavita, M., Charnay, B., Cudel, M., Daemgen, S., Delorme, P., Janin-Potiron, P., Janson, M., Keppler, M., Le Coroller, H., Ligi, R., Marleau, G. D., Messina, S., Mollière, P., Mordasini, C., Müller, A., Peretti, S., Perrot, C., Rodet, L., Rouan, D., Zurlo, A., Dominik, C., Henning, T., Menard, F., Schmid, H. M., Turatto, M., Udry, S., Vakili, F., Abe, L., Antichi, J., Baruffolo, A., Baudoz, P., Baudrand, J., Blanchard, P., Bazzon, A., Buey, T., Carbillet, M., Carle, M., Charton, J., Cascone, E., Claudi, R., Costille, A., Deboulbe, A., De Caprio, V., Dohlen, K., Fantinel, D., Feautrier, P., Fusco, T., Gigan, P., Giro, E., Gisler, D., Gluck, L., Hubin, N., Hugot, E., Jaquet, M., Kasper, M., Madec, F., Magnard, Y., Martinez, P., Maurel, D., Le Mignant, D., Möller-Nilsson, O., Llored, M., Moulin, T., Origné, A., Pavlov, A., Perret, D., Petit, C., Pragt, J., Puget, P., Rabou, P., Ramos, J., Rigal, R., Rochat, S., Roelfsema, R., Rousset, G., Roux, A., Salasnich, B., Sauvage, J. F., Sevin, A., Soenke, C., Stadler, E., Suarez, M., Weber, L., Wildi, F., Antoniucci, S., Augereau, J. C., Baudino, J. L., Brandner, W., Engler, N., Girard, J., Gry, C., Kral, Q., Kopytova, T., Lagadec, E., Milli, J., Moutou, C., Schlieder, J., Szulágyi, J., Thalmann, C., and Wahhaj, Z. (2017). Discovery of a warm, dusty giant planet around HIP 65426. Astronomy & Astrophysics, 605:L9.

Chilcote, J. et al. (2017). 1–2.4μm near-IR spectrum of the giant planet β Pictoris b obtained with the gemini planet imager. The Astronomical Journal, 153(4):182.

Christiaens, V., Cantalloube, F., Casassus, S., Price, D. J., Absil, O., Pinte, C., Girard, J., and Montesinos, M. (2019). Evidence for a Circumplanetary Disk around Protoplanet PDS 70 b. The Astrophysical Journal Letters, 877(2):L33.

Clement, M. S. and Sheppard, S. S. (2021). Stability of Neptunes Distant Resonances in the Presence of Planet Nine. The Astronomical Journal, 162(1):27.

Copernicus, N. (1543). De revolutionibus orbium coelestium.

Cox, A. N. (2000). Allen's astrophysical quantities. Springer.

Crossfield, I. J. M., Barman, T., Hansen, B., and Frewen, S. (2019). An upper limit on he absorption in GJ 1214b. RNAAS, 3(1):24.

Cugno, G., Quanz, S. P., Hunziker, S., Stolker, T., Schmid, H. M., Avenhaus, H., Baudoz, P., Bohn, A. J., Bonnefoy, M., Buenzli, E., Chauvin, G., Cheetham, A., Desidera, S., Dominik, C., Feautrier, P., Feldt, M., Ginski, C., Girard, J. H., Gratton, R., Hagelberg, J., Hugot, E., Janson, M., Lagrange, A.-M., Langlois, M., Magnard, Y., Maire, A.-L., Menard, F., Meyer, M., Milli, J., Mordasini, C., Pinte, C., Pragt, J., Roelfsema, R., Rigal, F., Szulágyi, J., van Boekel, R., van der Plas, G., Vigan, A., Wahhaj, Z., and Zurlo, A. (2019). A search for accreting young companions embedded in circumstellar disks - high-contrast hging with vlt/sphere. Astronomy & Astrophysics, 622:A156.

Currie, T., Burrows, A., Itoh, Y., Matsumura, S., Fukagawa, M., Apai, D., Madhusudhan, N., Hinz, P. M., Rodigas, T. J., Kasper, M., Pyo, T. S., and Ogino, S. (2011). A Combined Subaru/VLT/MMT 1-5 μm Study of Planets Orbiting HR 8799: Implications for Atmospheric Properties, Masses, and Formation. The Astrophysical Journal, 729(2):128.

Currie, T., Cloutier, R., Brittain, S., Grady, C., Burrows, A., Muto, T., Kenyon, S. J., and Kuchner, M. J. (2015). Resolving the HD 100546 Protoplanetary System with the Gemini Planet Imager: Evidence for Multiple Forming, Accreting Planets. The Astrophysical Journal Letters, 814(2):L27.

Currie, T., Muto, T., Kudo, T., Honda, M., Brandt, T. D., Grady, C., Fukagawa, M., Burrows, A., Janson, M., Kuzuhara, M., McElwain, M. W., Follette, K., Hashimoto, J., Henning, T., Kand ori, R., Kusakabe, N., Kwon, J., Mede, K., Morino, J.-i., Nishikawa, J., Pyo, T.-S., Serabyn, G., Suenaga, T., Takahashi, Y., Wisniewski, J., and Tamura, M. (2014). Recovery of the Candidate Protoplanet HD 100546 b with Gemini/NICI and Detection of Additional (Planet-induced?) Disk Structure at Small Separations. The Astrophysical Journal Letters, 796(2):L30.

D'Angelo, G. and Lissauer, J. J. (2018). Formation of Giant Planets, page 140. Springer.

de Wit, W.-J. (2020). personal communication.

Deeg, H. J. and Alonso, R. (2018). Transit Photometry as an Exoplanet Discovery Method, page 117. Springer.

Deming, D., Harrington, J., Laughlin, G., Seager, S., Navarro, S. B., Bowman, W. C., and Horning, K. (2007). SpitzerTransit and secondary eclipse photometry of GJ 436b. The Astrophysical Journal, 667(2):L199–L202.

Deming, D., Seager, S., Richardson, L. J., and Harrington, J. (2005). Infrared radiation from an extrasolar planet. Nature, 434:740–743.

Di Folco, E., Thévenin, F., Kervella, P., Domiciano de Souza, A., Coudé du Foresto, V., Ségransan, D., and Morel, P. (2004). VLTI near-IR interferometric observations of Vega-like stars. Radius and age of α PsA, β Leo, β Pic, $\in$ Eri and τ Cet. Astronomy & Astrophysics, 426:601–617.

Dieterich, S. B., Weinberger, A. J., Boss, A. P., Henry, T. J., Jao, W.-C., Gagné, J., Astraatmadja, T. L., Thompson, M. A., and Anglada-Escudé, G. (2018). Dynamical Masses of $\in$ Indi B and C: Two Massive Brown Dwarfs at the Edge of the Stellar-substellar Boundary. The Astrophysical Journal, 865(1):28.

Dietrich, J. and Apai, D. (2020). An Integrated Analysis with Predictions on the Architecture of the tau Ceti Planetary System, Including a Habitable Zone Planet. arXiv e-prints, page arXiv:2010.14675.

Dionatos, O., Woitke, P., Güdel, M., Degroote, P., Liebhart, A., Anthonioz, F., Antonellini, S., Baldovin-Saavedra, C., Carmona, A., Dominik, C., Greaves, J., Ilee, J. D., Kamp, I., Ménard, F., Min, M., Pinte, C., Rab, C., Rigon, L., Thi, W. F., and Waters, L. B. F. M. (2019). Consistent dust and gas models for protoplanetary disks. IV. A panchromatic view of protoplanetary disks. Astronomy & Astrophysics, 625:A66.

Dong, R., Liu, S.-y., Eisner, J., Andrews, S., Fung, J., Zhu, Z., Chiang, E., Hashimoto, J., Liu, H. B., Casassus, S., Esposito, T., Hasegawa, Y., Muto, T., Pavlyuchenkov, Y., Wilner, D., Akiyama, E., Tamura, M., and Wisniewski, J. (2018). The Eccentric Cavity, Triple Rings, Two-armed Spirals, and Double Clumps of the MWC 758 Disk. The Astrophysical Journal, 860(2):124.

Dong, R., Zhu, Z., Rafikov, R. R., and Stone, J. M. (2015). OBSERVATIONAL SIGNATURES OF PLANETS IN PROTOPLANETARY DISKS: SPIRAL ARMS OBSERVED IN SCATTERED LIGHT IMAGING CAN BE INDUCED BY PLANETS. The Astrophysical Journal, 809(1):L5.

Dorn, R. J., Anglada-Escude, G., Baade, D., Bristow, P., Follert, R., Gojak, D., Grunhut, J., Hatzes, A., Heiter, U., Hilker, M., Ives, D. J., Jung, Y., Käufl, H. U., Kerber, F., Klein, B., Lizon, J. L., Lockhart, M., Löwinger, T., Marquart, T., Oliva, E., Origlia, L., Pasquini, L., Paufique, J., Piskunov, N., Pozna, E., Reiners, A., Smette, A., Smoker, J., Seemann, U., Stempels, E., and Valenti, E. (2014). CRIRES+: Exploring the Cold Universe at High Spectral Resolution. The Messenger, 156:7–11.

Dorschner, J., Begemann, B., Henning, T., Jaeger, C., and Mutschke, H. (1995). Steps toward interstellar silicate mineralogy. II. Study of Mg-Fe-silicate glasses of variable composition. Astronomy & Astrophysics, 300:503.

dos Santos, L. A., Ehrenreich, D., Bourrier, V., Allart, R., King, G., Lendl, M., Lovis, C., Margheim, S., Meléndez, J., Seidel, J. V., and Sousa, S. G. (2020). Search for helium in the upper atmosphere of the hot Jupiter WASP-127 b using Gemini/Phoenix. Astronomy & Astrophysics, 640:A29.

Doucet, C., Pantin, E., Lagage, P. O., and Dullemond, C. P. (2006). Mid-infrared imaging of the circumstellar dust around three herbig ae stars: Hd 135344, cq tau, and hd 163296. Astronomy & Astrophysics, 460(1):117–124.

Doyon, R., Lafrenière, D., Artigau, E., Malo, L., and Marois, C. (2010). The age of HR8799. In In the Spirit of Lyot 2010, page E42.

Drummond, B., Tremblin, P., Baraffe, I., Amundsen, D. S., Mayne, N. J., Venot, O., and Goyal, J. (2016). The effects of consistent chemical kinetics calculations on the pressure-temperature profiles and emission spectra of hot Jupiters. Astronomy & Astrophysics, 594:A69.

Dullemond, C. P. and Monnier, J. D. (2010). The Inner Regions of Protoplanetary Disks. Annual Review of Astronomy and Astrophysics, 48:205–239.

Dupuy, T. J., Brandt, T. D., Kratter, K. M., and Bowler, B. P. (2019). A model-independent mass and moderate eccentricity for β Pic b. The Astrophysical Journal, 871(1):L4.

Eastman, J., Siverd, R., and Gaudi, B. S. (2010). Achieving Better Than 1 Minute Accuracy in the Heliocentric and Barycentric Julian Dates. Publications of the Astronomical Society of the Pacific, 122(894):935.

Eker, Z., Soydugan, F., Soydugan, E., Bilir, S., Yaz Gökçe, E., Steer, I., Tüysüz, M., Şenyüz, T., and Demircan, O. (2015). Main-Sequence Effective Temperatures from a Revised Mass-Luminosity Relation Based on Accurate Properties. The Astronomical Journal, 149(4):131.

Endl, M., Kürster, M., Els, S., Hatzes, A. P., Cochran, W. D., Dennerl, K., and Döbereiner, S. (2002). The planet search program at the ESO Coudé Echelle spectrometer. III. The complete Long Camera survey results. Astronomy & Astrophysics, 392:671–690.

Espaillat, C., Muzerolle, J., Najita, J., Andrews, S., Zhu, Z., Calvet, N., Kraus, S., Hashimoto, J., Kraus, A., and D'Alessio, P. (2014). An Observational Perspective of Transitional Disks. In Beuther, H., Klessen, R. S., Dullemond, C. P., and Henning, T., editors, Protostars and Planets VI, page 497.

Espinoza, N., Kossakowski, D., and Brahm, R. (2019). juliet: a versatile modelling tool for transiting and non-transiting exoplanetary systems. Monthly Notices of the Royal Astronomical Society, 490(2):2262–2283.

Esposito, S. et al. (2013). LBT observations of the HR 8799 planetary system - first detection of HR 8799e in h band. Astronomy & Astrophysics, 549:A52.

Exoplanet Team (2021). The extrasolar planet encyclopedia. http://exoplanet.eu/catalog/.

Fairlamb, J. R., Oudmaijer, R. D., Mendigutía, I., Ilee, J. D., and van den Ancker, M. E. (2015). A spectroscopic survey of Herbig Ae/Be stars with X-shooter - I. Stellar parameters and accretion rates. Monthly Notices of the Royal Society, 453(1):976–1001.

Fedele, D., Bruderer, S., van den Ancker, M. E., and Pascucci, I. (2015). On the Asymmetry of the OH Ro-vibrational Lines in HD 100546. The Astrophysical Journal, 800(1):23.

Fedele, D., Carney, M., Hogerheijde, M. R., Walsh, C., Miotello, A., Klaassen, P., Bruderer, S., Henning, Th., and van Dishoeck, E. F. (2017). Alma unveils rings and gaps in the protoplanetary system hd 169142: signatures of two giant protoplanets. Astronomy & Astrophysics, 600:A72.

Feng, F., Anglada-Escudé, G., Tuomi, M., Jones, H. R. A., Chanamé, J., Butler, P. R., and Janson, M. (2019). Detection of the nearest Jupiter analogue in radial velocity and astrometry data. Monthly Notices of the Royal Astronomical Society, 490(4):5002–5016.

Feng, F., Tuomi, M., Jones, H. R. A., Barnes, J., Anglada-Escudé, G., Vogt, S. S., and Butler, R. P. (2017). Color Difference Makes a Difference: Four Planet Candidates around τ Ceti. The Astronomical Journal, 154(4):135.

Fletcher, L. N., Helled, R., Roussos, E., Jones, G., Charnoz, S., André, N., Andrews, D., Bannister, M., Bunce, E., Cavalié, T., Ferri, F., Fortney, J., Grassi, D., Griton, L., Hartogh, P., Hueso, R., Kaspi, Y., Lamy, L., Masters, A., Melin, H., Moses, J., Mousis, O., Nettleman, N., Plainaki, C., Schmidt, J., Simon, A., Tobie, G., Tortora, P., Tosi, F., and Turrini, D. (2020). Ice giant systems: The scientific potential of orbital missions to uranus and neptune. Planetary and Space Science, 191:105030.

Follette, K. B., Rameau, J., Dong, R., Pueyo, L., Close, L. M., Duchêne, G., Fung, J., Leonard, C., Macintosh, B., Males, J. R., Marois, C., Millar-Blanchaer, M. A., Morzinski, K. M., Mullen, W., Perrin, M., Spiro, E., Wang, J., Ammons, S. M., Bailey, V. P., Barman, T., Bulger, J., Chilcote, J., Cotten, T., De Rosa, R. J., Doyon, R., Fitzgerald, M. P., Goodsell, S. J., Graham, J. R., Greenbaum, A. Z., Hibon, P., Hung, L.-W., Ingraham, P., Kalas, P., Konopacky, Q., Larkin, J. E., Maire, J., Marchis, F., Metchev, S., Nielsen, E. L., Oppenheimer, R., Palmer, D., Patience, J., Poyneer, L., Rajan, A., Rantakyrö, F. T., Savransky, D., Schneider, A. C., Sivaramakrishnan, A., Song, I., Soummer, R., Thomas, S., Vega, D., Wallace, J. K., Ward-Duong, K., Wiktorowicz, S., and Wolff, S. (2017). Complex Spiral Structure in the HD 100546 Transitional Disk as Revealed by GPI and MagAO. The Astronomical Journal, 153(6):264.

Foreman-Mackey, D., Agol, E., Angus, R., and Ambikasaran, S. (2017). Fast and scalable gaussian process modeling with applications to astronomical time series. the Astrophysical Journal, 154:220.

Forgan, D. and Rice, K. (2013). Towards a population synthesis model of objects formed by self-gravitating disc fragmentation and tidal downsizing. Monthly Notices of the Royal Astronomical Society, 432(4):3168–3185.

Fortney, J. J., Lodders, K., Marley, M. S., and Freedman, R. S. (2008). A Unified Theory for the Atmospheres of the Hot and Very Hot Jupiters: Two Classes of Irradiated Atmospheres. The Astrophysical Journal, 678(2):1419–1435.

Francis, L. and van der Marel, N. (2020). Dust-depleted Inner Disks in a Large Sample of Transition Disks through Long-baseline ALMA Observations. The Astrophysical Journal, 892(2):111.

Friedrich, S., Zinnecker, H., Correia, S., Brandner, W., Burleigh, M., and McCaughrean, M. (2007). Search for Giant Planets around White Dwarfs with HST, Spitzer, and VLT. In Napiwotzki, R. and Burleigh, M. R., editors, 15th European Workshop on White Dwarfs, volume 372 of Astronomical Society of the Pacific Conference Series, page 343.

Fuhrmeister, B., Czesla, S., Hildebrandt, L., Nagel, E., Schmitt, J. H. M. M., Jeffers, S. V., Caballero, J. A., Hintz, D., Johnson, E. N., Schöfer, P., Zechmeister, M., Reiners, A., Ribas, I., Amado, P. J., Quirrenbach, A., Nortmann, L., Bauer, F. F., Béjar, V. J. S., Cortés-Contreras, M., Dreizler, S., Galadí-Enríquez, D., Hatzes, A. P., Kaminski, A., Kürster, M., Lafarga, M., and Montes, D. (2020). The CARMENES search for exoplanets around M dwarfs. Variability of the He I line at 10830 Å. arXiv e-prints, page arXiv:2006.09372.

Fulton, B. J., Petigura, E. A., Howard, A. W., Isaacson, H., Marcy, G. W., Cargile, P. A., Hebb, L., Weiss, L. M., Johnson, J. A., Morton, T. D., Sinukoff, E., Crossfield, I. J. M., and Hirsch, L. A. (2017). The California-Kepler Survey. III. A Gap in the Radius Distribution of Small Planets. The Astronomical Journal, 154(3):109.

Gaia Collaboration, Brown, A. G. A., Vallenari, A., Prusti, T., de Bruijne, J. H. J., Babusiaux, C., Bailer-Jones, C. A. L., Biermann, M., Evans, D. W., Eyer, L., Jansen, F., Jordi, C., Klioner, S. A., Lammers, U., Lindegren, L., Luri, X., Mignard, F., Panem, C., Pourbaix, D., Randich, S., Sartoretti, P., Siddiqui, H. I., Soubiran, C., van Leeuwen, F., Walton, N. A., Arenou, F., Bastian, U., Cropper, M., Drimmel, R., Katz, D., Lattanzi, M. G., Bakker, J., Cacciari, C., Castañeda, J., Chaoul, L., Cheek, N., De Angeli, F., Fabricius, C., Guerra, R., Holl, B., Masana, E., Messineo, R., Mowlavi, N., Nienartowicz, K., Panuzzo, P., Portell, J., Riello, M., Seabroke, G. M., Tanga, P., Thévenin, F., Gracia-Abril, G., Comoretto, G., Garcia-Reinaldos, M., Teyssier, D., Altmann, M., Andrae, R., Audard, M., Bellas-Velidis, I., Benson, K., Berthier, J., Blomme, R., Burgess, P., Busso, G., Carry, B., Cellino, A., Clementini, G., Clotet, M., Creevey, O., Davidson, M., De Ridder, J., Delchambre, L., Dell'Oro, A., Ducourant, C., Fernández-Hernández, J., Fouesneau, M., Frémat, Y., Galluccio, L., García-Torres, M., González-Núñez, J., González-Vidal, J. J., Gosset, E., Guy, L. P., Halbwachs, J. L., Hambly, N. C., Harrison, D. L., Hernández, J., Hestroffer, D., Hodgkin, S. T., Hutton, A., Jasniewicz, G., Jean-Antoine-Piccolo, A., Jordan, S., Korn, A. J., Krone-Martins, A., Lanzafame, A. C., Lebzelter, T., Löffler, W., Manteiga, M., Marrese, P. M., Martín-Fleitas,

J. M., Moitinho, A., Mora, A., Muinonen, K., Osinde, J., Pancino, E., Pauwels, T., Petit, J. M., Recio-Blanco, A., Richards, P. J., Rimoldini, L., Robin, A. C., Sarro, L. M., Siopis, C., Smith, M., Sozzetti, A., Süveges, M., Torra, J., van Reeven, W., Abbas, U., Abreu Aramburu, A., Accart, S., Aerts, C., Altavilla, G., Álvarez, M. A., Alvarez, R., Alves, J., Anderson, R. I., Andrei, A. H., Anglada Varela, E., Antiche, E., Antoja, T., Arcay, B., Astraatmadja, T. L., Bach, N., Baker, S. G., Balaguer-Núñez, L., Balm, P., Barache, C., Barata, C., Barbato, D., Barblan, F., Barklem, P. S., Barrado, D., Barros, M., Barstow, M. A., Bartholomé Muñoz, S., Bassilana, J. L., Becciani, U., Bellazzini, M., Berihuete, A., Bertone, S., Bianchi, L., Bienaymé, O., Blanco-Cuaresma, S., Boch, T., Boeche, C., Bombrun, A., Borrachero, R., Bossini, D., Bouquillon, S., Bourda, G., Bragaglia, A., Bramante, L., Breddels, M. A., Bressan, A., Brouillet, N., Brüsemeister, T., Brugaletta, E., Bucciarelli, B., Burlacu, A., Busonero, D., Butkevich, A. G., Buzzi, R., Caffau, E., Cancelliere, R., Cannizzaro, G., Cantat-Gaudin, T., Carballo, R., Carlucci, T., Carrasco, J. M., Casamiquela, L., Castellani, M., Castro-Ginard, A., Charlot, P., Chemin, L., Chiavassa, A., Cocozza, G., Costigan, G., Cowell, S., Crifo, F., Crosta, M., Crowley, C., Cuypers, J., Dafonte, C., Damerdji, Y., Dapergolas, A., David, P., David, M., de Laverny, P., De Luise, F., De March, R., de Martino, D., de Souza, R., de Torres, A., Debosscher, J., del Pozo, E., Delbo, M., Delgado, A., Delgado, H. E., Di Matteo, P., Diakite, S., Diener, C., Distefano, E., Dolding, C., Drazinos, P., Durán, J., Edvardsson, B., Enke, H., Eriksson, K., Esquej, P., Eynard Bontemps, G., Fabre, C., Fabrizio, M., Faigler, S., Falcão, A. J., Farràs Casas, M., Federici, L., Fedorets, G., Fernique, P., Figueras, F., Filippi, F., Findeisen, K., Fonti, A., Fraile, E., Fraser, M., Frézouls, B., Gai, M., Galleti, S., Garabato, D., García-Sedano, F., Garofalo, A., Garralda, N., Gavel, A., Gavras, P., Gerssen, J., Geyer, R., Giacobbe, P., Gilmore, G., Girona, S., Giuffrida, G., Glass, F., Gomes, M., Granvik, M., Gueguen, A., Guerrier, A., Guiraud, J., Gutiérrez-Sánchez, R., Haigron, R., Hatzidimitriou, D., Hauser, M., Haywood, M., Heiter, U., Helmi, A., Heu, J., Hilger, T., Hobbs, D., Hofmann, W., Holland, G., Huckle, H. E., Hypki, A., Icardi, V., Janßen, K., Jevardat de Fombelle, G., Jonker, P. G., Juhász, Á. L., Julbe, F., Karampelas, A., Kewley, A., Klar, J., Kochoska, A., Kohley, R., Kolenberg, K., Kontizas, M., Kontizas, E., Koposov, S. E., Kordopatis, G., Kostrzewa-Rutkowska, Z., Koubsky, P., Lambert, S., Lanza, A. F., Lasne, Y., Lavigne, J. B., Le Fustec, Y., Le Poncin-Lafitte, C., Lebreton, Y., Leccia, S., Leclerc, N., Lecoeur-Taibi, I., Lenhardt, H., Leroux, F., Liao, S., Licata, E., Lindstrøm, H. E. P., Lister, T. A., Livanou, E., Lobel, A., López, M., Managau, S., Mann, R. G., Mantelet, G., Marchal, O., Marchant, J. M., Marconi, M., Marinoni, S., Marschalkó, G., Marshall, D. J., Martino, M., Marton, G., Mary, N., Massari, D., Matijevič, G., Mazeh, T., McMillan, P. J., Messina, S., Michalik, D., Millar, N. R., Molina, D., Molinaro, R., Molnár, L., Montegriffo, P., Mor, R., Morbidelli, R., Morel, T., Morris, D., Mulone, A. F., Muraveva, T., Musella, I., Nelemans, G., Nicastro, L., Noval, L., O'Mullane, W., Ordénovic, C., Ordóñez-Blanco, D., Osborne, P., Pagani, C., Pagano, I., Pailler, F., Palacin, H., Palaversa, L., Panahi, A., Pawlak, M., Piersimoni, A. M., Pineau, F. X., Plachy, E., Plum, G., Poggio, E., Poujoulet, E., Prša, A., Pulone, L., Racero, E., Ragaini, S., Rambaux, N., Ramos-Lerate, M., Regibo, S., Reylé, C., Riclet, F., Ripepi, V., Riva, A., Rivard, A., Rixon, G., Roegiers, T., Roelens, M., Romero-Gómez, M., Rowell, N., Royer, F., Ruiz-Dern, L., Sadowski, G., Sagristà Sellés, T., Sahlmann, J., Salgado, J., Salguero, E., Sanna, N., Santana-Ros, T., Sarasso, M., Savietto, H., Schultheis, M., Sciacca, E., Segol, M.,

Segovia, J. C., Ségransan, D., Shih, I. C., Siltala, L., Silva, A. F., Smart, R. L., Smith, K. W., Solano, E., Solitro, F., Sordo, R., Soria Nieto, S., Souchay, J., Spagna, A., Spoto, F., Stampa, U., Steele, I. A., Steidelmüller, H., Stephenson, C. A., Stoev, H., Suess, F. F., Surdej, J., Szabados, L., Szegedi-Elek, E., Tapiador, D., Taris, F., Tauran, G., Taylor, M. B., Teixeira, R., Terrett, D., Teyssand ier, P., Thuillot, W., Titarenko, A., Torra Clotet, F., Turon, C., Ulla, A., Utrilla, E., Uzzi, S., Vaillant, M., Valentini, G., Valette, V., van Elteren, A., Van Hemelryck, E., van Leeuwen, M., Vaschetto, M., Vecchiato, A., Veljanoski, J., Viala, Y., Vicente, D., Vogt, S., von Essen, C., Voss, H., Votruba, V., Voutsinas, S., Walmsley, G., Weiler, M., Wertz, O., Wevers, T., Wyrzykowski, Ł., Yoldas, A., Žerjal, M., Ziaeepour, H., Zorec, J., Zschocke, S., Zucker, S., Zurbach, C., and Zwitter, T. (2018). Gaia Data Release 2. Summary of the contents and survey properties. Astronomy & Astrophysics, 616:A1.

Gaia Collaboration, Brown, A. G. A., Vallenari, A., Prusti, T., de Bruijne, J. H. J., Babusiaux, C., and Biermann, M. (2020a). Gaia Early Data Release 3: Summary of the contents and survey properties. arXiv e-prints, page arXiv:2012.01533.

Gaia Collaboration, Brown, A. G. A., Vallenari, A., Prusti, T., de Bruijne, J. H. J., Babusiaux, C., and Biermann, M. (2020b). Gaia Early Data Release 3: Summary of the contents and survey properties. arXiv e-prints, page arXiv:2012.01533.

Gaidos, E., Hirano, T., Mann, A. W., Owens, D. A., Berger, T. A., France, K., Vanderburg, A., Harakawa, H., Hodapp, K. W., Ishizuka, M., Jacobson, S., Konishi, M., Kotani, T., Kudo, T., Kurokawa, T., Kuzuhara, M., Nishikawa, J., Omiya, M., Serizawa, T., Tamura, M., and Ueda, A. (2020). Zodiacal exoplanets in time - X. The orbit and atmosphere of the young 'neptune desert'-dwelling planet K2-100b. Monthly Notices of the Royal Astronomical Society, 495(1):650–662.

Galicher, R., Marois, C., Macintosh, B., Barman, T., and Konopacky, Q. (2011). M-band imaging of the HR 8799 planetary system using an innovative LOCI-based background subtraction technique. The Astrophysical Journal, 739(2):L41.

Galle, J. G. (1846). Account of the discovery of Le Verrier's planet Neptune, at Berlin, Sept. 23, 1846. Monthly Notices of the Royal Astronomical Society, 7:153.

Gänsicke, B. T., Schreiber, M. R., Toloza, O., Gentile Fusillo, N. P., Koester, D., and Manser, C. J. (2019). Accretion of a giant planet onto a white dwarf star. Nature, 576(7785):61–64.

Garhart, E., Deming, D., Mandell, A., Knutson, H., and Fortney, J. J. (2018). Spitzer secondary eclipses of Qatar-1b. Astronomy & Astrophysics, 610:A55.

Garufi, A., Quanz, S. P., Schmid, H. M., Avenhaus, H., Buenzli, E., and Wolf, S. (2014). Shadows and cavities in protoplanetary disks: Hd296, hd569a, and hd193a in polarized light. Astronomy & Astrophysics, 568:A40.

Geißler, K., Chauvin, G., and Sterzik, M. F. (2008). Mid-infrared imaging of brown dwarfs in binary systems. Astronomy & Astrophysics, 480(1):193–198.

Geißler, K., Kellner, S., Brandner, W., Masciadri, E., Hartung, M., Henning, T., Lenzen, R., Close, L., Endl, M., and Kürster, M. (2007). A direct and differential imaging search for sub-stellar companions to ∈ Indi A. Astronomy & Astrophysics, 461(2):665–668.

Gibson, N. P. (2014). Reliable inference of exoplanet light-curve parameters using deterministic and stochastic systematics models. Monthly Notices of the Astronomical Royal Society, 445(4):3401–3414.

Gibson, N. P., Aigrain, S., Roberts, S., Evans, T. M., Osborne, M., and Pont, F. (2012). A Gaussian process framework for modelling instrumental systematics: application to transmission spectroscopy. Monthly Notices of the Astronomical Royal Society, 419(3):2683–2694.

Gibson, N. P., Nikolov, N., Sing, D. K., Barstow, J. K., Evans, T. M., Kataria, T., and Wilson, P. A. (2017). VLT/FORS2 comparative transmission spectroscopy II: Confirmation of a cloud deck and Rayleigh scattering in WASP-31b, but no potassium? Monthly Notices of the Royal Astronomical Society, 467(4):4591–4605.

Gillon, M., Jehin, E., Lederer, S. M., Delrez, L., de Wit, J., Burdanov, A., Van Grootel, V., Burgasser, A. J., Triaud, A. H. M. J., Opitom, C., Demory, B.-O., Sahu, D. K., Bardalez Gagliuffi, D., Magain, P., and Queloz, D. (2016). Temperate Earth-sized planets transiting a nearby ultracool dwarf star. Nature, 533(7602):221–224.

Ginzburg, S., Schlichting, H. E., and Sari, R. (2018). Core-powered mass-loss and the radius distribution of small exoplanets. Monthly Notices of the Royal Astronomical Society, 476(1):759–765.

Glasse, A., Rieke, G. H., Bauwens, E., García-Marín, M., Ressler, M. E., Rost, S., Tikkanen, T. V., Vandenbussche, B., and Wright, G. S. (2015). The Mid-Infrared Instrument for the James Webb Space Telescope, IX: Predicted Sensitivity. Publications of the Astronomical Society of the Pacific, 127(953):686.

Gomez Gonzalez, C. A., Wertz, O., Absil, O., Christiaens, V., Defrère, D., Mawet, D., Milli, J., Absil, P.-A., Van Droogenbroeck, M., Cantalloube, F., Hinz, P. M., Skemer, A. J., Karlsson, M., and Surdej, J. (2017). VIP: Vortex Image Processing Package for High-contrast Direct Imaging. The Astronomical Journal, 154(1):7.

Gonzalez, J.-F., van der Plas, G., Pinte, C., Cuello, N., Nealon, R., Ménard, F., Revol, A., Rodet, L., Langlois, M., and Maire, A.-L. (2020). Spirals, shadows, and precession in HD 100453 - I. The orbit of the binary. Monthly Notices of the Royal Society, 499(3):3837–3856.

Goyal, J. M., Mayne, N., Sing, D. K., Drummond, B., Tremblin, P., Amundsen, D. S., Evans, T., Carter, A. L., Spake, J., Baraffe, I., Nikolov, N., Manners, J., Chabrier, G., and Hebrard, E. (2018). A library of ATMO forward model transmission spectra for hot Jupiter exoplanets. Monthly Notices of the Royal Astronomical Society, 474(4):5158–5185.

Goyal, J. M., Wakeford, H. R., Mayne, N. J., Lewis, N. K., Drummond, B., and Sing, D. K. (2019). Fully scalable forward model grid of exoplanet transmission spectra. Monthly Notices of the Royal Astronomical Society, 482(4):4503–4513.

Grady, C. A., Muto, T., Hashimoto, J., Fukagawa, M., Currie, T., Biller, B., Thalmann, C., Sitko, M. L., Russell, R., Wisniewski, J., Dong, R., Kwon, J., Sai, S., Hornbeck, J., Schneider, G., Hines, D., Moro Martín, A., Feldt, M., Henning, T., Pott, J. U., Bonnefoy, M., Bouwman, J., Lacour, S., Mueller, A., Juhász, A., Crida, A., Chauvin, G., Andrews, S., Wilner, D., Kraus, A., Dahm, S., Robitaille, T., Jang-Condell, H., Abe, L., Akiyama, E., Brandner, W., Brandt, T., Carson, J., Egner, S., Follette, K. B., Goto, M., Guyon, O., Hayano, Y., Hayashi, M., Hayashi, S., Hodapp, K., Ishii, M., Iye, M., Janson, M., Kandori, R., Knapp, G., Kudo, T., Kusakabe, N., Kuzuhara, M., Mayama, S., McElwain, M., Matsuo, T., Miyama, S., Morino, J. I., Nishimura, T., Pyo, T. S., Serabyn, G., Suto, H., Suzuki, R., Takami, M., Takato, N., Terada, H., Tomono, D., Turner, E., Watanabe, M., Yamada, T., Takami, H., Usuda, T., and Tamura, M. (2013). Spiral Arms in the Asymmetrically Illuminated Disk of MWC 758 and Constraints on Giant Planets. The Astrophysical Journal, 762(1):48.

Grady, C. A., Woodgate, B., Heap, S. R., Bowers, C., Nuth, J. A., I., Herczeg, G. J., and Hill, H. G. M. (2005). Resolving the Inner Cavity of the HD 100546 Disk: A Candidate Young Planetary System? The Astrophysical Journal, 620(1):470–480.

Gratton, R., D'Orazi, V., Pacheco, T. A., Zurlo, A., Desidera, S., Melendez, J., Mesa, D., Claudi, R., Janson, M., Langlois, M., Rickman, E., Samland, M., Moulin, T., Soenke, C., Cascone, E., Ramos, J., Rigal, F., Avenhaus, H., Beuzit, J. L., Biller, B., Boccaletti, A., Bonavita, M., Bonnefoy, M., Brandner, W., Chauvin, G., Cudel, M., Daemgen, S., Delorme, P., Desgrange, C., Engler, N., Feldt, M., Fontanive, C., Galicher, R., Garufi, A., Gasparri, D., Ginski, C., Girard, J., Hagelberg, J., Hunziker, S., Kasper, M., Keppler, M., Lagrange, A. M., Lannier, J., Lazzoni, C., Le Coroller, H., Ligi, R., Lombart, M., Maire, A. L., Mayer, M. R., Mazevet, S., Menard, F., Mouillet, D., Perrot, C., Peretti, S., Petrus, S., Potier, A., Rouan, D., Schmid, H. M., Schmidt, T. O. B., Sissa, E., Stolker, T., Salter, G., Vigan, A., and Wildi, F. (2020). Investigating three Sirius-like systems with SPHERE. arXiv e-prints, page arXiv:2012.05575.

Gratton, R., Ligi, R., Sissa, E., Desidera, S., Mesa, D., Bonnefoy, M., Chauvin, G., Cheetham, A., Feldt, M., Lagrange, A. M., Langlois, M., Meyer, M., Vigan, A., Boccaletti, A., Janson, M., Lazzoni, C., Zurlo, A., De Boer, J., Henning, T., D'Orazi, V., Gluck, L., Madec, F., Jaquet, M., Baudoz, P., Fantinel, D., Pavlov, A., and Wildi, F. (2019). Blobs, spiral arms, and a possible planet around HD 169142. Astronomy & Astrophysics, 623:A140.

Gray, R. O., Corbally, C. J., Garrison, R. F., McFadden, M. T., Bubar, E. J., McGahee, C. E., O'Donoghue, A. A., and Knox, E. R. (2006). Contributions to the Nearby Stars (NStars) Project: Spectroscopy of Stars Earlier than M0 within 40 pc-The Southern Sample. The Astronomical Journal, 132(1):161–170.

Greaves, J. S., Wyatt, M. C., Holland, W. S., and Dent, W. R. F. (2004). The debris disc around

τ Ceti: a massive analogue to the Kuiper Belt. Monthly Notices of the Royal Astronomical Society, 351(3):L54–L58.

Guidi, G., Ruane, G., Williams, J. P., Mawet, D., Testi, L., Zurlo, A., Absil, O., Bottom, M., Choquet, E., Christiaens, V., Femenía Castellá, B., Huby, E., Isella, A., Kastner, J., Meshkat, T., Reggiani, M., Riggs, A., Serabyn, E., and Wallack, N. (2018). High-contrast imaging of HD 163296 with the Keck/NIRC2 L'-band vortex coronograph. Monthly Notices of the Royal Astronomical Society, 479(2):1505–1513.

Guilluy, G., Andretta, V., Borsa, F., Giacobbe, P., Sozzetti, A., Covino, E., Bourrier, V., Fossati, L., Bonomo, A. S., Esposito, M., Giampapa, M. S., Harutyunyan, A., Rainer, M., Brogi, M., Bruno, G., Claudi, R., Frustagli, G., Lanza, A. F., Mancini, L., Pino, L., Poretti, E., Scandariato, G., Affer, L., Baffa, C., Baruffolo, A., Benatti, S., Biazzo, K., Bignamini, A., Boschin, W., Carleo, I., Cecconi, M., Cosentino, R., Damasso, M., Desidera, S., Falcini, G., Martinez Fiorenzano, A. F., Ghedina, A., González-Álvarez, E., Guerra, J., Hernandez, N., Leto, G., Maggio, A., Malavolta, L., Maldonado, J., Micela, G., Molinari, E., Nascimbeni, V., Pagano, I., Pedani, M., Piotto, G., and Reiners, A. (2020). The GAPS programme at TNG. XXII. The GIARPS view of the extended helium atmosphere of HD 189733 b accounting for stellar activity. Astronomy & Astrophysics, 639:A49.

Gupta, A. and Schlichting, H. E. (2019). Sculpting the valley in the radius distribution of small exoplanets as a by-product of planet formation: the core-powered mass-loss mechanism. Monthly Notices of the Royal Astronomical Society, 487(1):24–33.

Guyon, O. (2003). Phase-induced amplitude apodization of telescope pupils for extrasolar terrestrial planet imaging. Astronomy & Astrophysics, 404:379–387.

Habing, H. J. (1968). The interstellar radiation density between 912 A and 2400 A. Bulletin of the Astronomical Institutes of the Netherlands, 19:421.

Haffert, S. Y., Bohn, A. J., de Boer, J., Snellen, I. A. G., Brinchmann, J., Girard, J. H., Keller, C. U., and Bacon, R. (2019). Two accreting protoplanets around the young star PDS 70. Nature Astronomy, 3:749–754.

Harpsøe, K. B. W., Hardis, S., Hinse, T. C., Jørgensen, U. G., Mancini, L., Southworth, J., Alsubai, K. A., Bozza, V., Browne, P., Burgdorf, M. J., Calchi Novati, S., Dodds, P., Dominik, M., Fang, X. S., Finet, F., Gerner, T., Gu, S. H., Hundertmark, M., Jessen-Hansen, J., Kains, N., Kerins, E., Kjeldsen, H., Liebig, C., Lund, M. N., Lundkvist, M., Mathiasen, M., Nesvorný, D., Nikolov, N., Penny, M. T., Proft, S., Rahvar, S., Ricci, D., Sahu, K. C., Scarpetta, G., Schäfer, S., Schönebeck, F., Snodgrass, C., Skottfelt, J., Surdej, J., Tregloan-Reed, J., and Wertz, O. (2013). The transiting system GJ1214: high-precision defocused transit observations and a search for evidence of transit timing variation. Astronomy & Astrophysics, 549:A10.

Hatzes, A. P., Cochran, W. D., McArthur, B., Baliunas, S. L., Walker, G. A. H., Campbell, B., Irwin, A. W., Yang, S., Kürster, M., Endl, M., Els, S., Butler, R. P., and Marcy, G. W. (2000).

Evidence for a Long-Period Planet Orbiting ∈ Eridani. The Astrophysical Journal Letters, 544(2):L145–L148.

Henry, G. W., Marcy, G., Butler, R. P., and Vogt, S. S. (1999). HD 209458. IAU Circular, 7307:1.

Henry, T. J., Soderblom, D. R., Donahue, R. A., and Baliunas, S. L. (1996). A Survey of Ca II H and K Chromospheric Emission in Southern Solar-Type Stars. The Astronomical Journal, 111:439.

Herczeg, G. J. and Hillenbrand, L. A. (2014). An Optical Spectroscopic Study of T Tauri Stars. I. Photospheric Properties. The Astrophysical Journal, 786(2):97.

Herschel, W. and Watson, D. (1781). Account of a Comet. By Mr. Herschel, F. R. S.; Communicated by Dr. Watson, Jun. of Bath, F. R. S. Philosophical Transactions of the Royal Society of London Series I, 71:492–501.

Hinz, P. M. et al. (2010). Thermal infrared MMTAO observations of the HR 8799 planetary system. The Astrophysical Journal, 716(1):417.

Hoeijmakers, H., Schwarz, H., Snellen, I., de Kok, R., Bonnefoy, M., Chauvin, G., Lagrange, A., and Girard, J. (2018). Medium-resolution integral-field spectroscopy for high-contrast exoplanet imaging: Molecule maps of the beta pictoris system with sinfoni. arXiv preprint arXiv:1802.09721.

Hoeijmakers, H. J., Seidel, J. V., Pino, L., Kitzmann, D., Sindel, J. P., Ehrenreich, D., Oza, A. V., Bourrier, V., Allart, R., Gebek, A., Lovis, C., Yurchenko, S. N., Astudillo-Defru, N., Bayliss, D., Cegla, H., Lavie, B., Lendl, M., Melo, C., Murgas, F., Nascimbeni, V., Pepe, F., Ségransan, D., Udry, S., Wyttenbach, A., and Heng, K. (2020). Hot Exoplanet Atmospheres Resolved with Transit Spectroscopy (HEARTS). IV. A spectral inventory of atoms and molecules in the high-resolution transmission spectrum of WASP-121 b. Astronomy & Astrophysics, 641:A123.

Honda, M., Maaskant, K., Okamoto, Y. K., Kataza, H., Fukagawa, M., Waters, L. B. F. M., Dominik, C., Tielens, A. G. G. M., Mulders, G. D., Min, M., Yamashita, T., Fujiyoshi, T., Miyata, T., Sako, S., Sakon, I., Fujiwara, H., and Onaka, T. (2012). MID-INFRARED IMAGING OF THE TRANSITIONAL DISK OF HD 169142: MEASURING THE SIZE OF THE GAP. The Astrophysical Journal, 752(2):143.

Huang, J., Andrews, S. M., Cleeves, L. I., Öberg, K. I., Wilner, D. J., Bai, X., Birnstiel, T., Carpenter, J., Hughes, A. M., Isella, A., Pérez, L. M., Ricci, L., and Zhu, Z. (2018). CO and dust properties in the TW hya disk from high-resolution ALMA observations. The Astrophysical Journal, 852(2):122.

Hunziker, S., Schmid, H. M., Mouillet, D., Milli, J., Zurlo, A., Delorme, P., Abe, L., Avenhaus, H., Baruffolo, A., Bazzon, A., Boccaletti, A., Baudoz, P., Beuzit, J. L., Carbillet, M., Chauvin,

G., Claudi, R., Costille, A., Daban, J. B., Desidera, S., Dohlen, K., Dominik, C., Downing, M., Engler, N., Feldt, M., Fusco, T., Ginski, C., Gisler, D., Girard, J. H., Gratton, R., Henning, T., Hubin, N., Kasper, M., Keller, C. U., Langlois, M., Lagadec, E., Martinez, P., Maire, A. L., Menard, F., Meyer, M. R., Pavlov, A., Pragt, J., Puget, P., Quanz, S. P., Rickman, E., Roelfsema, R., Salasnich, B., Sauvage, J. F., Siebenmorgen, R., Sissa, E., Snik, F., Suarez, M., Szulágyi, J., Thalmann, C., Turatto, M., Udry, S., van Holstein, R. G., Vigan, A., and Wildi, F. (2020). RefPlanets: Search for reflected light from extrasolar planets with SPHERE/ZIMPOL. Astronomy & Astrophysics, 634:A69.

Husser, T. O., Wende-von Berg, S., Dreizler, S., Homeier, D., Reiners, A., Barman, T., and Hauschildt, P. H. (2013). A new extensive library of PHOENIX stellar atmospheres and synthetic spectra. Astronomy & Astrophysics, 553:A6.

IAU (2006). Iau 2006 general assembly: Result of the iau resolution votes. `https://www.iau.org/static/archives/releases/doc/iau0603.doc`. Accessed: 2021-06-09.

IAU Working Group on ExtraSolar Planets (2003). Position statement on the definiton of a "planet". `https://w.astro.berkeley.edu/~basri/defineplanet/IAU-WGExSP.htm`. Accessed: 2021-06-10.

Ireland, M. J., Kraus, A., Martinache, F., Law, N., and Hillenbrand, L. A. (2011). Two Wide Planetary-mass Companions to Solar-type Stars in Upper Scorpius. The Astrophysical Journal, 726(2):113.

Isella, A., Benisty, M., Teague, R., Bae, J., Keppler, M., Facchini, S., and Pérez, L. (2019). Detection of Continuum Submillimeter Emission Associated with Candidate Protoplanets. The Astrophysical Journal Letters, 879(2):L25.

Isella, A., Guidi, G., Testi, L., Liu, S., Li, H., Li, S., Weaver, E., Boehler, Y., Carperter, J. M., De Gregorio-Monsalvo, I., Manara, C. F., Natta, A., Pérez, L. M., Ricci, L., Sargent, A., Tazzari, M., and Turner, N. (2016). Ringed structures of the hd 163296 protoplanetary disk revealed by alma. Phys. Rev. Lett., 117:251101.

Isella, A., Huang, J., Andrews, S. M., Dullemond, C. P., Birnstiel, T., Zhang, S., Zhu, Z., Guzmán, V. V., Pérez, L. M., Bai, X.-N., Benisty, M., Carpenter, J. M., Ricci, L., and Wilner, D. J. (2018). The Disk Substructures at High Angular Resolution Project (DSHARP). IX. A High-definition Study of the HD 163296 Planet-forming Disk. The Astrophysical Journal Letters, 869(2):L49.

Isella, A., Natta, A., Wilner, D., Carpenter, J. M., and Testi, L. (2010). Millimeter Imaging of MWC 758: Probing the Disk Structure and Kinematics. The Astrophysical Journal, 725(2):1735–1741.

Ishihara, D., Onaka, T., Kataza, H., Salama, A., Alfageme, C., Cassatella, A., Cox, N., García-Lario, P., Stephenson, C., Cohen, M., Fujishiro, N., Fujiwara, H., Hasegawa, S., Ita, Y., Kim, W., Matsuhara, H., Murakami, H., Müller, T. G., Nakagawa, T., Ohyama, Y., Oyabu, S., Pyo,

J., Sakon, I., Shibai, H., Takita, S., Tanabé, T., Uemizu, K., Ueno, M., Usui, F., Wada, T., Watarai, H., Yamamura, I., and Yamauchi, C. (2010). The AKARI/IRC mid-infrared all-sky survey. Astronomy & Astrophysics, 514:A1.

Izidoro, A. and Raymond, S. N. (2018). Formation of Terrestrial Planets, page 142.

Izzo, C., de Bilbao, L., Larsen, J., Bagnulo, S., Freudling, W., Moehler, S., and Ballester, P. (2010). The new FORS pipeline. In Silva, D. R., Peck, A. B., and Soifer, B. T., editors, Observatory Operations: Strategies, Processes, and Systems III, volume 7737, pages 584 – 591. International Society for Optics and Photonics, SPIE.

Jamialahmadi, N., Ratzka, T., Panić, O., Fathivavsari, H., van Boekel, R., Flement, S., Henning, T., Jaffe, W., and Mulders, G. D. (2018). Constraining the Gap Size in the Disk around HD 100546 in the Mid-infrared. The Astrophysical Journal, 865(2):137.

Janson, M., Apai, D., Zechmeister, M., Brandner, W., Kürster, M., Kasper, M., Reffert, S., Endl, M., Lafrenière, D., Geißler, K., Hippler, S., and Henning, T. (2009). Imaging search for the unseen companion to $\in$ Ind A - improving the detection limits with 4 μm observations. Monthly Notices of the Royal Astronomical Society, 399(1):377–384.

Janson, M., Quanz, S. P., Carson, J. C., Thalmann, C., Lafrenière, D., and Amara, A. (2015). High-contrast imaging with Spitzer: deep observations of Vega, Fomalhaut, and $\in$ Eridani. Astronomy & Astrophysics, 574:A120.

Janson, M., Reffert, S., Brandner, W., Henning, T., Lenzen, R., and Hippler, S. (2008). A comprehensive examination of the $\in$ Eridani system. Verification of a 4 micron narrow-band high-contrast imaging approach for planet searches. Astronomy & Astrophysics, 488(2):771–780.

Jayawardhana, R., Fisher, R. S., Telesco, C. M., Piña, R. K., Barrado y Navascués, D., Hartmann, L. W., and Fazio, G. G. (2001). Mid-Infrared Imaging of Candidate Vega-like Systems. The Astronomical Journal, 122(4):2047–2054.

Jin, S. and Mordasini, C. (2018). Compositional Imprints in Density-Distance-Time: A Rocky Composition for Close-in Low-mass Exoplanets from the Location of the Valley of Evaporation. The Astrophysical Journal, 853(2):163.

Joblin, C., Berné, O., Simon, A., and Mulas, G. (2009). Laboratory Studies of Polycyclic Aromatic Hydrocarbons: the Search for Interstellar Candidates. In Henning, T., Grün, E., and Steinacker, J., editors, Cosmic Dust - Near and Far, volume 414 of Astronomical Society of the Pacific Conference Series, page 383.

Jovanovic, N., Martinache, F., Guyon, O., Clergeon, C., Singh, G., Kudo, T., Garrel, V., Newman, K., Doughty, D., Lozi, J., Males, J., Minowa, Y., Hayano, Y., Takato, N., Morino, J., Kuhn, J., Serabyn, E., Norris, B., Tuthill, P., Schworer, G., Stewart, P., Close, L., Huby, E., Perrin, G., Lacour, S., Gauchet, L., Vievard, S., Murakami, N., Oshiyama, F., Baba, N., Matsuo,

T., Nishikawa, J., Tamura, M., Lai, O., Marchis, F., Duchene, G., Kotani, T., and Woillez, J. (2015). The Subaru Coronagraphic Extreme Adaptive Optics System: Enabling High-Contrast Imaging on Solar-System Scales. Publications of the Astronomical Society of the Pacific, 127(955):890.

Kamp, I., Thi, W. F., Woitke, P., Rab, C., Bouma, S., and Ménard, F. (2017). Consistent dust and gas models for protoplanetary disks. II. Chemical networks and rates. Astronomy & Astrophysics, 607:A41.

Kamp, I., Tilling, I., Woitke, P., Thi, W. F., and Hogerheijde, M. (2010). Radiation thermochemical models of protoplanetary disks. II. Line diagnostics. Astronomy and Astrophysics, 510:A18.

Kapoor, A., Grauman, K., Urtasun, R., and Darrell, T. (2010). Gaussian processes for object categorization. International Journal of Computer Vision, 88:169–188.

Kasper, M., Arsenault, R., Käufl, H. U., Jakob, G., Fuenteseca, E., Riquelme, M., Siebenmorgen, R., Sterzik, M., Zins, G., Ageorges, N., Gutruf, S., Reutlinger, A., Kampf, D., Absil, O., Carlomagno, B., Guyon, O., Klupar, P., Mawet, D., Ruane, G., Karlsson, M., Pantin, E., and Dohlen, K. (2017a). NEAR: Low-mass Planets in α Cen with VISIR. The Messenger, 169:16–20.

Kasper, M., Arsenault, R., Käufl, H. U., Jakob, G., Fuenteseca, E., Riquelme, M., Siebenmorgen, R., Sterzik, M., Zins, G., Ageorges, N., Gutruf, S., Reutlinger, A., Kampf, D., Absil, O., Carlomagno, B., Guyon, O., Klupar, P., Mawet, D., Ruane, G., Karlsson, M., Pantin, E., and Dohlen, K. (2017b). NEAR: Low-mass Planets in α Cen with VISIR. The Messenger, 169:16–20.

Kasper, M., Arsenault, R., Käufl, U., Jakob, G., Leveratto, S., Zins, G., Pantin, E., Duhoux, P., Riquelme, M., Kirchbauer, J. P., Kolb, J., Pathak, P., Siebenmorgen, R., Soenke, C., Fuenteseca, E., Sterzik, M., Ageorges, N., Gutruf, S., Kampf, D., Reutlinger, A., Absil, O., Delacroix, C., Maire, A. L., Huby, E., Guyon, O., Klupar, P., Mawet, D., Ruane, G., Karlsson, M., Dohlen, K., Vigan, A., N'Diaye, M., Quanz, S., and Carlotti, A. (2019). NEAR: First Results from the Search for Low-Mass Planets in α Cen. The Messenger, 178:5–9.

Kasper, M., Burrows, A., and Brandner, W. (2009). Testing the Models: NIR Imaging and Spectroscopy of the Benchmark T-Dwarf Binary Eps Indi B. The Astrophysical Journal, 695(1):788–792.

Keles, E., Mallonn, M., von Essen, C., Carroll, T. A., Alexoudi, X., Pino, L., Ilyin, I., Poppenhäger, K., Kitzmann, D., Nascimbeni, V., Turner, J. D., and Strassmeier, K. G. (2019). The potassium absorption on HD189733b and HD209458b. Monthly Notices of the Royal Astronomical Society: Letters, 489(1):L37–L41.

Kenworthy, M., Quanz, S., Meyer, M., Kasper, M., Girard, J., Lenzen, R., Codona, J., and Hinz, P. (2010a). A New Coronagraph for NAOS-CONICA – the Apodising Phase Plate. The Messenger, 141:2–4.

Kenworthy, M. A., Quanz, S. P., Meyer, M. R., Kasper, M. E., Lenzen, R., Codona, J. L., Girard, J. H., and Hinz, P. M. (2010b). An apodizing phase plate coronagraph for VLT/NACO. In McLean, I. S., Ramsay, S. K., and Takami, H., editors, Ground-based and Airborne Instrumentation for Astronomy III, volume 7735 of Society of Photo-Optical Instrumentation Engineers (SPIE) Conference Series, page 773532.

Keppler, M., Benisty, M., Müller, A., Henning, T., van Boekel, R., Cantalloube, F., Ginski, C., van Holstein, R. G., Maire, A. L., Pohl, A., Samland , M., Avenhaus, H., Baudino, J. L., Boccaletti, A., de Boer, J., Bonnefoy, M., Chauvin, G., Desidera, S., Langlois, M., Lazzoni, C., Marleau, G. D., Mordasini, C., Pawellek, N., Stolker, T., Vigan, A., Zurlo, A., Birnstiel, T., Brandner, W., Feldt, M., Flock, M., Girard, J., Gratton, R., Hagelberg, J., Isella, A., Janson, M., Juhasz, A., Kemmer, J., Kral, Q., Lagrange, A. M., Launhardt, R., Matter, A., Ménard, F., Milli, J., Mollière, P., Olofsson, J., Pérez, L., Pinilla, P., Pinte, C., Quanz, S. P., Schmidt, T., Udry, S., Wahhaj, Z., Williams, J. P., Buenzli, E., Cudel, M., Dominik, C., Galicher, R., Kasper, M., Lannier, J., Mesa, D., Mouillet, D., Peretti, S., Perrot, C., Salter, G., Sissa, E., Wildi, F., Abe, L., Antichi, J., Augereau, J. C., Baruffolo, A., Baudoz, P., Bazzon, A., Beuzit, J. L., Blanchard, P., Brems, S. S., Buey, T., De Caprio, V., Carbillet, M., Carle, M., Cascone, E., Cheetham, A., Claudi, R., Costille, A., Delboulbé, A., Dohlen, K., Fantinel, D., Feautrier, P., Fusco, T., Giro, E., Gluck, L., Gry, C., Hubin, N., Hugot, E., Jaquet, M., Le Mignant, D., Llored, M., Madec, F., Magnard, Y., Martinez, P., Maurel, D., Meyer, M., Möller-Nilsson, O., Moulin, T., Mugnier, L., Origné, A., Pavlov, A., Perret, D., Petit, C., Pragt, J., Puget, P., Rabou, P., Ramos, J., Rigal, F., Rochat, S., Roelfsema, R., Rousset, G., Roux, A., Salasnich, B., Sauvage, J. F., Sevin, A., Soenke, C., Stadler, E., Suarez, M., Turatto, M., and Weber, L. (2018). Discovery of a planetary-mass companion within the gap of the transition disk around PDS 70. Astronomy & Astrophysics, 617:A44.

Keppler, M., Teague, R., Bae, J., Benisty, M., Henning, T., van Boekel, R., Chapillon, E., Pinilla, P., Williams, J. P., Bertrang, G. H. M., Facchini, S., Flock, M., Ginski, C., Juhasz, A., Klahr, H., Liu, Y., Müller, A., Pérez, L. M., Pohl, A., Rosotti, G., Samland, M., and Semenov, D. (2019). Highly structured disk around the planet host PDS 70 revealed by high-angular resolution observations with ALMA. Astronomy & Astrophysics, 625:A118.

Kervella, P., Arenou, F., Mignard, F., and Thévenin, F. (2019). Stellar and substellar companions of nearby stars from Gaia DR2. Binarity from proper motion anomaly. Astronomy & Astrophysics, 623:A72.

Khalafinejad, S., Maaskant, K. M., Mariñas, N., and Tielens, A. G. G. M. (2016). Large dust gaps in the transitional disks of HD 100453 and HD 34282. Connecting the gap size to the spectral energy distribution and mid-infrared imaging. Astronomy & Astrophysics, 587:A62.

Kiefer, F., Hébrard, G., Lecavelier des Etangs, A., Martioli, E., Dalal, S., and Vidal-Madjar, A. (2021). Determining the true mass of radial-velocity exoplanets with Gaia. Nine planet candidates in the brown dwarf or stellar regime and 27 confirmed planets. Astronomy & Astrophysics, 645:A7.

Kilpatrick, B. M., Lewis, N. K., Kataria, T., Deming, D., Ingalls, J. G., Krick, J. E., and Tucker, G. S. (2017). Spitzer Secondary Eclipse Depths with Multiple Intrapixel Sensitivity Correction Methods Observations of WASP-13b, WASP-15b, WASP-16b, WASP-62b, and HAT-P-22b. The Astornomical Journal, 153(1):22.

Kim, H.-C. and Lee, J. (2007). Clustering Based on Gaussian Processes. Neural Computation, 19(11):3088–3107.

King, R. R., McCaughrean, M. J., Homeier, D., Allard, F., Scholz, R. D., and Lodieu, N. (2010). ∈ Indi Ba, Bb: a detailed study of the nearest known brown dwarfs. Astronomy & Astrophysics, 510:A99.

Kipping, D. M. (2013). Efficient, uninformative sampling of limb darkening coefficients for two-parameter laws. Monthly Notices of the Royal Astronomical Society, 435(3):2152–2160.

Kluska, J., Berger, J. P., Malbet, F., Lazareff, B., Benisty, M., Le Bouquin, J. B., Absil, O., Baron, F., Delboulbé, A., Duvert, G., Isella, A., Jocou, L., Juhasz, A., Kraus, S., Lachaume, R., Ménard, F., Millan-Gabet, R., Monnier, J. D., Moulin, T., Perraut, K., Rochat, S., Pinte, C., Soulez, F., Tallon, M., Thi, W. F., Thiébaut, E., Traub, W., and Zins, G. (2020). A family portrait of disk inner rims around Herbig Ae/Be stars. Hunting for warps, rings, self shadowing, and misalignments in the inner astronomical units. Astronomy & Astrophysics, 636:A116.

Kramer, M. (2018). Pulsar Timing as an Exoplanet Discovery Method, page 5. Springer.

Kratter, K. and Lodato, G. (2016). Gravitational Instabilities in Circumstellar Disks. Annual Review of Astronomy and Astrophysics, 54:271–311.

Kreidberg, L. (2015). batman: BAsic Transit Model cAlculatioN in Python. Publications of the Astronomical Society of the Pacific, 127:1161.

Kreidberg, L. (2018). Exoplanet Atmosphere Measurements from Transmission Spectroscopy and Other Planet S page 100. Springer.

Kreidberg, L. and Oklopčić, A. (2018). Non-detection of a Helium Exosphere for the Hot Jupiter WASP-12b. RNAAS, 2(2):44.

Lachaume, R., Dominik, C., Lanz, T., and Habing, H. J. (1999). Age determinations of main-sequence stars: combining different methods. Astronomy & Astrophysics, 348:897–909.

Lagage, P. O., Pel, J. W., Authier, M., Belorgey, J., Claret, A., Doucet, C., Dubreuil, D., Durand, G., Elswijk, E., Girardot, P., Käufl, H. U., Kroes, G., Lortholary, M., Lussignol, Y., Marchesi, M., Pantin, E., Peletier, R., Pirard, J. F., Pragt, J., Rio, Y., Schoenmaker, T., Siebenmorgen,

R., Silber, A., Smette, A., Sterzik, M., and Veyssiere, C. (2004). Successful Commissioning of VISIR: The Mid-Infrared VLT Instrument. The Messenger, 117:12–16.

Lalitha, S., Poppenhaeger, K., Singh, K. P., Czesla, S., and Schmitt, J. H. M. M. (2014). X-Ray Emission from the Super-Earth Host GJ 1214. The Astrophysical Journal Letters, 790(1):L11.

Lambrechts, M. and Johansen, A. (2012). Rapid growth of gas-giant cores by pebble accretion. Astronomy & Astrophyics, 544:A32.

Lambrechts, M. and Johansen, A. (2014). Forming the cores of giant planets from the radial pebble flux in protoplanetary discs. Astronomy & Astrophysics, 572:A107.

Lawler, S. M., Di Francesco, J., Kennedy, G. M., Sibthorpe, B., Booth, M., Vandenbussche, B., Matthews, B. C., Holland, W. S., Greaves, J., Wilner, D. J., Tuomi, M., Blommaert, J. A. D. L., de Vries, B. L., Dominik, C., Fridlund, M., Gear, W., Heras, A. M., Ivison, R., and Olofsson, G. (2014). The debris disc of solar analogue τ Ceti: Herschel observations and dynamical simulations of the proposed multiplanet system. Monthly Notices of the Royal Astronomical Society, 444(3):2665–2675.

Lecavelier des Etangs, Vidal-Madjar, A., Désert, J.-M., and Sing, D. (2008). Rayleigh scattering by h2 in the extrasolar planet hd458b. A&A, 485(3):865–869.

Lecavelier des Etangs, A., Bourrier, V., Wheatley, P. J., Dupuy, H., Ehrenreich, D., Vidal-Madjar, A., Hébrard, G., Ballester, G. E., Désert, J. M., Ferlet, R., and Sing, D. K. (2012). Temporal variations in the evaporating atmosphere of the exoplanet HD 189733b. Astronomy & Astrophysics, 543:L4.

Leinert, C., van Boekel, R., Waters, L. B. F. M., Chesneau, O., Malbet, F., Köhler, R., Jaffe, W., Ratzka, T., Dutrey, A., Preibisch, T., Graser, U., Bakker, E., Chagnon, G., Cotton, W. D., Dominik, C., Dullemond, C. P., Glazenborg-Kluttig, A. W., Glindemann, A., Henning, T., Hofmann, K. H., de Jong, J., Lenzen, R., Ligori, S., Lopez, B., Meisner, J., Morel, S., Paresce, F., Pel, J. W., Percheron, I., Perrin, G., Przygodda, F., Richichi, A., Schöller, M., Schuller, P., Stecklum, B., van den Ancker, M. E., von der Lühe, O., and Weigelt, G. (2004). Mid-infrared sizes of circumstellar disks around Herbig Ae/Be stars measured with MIDI on the VLTI. Astronomy & Astrophysics, 423:537–548.

Lendl, M., Delrez, L., Gillon, M., Madhusudhan, N., Jehin, E., Queloz, D., Anderson, D. R., Demory, B. O., and Hellier, C. (2016). FORS2 observes a multi-epoch transmission spectrum of the hot Saturn-mass exoplanet WASP-49b. Astronomy & Astrophysics, 587:A67.

Lendl, M., Gillon, M., Queloz, D., Alonso, R., Fumel, A., Jehin, E., and Naef, D. (2013). A photometric study of the hot exoplanet WASP-19b. Astronomy & Astrophysics, 552:A2.

Li, A. and Draine, B. T. (2001). Infrared Emission from Interstellar Dust. II. The Diffuse Interstellar Medium. The Astrophysical Journal, 554(2):778–802.

Li, D., Telesco, C. M., Zhang, H., Wright, C. M., Pantin, E., Barnes, P. J., and Packham, C. (2018). Mid-infrared polarization of Herbig Ae/Be discs. Monthly Notices of the Royal Society, 473(2):1427–1437.

Liebert, J., Young, P. A., Arnett, D., Holberg, J. B., and Williams, K. A. (2005). The Age and Progenitor Mass of Sirius B. The Astrophysical Journal Letters, 630(1):L69–L72.

Ligi, R., Vigan, A., Gratton, R., de Boer, J., Benisty, M., Boccaletti, A., Quanz, S. P., Meyer, M., Ginski, C., Sissa, E., Gry, C., Henning, T., Beuzit, J. L., Biller, B., Bonnefoy, M., Chauvin, G., Cheetham, A. C., Cudel, M., Delorme, P., Desidera, S., Feldt, M., Galicher, R., Girard, J., Janson, M., Kasper, M., Kopytova, T., Lagrange, A. M., Langlois, M., Lecoroller, H., Maire, A. L., Ménard, F., Mesa, D., Peretti, S., Perrot, C., Pinilla, P., Pohl, A., Rouan, D., Stolker, T., Samland, M., Wahhaj, Z., Wildi, F., Zurlo, A., Buey, T., Fantinel, D., Fusco, T., Jaquet, M., Moulin, T., Ramos, J., Suarez, M., and Weber, L. (2018). Investigation of the inner structures around HD 169142 with VLT/SPHERE. Monthly Notices of the Royal Society, 473(2):1774–1783.

Liu, S.-F., Jin, S., Li, S., Isella, A., and Li, H. (2018). New Constraints on Turbulence and Embedded Planet Mass in the HD 163296 Disk from Planet-Disk Hydrodynamic Simulations. The Astrophysical Journal, 857(2):87.

Liu, W. M., Hinz, P. M., Meyer, M. R., Mamajek, E. E., Hoffmann, W. F., and Hora, J. L. (2003). A Resolved Circumstellar Disk around the Herbig Ae Star HD 100546 in the Thermal Infrared. The Astrophysical Journal Letters, 598(2):L111–L114.

Long, Z. C., Fernandes, R. B., Sitko, M., Wagner, K., Muto, T., Hashimoto, J., Follette, K., Grady, C. A., Fukagawa, M., Hasegawa, Y., Kluska, J., Kraus, S., Mayama, S., McElwain, M. W., Oh, D., Tamura, M., Uyama, T., Wisniewski, J. P., and Yang, Y. (2017). The shadow knows: Using shadows to investigate the structure of the pretransitional disk of HD 100453. The Astrophysical Journal, 838(1):62.

Luhman, K. L., Loutrel, N. P., McCurdy, N. S., Mace, G. N., Melso, N. D., Star, K. M., Young, M. D., Terrien, R. C., McLean, I. S., Kirkpatrick, J. D., and Rhode, K. L. (2012). NEW m, l, AND t DWARF COMPANIONS TO NEARBY STARS FROM THEWIDE-FIELD INFRARED SURVEY EXPLORER. The Astrophysical Journal, 760(2):152.

Luhman, K. L., Patten, B. M., Marengo, M., Schuster, M. T., Hora, J. L., Ellis, R. G., Stauffer, J. R., Sonnett, S. M., Winston, E., Gutermuth, R. A., Megeath, S. T., Backman, D. E., Henry, T. J., Werner, M. W., and Fazio, G. G. (2007). Discovery of two t dwarf companions with theSpitzer space telescope. The Astrophysical Journal, 654(1):570–579.

Lyot, B. (1939). The study of the solar corona and prominences without eclipses (George Darwin Lecture, 1939). Monthly Notices of the Royal Astronomical Society, 99:580.

Maaskant, K. M., Honda, M., Waters, L. B. F. M., Tielens, A. G. G. M., Dominik, C., Min, M., Verhoeff, A., Meeus, G., and van den Ancker, M. E. (2013). Identifying gaps in flaring Herbig

Ae/Be disks using spatially resolved mid-infrared imaging. Are all group I disks transitional? Astronomy & Astrophysics, 555:A64.

Maaskant, K. M., Min, M., Waters, L. B. F. M., and Tielens, A. G. G. M. (2014). Polycyclic aromatic hydrocarbon ionization as a tracer of gas flows through protoplanetary disk gaps. Astronomy & Astrophysics, 563:A78.

MacGregor, M. A., Lawler, S. M., Wilner, D. J., Matthews, B. C., Kennedy, G. M., Booth, M., and Di Francesco, J. (2016). ALMA Observations of the Debris Disk of Solar Analog τ Ceti. The Astrophysical Journal, 828(2):113.

Macías, E., Anglada, G., Osorio, M., Torrelles, J. M., Carrasco-González, C., Gómez, J. F., Rodríguez, L. F., and Sierra, A. (2017). Imaging a central ionized component, a narrow ring, and the CO snowline in the multigapped disk of HD 169142. The Astrophysical Journal, 838(2):97.

Macintosh, B., Graham, J. R., Barman, T., De Rosa, R. J., Konopacky, Q., Marley, M. S., Marois, C., Nielsen, E. L., Pueyo, L., Rajan, A., Rameau, J., Saumon, D., Wang, J. J., Patience, J., Ammons, M., Arriaga, P., Artigau, E., Beckwith, S., Brewster, J., Bruzzone, S., Bulger, J., Burningham, B., Burrows, A. S., Chen, C., Chiang, E., Chilcote, J. K., Dawson, R. I., Dong, R., Doyon, R., Draper, Z. H., Duchêne, G., Esposito, T. M., Fabrycky, D., Fitzgerald, M. P., Follette, K. B., Fortney, J. J., Gerard, B., Goodsell, S., Greenbaum, A. Z., Hibon, P., Hinkley, S., Cotten, T. H., Hung, L. W., Ingraham, P., Johnson-Groh, M., Kalas, P., Lafreniere, D., Larkin, J. E., Lee, J., Line, M., Long, D., Maire, J., Marchis, F., Matthews, B. C., Max, C. E., Metchev, S., Millar-Blanchaer, M. A., Mittal, T., Morley, C. V., Morzinski, K. M., Murray-Clay, R., Oppenheimer, R., Palmer, D. W., Patel, R., Perrin, M. D., Poyneer, L. A., Rafikov, R. R., Rantakyrö, F. T., Rice, E. L., Rojo, P., Rudy, A. R., Ruffio, J. B., Ruiz, M. T., Sadakuni, N., Saddlemyer, L., Salama, M., Savransky, D., Schneider, A. C., Sivaramakrishnan, A., Song, I., Soummer, R., Thomas, S., Vasisht, G., Wallace, J. K., Ward-Duong, K., Wiktorowicz, S. J., Wolff, S. G., and Zuckerman, B. (2015). Discovery and spectroscopy of the young jovian planet 51 Eri b with the Gemini Planet Imager. Science, 350(6256):64–67.

Macintosh, B., Graham, J. R., Ingraham, P., Konopacky, Q., Marois, C., Perrin, M., Poyneer, L., Bauman, B., Barman, T., Burrows, A. S., Cardwell, A., Chilcote, J., De Rosa, R. J., Dillon, D., Doyon, R., Dunn, J., Erikson, D., Fitzgerald, M. P., Gavel, D., Goodsell, S., Hartung, M., Hibon, P., Kalas, P., Larkin, J., Maire, J., Marchis, F., Marley, M. S., McBride, J., Millar-Blanchaer, M., Morzinski, K., Norton, A., Oppenheimer, B. R., Palmer, D., Patience, J., Pueyo, L., Rantakyro, F., Sadakuni, N., Saddlemyer, L., Savransky, D., Serio, A., Soummer, R., Sivaramakrishnan, A., Song, I., Thomas, S., Wallace, J. K., Wiktorowicz, S., and Wolff, S. (2014). First light of the Gemini Planet Imager. Proceedings of the National Academy of Science, 111(35):12661–12666.

Macintosh, B. A., Becklin, E. E., Kaisler, D., Konopacky, Q., and Zuckerman, B. (2003). Deep Keck Adaptive Optics Searches for Extrasolar Planets in the Dust of $\in$ Eridani and Vega. The Astrophysical Journal, 594(1):538–544.

Mackay, D. J. C. (2003). Information Theory, Inference and Learning Algorithms, chapter 45: Gaussian Processes.

Madhusudhan, N. (2019). Exoplanetary Atmospheres: Key Insights, Challenges, and Prospects. Annual Review of Astronomy and Astrophysics, 57:617–663.

Mahabal, A., Djorgovski, S. G., Turmon, M., Jewell, J., Williams, R. R., Drake, A. J., Graham, M. G., Donalek, C., Glikman, E., and Palomar-QUEST Team (2008). Automated probabilistic classification of transients and variables. Astronomische Nachrichten, 329(3):288–291.

Maire, A.-L., Huby, E., Absil, O., Zins, G., Kasper, M., Delacroix, C., Leveratto, S., Karlsson, M., Ruane, G., Käufl, H.-U., de Xivry, G. O., Pathak, P., Pettazzi, L., Duhoux, P., Kolb, J., Éric Pantin, Riggs, A. J. E., Siebenmorgen, R., and Mawet, D. (2020). Design, pointing control, and on-sky performance of the mid-infrared vortex coronagraph for the VLT/NEAR experiment. Journal of Astronomical Telescopes, Instruments, and Systems, 6(3):1 – 16.

Malfait, K., Waelkens, C., Waters, L. B. F. M., Vand enbussche, B., Huygen, E., and de Graauw, M. S. (1998). The spectrum of the young star HD 100546 observed with the Infrared Space Observatory. Astronomy & Astrophysics, 332:L25–L28.

Mamajek, E. E. and Hillenbrand, L. A. (2008). Improved Age Estimation for Solar-Type Dwarfs Using Activity-Rotation Diagnostics. The Astrophysical Journal, 687(2):1264–1293.

Mariñas, N., Telesco, C. M., Fisher, R. S., and Packham, C. (2011). HIGH-RESOLUTION MID-INFRARED IMAGING OF THE CIRCUMSTELLAR DISKS OF HERBIG ae/be STARS. The Astrophysical Journal, 737(2):57.

Marley, M. S., Fortney, J. J., Hubickyj, O., Bodenheimer, P., and Lissauer, J. J. (2007). On the luminosity of young jupiters. The Astrophysical Journal, 655(1):541–549.

Marois, C., Lafrenière, D., Doyon, R., Macintosh, B., and Nadeau, D. (2006). Angular differential imaging: A powerful high-contrast imaging technique. The Astrophysical Journal, 641(1):556.

Marois, C., Macintosh, B., Barman, T., Zuckerman, B., Song, I., Patience, J., Lafrenière, D., and Doyon, R. (2008). Direct Imaging of Multiple Planets Orbiting the Star HR 8799. Science, 322(5906):1348.

Marois, C., Zuckerman, B., Konopacky, Q. M., Macintosh, B., and Barman, T. (2010). Images of a fourth planet orbiting HR8799. Nature, 468:1080–1083.

Martin, R. G. and Lubow, S. H. (2011). Tidal truncation of circumplanetary discs. Monthly Notices of the Royal Astronomical Society, 413(2):1447–1461.

Mawet, D., Hirsch, L., Lee, E. J., Ruffio, J.-B., Bottom, M., Fulton, B. J., Absil, O., Beichman, C., Bowler, B., Bryan, M., Choquet, E., Ciardi, D., Christiaens, V., Defrère, D., Gomez Gonzalez, C. A., Howard, A. W., Huby, E., Isaacson, H., Jensen-Clem, R., Kosiarek, M., Marcy,

G., Meshkat, T., Petigura, E., Reggiani, M., Ruane, G., Serabyn, E., Sinukoff, E., Wang, J., Weiss, L., and Ygouf, M. (2019). Deep Exploration of ∈ Eridani with Keck Ms-band Vortex Coronagraphy and Radial Velocities: Mass and Orbital Parameters of the Giant Exoplanet. The Astronomical Journal, 157(1):33.

Mawet, D., Milli, J., Wahhaj, Z., Pelat, D., Absil, O., Delacroix, C., Boccaletti, A., Kasper, M., Kenworthy, M., Marois, C., Mennesson, B., and Pueyo, L. (2014). Fundamental Limitations of High Contrast Imaging Set by Small Sample Statistics. The Astrophysical Journal, 792(2):97.

Mawet, D., Riaud, P., Absil, O., and Surdej, J. (2005). Annular Groove Phase Mask Coronagraph. The Astrophysical Journal, 633(2):1191–1200.

Mawet, D., Serabyn, E., Liewer, K., Burruss, R., Hickey, J., and Shemo, D. (2010). The Vector Vortex Coronagraph: Laboratory Results and First Light at Palomar Observatory. The Astrophysical Journal, 709(1):53–57.

Mayer, L., Quinn, T., Wadsley, J., and Stadel, J. (2002). Formation of Giant Planets by Fragmentation of Protoplanetary Disks. Science, 298(5599):1756–1759.

Mayor, M. and Queloz, D. (1995). A Jupiter-mass companion to a solar-type star. Nature, 378(6555):355–359.

McCaughrean, M. J., Close, L. M., Scholz, R. D., Lenzen, R., Biller, B., Brandner, W., Hartung, M., and Lodieu, N. (2004). ∈ Indi Ba,Bb: The nearest binary brown dwarf. Astronomy & Astrophysics, 413:1029–1036.

Meadows, V. and Seager, S. (2010). Terrestrial Planet Atmospheres and Biosignatures, pages 441–470. University of Arizona Press.

Meeus, G., Montesinos, B., Mendigutía, I., Kamp, I., Thi, W. F., Eiroa, C., Grady, C. A., Mathews, G., Sandell, G., Martin-Zaïdi, C., Brittain, S., Dent, W. R. F., Howard, C., Ménard, F., Pinte, C., Roberge, A., Vand enbussche, B., and Williams, J. P. (2012). Observations of Herbig Ae/Be stars with Herschel/PACS. The atomic and molecular contents of their protoplanetary discs. Astronomy & Astrophysics, 544:A78.

Meeus, G., Waters, L. B. F. M., Bouwman, J., van den Ancker, M. E., Waelkens, C., and Malfait, K. (2001). ISO spectroscopy of circumstellar dust in 14 Herbig Ae/Be systems: Towards an understanding of dust processing. Astronomy & Astrophysics, 365:476–490.

Mendigutía, I., Oudmaijer, R. D., Garufi, A., Lumsden, S. L., Huélamo, N., Cheetham, A., de Wit, W. J., Norris, B., Olguin, F. A., and Tuthill, P. (2017). The protoplanetary system HD 100546 in Hα polarized light from SPHERE/ZIMPOL. A bar-like structure across the disk gap? Astronomy & Astrophysics, 608:A104.

Menu, J., van Boekel, R., Henning, T., Leinert, C., Waelkens, C., and Waters, L. B. F. M. (2015). The structure of disks around intermediate-mass young stars from mid-infrared interferometry. Astronomy & Astrophysics, 581:A107.

Mesa, D., Langlois, M., Garufi, A., Gratton, R., Desidera, S., D'Orazi, V., Flasseur, O., Barbieri, M., Benisty, M., Henning, T., Ligi, R., Sissa, E., Vigan, A., Zurlo, A., Boccaletti, A., Bonnefoy, M., Cantalloube, F., Chauvin, G., Cheetham, A., De Caprio, V., Delorme, P., Feldt, M., Fusco, T., Gluck, L., Hagelberg, J., Lagrange, A.-M., Lazzoni, C., Madec, F., Maire, A.-L., Menard, F., Meyer, M., Ramos, J., Rickman, E. L., Rouan, D., Schmidt, T., and Van der Plas, G. (2019). Determining mass limits around HD 163296 through SPHERE direct imaging data. Monthly Notices of the Royal Astronomical Society, 488(1):37–46.

Metchev, S., Marois, C., and Zuckerman, B. (2009). Pre-discovery 2007 image of the HR 8799 planetary system. The Astrophysical Journal Letters, 705(2):L204.

Meyer, M. R., Currie, T., Guyon, O., Hasegawa, Y., Kasper, M., Marois, C., Monnier, J., Morzinski, K., Packham, C., and Quanz, S. (2018). Finding and Characterizing Other Worlds: the Thermal-IR ELT Opportunity. arXiv e-prints, page arXiv:1804.03218.

Miley, J. M., Panić, O., Haworth, T. J., Pascucci, I., Wyatt, M., Clarke, C., Richards, A. M. S., and Ratzka, T. (2019). Asymmetric mid-plane gas in ALMA images of HD 100546. Monthly Notices of the Royal Society, 485(1):739–752.

Millholland, S., Wang, S., and Laughlin, G. (2017). Kepler Multi-planet Systems Exhibit Unexpected Intra-system Uniformity in Mass and Radius. The Astrophysical Journal Letters, 849(2):L33.

Min, M., Rab, C., Woitke, P., Dominik, C., and Ménard, F. (2016). Multiwavelength optical properties of compact dust aggregates in protoplanetary disks. Astronomy & Astrophysics, 585:A13.

Mitchell, T. R. and Stewart, G. R. (2011). Photoevaporation as a truncation mechanism for circumplanetary disks. The Astronomical Journal, 142(5):168.

Mizuki, T., Yamada, T., Carson, J. C., Kuzuhara, M., Nakagawa, T., Nishikawa, J., Sitko, M. L., Kudo, T., Kusakabe, N., Hashimoto, J., Abe, L., Brander, W., Brandt, T. D., Egner, S., Feldt, M., Goto, M., Grady, C. A., Guyon, O., Hayano, Y., Hayashi, M., Hayashi, S. S., Henning, T., Hodapp, K. W., Ishii, M., Iye, M., Janson, M., Kandori, R., Knapp, G. R., Kwon, J., Matsuo, T., McElwain, M. W., Miyama, S., Morino, J., Moro-Martin, A., Nishimura, T., Pyo, T., Serabyn, E., Suenaga, T., Suto, H., Suzuki, R., Takahashi, Y. H., Takami, M., Takato, N., Terada, H., Thalmann, C., Turner, E. L., Watanabe, M., Wisniewski, J., Takami, H., Usuda, T., and Tamura, M. (2016). High-contrast imaging of $\in$ Eridani with ground-based instruments. Astronomy & Astrophysics, 595:A79.

Mizuno (1980). Formation of the Giant Planets. Progress of Theoretical Physics, 64(2):544–557.

Modirrousta-Galian, D., Locci, D., and Micela, G. (2020). The bimodal distribution in exoplanet radii: Considering varying core compositions and h2 envelope's sizes. The Astrophysical Journal, 891(2):158.

Moehler, S., Freudling, W., Møller, P., Patat, F., Rupprecht, G., and O'Brien, K. (2010). Correction of Field Rotator-Induced Flat-Field Systematics—A Case Study Using Archived VLT-FORS Data. Publications of the Astronomical Society of the Pacific, 122(887):93.

Momose, M., Morita, A., Fukagawa, M., Muto, T., Takeuchi, T., Hashimoto, J., Honda, M., Kudo, T., Okamoto, Y. K., Kanagawa, K. D., Tanaka, H., Grady, C. A., Sitko, M. L., Akiyama, E., Currie, T., Follette, K. B., Mayama, S., Kusakabe, N., Abe, L., Brandner, W., Brand t, T. D., Carson, J. C., Egner, S., Feldt, M., Goto, M., Guyon, O., Hayano, Y., Hayashi, M., Hayashi, S. S., Henning, T., Hodapp, K. W., Ishii, M., Iye, M., Janson, M., Kandori, R., Knapp, G. R., Kuzuhara, M., Kwon, J., Matsuo, T., McElwain, M. W., Miyama, S., Morino, J.-I., Moro-Martin, A., Nishimura, T., Pyo, T.-S., Serabyn, E., Suenaga, T., Suto, H., Suzuki, R., Takahashi, Y. H., Takami, M., Takato, N., Terada, H., Thalmann, C., Tomono, D., Turner, E. L., Watanabe, M., Wisniewski, J., Yamada, T., Takami, H., Usuda, T., and Tamura, M. (2015). Detailed structure of the outer disk around HD 169142 with polarized light in H-band. Publications of the Astronomical Society of Japan, 67(5):83.

Mordasini, C. (2020). Planetary evolution with atmospheric photoevaporation. I. Analytical derivation and numerical study of the evaporation valley and transition from super-Earths to sub-Neptunes. Astronomy & Astrophyscs, 638:A52.

Mordasini, C., Alibert, Y., Klahr, H., and Henning, T. (2012). Characterization of exoplanets from their formation - i. models of combined planet formation and evolution. Astronomy & Astrophysics, 547:A111.

NASA Jet Propulsion Laboratory (2021). Neocam: Finding asteroids before they find us.

Naud, M.-E., Artigau, É., Doyon, R., Malo, L., Gagné, J., Lafrenière, D., Wolf, C., and Magnier, E. A. (2017). PSYM-WIDE: A Survey for Large-separation Planetary-mass Companions to Late Spectral Type Members of Young Moving Groups. The Astronomical Journal, 154(3):129.

Nayakshin, S. (2010). Formation of planets by tidal downsizing of giant planet embryos. Monthly Notices of the Royal Astronomical Society, 408(1):L36–L40.

Nayakshin, S., Tsukagoshi, T., Hall, C., Vazan, A., Helled, R., Humphries, J., Meru, F., Neunteufel, P., Panic, O., and Price, D. (2020). TW Hya: an old protoplanetary disc revived by its planet. arXiv e-prints, page arXiv:2004.10094.

Nealon, R., Cuello, N., Gonzalez, J.-F., van der Plas, G., Pinte, C., Alexander, R., Ménard, F., and Price, D. J. (2020). Spirals, shadows & precession in HD 100453 - II. The hidden companion. Monthly Notices of the Royal Society, 499(3):3857–3867.

Nettelmann, N., Fortney, J. J., Kramm, U., and Redmer, R. (2011). Thermal Evolution and Structure Models of the Transiting Super-Earth GJ 1214b. The Astrophysical Journal, 733(1):2.

Neuhäuser, R., Guenther, E. W., Wuchterl, G., Mugrauer, M., Bedalov, A., and Hauschildt, P. H. (2005). Evidence for a co-moving sub-stellar companion of GQ Lup. Astronomy & Astrophysics, 435(1):L13–L16.

Newton, I. (1687). Philosophiae Naturalis Principia Mathematica. Auctore Js. Newton.

Nielsen, E. L., De Rosa, R. J., Macintosh, B., Wang, J. J., Ruffio, J.-B., Chiang, E., Marley, M. S., Saumon, D., Savransky, D., Ammons, S. M., Bailey, V. P., Barman, T., Blain, C., Bulger, J., Chilcote, J., Cotten, T., Czekala, I., Doyon, R., Duchene, G., Esposito, T. M., Fabrycky, D., Fitzgerald, M. P., Follette, K. B., Fortney, J. J., Gerard, B. L., Goodsell, S. J., Graham, J. R., Greenbaum, A. r. Z., Hibon, P., Hinkley, S., Hirsch, L. A., Hom, J., Hung, L.-W., Dawson, R. I., Ingraham, P., Kalas, P., Konopacky, Q., Larkin, J. E., Lee, E. J., Lin, J. W., Maire, J., Marchis, F., Marois, C., Metchev, S., Millar-Blanchaer, M. A., Morzinski, K. M., Oppenheimer, R., Palmer, D., Patience, J., Perrin, M., Poyneer, L., Pueyo, L., Rafikov, R. R., Rajan, A., Rameau, J., Rantakyro, F. T., Ren, B., Schneider, A. C., Sivaramakrishnan, A., Song, I., Soummer, R., Tallis, M., Thomas, S., Ward-Duong, K., and Wolff, S. (2019). The Gemini Planet Imager Exoplanet Survey: Giant Planet and Brown Dwarf Demographics From 10-100 AU. arXiv e-prints, page arXiv:1904.05358.

Nikolov, N., Sing, D. K., Fortney, J. J., Goyal, J. M., Drummond, B., Evans, T. M., Gibson, N. P., De Mooij, E. J. W., Rustamkulov, Z., Wakeford, H. R., Smalley, B., Burgasser, A. J., Hellier, C., Helling, C., Mayne, N. J., Madhusudhan, N., Kataria, T., Baines, J., Carter, A. L., Ballester, G. E., Barstow, J. K., McCleery, J., and Spake, J. J. (2018). An absolute sodium abundance for a cloud-free 'hot Saturn' exoplanet. Nature, 557(7706):526–529.

Nomura, H., Tsukagoshi, T., Kawabe, R., Ishimoto, D., Okuzumi, S., Muto, T., Kanagawa, K. D., Ida, S., Walsh, C., Millar, T. J., and Bai, X.-N. (2016). ALMA OBSERVATIONS OF a GAP AND a RING IN THE PROTOPLANETARY DISK AROUND TW HYA. The Astrophysical Journal, 819(1):L7.

Nortmann, L., Pallé, E., Salz, M., Sanz-Forcada, J., Nagel, E., Alonso-Floriano, F. J., Czesla, S., Yan, F., Chen, G., Snellen, I. A. G., Zechmeister, M., Schmitt, J. H. M. M., López-Puertas, M., Casasayas-Barris, N., Bauer, F. F., Amado, P. J., Caballero, J. A., Dreizler, S., Henning, T., Lampón, M., Montes, D., Molaverdikhani, K., Quirrenbach, A., Reiners, A., Ribas, I., Sánchez-López, A. r., Schneider, P. C., and Zapatero Osorio, M. R. (2018). Ground-based detection of an extended helium atmosphere in the Saturn-mass exoplanet WASP-69b. Science, 362(6421):1388–1391.

Nowak, M., Lacour, S., Lagrange, A. M., Rubini, P., Wang, J., Stolker, T., Abuter, R., Amorim, A., Asensio-Torres, R., Bauböck, M., Benisty, M., Berger, J. P., Beust, H., Blunt, S., Boccaletti, A., Bonnefoy, M., Bonnet, H., Brandner, W., Cantalloube, F., Charnay, B., Choquet, E., Christiaens, V., Clénet, Y., Coudé Du Foresto, V., Cridland, A., de Zeeuw, P. T., Dembet, R., Dexter, J., Drescher, A., Duvert, G., Eckart, A., Eisenhauer, F., Gao, F., Garcia, P., Garcia Lopez, R., Gardner, T., Gendron, E., Genzel, R., Gillessen, S., Girard, J., Grandjean, A., Haubois, X., Heißel, G., Henning, T., Hinkley, S., Hippler, S., Horrobin, M., Houllé, M.,

Hubert, Z., Jiménez-Rosales, A., Jocou, L., Kammerer, J., Kervella, P., Keppler, M., Kreidberg, L., Kulikauskas, M., Lapeyrère, V., Le Bouquin, J. B., Léna, P., Mérand, A., Maire, A. L., Mollière, P., Monnier, J. D., Mouillet, D., Müller, A., Nasedkin, E., Ott, T., Otten, G., Paumard, T., Paladini, C., Perraut, K., Perrin, G., Pueyo, L., Pfuhl, O., Rameau, J., Rodet, L., Rodríguez-Coira, G., Rousset, G., Scheithauer, S., Shangguan, J., Stadler, J., Straub, O., Straubmeier, C., Sturm, E., Tacconi, L. J., van Dishoeck, E. F., Vigan, A., Vincent, F., von Fellenberg, S. D., Ward-Duong, K., Widmann, F., Wieprecht, E., Wiezorrek, E., Woillez, J., and Gravity Collaboration (2020). Direct confirmation of the radial-velocity planet β Pictoris c. Astronomy & Astrophysics, 642:L2.

Nutzman, P. and Charbonneau, D. (2008). Design Considerations for a Ground-Based Transit Search for Habitable Planets Orbiting M Dwarfs. Publications of the Astronomical Society of the Pacific, 120(865):317.

Oberg, N., Kamp, I., Cazaux, S., and Rab, C. (2020). Photoevaporation of the Jovian circumplanetary disk. I. Explaining the orbit of Callisto and the lack of outer regular satellites. Astronomy & Astrophysics, 638:A135.

Okamoto, Y. K., Kataza, H., Honda, M., Yamashita, T., Fujiyoshi, T., Miyata, T., Sako, S., Fujiwara, H., Sakon, I., Fukagawa, M., Momose, M., and Onaka, T. (2017). A Circumstellar Disk around HD 169142 in the Mid-Infrared (N-Band). The Astronomical Journal, 154(1):16.

Oklopčić, A. (2019). Helium Absorption at 1083 nm from Extended Exoplanet Atmospheres: Dependence on Stellar Radiation. The Astrophysical Journal, 881(2):133.

Oklopčić, A. and Hirata, C. M. (2018). A New Window into Escaping Exoplanet Atmospheres: 10830 Å Line of Helium. The Astrophysical Journal Letters, 855(1):L11.

Osorio, M., Anglada, G., Carrasco-González, C., Torrelles, J. M., Macías, E., Rodríguez, L. F., Gómez, J. F., D'Alessio, P., Calvet, N., Nagel, E., Dent, W. R. F., Quanz, S. P., Reggiani, M., and Mayen-Gijon, J. M. (2014). Imaging the Inner and Outer Gaps of the Pre-transitional Disk of HD 169142 at 7 mm. The Astrophysical Journal Letters, 791(2):L36.

Owen, J. E. (2019). Atmospheric Escape and the Evolution of Close-In Exoplanets. Annual Review of Earth and Planetary Sciences, 47:67–90.

Owen, J. E. and Wu, Y. (2013). Kepler Planets: A Tale of Evaporation. The Astrophysical Journal, 775(2):105.

Owen, J. E. and Wu, Y. (2017). The Evaporation Valley in the Kepler Planets. The Astrophysical Journal, 847(1):29.

Pagano, M., Truitt, A., Young, P. A., and Shim, S.-H. (2015). The Chemical Composition of τ Ceti and Possible Effects on Terrestrial Planets. The Astrophysical Journal, 803(2):90.

Palle, E., Nortmann, L., Casasayas-Barris, N., Lampón, M., López-Puertas, M., Caballero, J. A., Sanz-Forcada, J., Lara, L. M., Nagel, E., Yan, F., Alonso-Floriano, F. J., Amado, P. J., Chen, G., Cifuentes, C., Cortés-Contreras, M., Czesla, S., Molaverdikhani, K., Montes, D., Passegger, V. M., Quirrenbach, A., Reiners, A., Ribas, I., Sánchez-López, A., Schweitzer, A., Stangret, M., Zapatero Osorio, M. R., and Zechmeister, M. (2020). A He I upper atmosphere around the warm Neptune GJ 3470 b. Astronomy & Astrophysics, 638:A61.

Panić, O., Hogerheijde, M. R., Wilner, D., and Qi, C. (2008). Gas and dust mass in the disc around the Herbig Ae star HD 169142. Astronomy & Astrophysics, 491(1):219–227.

Panić, O., Ratzka, T., Mulders, G. D., Dominik, C., van Boekel, R., Henning, T., Jaffe, W., and Min, M. (2014). Resolving HD 100546 disc in the mid-infrared: Small inner disc and asymmetry near the gap. Astronomy & Astrophysics, 562:A101.

Paragas, K., Vissapragada, S., Knutson, H. A., Oklopčić, A., Chachan, Y., Greklek-McKeon, M., Dai, F., Tinyanont, S., and Vasisht, G. (2021). Metastable Helium Reveals an Extended Atmosphere for the Gas Giant HAT-P-18b. The Astrophysical Journal Letters, 909(1):L10.

Parviainen, H. and Aigrain, S. (2015). LDTK: Limb Darkening Toolkit. Monthly Notices of the Royal Astronomical Society, 453(4):3821–3826.

Pepe, F. A., Cristiani, S., Rebolo Lopez, R., Santos, N. C., Amorim, A., Avila, G., Benz, W., Bonifacio, P., Cabral, A., Carvas, P., Cirami, R., Coelho, J., Comari, M., Coretti, I., De Caprio, V., Dekker, H., Delabre, B., Di Marcantonio, P., D'Odorico, V., Fleury, M., García, R., Herreros Linares, J. M., Hughes, I., Iwert, O., Lima, J., Lizon, J.-L., Lo Curto, G., Lovis, C., Manescau, A., Martins, C., Mégevand, D., Moitinho, A., Molaro, P., Monteiro, M., Monteiro, M., Pasquini, L., Mordasini, C., Queloz, D., Rasilla, J. L., Rebordão, J. M., Santana Tschudi, S., Santin, P., Sosnowska, D., Spanò, P., Tenegi, F., Udry, S., Vanzella, E., Viel, M., Zapatero Osorio, M. R., and Zerbi, F. (2010). ESPRESSO: the Echelle spectrograph for rocky exoplanets and stable spectroscopic observations. In McLean, I. S., Ramsay, S. K., and Takami, H., editors, Ground-based and Airborne Instrumentation for Astronomy III, volume 7735 of Society of Photo-Optical Instrumentation Engineers (SPIE) Conference Series, page 77350F.

Pérez, S., Casassus, S., Baruteau, C., Dong, R., Hales, A., and Cieza, L. (2019). Dust unveils the formation of a mini-neptune planet in a protoplanetary ring. The Astronomical Journal, 158(1):15.

Pérez, S., Casassus, S., Hales, A., Marino, S., Cheetham, A., Zurlo, A., Cieza, L., Dong, R., Alarcón, F., Benítez-Llambay, P., Fomalont, E., and Avenhaus, H. (2020). Long Baseline Observations of the HD 100546 Protoplanetary Disk with ALMA. The Astrophysical Journal Letters, 889(1):L24.

Perryman, M., Hartman, J., Bakos, G. Á., and Lindegren, L. (2014). Astrometric Exoplanet Detection with Gaia. The Astrophysical Journal, 797(1):14.

Petit dit de la Roche, D. J. M., Hoeijmakers, H. J., and Snellen, I. A. G. (2018). Molecule mapping of HR8799b using OSIRIS on Keck - Strong detection of water and carbon monoxide, but no methane. Astronomy & Astrophysics, 616:A146.

Petit dit de la Roche, D. J. M., van den Ancker, M. E., Kissler-Patig, M., Ivanov, V. D., and Fedele, D. (2020). New constraints on the HR 8799 planetary system from mid-infrared direct imaging. Monthly Notices of the Royal Society, 491(2):1795–1799.

Phillips, M. W., Tremblin, P., Baraffe, I., Chabrier, G., Allard, N. F., Spiegelman, F., Goyal, J. M., Drummond, B., and Hébrard, E. (2020). A new set of atmosphere and evolution models for cool T-Y brown dwarfs and giant exoplanets. Astronomy & Astrophysics, 637:A38.

Pineda, J. E., Quanz, S. P., Meru, F., Mulders, G. D., Meyer, M. R., Panić, O., and Avenhaus, H. (2014). Resolved Images of the Protoplanetary Disk around HD 100546 with ALMA. The Astrophysical Journal Letters, 788(2):L34.

Pineda, J. E., Szulágyi, J., Quanz, S. P., van Dishoeck, E. F., Garufi, A., Meru, F., Mulders, G. D., Testi, L., Meyer, M. R., and Reggiani, M. (2019). High-resolution ALMA Observations of HD 100546: Asymmetric Circumstellar Ring and Circumplanetary Disk Upper Limits. The Astrophysical Journal, 871(1):48.

Pinilla, P., Birnstiel, T., Benisty, M., Ricci, L., Natta, A., Dullemond, C. P., Dominik, C., and Testi, L. (2013). Explaining millimeter-sized particles in brown dwarf disks. Astronomy & Astrophysics, 554:A95.

Pinte, C., Price, D. J., Ménard, F., Duchêne, G., Dent, W. R. F., Hill, T., de Gregorio-Monsalvo, I., Hales, A., and Mentiplay, D. (2018). Kinematic Evidence for an Embedded Protoplanet in a Circumstellar Disk. The Astrophysical Journal Letters, 860(1):L13.

Poddaný, S., Brát, L., and Pejcha, O. (2010). Exoplanet transit database. reduction and processing of the photometric data of exoplanet transits. New Astronomy, 15(3):297–301.

Pohl, A., Benisty, M., Pinilla, P., Ginski, C., de Boer, J., Avenhaus, H., Henning, T., Zurlo, A., Boccaletti, A., Augereau, J. C., Birnstiel, T., Dominik, C., Facchini, S., Fedele, D., Janson, M., Keppler, M., Kral, Q., Langlois, M., Ligi, R., Maire, A. L., Ménard, F., Meyer, M., Pinte, C., Quanz, S. P., Sauvage, J. F., Sezestre, É., Stolker, T., Szulágyi, J., van Boekel, R., van der Plas, G., Villenave, M., Baruffolo, A., Baudoz, P., Le Mignant, D., Maurel, D., Ramos, J., and Weber, L. (2017). The Circumstellar Disk HD 169142: Gas, Dust, and Planets Acting in Concert? The Astrophysical Journal, 850(1):52.

Pollack, J. B., Hubickyj, O., Bodenheimer, P., Lissauer, J. J., Podolak, M., and Greenzweig, Y. (1996). Formation of the Giant Planets by Concurrent Accretion of Solids and Gas. Icarus, 124(1):62–85.

Quanz, S. P., Amara, A., Meyer, M. R., Girard, J. H., Kenworthy, M. A., and Kasper, M. (2015). Confirmation and characterization of the protoplanet HD 100546 b—direct evidence for gas giant planet formation at 50 AU. The Astrophysical Journal, 807(1):64.

Quanz, S. P., Amara, A., Meyer, M. R., Kenworthy, M. A., Kasper, M., and Girard, J. H. (2013). A Young Protoplanet Candidate Embedded in the Circumstellar Disk of HD 100546. The Astrophysical Journal Letters, 766(1):L1.

Quanz, S. P., Crossfield, I., Meyer, M. R., Schmalzl, E., and Held, J. (2015). Direct detection of exoplanets in the 3-10 μm range with E-ELT/METIS. International Journal of Astrobiology, 14(2):279–289.

Quillen, A. C. (2006). The Warped Circumstellar Disk of HD 100546. The Astrophysical Journal, 640(2):1078–1085.

Quillen, A. C. and Trilling, D. E. (1998). Do Proto-jovian Planets Drive Outflows? The Astrophysical Journal, 508(2):707–713.

Quirrenbach, A., Amado, P. J., Caballero, J. A., Mandel, H., Mundt, R., Reiners, A., Ribas, I., Sánchez Carrasco, M. A., Seifert, W., Azzaro, M., Galadí, D., and CARMENES Consortium (2014). The CARMENES Survey: A Search for Terrestrial Planets in the Habitable Zones of M Dwarfs. In Haghighipour, N., editor, Formation, Detection, and Characterization of Extrasolar Habitable Planets, volume 293, pages 177–182.

Rab, C., Kamp, I., Ginski, C., Oberg, N., Muro-Arena, G. A., Dominik, C., Waters, L. B. F. M., Thi, W. F., and Woitke, P. (2019). Observing the gas component of circumplanetary disks around wide-orbit planet-mass companions in the (sub)mm regime. Astronomy & Astrophysics, 624:A16.

Raman, A., Lisanti, M., Wilner, D. J., Qi, C., and Hogerheijde, M. (2006). A Keplerian Disk around the Herbig Ae Star HD 169142. The Astronomical Journal, 131(4):2290–2293.

Rameau, J., Follette, K. B., Pueyo, L., Marois, C., Macintosh, B., Millar-Blanchaer, M., Wang, J. J., Vega, D., Doyon, R., Lafrenière, D., Nielsen, E. L., Bailey, V., Chilcote, J. K., Close, L. M., Esposito, T. M., Males, J. R., Metchev, S., Morzinski, K. M., Ruffio, J.-B., Wolff, S. G., Ammons, S. M., Barman, T. S., Bulger, J., Cotten, T., Rosa, R. J. D., Duchene, G., Fitzgerald, M. P., Goodsell, S., Graham, J. R., Greenbaum, A. Z., Hibon, P., Hung, L.-W., Ingraham, P., Kalas, P., Konopacky, Q., Larkin, J. E., Maire, J., Marchis, F., Oppenheimer, R., Palmer, D., Patience, J., Perrin, M. D., Poyneer, L., Rajan, A., Rantakyrö, F. T., Marley, M. S., Savransky, D., Schneider, A. C., Sivaramakrishnan, A., Song, I., Soummer, R., Thomas, S., Wallace, J. K., Ward-Duong, K., and Wiktorowicz, S. (2017). An optical/near-infrared investigation of HD 100546 b with the gemini planet imager and MagAO. The Astronomical Journal, 153(6):244.

Rasmussen, C. E. and Williams, C. K. I. (2006). Gaussian Processes for Machine Learning, chapter 4: Covariance Functions, pages 79–104. MIT press, 2nd edition.

Ratzka, T., Leinert, C., Henning, T., Bouwman, J., Dullemond, C. P., and Jaffe, W. (2007). High spatial resolution mid-infrared observations of the low-mass young star TW Hydrae. Astronomy & Astrophysics, 471(1):173–185.

Rauer, H., Gebauer, S., Paris, P. v., Cabrera, J., Godolt, M., Grenfell, J. L., Belu, A., Selsis, F., Hedelt, P., and Schreier, F. (2011). Potential biosignatures in super-earth atmospheres - i. spectral appearance of super-earths around m dwarfs. Astronomy & Astrophysics, 529:A8.

Rebolo, R. et al. (1998). Discovery of a low-mass brown dwarf companion of the young nearby star g 196-3. Science, 282(5392):1309–1312.

Reggiani et al. (2016). The VLT/NaCo large program to probe the occurrence of exoplanets and brown dwarfs at wide orbits . III. The frequency of brown dwarfs and giant planets as companions to solar-type stars. A&A, 586:A147.

Reggiani, M., Christiaens, V., Absil, O., Mawet, D., Huby, E., Choquet, E., Gomez Gonzalez, C. A., Ruane, G., Femenia, B., Serabyn, E., Matthews, K., Barraza, M., Carlomagno, B., Defrère, D., Delacroix, C., Habraken, S., Jolivet, A., Karlsson, M., Orban de Xivry, G., Piron, P., Surdej, J., Vargas Catalan, E., and Wertz, O. (2018). Discovery of a point-like source and a third spiral arm in the transition disk around the Herbig Ae star MWC 758. Astronomy & Astrophysics, 611:A74.

Reggiani, M., Quanz, S. P., Meyer, M. R., Pueyo, L., Absil, O., Amara, A., Anglada, G., Avenhaus, H., Girard, J. H., Carrasco Gonzalez, C., Graham, J., Mawet, D., Meru, F., Milli, J., Osorio, M., Wolff, S., and Torrelles, J.-M. (2014). Discovery of a Companion Candidate in the HD 169142 Transition Disk and the Possibility of Multiple Planet Formation. The Astrophysical Journal Letters, 792(1):L23.

Rice, W. K. M., Armitage, P. J., Wood, K., and Lodato, G. (2006). Dust filtration at gap edges: implications for the spectral energy distributions of discs with embedded planets. Monthly Notices of the Royal Society, 373(4):1619–1626.

Rieke, G. H., Wright, G. S., Böker, T., Bouwman, J., Colina, L., Glasse, A., Gordon, K. D., Greene, T. P., Güdel, M., Henning, T., Justtanont, K., Lagage, P. O., Meixner, M. E., Nørgaard-Nielsen, H. U., Ray, T. P., Ressler, M. E., van Dishoeck, E. F., and Waelkens, C. (2015). The Mid-Infrared Instrument for the James Webb Space Telescope, I: Introduction. Publications of the Astronomical Society of the Pacific, 127(953):584.

Rogers, L. A. and Seager, S. (2010). Three Possible Origins for the Gas Layer on GJ 1214b. The Astrophysical Journal, 716(2):1208–1216.

Rosotti, G. P., Benisty, M., Juhász, A., Teague, R., Clarke, C., Dominik, C., Dullemond, C. P., Klaassen, P. D., Matrà, L., and Stolker, T. (2020). Spiral arms in the protoplanetary disc HD100453 detected with ALMA: evidence for binary-disc interaction and a vertical temperature gradient. Monthly Notices of the Royal Society, 491(1):1335–1347.

Rowe, J. F., Matthews, J. M., Seager, S., Miller-Ricci, E., Sasselov, D., Kuschnig, R., Guenther, D. B., Moffat, A. F. J., Rucinski, S. M., Walker, G. A. H., and Weiss, W. W. (2008). The Very Low Albedo of an Extrasolar Planet: MOST Space-based Photometry of HD 209458. The Astrophysical Journal, 689(2):1345–1353.

Schneider, J., Dedieu, C., Le Sidaner, P., Savalle, R., and Zolotukhin, I. (2011). Defining and cataloging exoplanets: the exoplanet.eu database. Astronomy & Astrophysics, 532:A79.

Schneider, P. C., Dougados, C., Whelan, E. T., Eislöffel, J., Günther, H. M., Huélamo, N., Mendigutía, I., Oudmaijer, R. D., and Beck, T. L. (2020). Discovery of a jet from the single HAe/Be star HD 100546. arXiv e-prints, page arXiv:2006.00573.

Scholz, R. D., McCaughrean, M. J., Lodieu, N., and Kuhlbrodt, B. (2003). varepsilon Indi B: A new benchmark T dwarf. Astronomy & Astrophysics, 398:L29–L33.

Schwamb, M. E., Orosz, J. A., Carter, J. A., Welsh, W. F., Fischer, D. A., Torres, G., Howard, A. W., Crepp, J. R., Keel, W. C., Lintott, C. J., Kaib, N. A., Terrell, D., Gagliano, R., Jek, K. J., Parrish, M., Smith, A. M., Lynn, S., Simpson, R. J., Giguere, M. J., and Schawinski, K. (2013). Planet Hunters: A Transiting Circumbinary Planet in a Quadruple Star System. The Astrophysical Journal, 768(2):127.

Sedaghati, E., Boffin, H. M. J., Csizmadia, S., Gibson, N., Kabath, P., Mallonn, M., and Van den Ancker, M. E. (2015). Regaining the FORS: optical ground-based transmission spectroscopy of the exoplanet WASP-19b with VLT+FORS2. Astronomy & Astrophysics, 576:L11.

Serabyn, E., Mawet, D., and Burrus, R. (2010). An image of an exoplanet separated by two diffraction beamwidths from a star. Nature, 464:1018.

Serindag, D. B. and Snellen, I. A. G. (2019). Testing the Detectability of Extraterrestrial O_2 with the Extremely Large Telescopes Using Real Data with Real Noise. The Astrophysical Journal Letters, 871(1):L7.

Sharples, R., Bender, R., Agudo Berbel, A., Bezawada, N., Castillo, R., Cirasuolo, M., Davidson, G., Davies, R., Dubbeldam, M., Fairley, A., Finger, G., Förster Schreiber, N., Gonte, F., Hess, A., Jung, I., Lewis, I., Lizon, J. L., Muschielok, B., Pasquini, L., Pirard, J., Popovic, D., Ramsay, S., Rees, P., Richter, J., Riquelme, M., Rodrigues, M., Saviane, I., Schlichter, J., Schmidtobreick, L., Segovia, A., Smette, A., Szeifert, T., van Kesteren, A., Wegner, M., and Wiezorrek, E. (2013). First Light for the KMOS Multi-Object Integral-Field Spectrometer. The Messenger, 151:21–23.

Siebenmorgen, R. and Heymann, F. (2012). Shadows, gaps, and ring-like structures in proto-planetary disks. Astronomy & Astrophysics, 539:A20.

Sissa, E., Gratton, R., Garufi, A., Rigliaco, E., Zurlo, A., Mesa, D., Langlois, M., de Boer, J., Desidera, S., Ginski, C., Lagrange, A.-M., Maire, A.-L., Vigan, A., Dima, M., Antichi, J., Baruffolo, A., Bazzon, A., Benisty, M., Beuzit, J.-L., Biller, B., Boccaletti, A., Bonavita, M., Bonnefoy, M., Brandner, W., Bruno, P., Buenzli, E., Cascone, E., Chauvin, G., Cheetham, A., Claudi, R. U., Cudel, M., De Caprio, V., Dominik, C., Fantinel, D., Farisato, G., Feldt, M., Fontanive, C., Galicher, R., Giro, E., Hagelberg, J., Incorvaia, S., Janson, M., Kasper, M., Keppler, M., Kopytova, T., Lagadec, E., Lannier, J., Lazzoni, C., LeCoroller, H., Lessio, L., Ligi, R., Marzari, F., Menard, F., Meyer, M. R., Mouillet, D., Peretti, S., Perrot, C., Potiron,

P. J., Rouan, D., Salasnich, B., Salter, G., Samland, M., Schmidt, T., Scuderi, S., and Wildi, F. (2018). High-contrast study of the candidate planets and protoplanetary disk around hd 100546. Astronomy & Astrophysics, 619:A160.

Skemer, A. J. and Close, L. M. (2011). Sirius B Imaged in the Mid-infrared: No Evidence for a Remnant Planetary System. The Astrophysical Journal, 730(1):53.

Slipher, V. M. (1930). Planet X-Lowell Observatory Observation Circular. Journal of the Royal Astronomical Society of Canada, 24:282.

Snellen, I., de Kok, R., Birkby, J. L., Brandl, B., Brogi, M., Keller, C., Kenworthy, M., Schwarz, H., and Stuik, R. (2015). Combining high-dispersion spectroscopy with high contrast imaging: Probing rocky planets around our nearest neighbors. Astronomy & Astrophysics, 576:A59.

Snellen, I. A. G., Brandl, B. R., de Kok, R. J., Brogi, M., Birkby, J., and Schwarz, H. (2014). Fast spin of the young extrasolar planet [bgr][thinsp]pictoris[thinsp]b. Nature, 509(7498):63–65.

Snellen, I. A. G., de Kok, R. J., de Mooij, E. J. W., and Albrecht, S. (2010). The orbital motion, absolute mass and high-altitude winds of exoplanet hd209458b. Nature, 465:1049–1051.

Snik, F., Otten, G., Kenworthy, M., Miskiewicz, M., Escuti, M., Packham, C., and Codona, J. (2012). The vector-APP: a broadband apodizing phase plate that yields complementary PSFs. In Navarro, R., Cunningham, C. R., and Prieto, E., editors, Modern Technologies in Space- and Ground-based Telescopes and Instrumentation II, volume 8450 of Society of Photo-Optical Instrumentation Engineers (SPIE) Conference Series, page 84500M.

Sokal, K. R., Deen, C. P., Mace, G. N., Lee, J.-J., Oh, H., Kim, H., Kidder, B. T., and Jaffe, D. T. (2018). Characterizing TW Hydra. The Astrophysical Journal, 853(2):120.

Song, I., Caillault, J. P., Barrado y Navascués, D., Stauffer, J. R., and Rand ich, S. (2000). Ages of Late Spectral Type Vega-like Stars. The Astrophysical Journal Letters, 533(1):L41–L44.

Southworth, J., Mancini, L., Browne, P., Burgdorf, M., Calchi Novati, S., Dominik, M., Gerner, T., Hinse, T. C., Jørgensen, U. G., Kains, N., Ricci, D., Schäfer, S., Schönebeck, F., Tregloan-Reed, J., Alsubai, K. A., Bozza, V., Chen, G., Dodds, P., Dreizler, S., Fang, X. S., Finet, F., Gu, S. H., Hardis, S., Harpsøe, K., Henning, T., Hundertmark, M., Jessen-Hansen, J., Kerins, E., Kjeldsen, H., Liebig, C., Lund, M. N., Lundkvist, M., Mathiasen, M., Nikolov, N., Penny, M. T., Proft, S., Rahvar, S., Sahu, K., Scarpetta, G., Skottfelt, J., Snodgrass, C., Surdej, J., and Wertz, O. (2013). High-precision photometry by telescope defocusing - V. WASP-15 and WASP-16. Monthly Notices of the Royal Astronomical Society, 434(2):1300–1308.

Spake, J. J., Sing, D. K., Evans, T. M., Oklopčić, , A., Bourrier, V., Kreidberg, L., Rackham, B. V., Irwin, J., Ehrenreich, D., Wyttenbach, A., Wakeford, H. R., Zhou, Y., Chubb, K. L., Nikolov, N., Goyal, J. M., Henry, G. W., Williamson, M. H., Blumenthal, S., Anderson, D. R., Hellier, C., Charbonneau, D., Udry, S., and Madhusudhan, N. (2018). Helium in the eroding atmosphere of an exoplanet. Nature, 557(7703):68–70.

Speagle, J. S. (2020). DYNESTY: a dynamic nested sampling package for estimating Bayesian posteriors and evidences. Monthly Notices of the Royal Astronomical Society, 493(3):3132–3158.

Spiegel, D. S. and Burrows, A. (2012). Spectral and Photometric Diagnostics of Giant Planet Formation Scenarios. The Astrophysical Journal, 745(2):174.

Stein, M. (1999). Interpolation of Spatial Data: Some Theory For Kriging. Springer.

Su, K. Y. L., Rieke, G. H., Stapelfeldt, K. R., Malhotra, R., Bryden, G., Smith, P. S., Misselt, K. A., Moro-Martin, A., and Williams, J. P. (2009). The debris disk around hr 8799. The Astrophysical Journal, 705(1):314.

Sudarsky, D., Burrows, A., and Hubeny, I. (2003). Theoretical Spectra and Atmospheres of Extrasolar Giant Planets. The Astrophysical Journal, 588(2):1121–1148.

Swain, M. R., Bouwman, J., Akeson, R. L., Lawler, S., and Beichman, C. A. (2008). The Mid-Infrared Spectrum of the Transiting Exoplanet HD 209458b. The Astrophysical Journal, 674(1):482–497.

Tang, Y. K. and Gai, N. (2011). Asteroseismic modelling of the metal-poor star τ Ceti. Astronomy & Astrophysics, 526:A35.

Teague, R., Bae, J., and Bergin, E. A. (2019). Meridional flows in the disk around a young star. Nature, 574(7778):378–381.

Teague, R., Bae, J., Bergin, E. A., Birnstiel, T., and Foreman-Mackey, D. (2018). A Kinematical Detection of Two Embedded Jupiter-mass Planets in HD 163296. The Astrophysical Journal Letters, 860(1):L12.

Thalmann, C., Usuda, T., Kenworthy, M., Janson, M., Mamajek, E. E., Brandner, W., Dominik, C., Goto, M., Hayano, Y., Henning, T., Hinz, P. M., Minowa, Y., and Tamura, M. (2011). Piercing the Glare: A Direct Imaging Search for Planets in the Sirius System. The Astrophysical Journal Letters, 732(2):L34.

Thi, W. F., Woitke, P., and Kamp, I. (2011). Radiation thermo-chemical models of protoplanetary discs - III. Impact of inner rims on spectral energy distributions. Monthly Notices of the Royal Astronomical Society, 412(2):711–726.

Toomre, A. (1964). On the gravitational stability of a disk of stars. The Astrophysical Journal, 139:1217–1238.

Tremblin, P., Amundsen, D. S., Chabrier, G., Baraffe, I., Drummond, B., Hinkley, S., Mourier, P., and Venot, O. (2016a). Cloudless Atmospheres for L/T Dwarfs and Extrasolar Giant Planets. The Astrophysical Journal Letters, 817(2):L19.

Tremblin, P., Amundsen, D. S., Chabrier, G., Baraffe, I., Drummond, B., Hinkley, S., Mourier, P., and Venot, O. (2016b). Cloudless Atmospheres for L/T Dwarfs and Extrasolar Giant Planets. The Astrophysical Journal Letters, 817(2):L19.

Tremblin, P., Amundsen, D. S., Mourier, P., Baraffe, I., Chabrier, G., Drummond, B., Homeier, D., and Venot, O. (2015). Fingering Convection and Cloudless Models for Cool Brown Dwarf Atmospheres. The Astrophysical Journal Letters, 804(1):L17.

Tremblin, P., Chabrier, G., Mayne, N. J., Amundsen, D. S., Baraffe, I., Debras, F., Drummond, B., Manners, J., and Fromang, S. (2017). Advection of Potential Temperature in the Atmosphere of Irradiated Exoplanets: A Robust Mechanism to Explain Radius Inflation. The Astrophysical Journal, 841(1):30.

Triaud, A. H. M. J., Collier Cameron, A., Queloz, D., Anderson, D. R., Gillon, M., Hebb, L., Hellier, C., Loeillet, B., Maxted, P. F. L., Mayor, M., Pepe, F., Pollacco, D., Ségransan, D., Smalley, B., Udry, S., West, R. G., and Wheatley, P. J. (2010). Spin-orbit angle measurements for six southern transiting planets. New insights into the dynamical origins of hot Jupiters. Astronomy & Astrophysics, 524:A25.

Trilling, D. E., Bryden, G., Beichman, C. A., Rieke, G. H., Su, K. Y. L., Stansberry, J. A., Blaylock, M., Stapelfeldt, K. R., Beeman, J. W., and Haller, E. E. (2008). Debris Disks around Sun-like Stars. The Astrophysical Journal, 674(2):1086–1105.

Tsukagoshi, T., Muto, T., Nomura, H., Kawabe, R., Kanagawa, K. D., Okuzumi, S., Ida, S., Walsh, C., Millar, T. J., Takahashi, S. Z., Hashimoto, J., Uyama, T., and Tamura, M. (2019). Discovery of An au-scale Excess in Millimeter Emission from the Protoplanetary Disk around TW Hya. The Astrophysical Journal Letters, 878(1):L8.

Tsukagoshi, T., Nomura, H., Muto, T., Kawabe, R., Ishimoto, D., Kanagawa, K. D., Okuzumi, S., Ida, S., Walsh, C., and Millar, T. J. (2016). A Gap with a Deficit of Large Grains in the Protoplanetary Disk around TW Hya. The Astrophysical Journal Letters, 829(2):L35.

Tuomi, M., Jones, H. R. A., Jenkins, J. S., Tinney, C. G., Butler, R. P., Vogt, S. S., Barnes, J. R., Wittenmyer, R. A., O'Toole, S., Horner, J., Bailey, J., Carter, B. D., Wright, D. J., Salter, G. S., and Pinfield, D. (2013). Signals embedded in the radial velocity noise. Periodic variations in the τ Ceti velocities. Astronomy & Astrophysics, 551:A79.

Turchi, A., Masciadri, E., Pathak, P., and Kasper, M. (2020). High-accuracy short-term precipitable water-vapour operational forecast at the Very Large Telescope and perspectives for sky background forecast. Monthly Notices of the Royal Astronomical Society, 497(4):4910–4920.

Urban, P. A. and Schortman, E. (2019). Multiple views of Stonehenge, page 32. Routledge.

Vacca, W. D. and Sandell, G. (2011). Near-infrared Spectroscopy of TW Hya: A Revised Spectral Type and Comparison with Magnetospheric Accretion Models. The Astrophysical Journal, 732(1):8.

van Boekel, R., Henning, T., Menu, J., de Boer, J., Langlois, M., Müller, A., Avenhaus, H., Boccaletti, A., Schmid, H. M., Thalmann, C., Benisty, M., Dominik, C., Ginski, C., Girard, J. H., Gisler, D., Lobo Gomes, A., Menard, F., Min, M., Pavlov, A., Pohl, A., Quanz, S. P., Rabou, P., Roelfsema, R., Sauvage, J. F., Teague, R., Wildi, F., and Zurlo, A. (2017). Three Radial Gaps in the Disk of TW Hydrae Imaged with SPHERE. The Astrophysical Journal, 837(2):132.

van Boekel, R., Min, M., Waters, L. B. F. M., de Koter, A., Dominik, C., van den Ancker, M. E., and Bouwman, J. (2005). A 10 μm spectroscopic survey of Herbig Ae star disks: Grain growth and crystallization. Astronomy & Astrophysics, 437(1):189–208.

van Boekel, R., Waters, L. B. F. M., Dominik, C., Dullemond, C. P., Tielens, A. G. G. M., and de Koter, A. (2004). Spatially and spectrally resolved 10 μm emission in Herbig Ae/Be stars. Astronomy & Astrophysics, 418:177–184.

van den Ancker, M. E., The, P. S., Tjin A Djie, H. R. E., Catala, C., de Winter, D., Blondel, P. F. C., and Waters, L. B. F. M. (1997). HIPPARCOS data on Herbig Ae/Be stars: an evolutionary scenario. Astronomy & Astrophysics, 324:L33–L36.

van der Marel, N., Williams, J. P., and Bruderer, S. (2018). Rings and gaps in protoplanetary disks: Planets or snowlines? The Astrophysical Journal, 867(1):L14.

van der Plas, G., Ménard, F., Gonzalez, J.-F., Perez, S., Rodet, L., Pinte, C., Cieza, L., Casassus, S., and Benisty, M. (2019). Alma study of the hd 100453 ab system and the tidal interaction of the companion with the disk. Astronomy & Astrophysics, 624:A33.

Vanderburg, A., Rappaport, S. A., Xu, S., Crossfield, I. J. M., Becker, J. C., Gary, B., Murgas, F., Blouin, S., Kaye, T. G., Palle, E., Melis, C., Morris, B. M., Kreidberg, L., Gorjian, V., Morley, C. V., Mann, A. W., Parviainen, H., Pearce, L. A., Newton, E. R., Carrillo, A., Zuckerman, B., Nelson, L., Zeimann, G., Brown, W. R., Tronsgaard, R., Klein, B., Ricker, G. R., Vanderspek, R. K., Latham, D. W., Seager, S., Winn, J. N., Jenkins, J. M., Adams, F. C., Benneke, B., Berardo, D., Buchhave, L. A., Caldwell, D. A., Christiansen, J. L., Collins, K. A., Colón, K. D., Daylan, T., Doty, J., Doyle, A. E., Dragomir, D., Dressing, C., Dufour, P., Fukui, A., Glidden, A., Guerrero, N. M., Guo, X., Heng, K., Henriksen, A. I., Huang, C. X., Kaltenegger, L., Kane, S. R., Lewis, J. A., Lissauer, J. J., Morales, F., Narita, N., Pepper, J., Rose, M. E., Smith, J. C., Stassun, K. G., and Yu, L. (2020). A giant planet candidate transiting a white dwarf. Nature, 585(7825):363–367.

Verhoeff, A. (2009). Dusty Disks around Young Stars. PhD thesis, Sterrenkundig Instituuut "Anton Pannekoek", University of Amsterdam.

Vernet, J., Dekker, H., D'Odorico, S., Kaper, L., Kjaergaard, P., Hammer, F., Randich, S., Zerbi, F., Groot, P. J., Hjorth, J., Guinouard, I., Navarro, R., Adolfse, T., Albers, P. W., Amans, J. P., Andersen, J. J., Andersen, M. I., Binetruy, P., Bristow, P., Castillo, R., Chemla, F., Christensen, L., Conconi, P., Conzelmann, R., Dam, J., de Caprio, V., de Ugarte Postigo, A.,

Delabre, B., di Marcantonio, P., Downing, M., Elswijk, E., Finger, G., Fischer, G., Flores, H., François, P., Goldoni, P., Guglielmi, L., Haigron, R., Hanenburg, H., Hendriks, I., Horrobin, M., Horville, D., Jessen, N. C., Kerber, F., Kern, L., Kiekebusch, M., Kleszcz, P., Klougart, J., Kragt, J., Larsen, H. H., Lizon, J. L., Lucuix, C., Mainieri, V., Manuputy, R., Martayan, C., Mason, E., Mazzoleni, R., Michaelsen, N., Modigliani, A., Moehler, S., Møller, P., Norup Sørensen, A., Nørregaard, P., Péroux, C., Patat, F., Pena, E., Pragt, J., Reinero, C., Rigal, F., Riva, M., Roelfsema, R., Royer, F., Sacco, G., Santin, P., Schoenmaker, T., Spano, P., Sweers, E., Ter Horst, R., Tintori, M., Tromp, N., van Dael, P., van der Vliet, H., Venema, L., Vidali, M., Vinther, J., Vola, P., Winters, R., Wistisen, D., Wulterkens, G., and Zacchei, A. (2011). X-shooter, the new wide band intermediate resolution spectrograph at the ESO Very Large Telescope. Astronomy & Astrophysics, 536:A105.

Vidal-Madjar, A., Désert, J. M., Lecavelier des Etangs, A., Hébrard, G., Ballester, G. E., Ehrenreich, D., Ferlet, R., McConnell, J. C., Mayor, M., and Parkinson, C. D. (2004). Detection of Oxygen and Carbon in the Hydrodynamically Escaping Atmosphere of the Extrasolar Planet HD 209458b. The Astrophysical Journal Letters, 604(1):L69–L72.

Vidal-Madjar, A., Lecavelier des Etangs, A., Désert, J. M., Ballester, G. E., Ferlet, R., Hébrard, G., and Mayor, M. (2003). An extended upper atmosphere around the extrasolar planet HD209458b. Nature, 422(6928):143–146.

Vigan, A., Bonavita, M., Biller, B., Forgan, D., Rice, K., Chauvin, G., Desidera, S., Meunier, J. C., Delorme, P., Schlieder, J. E., Bonnefoy, M., Carson, J., Covino, E., Hagelberg, J., Henning, T., Janson, M., Lagrange, A. M., Quanz, S. P., Zurlo, A., Beuzit, J. L., Boccaletti, A., Buenzli, E., Feldt, M., Girard, J. H. V., Gratton, R., Kasper, M., Le Coroller, H., Mesa, D., Messina, S., Meyer, M., Montagnier, G., Mordasini, C., Mouillet, D., Moutou, C., Reggiani, M., Segransan, D., and Thalmann, C. (2017). The VLT/NaCo large program to probe the occurrence of exoplanets and brown dwarfs at wide orbits. IV. Gravitational instability rarely forms wide, giant planets. Astronomy & Astrophysics, 603:A3.

Vigan, A., Gry, C., Salter, G., Mesa, D., Homeier, D., Moutou, C., and Allard, F. (2015). High-contrast imaging of Sirius A with VLT/SPHERE: looking for giant planets down to one astronomical unit. Monthly Notices of the Royal Astronomical Society, 454(1):129–143.

Vissapragada, S., Knutson, H. A., Jovanovic, N., Harada, C. K., Oklopčić, A., Eriksen, J., Mawet, D., Millar-Blanchaer, M. A., Tinyanont, S., and Vasisht, G. (2020). Constraints on Metastable Helium in the Atmospheres of WASP-69b and WASP-52b with Ultranarrowband Photometry. The Astronomical Journal, 159(6):278.

Viswanath, G. (2021). Constraints on the nearby exoplanet Eps Ind Ab from deep near/mid-infrared imaging limits. in preparation.

Vorobyov, E. I. (2013). Formation of giant planets and brown dwarfs on wide orbits. Astronomy & Astrophysics, 552:A129.

Wagner, K., Apai, D., Kasper, M., and Robberto, M. (2015). DISCOVERY OF a TWO-ARMED SPIRAL STRUCTURE IN THE GAPPED DISK AROUND HERBIG ae STAR HD 100453. The Astrophysical Journal, 813(1):L2.

Wagner, K., Boehle, A., Pathak, P., Kasper, M., Arsenault, R., Jakob, G., Käufl, U., Leveratto, S., Maire, A.-L., Pantin, E., Siebenmorgen, R., Zins, G., Absil, O., Ageorges, N., Apai, D., Carlotti, A., Choquet, É., Delacroix, C., Dohlen, K., Duhoux, P., Forsberg, P., Fuenteseca, E., Gutruf, S., Guyon, O., Huby, E., Kampf, D., Karlsson, M., Kervella, P., Kirchbauer, J.-P., Klupar, P., Kolb, J., Mawet, D., N'Diaye, M., Orban de Xivry, G., Quanz, S. P., Reutlinger, A., Ruane, G., Riquelme, M., Soenke, C., Sterzik, M., Vigan, A., and de Zeeuw, T. (2021). Imaging low-mass planets within the habitable zone of α centauri. Nature Communications, 12(1):922.

Wagner, K., Dong, R., Sheehan, P., Apai, D., Kasper, M., McClure, M., Morzinski, K. M., Close, L., Males, J., Hinz, P., Quanz, S. P., and Fung, J. (2018). The orbit of the companion to HD 100453a: Binary-driven spiral arms in a protoplanetary disk. The Astrophysical Journal, 854(2):130.

Wagner, K., Stone, J. M., Spalding, E., Apai, D., Dong, R., Ertel, S., Leisenring, J., and Webster, R. (2019). Thermal Infrared Imaging of MWC 758 with the Large Binocular Telescope: Planetary-driven Spiral Arms? The Astrophysical Journal, 882(1):20.

Wahhaj, Z. et al. (2011). The GEMINI NICI planet-finding campaign: Discovery of a substellar L dwarf companion to the nearby young M dwarf CD–35 2722. The Astrophysical Journal, 729(2):139.

Walker, G. A. H., Walker, A. R., Irwin, A. W., Larson, A. M., Yang, S. L. S., and Richardson, D. C. (1995). A search for Jupiter-mass companions to nearby stars. Icarus, 116(2):359–375.

Walsh, C., Daley, C., Facchini, S., and Juhász, A. (2017). CO emission tracing a warp or radial flow within $\lesssim$100 au in the HD 100546 protoplanetary disk. Astronomy & Astrophysics, 607:A114.

Walsh, C., Juhász, A., Pinilla, P., Harsono, D., Mathews, G. S., Dent, W. R. F., Hogerheijde, M. R., Birnstiel, T., Meeus, G., Nomura, H., Aikawa, Y., Millar, T. J., and Sand ell, G. (2014). ALMA Hints at the Presence of two Companions in the Disk around HD 100546. The Astrophysical Journal Letters, 791(1):L6.

Walsh, K. J., Morbidelli, A., Raymond, S. N., O'Brien, D. P., and Mandell, A. M. (2011). A low mass for Mars from Jupiter's early gas-driven migration. Nature, 475(7355):206–209.

Wang, J., Fischer, D. A., Horch, E. P., and Huang, X. (2015). On the Occurrence Rate of Hot Jupiters in Different Stellar Environments. The Astrophysical Journal, 799(2):229.

Wang, J. J. et al. (2018). Dynamical constraints on the HR 8799 planets with GPI. The Astronomical Journal, 156(5):192.

Way, M. J. and Srivastava, A. N. (2006). Novel Methods for Predicting Photometric Redshifts from Broadband Photometry Using Virtual Sensors. The Astrophysical Journal, 647(1):102–115.

Weinberger, A. J., Anglada-Escudé, G., and Boss, A. P. (2013). Distance and Kinematics of the TW Hydrae Association from Parallaxes. The Astrophysical Journal, 762(2):118.

Welsh, W. F., Orosz, J. A., Carter, J. A., Fabrycky, D. C., Ford, E. B., Lissauer, J. J., Prša, A., Quinn, S. N., Ragozzine, D., Short, D. R., et al. (2012). Transiting circumbinary planets kepler-34 b and kepler-35 b. Nature, 481(7382):475–479.

Wertz, O., Absil, O., Gómez González, C. A., Milli, J., Girard, J. H., Mawet, D., and Pueyo, L. (2017). VLT/SPHERE robust astrometry of the HR8799 planets at milliarcsecond-level accuracy. Orbital architecture analysis with PyAstrOFit. Astronomy & Astrophysics, 598:A83.

West, R. G., Anderson, D. R., Gillon, M., Hebb, L., Hellier, C., Maxted, P. F. L., Queloz, D., Smalley, B., Triaud, A. H. M. J., Wilson, D. M., Bentley, S. J., Collier Cameron, A., Enoch, B., Horne, K., Irwin, J., Lister, T. A., Mayor, M., Parley, N., Pepe, F., Pollacco, D., Segransan, D., Spano, M., Udry, S., and Wheatley, P. J. (2009). The Low Density Transiting Exoplanet WASP-15b. The Astronomical Journal, 137(6):4834–4836.

White, J. A., Aufdenberg, J., Boley, A. C., Devlin, M., Dicker, S., Hauschildt, P., Hughes, A. G., Hughes, A. M., Mason, B., Matthews, B., Moór, A., Mroczkowski, T., Romero, C., Sievers, J., Stanchfield, S., Tapia, F., and Wilner, D. (2019). The MESAS Project: Long-wavelength Follow-up Observations of Sirius A. The Astrophysical Journal, 875(1):55.

Wichittanakom, C., Oudmaijer, R. D., Fairlamb, J. R., Mendigutía, I., Vioque, M., and Ababakr, K. M. (2020). The accretion rates and mechanisms of Herbig Ae/Be stars. Monthly Notices of the Royal Society, 493(1):234–249.

Winters, J. G., Medina, A. A., Irwin, J. M., Charbonneau, D., Astudillo-Defru, N., Horch, E. P., Eastman, J. D., Vrijmoet, E. H., Henry, T. J., Diamond-Lowe, H., Winston, E., Barclay, T., Bonfils, X., Ricker, G. R., Vanderspek, R., Latham, D. W., Seager, S., Winn, J. N., Jenkins, J. M., Udry, S., Twicken, J. D., Teske, J. K., Tenenbaum, P., Pepe, F., Murgas, F., Muirhead, P. S., Mink, J., Lovis, C., Levine, A. M., Lépine, S., Jao, W.-C., Henze, C. E., Furész, G., Forveille, T., Figueira, P., Esquerdo, G. A., Dressing, C. D., Díaz, R. F., Delfosse, X., Burke, C. J., Bouchy, F., Berlind, P., and Almenara, J.-M. (2019). Three Red Suns in the Sky: A Transiting, Terrestrial Planet in a Triple M-dwarf System at 6.9 pc. The Astronomical Journal, 158(4):152.

Woitke, P., Kamp, I., Antonellini, S., Anthonioz, F., Baldovin-Saveedra, C., Carmona, A., Dionatos, O., Dominik, C., Greaves, J., Güdel, M., Ilee, J. D., Liebhardt, A., Menard, F., Min, M., Pinte, C., Rab, C., Rigon, L., Thi, W. F., Thureau, N., and Waters, L. B. F. M. (2019). Consistent Dust and Gas Models for Protoplanetary Disks. III. Models for Selected Objects from the FP7 DIANA Project. Publications of the Astronomical Society of the Pacific, 131(1000):064301.

Woitke, P., Kamp, I., and Thi, W.-F. (2009). Radiation thermo-chemical models of protoplanetary disks. I. Hydrostatic disk structure and inner rim. Astronomy & Astrophysics, 501:383–406.

Woitke, P., Min, M., Pinte, C., Thi, W. F., Kamp, I., Rab, C., Anthonioz, F., Antonellini, S., Baldovin-Saavedra, C., Carmona, A., Dominik, C., Dionatos, O., Greaves, J., Güdel, M., Ilee, J. D., Liebhart, A., Ménard, F., Rigon, L., Waters, L. B. F. M., Aresu, G., Meijerink, R., and Spaans, M. (2016). Consistent dust and gas models for protoplanetary disks. I. Disk shape, dust settling, opacities, and PAHs. Astronomy & Astrophysics, 586:A103.

Wolszczan, A. and Frail, D. A. (1992). A planetary system around the millisecond pulsar PSR1257 + 12. Nature, 355(6356):145–147.

Wright, J. T. (2018). Radial Velocities as an Exoplanet Discovery Method, page 4. Springer.

Youdin, A. N. and Goodman, J. (2005). Streaming Instabilities in Protoplanetary Disks. The Astrophysical Journal, 620(1):459–469.

Yu, S.-Y., Ho, L. C., and Zhu, Z. (2019). A Tight Relation between Spiral Arm Pitch Angle and Protoplanetary Disk Mass. The Astrophysical Journal, 877(2):100.

Zapatero Osorio, M. R., Martín, E. L., Bouy, H., Tata, R., Deshpande, R., and Wainscoat, R. J. (2006). Spectroscopic Rotational Velocities of Brown Dwarfs. The Astrophysical Journal, 647(2):1405–1412.

Zechmeister, M., Kürster, M., Endl, M., Lo Curto, G., Hartman, H., Nilsson, H., Henning, T., Hatzes, A. P., and Cochran, W. D. (2013). The planet search programme at the ESO CES and HARPS. IV. The search for Jupiter analogues around solar-like stars. Astronomy & Astrophysics, 552:A78.

Zhu, W., Petrovich, C., Wu, Y., Dong, S., and Xie, J. (2018a). About 30% of Sun-like Stars Have Kepler-like Planetary Systems: A Study of Their Intrinsic Architecture. The Astrophysical Journal, 860(2):101.

Zhu, Z. (2015). ACCRETING CIRCUMPLANETARY DISKS: OBSERVATIONAL SIGNATURES. The Astrophysical Journal, 799(1):16.

Zhu, Z., Andrews, S. M., and Isella, A. (2018b). On the radio detectability of circumplanetary discs. Monthly Notices of the Royal Society, 479(2):1850–1865.

Zubko, V. G., Mennella, V., Colangeli, L., and Bussoletti, E. (1996). Optical constants of cosmic carbon analogue grains - I. Simulation of clustering by a modified continuous distribution of ellipsoids. Monthly Notices of the Royal Society, 282(4):1321–1329.

Zuckerman, B., Rhee, J. H., Song, I., and Bessell, M. S. (2011). The Tucana/Horologium, Columba, AB Doradus and Argus associations: New members and dusty debris disks. The Astrophysical Journal, 732(2):61.

Zurlo, A. et al. (2016). First light of the VLT planet finder SPHERE - III. New spectrophotometry and astrometry of the HR9 exoplanetary system. Astronomy & Astrophysics, 587:A57.

Acknowledgements

First and foremost, I would like to thank my supervisor, Mario van den Ancker, for all his support and advice over the last three years. You have truly been the best supervisor a student could ask for and I immensely appreciate all your time and effort. Thank you for your guidance, for sending me to Paranal, for involving me in collaborations, for helping to improve my job applications, for expressing faith in my abilities when I was unsure and too many other things to mention.

Thank you also to my mentors Laura Watkins and Paulo Miles-Paéz. Thank you, Laura, for your career advice and I enjoyed organising the science day together (thank you to Miranda Jarvis too!). Thank you, Paulo, for all your technical help in the past year.

My thanks to all the members of the thesis committee for their time and advice. Especially to Markus Kissler-Patig for being my official supervisor and helping with all the logistics of the university, both at the beginning and the end of the PhD.

At ESO, I want to thank Nelma Silva, who is always ready to help the students with whatever they need and takes the best cat pictures, my office mate Souradeep Bhattacharya, who always had time for a chat and helped me find my way around ESO, Katja Fahrion, for translating the German summary of this thesis, the NEAR science verification team, who have taught me so much about observing at the telescope and everything leading up to it, to everyone at the boardgames evenings, where I was introduced to many great people and learned a lot of new games and finally, to all my fellow students at ESO, however long or short our stays may have overlapped, for making my stay a fun one too.

My thanks also to everyone at the Stockholm astronomy department who has been incredibly welcoming and made me feel accepted when my two week pandemic visit became almost a year.

Thank you to my parents and to Olivier and Nicolaas, for their support ever since I decided to get into astronomy and especially since I moved abroad (and long before), and to Audinga-Dea Hazewinkel (who knew thrillers are such good stress relief?).

Finally, I want to thank my boyfriend Alex Pietrow. You may not have made it to co-author, but I really could not have done it without your support.